Photosensitizing Diiron Hydrogenase Mimics: Excited State Dynamics

Lewis Cletheroe, Department of Chemistry

Supervisor: Prof. Julia Weinstein

Submitted for the Award of Doctor of Philosophy

December 2017

ABSTRACT

Catalytically evolving hydrogen from a system that photosensitizes diiron hydrogenase could be a carbon neutral method for converting and storing energy. Two methods for producing a photocatalytic system are investigated; the covalently linking of photosensitizer and catalyst moieties to enhance electron transfer, or keeping them separate and relying on collisions to transfer the energy necessary to drive the reaction.

A new covalently linked dyad has been synthesized that has a Charge Separated State (CSS) as its excited state. The charge separation is between the platinum (II) photosensitizer (PS) and the diiron hydrogenase mimic catalyst moieties. A CSS state has been observed, quenching the emission of the PS moiety. The CSS has a lifetime of 247 ± 25 ps determined by picosecond time-resolved infrared spectroscopy. This is a similar lifetime to previously studied PS-hydrogenase dyads and is unlikely to be long enough to effectively initiate a hydrogen evolution reaction.

New photosensitizer complexes have been developed to drive photo-catalysed hydrogen evolution. These complexes feature a platinum (II) centre ligated by a phenyl-bipyridine cyclometalating ligand and a substituted phenyl acetylide ligand. Their ground and excited states have been probed using photophysical techniques, revealing emissive states with lifetimes of 63 – 703 ns and quantum yields of 0.002 – 0.27. This broad range of lifetimes and quantum yields was further investigated using picosecond time-resolved infrared spectroscopy to reveal that there is intramolecular quenching of emissive states by an equilibrium with a dark charge transfer excited state.

Investigation of how these new PS complexes in their excited state interact with [FeFe] complexes was undertaken by utilizing Stern Volmer quenching kinetics. These PS complexes were found to be quenched at close to the diffusion limited rate ($1.4 – 2.6 \times 10^9$ mol^{-1} dm^3 s^{-1}), indicating that there is energy transfer between the PS and catalyst complexes. A false Marcus inverted region was observed for these complexes and further investigation revealed new information on the nature of the excited state equilibria present in the PS complexes.

ACKNOWLEDGEMENTS

Completion of this thesis would not have been possible without the help and advice of my friends and colleagues. I would like to thank these people for their hard work and patience in helping me reach the end of my studies.

I would like to thank Prof Julia Weinstein for giving me the chance to work in her group and for all the help and support she has provided throughout my studies. Her enthusiasm towards research and engaging with the wider scientific community has inspired me to meet with new collaborators, attend national and international conferences and think about how science integrates into the wider world. Thanks must also be given to the University of Sheffield and Project Sunshine DTC for funding and providing excellent training opportunities.

During my time working at the University of East Anglia I benefitted from the experience and knowledge of Professor Chris Pickett and James Woods. Their assistance was greatly appreciated and provided a starting point to reaching some of the goals described further. It was a pleasure to travel back to my home city and experience the collegiate atmosphere that exists there.

I have had the opportunity to perform experiments at the Rutherford Appleton Laboratories in Oxfordshire and feel extremely privileged for having done so. I have to thank Professor Mike Towrie, Dr Igor Sazanovich, Dr Milan Delor and others for their help with TRIR and TA measurements.

The computational chemistry presented in this thesis would not have been possible without the help of Dr Anthony Meijer and Theo Keane, whose expertise and skills were essential to providing a theoretical basis to my experimental ramblings.

It has been a pleasure to work in the University's chemistry department, thanks to the Weinstein group, past and present, and the other friends I have in the department. Incredibly supportive and always helpful, these people have made living and working in Sheffield enjoyable. Thank you to my friends outside of the department, for reminding me of my life outside science, and my family, for their constant love and support.

Finally, to Alix, you have been the most important person on my voyage here, convincing me that I should follow my dream of being a scientist, and then being the support I needed to decide that I need a new dream. You have provided the love I need to get through this and get out. I will always be grateful that you were with me on this journey.

ABBREVIATIONS

aq	aqueous
2D	two dimensional
2DIR	two dimensional infrared
A	acceptor
Å	Angstrom
ASAP	atmospheric solids analysis probe
ATR	attenuated total reflectance
BAL	British anti-Lewisite
bdt	benzenedithiolate
bpy	2,2'-bipyridyl
c	centi
C.	Clostridium
Cat.	catalyst
cc	acetylide
CCD	Charge Coupled Device
COSY	Correlated Spectroscopy
CS	Charge-separated
CSS	Charge Separated State
CT	Charge Transfer
CV	Cyclic Voltammetry
d	doublet / deci
D	donor
D.	Desulfovibrio
DAS	decay associated spectra
DCC	N,N'-dicyclohexylcarbodiimide
DCM	dichloromethane
dd	doublet-of-doublets
DFT	Density Functional Theory
diff	diffusion
DMAP	N,N-dimethyl-4-aminopyridine
DMF	N,N-dimethylformamide
DMSO	dimethyl sulfoxide
DSSC	Dye Sensitised Solar Cell
E	energy
EAS	evolution associated spectra
edt	ethylene-2,2-dithiolate
EI	Electron Ionisation
EM	emission
EPR	Electron Paramagnetic Resonance
ES	Electrospray
ET	electron transfer
Et	ethyl
eV	electron Volt
f	femto
Fc	Ferrocene

Fc⁺	Ferrocinium
FTIR	Fourier transform infra-red
FWHM	full width half maximum
g	gram
GS	Ground State
HMDS	hexamethyldisilazane
HOMO	Highest Occupied Molecular Orbital
Hz	Hertz
hv	Photon energy
IC	Internal Conversion
IL	Intra-Ligand
^{i}Pr	isopropyl
IR	Infra-Red
ISC	Inter-System Crossing
J	coupling constant / Joule
K	Kelvin
k	rate constant
L	litre
LLCT	Ligand-to-Ligand Charge Transfer
LUMO	Lowest Unoccupied Molecular Orbital
m	milli / metre / multiplet
M	mol dm^{-3}
MALDI	Matrix Assisted Laser Desorption Ionisation
Me	Methyl
MesBIAN	mesityl bisiminoacenaphthene
min	minute
MLCT	Metal-to-Ligand Charge Transfer
MMLL'CT	Mixed Metal-Ligand-to-Ligand Charge Transfer
MO	molecular orbital
MS	Mass Spectrometry
n	nano
Nd:YAG	Neodynium doped Yttrium Aluminium Garnet
NMI	naphthalene monoimide
NMR	Nuclear Magnetic Resonance
OD	Optical Density
OLED	organic light emitting diode
OPA	optical parametric amplifier
OPO	optical parametric oscillator
OX	oxidation
p	pico
PCM	polarizable continuum model
pdt	propanedithiolate
Ph	phenyl
ppm	parts per million
PS	photosensitizer
Q	quencher
RED	reduction
Redox	reduction oxidation

RT	room temperature
s	second / singlet
S	singlet energy level
s2	step scan
S$_N$2	substitution, nucleophilic, second order
SOMO	Singly Occupied Molecular Orbital
t	triplet
T	tera /triplet energy level
T2DIR	Time Resolved 2D Infra-Red
TA	transient absorption
^{t}Bu	tertiary butyl
td	triplet-of-doublets
TD-DFT	time dependent density functional theory
tdt	toluenedithiolate
TEA	triethylamine
TEOA	triethanolamine
THF	tetrahydrofuran
Ti:Sapph	titanium doped sapphire
TLC	Thin Layer Chromatography
TOF	Time Of Flight
TOF	turnover frequency
TON	turnover number
tpy	terpyridyl
TRIR	Time Resolved Infra-Red
tt	triplet-of-triplets
UV	Ultra-Violet
V	Volt
vis	visible
W	Watt
w	work
X	halogen
δ	chemical shift
ε	extinction coefficient
λ	wavelength
μ	micro
ν	frequency
τ	lifetime
ɸ	quantum yield

TABLE OF CONTENTS

x

1. Hydrogen Production from Photosensitized Diiron Hydrogenase Model Complexes

INTRODUCTION

Sources of harmful anthropogenic greenhouse gases, such as carbon dioxide and methane, have caused an unprecedented rate of change in the surface temperature of the Earth since the early 20th century. According to working group 1 of the fifth assessment report of the intergovernmental panel on climate change (IPCC AR5 WG1), "It is certain that Global Mean Surface Temperature has increased since the late 19th century. Each of the past three decades has been successively warmer at the Earth's surface than all the previous decades in the instrumental record, and the first decade of the 21st century has been the warmest." Atmospheric carbon dioxide concentrations are 40% higher than pre-industrialized levels, methane concentrations are 150% higher than pre-industrialized levels and the average surface temperature of the Earth has risen 0.85°C since 1880, with 0.61°C of this rise occurring between 1986 and 2005, an example of the changes measured is given in Figure 1.[1] These changes may all lead to a global shift in climate, which may have severe effects on the wildlife, habitats and people of Earth.
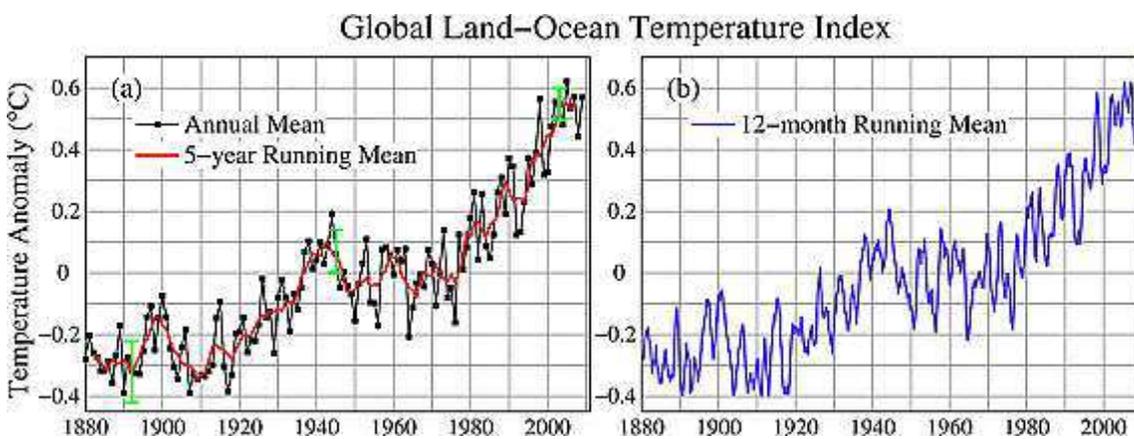
Figure 1 Global surface temperature anomalies relative to 1951–1980 mean for (a) annual and 5 year running means through 2009 and (b) 12 month running mean using data through June 2010.[2]

Based on data from the first assessment report of the IPCC and due to concern that anthropogenic greenhouse gas emissions will result in a warming of the Earth's surface and atmosphere that may adversely affect natural ecosystems and humankind, the United Nations Framework Convention on Climate Change (UNFCCC) was negotiated at an international summit in Rio de Janeiro, in 1992. This treaty aimed to set a framework for, "stabilization of greenhouse gas concentrations in the atmosphere at a level that would prevent dangerous anthropogenic interference with the climate system."[3] This treaty also set out that developed countries, having disproportionately high historical emissions, should lead the way in reducing their harmful emissions. Countries that are signatories to the UNFCCC have been compelled to act by the 1997 Kyoto protocol and further commitment has been affirmed in the 2015 Paris agreement.

These agreements set out economic routes to the mitigation of the effects of greenhouse gas emissions. This is done by setting caps on the emissions a nation may produce and allowing the economic trading of underspent GHG allowances from low emitting nations to nations that have emitted more than their cap allows. These measures have been highly criticized as being ineffective, producing very little change and allowing a "business as usual" approach for some actors.[4] By only changing the market conditions considered in GHG emissions and without changing how the world considers its energy use and the fuels used to generate useful heat and electricity, there will be no way to meet the targets set out in international climate agreements.

This requires a re-evaluation of international energy policy.[5-9] Investment in new, low carbon technology must feature in this policy. The abundant, convenient fuels of the past must be deprioritised in favour of alternative sources of energy. As the world switches from coal to

natural gas, in order to lower its emissions to meet current targets, so it will have to move from unabated fossil fuels to more modern energy sources to meet future, stricter targets. This will involve a diverse array of primary and secondary energy sources, including carbon neutral biofuels, wind and solar generation, new nuclear and hydroelectric power. Unfortunately, these methods offer no cost-effective solution for the problem of heat generation; meeting the peak demand for heat using electricity would require extremely expensive grid reinforcement. This problem is further compounded by the efforts to move transport, now the single highest GHG emitting sector in the UK, towards electrification. One of the fuels that may allow GHG emissions to be cut, whilst still allowing the electricity grid to meet peak demand cost effectively, is molecular hydrogen.

Hydrogen, when combined with oxygen or air, can be used as a fuel to produce either heat or electricity in fuel cells and combustion processes.[10-17] When hydrogen is used as a fuel, it produces zero carbon dioxide at its point of use and when used in a hydrogen fuel cell it produces only water emissions. Molecular hydrogen has high specific energy (kWh kg^{-1}) but low energy density (kWh dm^{-3}) due to a large, negative enthalpy of combustion, of -285.9 kJ mol^{-1}, but a low volumetric density, of 0.08988 g dm^{-1} at stp. These properties make it attractive for stationary applications but less so for transport applications; even when compressed at the 700 bar currently used in fuel cell electric vehicles (FCEVs), hydrogen gas has a much lower energy density than other "low carbon" fuels such as compressed natural gas and biofuels, although this problem is often offset by the higher efficiencies of electric motors compared to internal combustion engines. These features make hydrogen an attractive fuel when considering how to decarbonise modern society.

Unfortunately, despite atomic hydrogen being the most abundant element in the universe, molecular hydrogen is not abundant, in nature, on earth; it cannot be a source of energy but must be considered an energy vector. The method for producing hydrogen should always be considered when assessing whether it has any effect on reducing CO_2 emissions. There are numerous routes for hydrogen production, each with their own advantages and disadvantages when it comes to decarbonising modern life. These methods include:

- Electrolysis of water
- Steam-methane reforming
- Gasification
- Thermochemical water hydrolysis
- Biochemical hydrogen production

These methods rely on an energy input to produce hydrogen. Although electrolysis can be powered using electricity generated from renewables, when electrolysers are powered by grid electricity they inevitably use electricity generated using fossil fuels. SMR and gasification require the use of carbon based fuels to produce hydrogen and the production of by-product carbon dioxide is inherent in their operation. To prevent the carbon dioxide emissions associated with the production of hydrogen, more efficient use of renewable fuel sources is needed. Using solar energy for the production of molecular hydrogen from water requires that methods already used for converting solar energy into electricity and other products are tailored, to efficiently use solar energy to drive the water splitting reaction. There is a large body of evidence dedicated to hydrogen production and electricity generation using solar energy.

PHOTOCHEMICAL HYDROGEN PRODUCTION

Solid state methods

Although the use of a p-n junction silicon semiconductor to convert solar energy into electricity was pioneered in 1954,[18] the use of titanium dioxide as a part of a photoelectrochemical system, by Fujishima and Honda in 1972, could be considered the first effective attempt to produce hydrogen using solar energy (Figure 2).[19] Briefly, a cathode comprising rutile TiO_2, a predominantly n-type semiconductor, was introduced into a photoelectrochemical cell under a 1 M NaOH electrolyte. This cathode was linked to a platinum black anode under 0.5 M H_2SO_4 electrolyte. When irradiated with UV light, the photoelectrochemical cell evolved hydrogen at the anode and oxygen at the cathode. This work has been consistently built on over the last 45 years and as such, the photocatalytic activity of TiO_2 is a well-reviewed area of chemistry.[20-29]
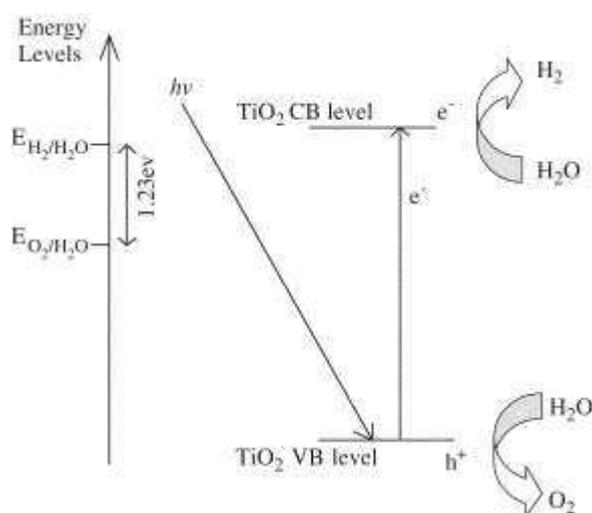
Figure 2 Mechanism of TiO_2 photocatalytic water-splitting for hydrogen production.[30]

The use of TiO_2 to photoelectrochemically produce hydrogen is not without its drawbacks. Principally, the band gap of TiO_2 in each of its forms does not allow visible light to be used to drive the water splitting reaction. The band gaps of the three polymorphs of TiO_2; rutile, anatase and brookite are 2.98, 3.19 and 3.26 eV respectively.[31-32] This corresponds to wavelengths of light in the far blue and UV spectrum (< 415 nm). UV light only accounts for around 8.3% of the light output of the sun and much less reaches the Earth's surface due to atmospheric absorption,[33] therefore devices based upon simple TiO_2 photocatalysts do not make the best use of solar radiation. Several methods have been proposed to help mitigate this issue; such as doping with non-metals or metals,[34-39] coupling to small band gap semiconductors[40] and dye sensitization.[41-44]

Improved solar energy capture using DSSC

Dye sensitized solar cells (DSSCs) have presented a method of harvesting light to produce an electrical current, using solar energy to drive electronic devices (Figure 3), which may include electrolysers. This method of solar energy conversion requires the separation of light harvesting from charge carrier transport, in contrast to the mechanism of the solid state devices mentioned above. This was first demonstrated in a system that could be considered both technically and economically effective that featured a nanocrystalline TiO_2 charge carrier with anchored $RuL_2(\mu$-$(CN)Ru(CN)L'_2)_2$, where L is 2,2'-bipryidne-4,4'dicarboxylic acid and L' is 2,2'-bipyridine light harvester.[45] This initial system provided a 7 – 8 % efficiency in converting simulated solar light to electrical energy conversion and has been adapted by the original author and several others to reach 14.1 % efficiency, with the utilisation of perovskite light absorbers.[46-47]
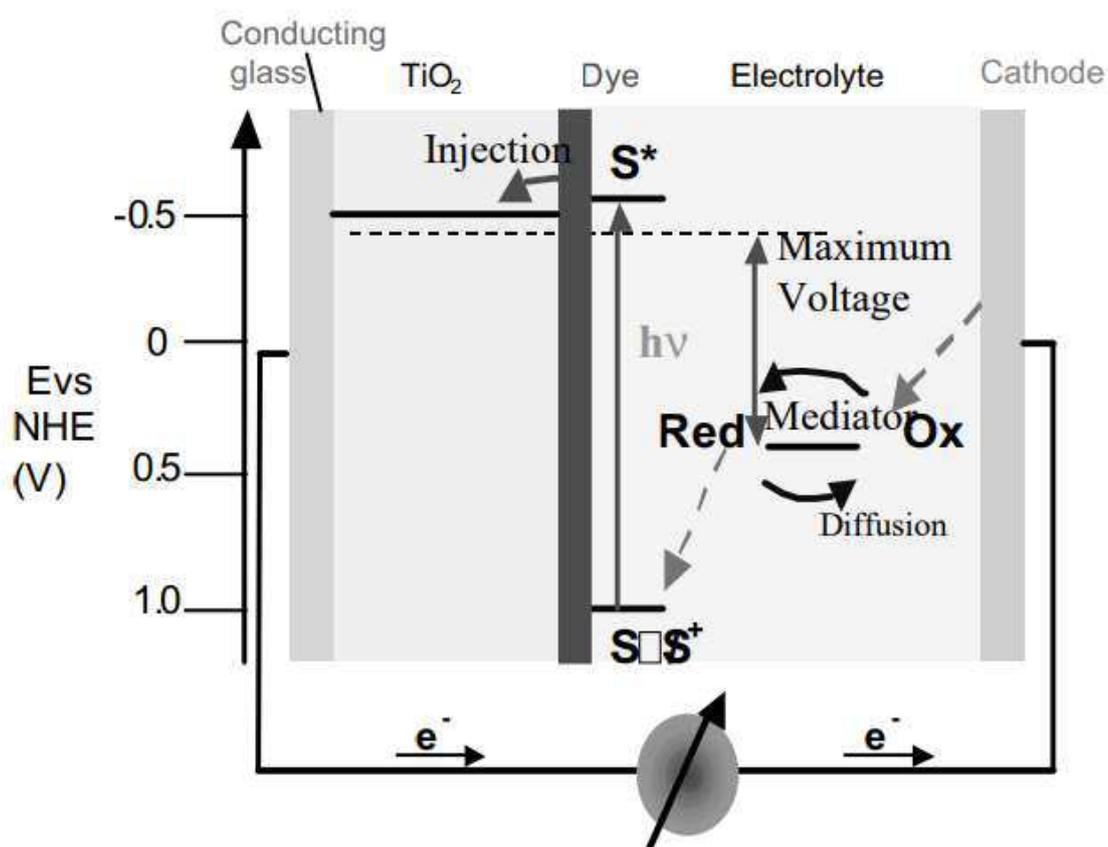
Figure 3 Principle of operation and energy level scheme of the dye-sensitized nanocrystalline solar cell. Photo-excitation of the sensitizer (S) is followed by electron injection into the conduction band of the mesoporous oxide semiconductor. The dye molecule is regenerated by the redox system, which itself is regenerated at the counter electrode by electrons passed through the load. Potentials are referred to the normal hydrogen electrode (NHE). The open-circuit voltage of the solar cell corresponds to the difference between the redox potential of the mediator and the Fermi level of the nanocrystallline film indicated with a dashed line.[48]

The general process for converting solar energy into electrical energy for a DSSC is as follows. The dye absorbs a photon and promotes an electron in the dye to an energy level above the conduction band of the electron relay, this electron is then transferred into the relay and used to power a circuit and regenerate the ground state dye molecule.[48] These cells feature a number of benefits over purely solid state cells based on TiO_2 or SiO_2 including;

- Utilizing a wider range of the solar spectrum and therefore increasing the amount of solar energy that can be converted,

- The cells are flexible and durable, allowing a greater number of use cases, allowing them to be used for non-static and in extreme environments,
- Optimisation of performance for different environments and conditions can be achieved by modifying the dye, allowing the light absorption to take place in the excitation bands of the dye.

A very wide range of dyes have been examined for their ability to be used in DSSCs beyond the more widely known perovskite and ruthenium materials mentioned above. In addition to these materials, platinum based photosensitizers have been investigated for their effectiveness when included in DSSCs.[49] The first examples of platinum dye based DSSCs incorporate platinum quinoline ditholates with either a 2,2'-bipyridine-4.4'-dicarboxylic acid or a 1,10-Phenanthroline-4,7-dicarboxylic acid ligand, which achieved conversion efficiencies of 2.57% and 2.33% respectively. These complexes were unable to absorb light from the low energy portion of the solar spectrum, limiting their efficiencies but they were effective in demonstrating that platinum photosensitizing complexes can be used in DSSC devices.[50]

8.2	3,3'	R = H
8.3	3,3'	R = Et
8.4	4,4'	R = H
8.5	4,4'	R = Et
8.6	5,5'	R = H
8.7	5,5'	R = Et
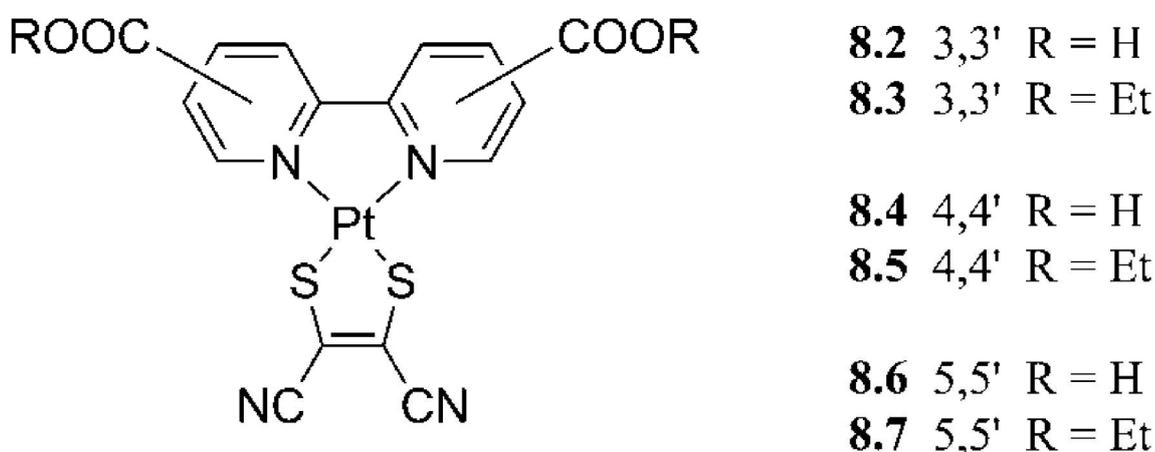
Figure 4 Examples of platinum bipyridine dithiolate light absorbing complexes used to investigate the effect of anchoring group position on complex electronics.[51]

Platinum dithiolate photosensitizers have also been used to demonstrate the effect anchoring groups have on the electronics of the light absorbing complexes and also the efficiencies of the DSSC (Figure 4). Phosphonates,[52] carboxylates[53-54] and catecholates[55] have all been considered for their use as anchoring groups, each with different effects on the electronic properties of platinum complexes. In addition, position of the anchoring groups within the complex has a strong effect on charge separation and therefore on injection into the semiconductor, as demonstrated by a series of complexes featuring carboxylate anchoring groups (Figure 4). Further investigation using EPR spectroscopy, supported by DFT modelling, revealed that for these complexes, **8.2** had significantly less contribution to the LUMO than **8.4** from the Pt orbitals and would therefore be at a disadvantage in charge separation due to lower coupling of the HOMO and LUMO in a charge transfer mechanism.[51]

Square planar platinum complexes are often considered for DSSC applications; complexes with catecholate,[49] thiolate[51, 53-54] and acetylide[56] have all been examined for their suitability for the possibility to act as a light harvester in the system. Despite their highly tuneable properties, these complexes have never shown high power conversion efficiencies (<3%) in comparison to the efficiencies of up to 11% seen in ruthenium photosensitizers.[57] However, the relatively small number of studies published on their use as photosensitizers suggests that large gains can be made if further investigation is pursued.

Forming a DSSC using a ruthenium light absorber was the first step in using metal complex dyes to convert solar energy into electrical energy and therefore should be considered a first step to

creating more complex cycles with chemical products using the same basic constituents and additional catalysts. In order to perform an artificial photosynthetic reaction requires the selection of a catalyst that can use the electrons produced from light harvesting complexes.

HYDROGEN PRODUCTION CATALYSTS

Small-scale electro-catalytic water splitting is typically achieved using expensive noble metal catalysts, with significant research performed to identify more cost effective catalysts.[58] The catalysts used for achieving solar water splitting (Eq. 1) or hydrogen production (Eq. 2) have also traditionally been based on the use of noble metal nanoparticles, which have been combined with transition metal light harvesters to achieve hydrogen evolution. This has been achieved historically with ruthenium[59-60] and more recently with iridium photosensitizer complexes.[61-66] Although these systems show strong activity in catalytically producing hydrogen using solar energy, they use expensive, non-abundant metals in their active centres and have limited lifetimes. Replacing the expensive noble metals in the catalyst is a priority for building a successful light driven hydrogen evolution system.

$$H_2O \longrightarrow H_2 + \frac{1}{2}O_2 \qquad\qquad \textbf{Eq. 1}$$

$$2H^+ \longrightarrow H_2 \qquad\qquad \textbf{Eq. 2}$$
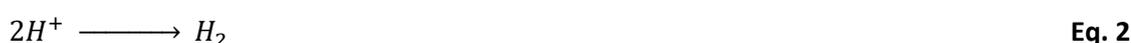
As such, new catalysts featuring more abundant first row transition metals have been developed. These catalysts are either used to split water and produce hydrogen or reduce protons to produce hydrogen. The choice of first row transition metal catalyst depends on the feedstock that is going to be converted to hydrogen. If the feedstock is water then a transition metal based water oxidation catalyst (WOC) should be considered. If protons are going to be considered as the feedstock for producing hydrogen, then a hydrogenase should be considered.

Water oxidation catalysts

Water oxidation catalysts featuring manganese, iron, cobalt and copper active centres have all been explored in the literature. Many of these metals have been used in metal oxide nanoparticles that show water splitting activity.[67] Although these complexes are based on the principles of the highly active biological system of photosystem II (PSII), none of these synthetic analogues show anything close to the turnover number or turnover frequency of PSII's oxygen evolution centre (OEC). PSII's OEC can achieve a TON of up to 180,000 per site, with a TOF of $100 - 400$ s^{-1}.[68-69] No synthetic analogue has achieved performance close to this, due to issues with stability and require restrictive conditions for their use. This class of catalyst is extremely difficult to photosensitise and characterise due to wide array of side reactions and products that take place and are produced in the cycle. As such, these will not be studied further in this thesis.

Hydrogenases

The primary alternative when considering hydrogen evolution using inexpensive 1st row transition metal catalysts are biologically inspired complexes based on a series of enzymes called hydrogenases.[70] This diverse group of metalloenzymes is often characterized by the nature of the active centre, as either [Fe] only, [NiFe] or [FeFe].[71] The [Fe] only hydrogenase enzyme group features an active site that comprises a single ligated iron atom and is unable to perform the conversion of protons into hydrogen, as the iron site is not redox active.[72] This leaves the [NiFe] and [FeFe] hydrogenases as targets for use in converting protons into hydrogen. Both these enzyme families feature an active site that contains a bimetallic core linked by sulfide ligands in a butterfly arrangement.

This thesis considers the hydrogenase enzyme family for its catalyst and more specifically, a catalyst inspired by the [FeFe] hydrogenase enzyme family, which has been shown to be electrochemically active in producing hydrogen gas from protons at high TOF.[73]

Diiron hydrogenases and their models

Diiron hydrogenases are a group of enzymes that all feature metallosulfur clusters of iron and sulfur to perform the reversible transformation of protons into molecular hydrogen. This reaction is used in anaerobic bacteria, such as C. Pasteurianum. The active site of these enzymes feature a metallosulfur cluster featuring two irons linked by cysteines in a butterfly configuration (Figure 5). There has been extensive study into the behaviour and properties of this class of enzymes.[71, 73-75]
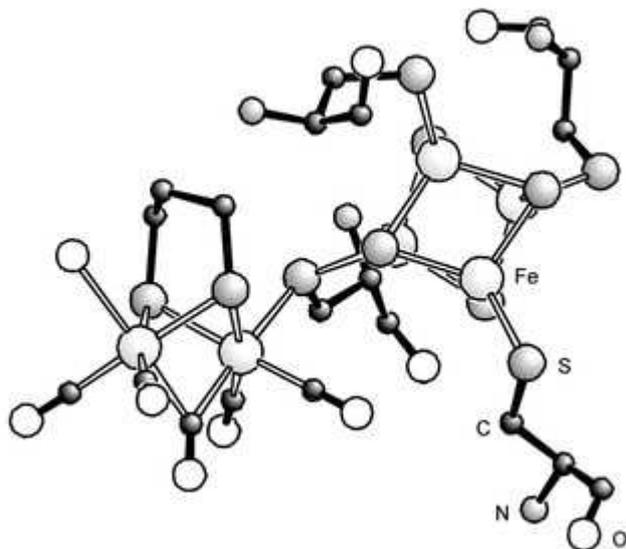
Figure 5 A composite structure of the H-centre of [FeFe] hydrogenase constructed from the crystal structures of hydrogenases isolated from D. desulfuricans and C. pasteurianum and FTIR data from D. vulgaris.[73]

The crucial details to note about this structure are the bridged disulfide linker between the iron centres, the carbon monoxide and cyanide ligands and the iron sulfur cubane redox shuttle located close to the active site. The Fe_4S_4 cluster acts as an electron shuttle, providing the necessary electrons for the active site. The CO and CN^- ligands, typically poisonous to living organisms, play important mechanistic and electronic roles. The disulfide bridge link is suggested to be important as a proton shuttle, especially when the bridge features a nitrogen atom.

Naturally occurring diiron hydrogenase enzymes catalyse the conversion of protons into dihydrogen at high rates. In an effort to exploit the high activity of this enzyme for fuel production, a large number of synthetic analogues have been synthesised in many studies, involving examination of their mechanistic details and have been investigated for their use in hydrogen production.[70, 73, 76-80]

The incorporation of these catalysts into systems that offer a way to harvest light should allow for an artificial photosynthetic system, due to the well-studied and exploited nature of the underlying electrochemically active catalyst. This requires that some method of absorbing photons and promoting electrons to do the hydrogen production reaction is needed, with the accompanying issues of attempting to couple two structurally unique complexes in a way that prevents either losing their initial activity for their role. Attempts to do this have been described below.

MOLECULAR DYADS FOR PHOTOSENSITISED HYDROGEN EVOLUTION

The first PS-[FeFe] dyads reported incorporated a ruthenium photosensitizer (Figure 6) and the first reported synthesis included a $[Ru(terpy)_2]^{2+}$ PS covalently linked through an amide to an azadithiolate diiron moiety. This compound was not characterized in its excited state and the only photphysical properties noted are its lack of ground state coupling between the metal centres, inferred from FTIR data.[81] Subsequent development of a $[Ru(bpy)_3]^{2+}$ PS coupled in the same fashion to a propyldithiolate bridged iron catalyst was explored photophysically, with a noted but slight quenching of its luminescence when compared to the relevant $[Ru(bpy)_3]^{2+}$ model. The excited state of the dyad featured two lifetimes (260 ns & 1100 ns); the authors considered these to reflect two conformers of the dyad.[82] Further developments of ruthenium sensitized diiron hydrogenase mimics include linking through a conjugated alkynyl bond to either the diiron bridge or a ligated phosphine.[83-84] Despite the useful synthetic routes of these examples, none of them happen to be useful for producing hydrogen. The free energy of electron transfer to catalyst is uphill in all cases, preventing catalytic hydrogen production. The ruthenium photosensitizers also do not absorb a broad range of light, preventing their use in solar driven cells.
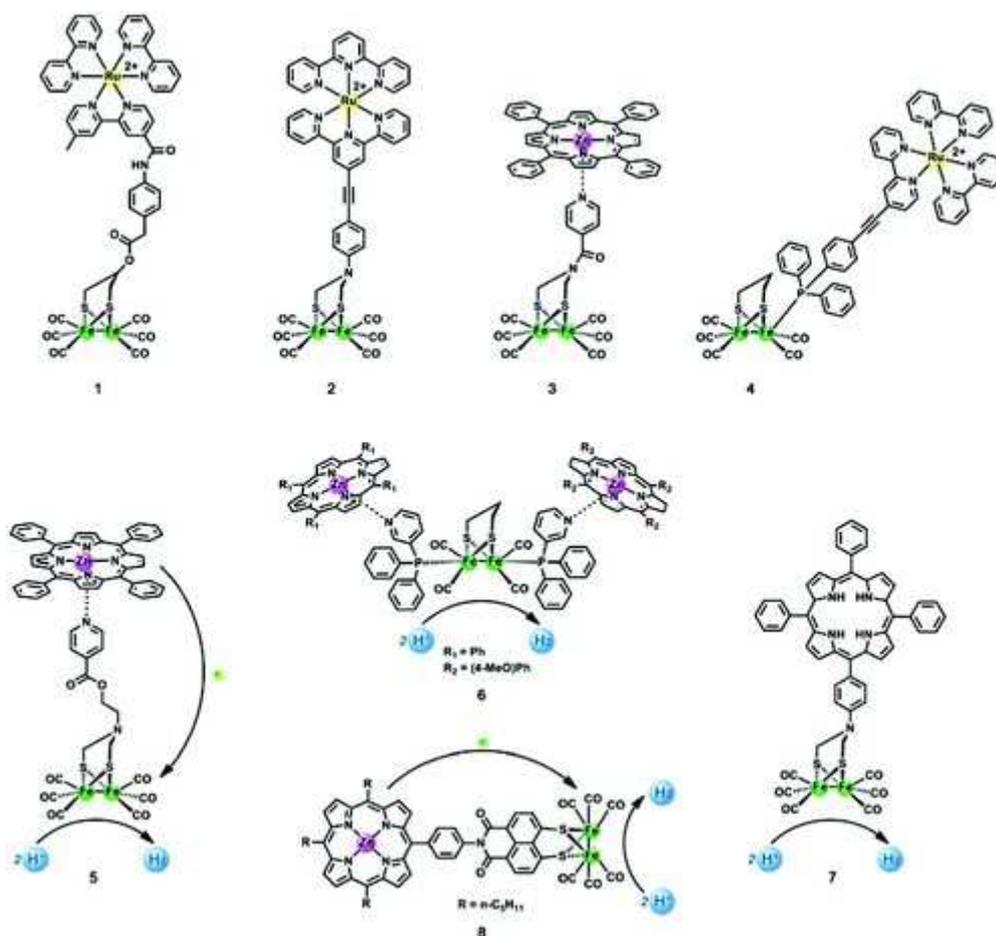
Figure 6 Structures of previously reported PS – [FeFe] dyads, featuring ruthenium and porphyrin PS moieties.[85]

Similar problems have been encountered for rhenium PS – [Fe-Fe] dyads (Figure 7).[86-87] These complexes feature long excited state lifetimes of 780 ns to > 2 ms. The complexes feature almost total quenching of emission, implying energy or electron transfer to the catalyst from the PS. The complexes do not catalyse the transformation of protons into hydrogen photochemically; turnover numbers (TON) of < 0.15 were achieved.[86] In these cases, compared to the ruthenium complexes, the change in free energy of electron transfer from PS to [FeFe] is negative, therefore electron transfer is thermodynamically possible. Further attempts to stabilize the reduced iron

centre, by appending a ferrocene unit to the PS and extending charge separation distances, increase TON to just 0.35.[87] These results indicate that forming a successful photocatalyst requires more than just making the forward electron transfer feasible and connecting the two centres together, a method of forcing the cycle to progress is required. This is first among many factors, such as kinetic factors and stability, which must be considered. Further low TON examples of PS-[FeFe] dyads include those with Zn porphyrin and platinum PS moieties, again failing to achieve catalytic activity.[88-93]
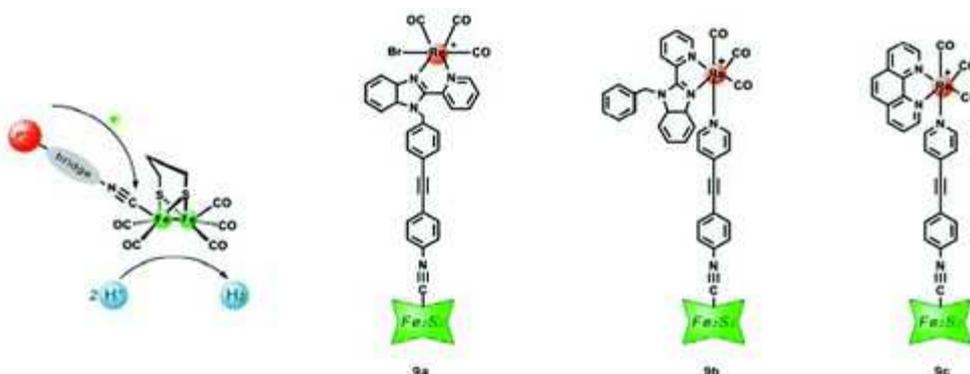
Figure 7 Previously reported rhenium PS – [FeFe] dyads.[85]
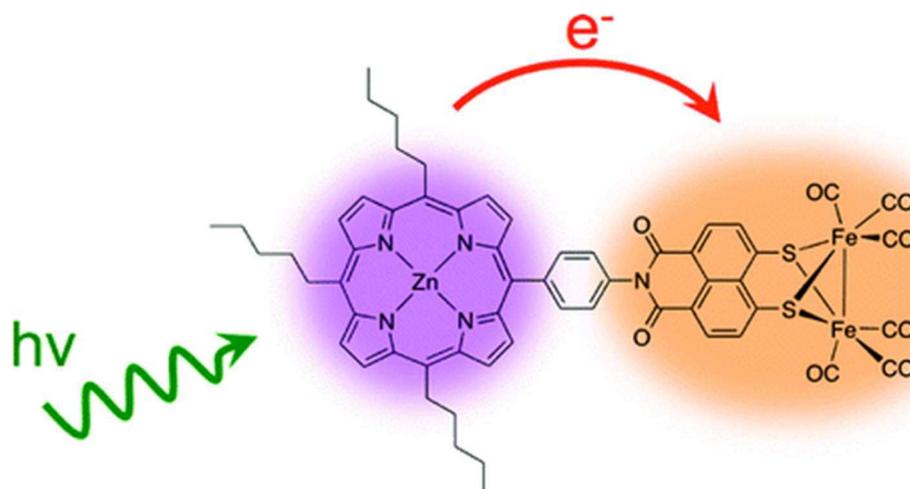
Figure 8 An example of a covalently linked zinc porphyrin PS and NMI bearing [FeFe] hydrogenase model.[92]

Investigation of the conditions necessary for a catalytic cycle to form requires spectroscopic investigation of the component parts of the cycle. Zinc porphyrin complexes have been useful PS for these investigations due to their very strong visible light absorption, long excited state lifetimes and ability to easily form supramolecular complexes with pyridyl functionalized diiron catalysts (Figure 8).[88-92] Important among these contributions is the time-resolved infra-red (TRIR) characterization of a PS-[Fe-Fe] charge separated state (CSS).[94] The charge separated state formed after excitation had a lifetime of 205 ps. The CSS was characterized by a slight red shifting of carbonyl stretching vibrations in the TRIR spectrum to lower energy, indicating a higher electron density on the iron centres. Unfortunately it was not useful for catalytically reducing protons to hydrogen. The rationalisation for this lack of activity was given; the naphthalene monoimide (NMI) disulfide bearing diiron catalyst does not keep enough electron density on the iron centres to make catalysis possible, instead the electron density is located on the organic NMI ligand.

Dyads featuring iridium PS complexes supra-molecularly linked to diiron hydrogenase mimics have been shown to achieve high TON of catalytic H_2 production in aqueous media.[95-97] These

systems feature the aforementioned dyad in an acetonitrile/water mixture and use a trimethylamine as a combined electron and proton donor. The trimethylamine photoproduct decomposes to release a proton after acting as an electron donor. This mixture was irradiated with a 500 W xenon lamp with a λ < 400 nm cutoff filter. The systems were able to achieve a TON of up to 127 before loss of activity. This loss of activity was found to be due to degradation of the iridum PS and activity was restored by adding more PS to the mixture and continuing irradiation. Although this displays high activity, this result indicates a lack of photostability in the system components that also runs contrary to the advantage of using inexpensive iron catalysts to produce hydrogen. However, a system that is limited by the breakdown of its most expensive and scarce component does not take advantage of the relatively inexpensive catalyst.[95] Similar components have been used in systems featuring unlinked PS - catalyst systems to yield even higher TON, however these bimolecular systems still lose activity over time whilst using the same PS complexes, implying that loss of the PS is still the limiting factor in their deployment (Figure 9).[96-97]
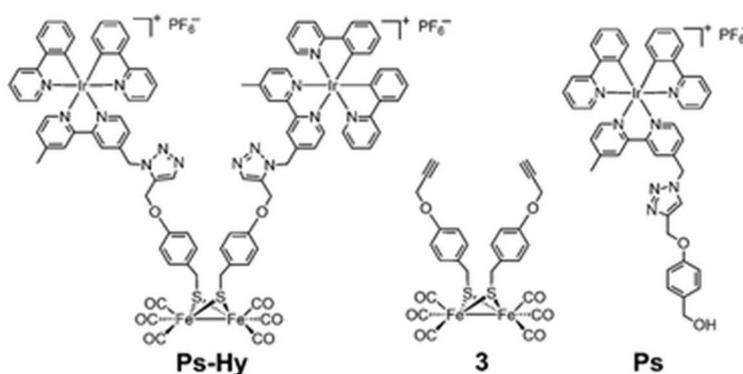
Figure 9 Iridium PS – [FeFe] complex used in studies of catalytic activity increase upon inclusion in a molecular sieve MCM-41. Activity was found to be ~3x higher with the MCM-41 than without, but activity was limited by the durability of the iridium PS.[97]

Although these systems have shown that it is possible to link the PS and catalyst to construct a hybrid molecular device that can catalyse the production of hydrogen, none could be considered to be scalable. Either the dyad complex does not have a high TOF or TON needed to produce hydrogen on a large scale, or the complex has a high TON but the noble metal based PS moiety is not stable. When selecting a PS to link to a hydrogenase catalyst, it must be durable, have good potential to act as a reductant in the excited state and have a excited state lifetime long enough to achieve onward reactions.

Electron transfer in [FeFe] containing dyads

The poor performance of the existing systems for photogenic hydrogen evolution is underpinned by a poor understanding of the mechanism of the reactions taking place, especially when considering the electron transfer reaction to the diiron hydrogenase mimic. Insight into this important step requires examination of the procedure at a more basic level. By understanding the character of reduced diiron hydrogenase mimics, the reduced species can be recognized when it occurs in a dyad or a system featuring a photoinduced electron transfer. The electrolytically reduced state of a dithiolate bridged diiron hexacarbonyl complex has been characterized and mechanisms for interconversion between the ground state complex and electrolysis products proposed.[98]
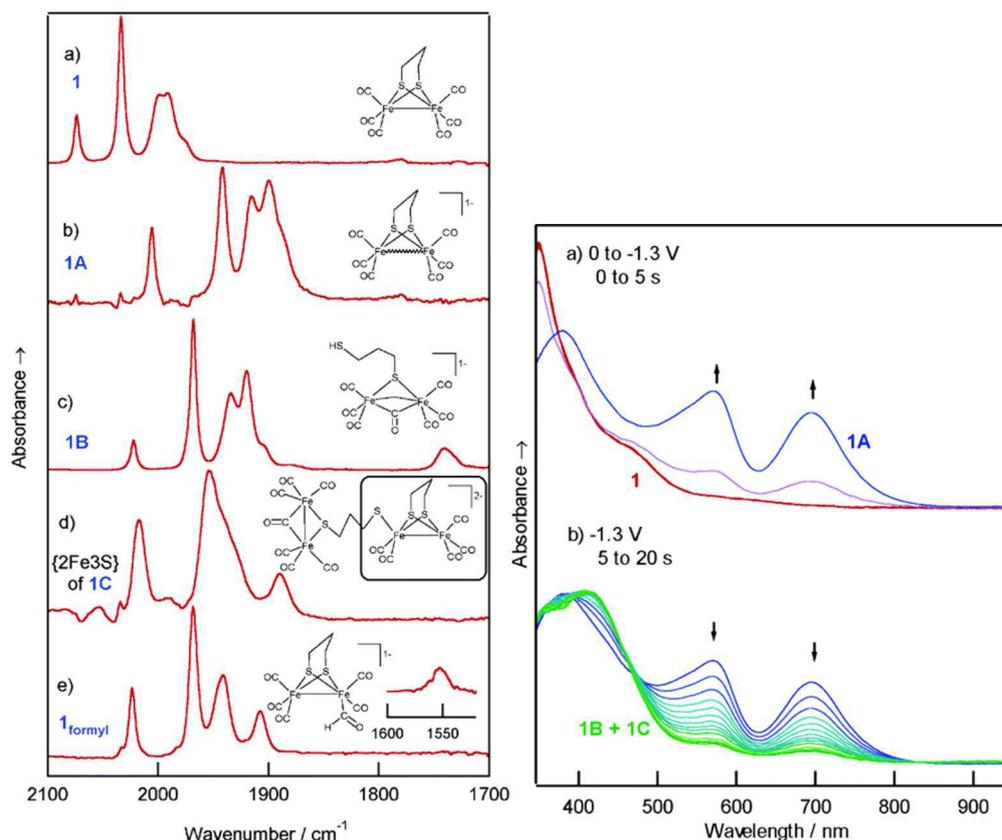
Figure 10 left) IR spectra in the ν(CO) region of [Fe$_2$(μ-pdt)(CO)$_6$] and the electrochemically or chemically reduced products thereof. Right) UV–vis spectra recorded during the reduction and reoxidation of [Fe$_2$(μ-pdt)(CO)$_6$] in DMF in the SEC cell under 0.7 MPa of CO. The species associated with each set of spectra are based on the analysis of the time and potential dependence of the IR spectra.[98]

This study examined the infra-red and UV/vis spectra of electrolytically reduced [Fe$_2$(μ-pdt)(CO)$_6$] and its electrolysis products, performed using a range of spectroelectrochemical techniques (Figure 10). A significant concentration of [Fe$_2$(μ-pdt)(CO)$_6$]$^-$ could be generated using thin-film SEC techniques to effectively characterize the species using infra-red spectroscopy; upon reduction a red shift of all ν(CO) bands of [Fe$_2$(μ-pdt)(CO)$_6$] is seen, indicating a large increase in the electron density at the metal centres and an accompanying lengthening of the iron-iron bond. The same reduction when monitored using UV/vis spectroelectrochemistry reveals an increase of intensity of bands centred at 400, 550 and 700 nm (Figure 10).

This characterization has allowed researchers focussing on photoinitiated electron transfer in systems featuring diiron hydrogenase mimics to recognize when a complex has successfully transferred an electron from the PS complex to the enzyme mimic. It forms the basis for recognizing that the first step in the catalytic cycle is taking place.

The use of this characterization of a monoreduced diiron hydrogenase has allowed groups exploring the photochemistry of systems linking a PS with a diiron hydrogenase mimic to observe photoinitiated electron transfer and assess the suitability of these interactions as a basis for photocatalytic systems. These electron transfer steps characterizing a movement of an electron from the PS to the hydrogenase mimic have been observed using time-resolved infra-red spectroscopy and UV/vis transient absorption spectroscopy.

There are several examples of UV/vis transient absorption spectra recorded to characterize an electron transfer reaction between a PS and the diiron complex, featuring both ruthenium and zinc based photosensitive complexes.[92, 99-101] These studies all show evidence of the characteristic bands of monoreduced diiron hydrogenase complex after photoinitiated electron transfer (Figure 11), but none of the systems featured were capable of producing a large quantity of hydrogen through catalytic activity.
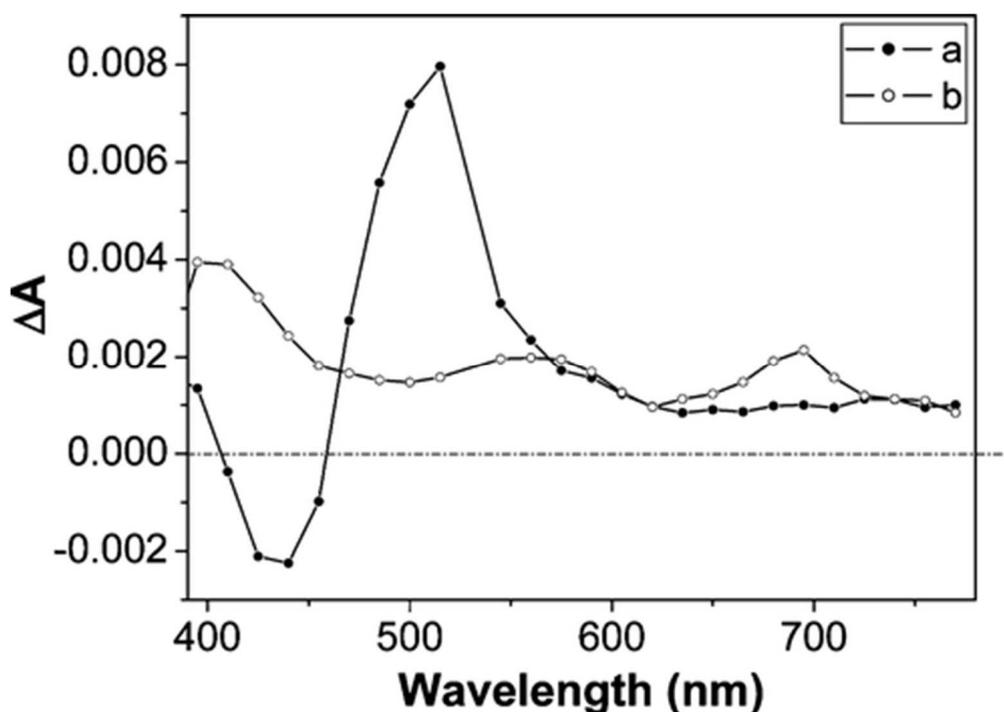
Figure 11 Transient absorption spectra obtained at 0.1 μs (a) and 10 μs (b) following laser flash photolysis of a deoxygenated CH$_3$CN solution containing [Ru(bpy)$_3$]$^{2+}$ (3 × 10^{-5} M), dtc$^-$ (10^{-3} M), and [Fe$_2$(μ-adt)CO$_6$] based hydrogenase mimic (4 × 10^{-4} M) under an argon atmosphere. Absorptions indicating a monoreduced diiron species can be seen at 400, 550 and 700 nm.[99]

Kinetics observed in these studies show that where the PS complex, diiron complex and sacrificial reductant are separate moieties, not covalently linked to one another, the PS has the possibility to become reduced before transferring electrons to the diiron complex, preventing back electron transfer from the reduced catalyst complex to the oxidized PS complex. The photoreduced PS complex is long lived, greatly increasing the chance of transferring electrons compared to a dyadic system. Where the system has the PS and diiron complex covalently linked in a dyad, charge recombination times are extremely short, estimated at 57 ps in CH$_2$Cl$_2$ or 3 ns in toluene for a zinc porphyrin derived PS in combination with an NMI based diiron hydrogenase mimic.[92] These short times required for charge recombination prevents the reduction of the transiently oxidized PS before back electron transfer from diiron moiety.

The studies above featuring transient absorption spectra confirm the presence of a photoinitiated electron transfer mechanism for these systems and can be used to understand the kinetics of charge separation and recombination, but they do not offer the spectral resolution to identify structural changes that accompany these processes. This detailed study of

what is being produced upon photoinitiated electron transfer can be achieved using time-resolved infra-red spectroscopy (TRIR). Infra-red spectra offer the detail needed to understand the species involved in electron transfer processes and the subtle electron density changes that accompany them.
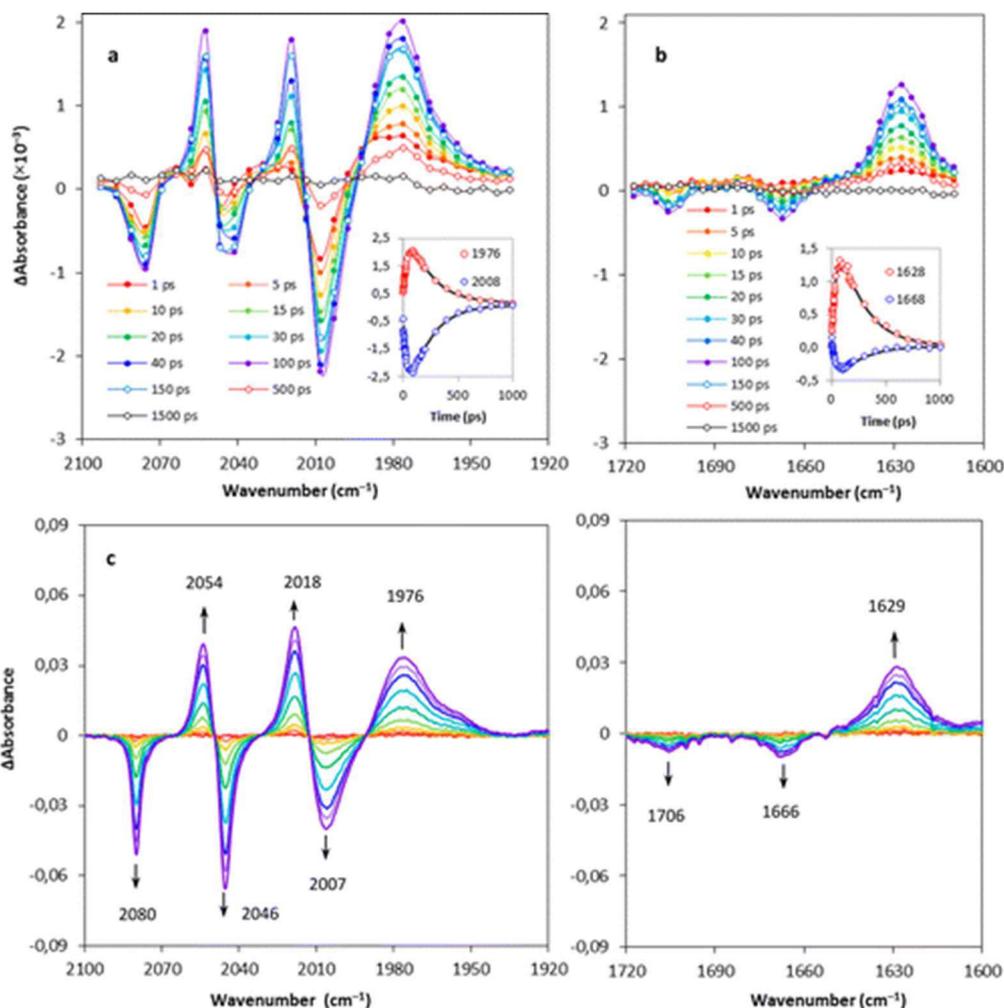
Figure 12 (top) TRIR spectra recorded in different wavenumber regions (a) $v(C\equiv O)$ and (b) $v(C=O)_{NMI}$ for 2.0 mM $[\mu$-(4-pyCH$_2$–NMI-S$_2$)Fe$_2$(CO)$_6$] (3) and 2.0 mM ZnTPP in CH$_2$Cl$_2$ at 293 K, following the 553 nm fs laser excitation. The insets show the corresponding kinetic traces at 1976 and 2008 cm^{-1} (a), and at 1628 and 1668 cm^{-1} (b), respectively. The curves through the data points are the result of a global least-squares fit. (bottom) Absorbance difference IR SEC spectra recorded in different wavenumber regions (c) $v(C\equiv O)$ and (d) $v(C=O)_{NMI}$ during the one-electron reduction of 1.0 mM 3 in CH$_2$Cl$_2$ (0.1 M ^{n}Bu$_4$NPF$_6$) within an OTTLE cell at 293 K.[94]

To date, the only TRIR study of a PS-diiron hydrogenase mimic interaction is for a zinc porphyrin complex supramolecularly bound to a NMI bearing diiron hydrogenase mimic. These findings indicate the presence of a photoinduced electron transfer state, but one that is unable to participate in a photocatalytic hydrogen evolution cycle (Figure 12).

Upon photoexcitation, the IR pattern of the excited diiron complex remained as three well-defined peaks after charge separation. This indicated that no significant geometry change occurred for the diiron moiety during photo reduction, in comparison to the electrolytically reduced diiron complex described above, which experienced significant structural changes likely related to a lengthened Fe-Fe bond. It may be that despite the possibility of an electron transfer event, without the more subtle structural changes that take place for alkyl bridged diiron hydrogenase mimics, catalytic activity cannot be achieved.

Considering the kinetics; the maximum ground state bleach was achieved in around 100 ps, followed by the decay of the charge separated state. The ground state was re-established in under 1.5 ns, indicating the charge separated state fully recovered to the ground state and the lifetimes for the charge separation and charge recombination were found to be τ_{CS} = 40 ± 3 ps and τ_{CR} = 205 ± 14 ps, respectively. Despite the supramolecular nature of this complex, the lifetime of charge separation is still short, preventing the reduction of the oxidised PS by a sacrificial reductant by the preferential occurrence of back electron transfer from the diiron moiety. As indicated in the former electrolytic reduction studies, the monoreduced diiron complex undergoes loss of a CO ligand to propagate the cycle. This does not take place in this supramolecular complex, as the charge separated step decays rapidly and completely to the ground state.

As a result of this work, it can be seen that where there is no change in structure for the diiron complex in the excited state, there is no opportunity to advance the cycle. Although it is important to form a charge separated state to start the catalytic mechanism, enough electron density must reside on the iron centres to promulgate the next steps.

Excited state properties of diiron hydrogenase models

The basis for understanding the reaction of diiron hydrogenase type complexes to light stems from multiple TRIR studies, where the diiron complex has been excited under different conditions to identify the mechanisms of its own complex photochemistry. While it is important to understand the mechanism of decay in a photosensitised system, clues to making the catalytic process work under solar irradiation could be identified from study of the catalyst alone.

These studies have attempted to deduce the character of any photoproducts that occur for [Fe$_2$(μ-pdt)(CO)$_6$] post excitation using either UV or visible light.

In all of these studies, the reported mechanism for decay of the photoexcited species occurs at least partially through the loss of, and recombination with, one of the carbonyl ligands (Figure 13). This was seen in the earliest study using TRIR spectroscopy,[102] and the same mechanism has been proposed in other studies,[103-104] including diiron complexes featuring phosphine ligands.[105-106] The assignment of photoproducts due to CO loss with a lifetime less than 300 ps in all cases is supported by red shifted vCO stretches in the 1900 – 2200 cm^{-1} region, accompanied by an almost complete recovery to the ground state at long time scales of seconds or greater.

Although this is consistent for all studies using UV light to excite the diiron complexes, when visible light of 532 nm was used, a different state was observed, whereby the lengthening of the iron-iron bond is responsible for the observed red shifted vCO stretches, similar to the lengthened iron-iron bond of electrolytically reduced [Fe$_2$(μ-pdt)(CO)$_6$].[104] This state was more accessible for complexes with greater conformational flexibility, with the pdt bridged hydrogenase mimic displaying far greater excitation into this regime than an edt bridged diiron complex.

The proposed mechanisms and the assignments of the products has been challenged by a study using an aryl bridged diiron hexacarbonyl.[107] In this study, [Fe$_2$(μ-bdt)(CO)$_6$] was excited using 400 nm light and the v(CO) frequencies probed in the region 1900 – 2100 cm^{-1}. Here, the mid timescale decays were attributed to vibrational relaxation of the higher frequency CO modes, due to the solvent dependent nature of the lifetimes. The authors suggest that this may be the true nature of the signals seen for post excitation dithiolate bridged diiron hexacarbonyl complexes, but this may be down to subtle experimental differences.[108]
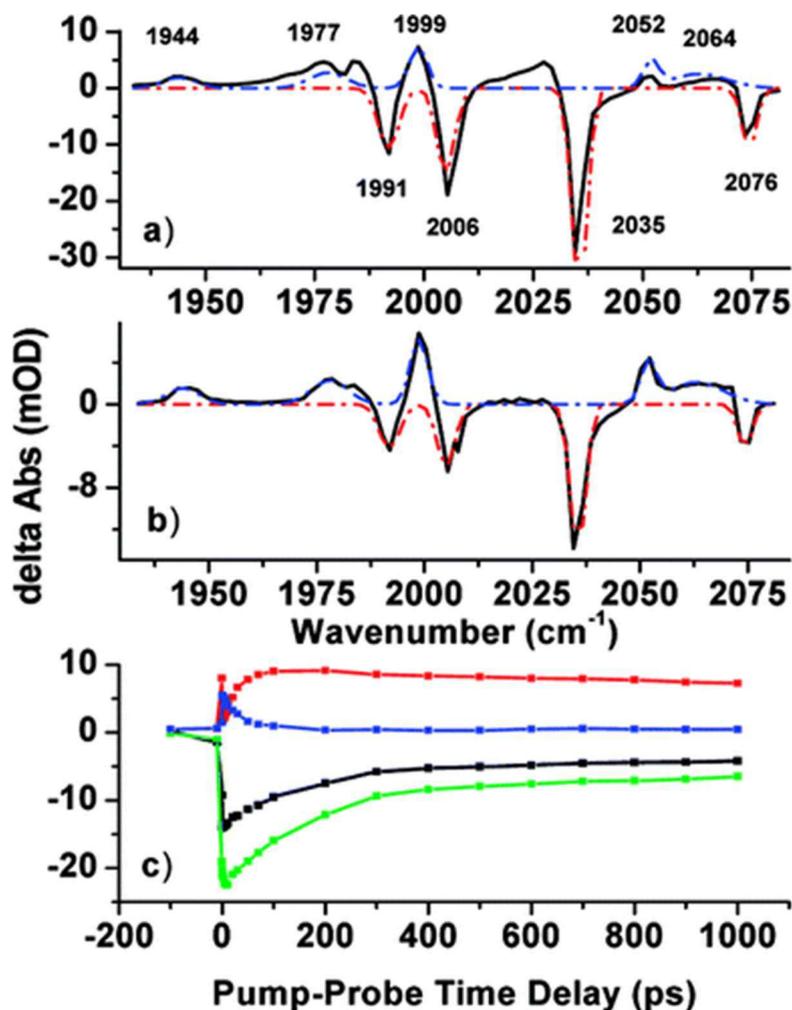
Figure 13 Ultrafast UV-pump IR-probe data for[Fe$_2$(μ-pdt)(CO)$_6$] demonstrating the spectra of a possible CO loss photoproduct. (a) Difference spectrum recorded with a pump–probe delay time of 50 ps. (b) Like part a but with pump–probe delay time = 1 ns. (c) Magic-angle temporal dependence of 1 bleaches at 1991 and 2005 cm^{-1} (black and green), a photoproduct band at 1999 cm^{-1} (red), and cooling effects at 2010 cm^{-1} (blue). In parts a and b, dashed lines are fits to reactant and product spectra.[102]

These studies have demonstrated the complex photochemistry of the diiron hydrogenase model complexes and suggest that photosensitized catalytic system featuring one of these complexes may also have complex excited state behaviour. This complexity can only be compounded by the excited state behaviour of the photosensitizer itself, which may have multiple pathways and transition states on its route from excited state to the ground state.

EXCITED STATE PROPERTIES OF PLATINUM PHOTOSENSITISERS

Square planar platinum compounds have seen a great deal of interest for their excited state chemistry and photophysics. This is due to relative ease of achieving steric and electronic control in a square planar complex compared to octahedral chromophores, such as those based on ruthenium or iridum. By studying the way electrons and charge move within square planar platinum complexes, insight can be drawn into the way electrons move in different situations using different ligand sets.

4.9 $R_1 = tBu, R_2 = H, R_3 = H$
4.10 $R_1 = tBu, R_2 = H, R_3 = OMe$
4.11 $R_1 = tBu, R_2 = H, R_3 = F$
4.12 $R_1 = tBu, R_2 = H, R_3 = NO_2$
4.13 $R_1, R_2, R_3 = Me$
4.14 $R_1 = tBu, R_2 = H, R_3 = Me$
4.15 $R_1 = CONEt_2, R_2 = H, R_3 = Me$
4.16 $R_1 = COOEt, R_2 = H, R_3 = Me$
4.17 $R_1 = tBu, R_2 = H, R_3 = CF_3$
4.18 $R_1 = tBu, R_2 = H, R_3 = NMe_2$
4.19 $R_1 = tBu, R_2 = H, R_3 = OMe$
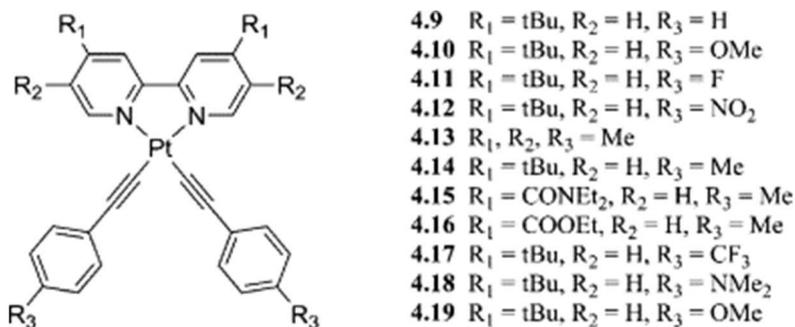
Figure 14 Examples of the broad range of complexes derived from the Pt(Diimine)bisacetylide base used to understand how electronics control excited state properties. This set of complexes were found in a single study.[109]

There exists a significant body of literature dedicated to understanding the way square planar platinum complexes react to light.[49] For the use of platinum in molecular photochemical devices, typically platinum diimines with acetylide or thiolate ligands are considered.[110] These complexes have been considered for their bright luminescence and options for steric and electronic control of ligand sets (Figure 14).

Particularly interesting are square planar platinum complexes featuring acetylide ligands, as these produce strong, high energy luminescence with long emission lifetime. Initial studies of platinum(diimine)bisacetylide revealed lifetimes from hundreds of nanoseconds up to microseconds, with emission energies greater than 2 eV and quantum yields double those of $[Ru(bpy)_3]^{2+}$.[110-111] The effect of variation in the arylacetylide ligand has been studied for its effect on ground and excited state properties in platinum(diimine)bisacetylide systems, revealing that arylacetylide ligands effect only minor changes in the platinum based HOMO, while LUMO character is controlled by the character of the diimine ligand.[112] By exploiting these effects on the orbital character of the complexes, platinum(diimine)bisacetylide systems demonstrate the electronic tunability of the acceptor orbitals.

As a result of square planar platinum complexes strong response to photostimuli, they have been used to understand the steric and electronic effects of different ligands on chromophore photophyscial properties. This has been extended to understand how more stimuli can affect the mechanism of decay.

Controlling the pathways of excited state decay

Square planar platinum complexes featuring acetylide ligands in a linear configuration display complex decay spectra and kinetics, due to competing pathways to the ground state. Often, one of these pathways is preferred, in order to force a molecule to perform an action in a particular cycle.

This shifting of decay pathways using external stimuli has been achieved through the use of double pump probe spectroscopy, where the chromophore is first excited by a UV pump beam, then an infra-red pump beam and finally examined using an infra-red probe to identify changes to the typical decay pathways.

Vibrational control of excited state pathways, in platinum complexes with acetylide ligands, has been achieved in two studies.[113-114] The first of these uses a platinum bisphosphine bis acetylide complex, with a close grouping of triplet and charge separated states,[93] to have a change effected through the use of mid-infrared pump centred on the vibrational frequency of the acetylide stretches in the excited state. This study revealed that four important conditions must be met to achieve vibrational control of a complex like this:

"The complex mechanisms involved dictate the following necessary conditions for infrared control to work:

(1) the driving force between excited states involved must be close to or within the energy of selectively excitable intramolecular vibrations;
(2) the targeted vibration must be strongly coupled to electronic processes (in specific DBA systems where bridge orbitals are involved in charge separation, bridge-localized vibrations can often satisfy this requirement);
(3) for ET reactions in solution, delaying the infrared excitation with respect to the initial solvation response is necessary to avoid solvation-enhanced IVR; and
(4) electronic transitions must occur within the vibrational lifetime of the excited vibrations."[114]
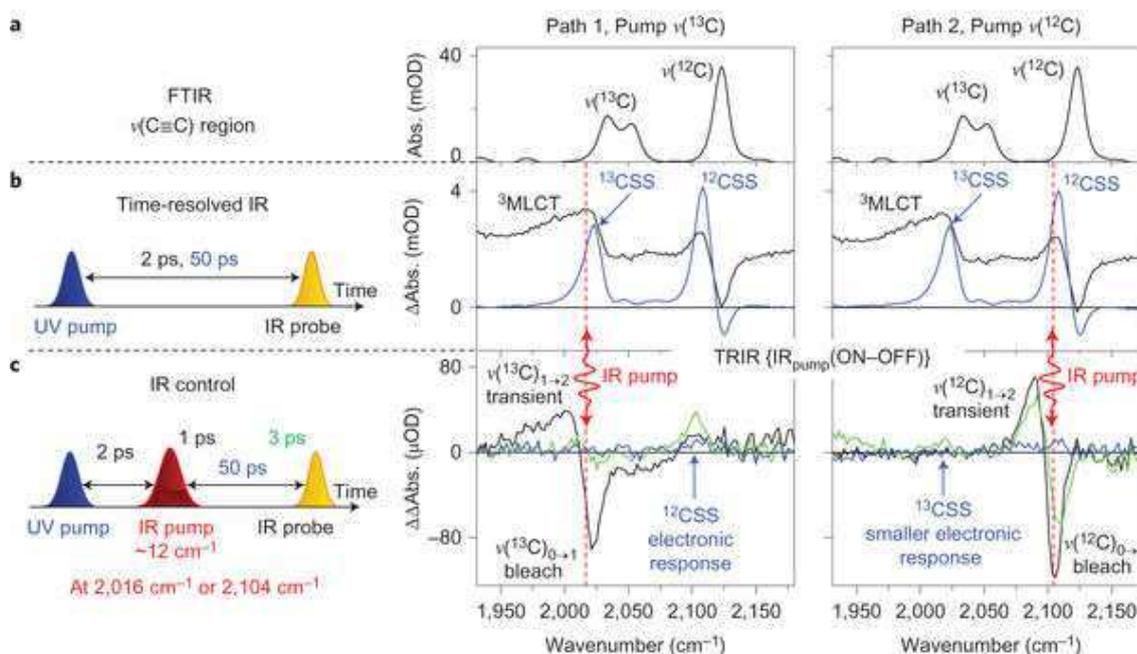
Figure 15 Schematic representation of a double pump probe experiment and results obtained for Pt(Diimine)bisacetylide with differently labelled acetylides. a, FTIR of the molecular fork complex. b, TRIR spectra at 2 and 50 ps time delay following 400 nm excitation, displaying the spectral profiles of $\nu(^{12}C)$ and $\nu(^{13}C)$ in ^{3}MLCT* and CSS, respectively. The apparent difference in shape of the ^{12}CSS versus ^{13}CSS TRIR signals is due to a larger bleach/transient overlap for the latter. c, IR-control experiments: the IRpump is introduced 2 ps after the UVpump, and the spectra shown are recorded with the IRprobe at 1 ps (black), 3 ps (green) and 50 ps (blue) after the IRpump. The bleach–transient peak pairs are signatures of depopulation of the v = 0 and population of the v = 1 state of the excited mode. The off-diagonal signals arising at frequencies not excited by the IRpump are due to a change in electronic dynamics, specifically the rate of formation of the ^{12}CSS and ^{13}CSS. The presence and sign of the off-diagonal signals suggests that vibrational excitation of one pathway accelerates electron transfer through the opposite pathway.[113]

The follow up to this study involves the use of a square planar platinum diimine bisacetylide complex, which instead of featuring a linear array of acetylide, features cis-acetylides that are chemically and electronically indistinct (Figure 16).[113] These acetylides differ only in the masses of their acetylide carbons with one ^{13}C labelled acetylide and one unlabelled acetylide. When vibronic perturbations are applied to the excited state, centred on acetylide vibrational

frequencies, the charge separation pathways can be selectively enhanced (Figure 15). This work further demonstrates that rational design of photoactive complexes can be used to produce materials that can be influenced to undertake certain decay pathways to the ground state, important in preventing charge recombination in systems where back electron transfer is rapid.
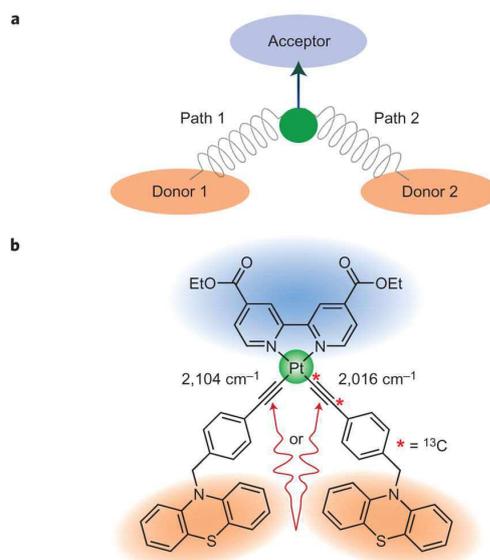
Figure 16a, Hypothesis: directing electron transfer along a preselected pathway in a D–B–A–B–D system. b, Asymmetrically isotopically labelled D–B–A–[13]B–D molecular 'fork' 1*. The IR pump frequency is tuned to the [12]C≡[12]C or [13]C≡[13]C acetylide stretching frequency at the 'gateway' excited state; that is, in the hot triplet metal-to-ligand charge-transfer ([3]MLCT*) state as it is about to decay to a charge-separated state with the hole located either on donor 1 ([12]CSS) or donor 2 ([13]CSS).[113]

This work has demonstrated that should there be multiple competing pathways to the ground state, under the correct circumstances, one mechanism can be selected over the other. This has strong implications for influencing catalytic cycles, indicating that the use of external stimuli could affect product outcome.

CONCLUSIONS AND AIMS

Although the methods describe above are powerful tools for attempting to produce a photosensitized diiron hydrogenase mimicking hydrogen evolution cycle, they have not been used to produce a successful system. These methods have been inadequate in attempting to capture the steps required to produce hydrogen and they must be combined to form a more complete understanding of the process.

This thesis describes the efforts made to synthesize a dyad based on a platinum photosensitizer covalently attached to a diiron hydrogenase mimic. The mechanistic behaviour of electron transfer in PS-hydrogenase dyads has been probed by exploring the excited state dynamics of this dyad, platinum PS complexes and diiron hydrogenase mimics related to the dyad structurally.

As described above, the dyads that have been described in the literature have limited or no activity when it comes to photocatalytic hydrogen evolution. The steps required to achieve this in a photocatalytic dyad are poorly characterised and obvious routes for future development are not obvious. The work presented in chapter 3 describes the synthesis and characterisation of a new dyad. This dyad has then been examined using time resolved spectroscopy to identify the key electron transfer step. The observations made about this important step could explain the lack of activity seen in some other PS-hydrogenase dyads. The complexity of the dyad's

dynamics preclude a complete analysis and further investigation of the excited state dynamics of Pt N^N^C PS complexes should first be investigated before further work on dyads.

Chapter 4 describes the synthesis and characterization of two series of Pt N^N^C PS with substituted phenyl acetylide donor moieties. These complexes have been characterized in their ground state by ^{1}H NMR, IR and UV/vis spectroscopies, X ray crystallography and mass spectrometry. In their excited state, these complexes have been characterized using fluorimetry and single photon counting methods to determine quantum yields and lifetimes of emission, radiative and non-radiative decay rates. These properties have been compared with the electron withdrawing properties of the substituted phenyl acetylide ligands of each PS complex using Hammett theory, in order to determine how the electronics of the ligand that determines the HOMO energy affect the excited state decay mechanics. This comparison not only revealed that the mechanism of excited state decay is heavily dependent upon the electronic properties but also that the cause of the change in mechanism is due to close lying excited states interacting to deactivate the emissive excited state.

This mechanism change required further investigation, performed using time resolved spectroscopies. This work is described in chapter 5. The excited state decay species are characterized using picosecond and nanosecond IR and UV/vis spectroscopies. This spectroscopy study revealed that there were three observed paradigms for the evolution of spectra. It was also revealed that emission in some of the platinum N^N^C acetylide PS complexes was not from the lowest in energy excited state. These observations align with the prediction made using Hammett theory about the change in decay mechanism as the electron withdrawing potential of the phenyl acetylide ligand changes. Observations made in this chapter allow the possibility of predicting the conditions required to force charge separated states to form in Pt N^N^C complexes.

Chapter 6 shows how electron transfer between separate PS and catalyst molecules in a bimolecular system has also been investigated using Stern Volmer theory. This is intended to show that electron transfer by collisions in possible and explore the paradigm of whether not using a linker to provide favourable ET actually hinders the ability to photosensitize the hydrogenase mimic catalyst.

Based on the findings of chapters 4 and 5, chapter 6 investigates the efficacy of transferring energy from an excited state PS complexes in order to complete the first step in a catalytic cycle, electron transfer from PS to catalyst. This is performed using an analysis of the Stern-Volmer relationship of excited, emissive state deactivation when these PS complexes are in the presence of a diiron hydrogenase mimic. This analysis revealed that changing the PS complex has very little effect on the ability to transfer energy to the hydrogenase mimic and the main factor affecting quenching rates is PS LUMO energy. More in depth analysis of a series of platinum N^N^C acetylide PS complexes revealed that changes in the quenching rate from a baseline value may be able to provide information about other deactivation processes taking place concurrently.

Overall, the purpose of this thesis is to investigate how the excited state properties of PS complexes affect the ability to transfer an electron in a photocatalytic hydrogen evolution cycle. This is demonstrated with both ground state and excited state methods, looking at intermolecular and intramolecular pathways. The purpose of this thesis is not to quantify the catalytic activity of dyads or combinations of PS complexes and hydrogenase catalysts. As such, the turnover frequencies and turnover numbers of hydrogen evolution for these complexes and systems has not been investigated.

REFERENCES

1.   IPCC, Climate Change 2013: The Physical Science Basis. Contribution of Working Group I to the Fifth Assessment Report of the Intergovernmental Panel on Climate Change. Stocker, T. F., D. Qin, G.-K. Plattner, M. Tignor, S.K. Allen, J. Boschung, A. Nauels, Y. Xia, V. Bex and P.M. Midgley (eds.), Ed. Cambridge University Press: Cambridge, United Kingdom and New York, NY, USA, 2013; p 1535.

2.   Hansen, J.; Ruedy, R.; Sato, M.; Lo, K., *Rev. Geophys.* **2010,** *48* (4), n/a-n/a.

3.   UNFCCC, *United Nations Framework Convention on Climate Change. Convention on climate change. http://www.unfccc.de/resource/conv/index.html UNFCCC.* 1992.

4.   Hepburn, C., *Annu. Rev. Environ. Resour.* **2007,** *32* (1), 375-393.

5.   Sperling, D.; Yeh, S., *Transport Policy* **2010,** *17* (1), 47-49.

6.   Abbasi, T.; Abbasi, S. A., *Renew, Sust. Energ. Rev.* **2011,** *15* (4), 1828-1834.

7.   van der Zwaan, B.; Keppo, I.; Johnsson, F., *Energy Policy* **2013,** *61*, 562-573.

8.   Kranzl, L.; Hummel, M.; Müller, A.; Steinbach, J., *Energy Policy* **2013,** *59*, 44-58.

9.   Armstrong, R. C.; Wolfram, C.; de Jong, K. P.; Gross, R.; Lewis, N. S.; Boardman, B.; Ragauskas, A. J.; Ehrhardt-Martinez, K.; Crabtree, G.; Ramana, M. V., *Nat. Energy* **2016,** *1*, 15020.

10.   Dodds, P. E.; Staffell, I.; Hawkes, A. D.; Li, F.; Grünewald, P.; McDowall, W.; Ekins, P., *Int. J. Hydrogen Energy* **2015,** *40* (5), 2065-2083.

11.   Dutta, S., *Ind. Eng. Chem. Res.* **2014,** *20* (4), 1148-1156.

12.   Lucia, U., *Renew, Sust. Energ. Rev.* **2014,** *30*, 164-169.

13.   Gröger, O.; Gasteiger, H. A.; Suchsland, J.-P., *J. Electrochem. Soc.* **2015,** *162* (14), A2605-A2622.

14.   Buonomano, A.; Calise, F.; d'Accadia, M. D.; Palombo, A.; Vicidomini, M., *Appl. Energ.* **2015,** *156*, 32-85.

15.   Verhelst, S., *Int. J. Hydrogen Energy* **2014,** *39* (2), 1071-1085.

16.   Ugurlu, A.; Oztuna, S., *Int. J. Hydrogen Energy* **2015,** *40* (34), 11178-11188.

17.   Kaya, N.; Turan, Ö.; Midilli, A.; Karakoç, T. H., *Int. J. Hydrogen Energy* **2016,** *41* (19), 8307-8322.

18.   Chapin, D. M.; Fuller, C. S.; Pearson, G. L., *J. Appl. Phys.* **1954,** *25* (5), 676-677.

19.   Fujishima, A.; Honda, K., *Nature* **1972,** *238* (5358), 37-38.

20.   Fujishima, A.; Rao, T. N.; Tryk, D. A., *J. Photochem. Photobiol., C* **2000,** *1* (1), 1-21.

21.   Konstantinou, I. K.; Albanis, T. A., *Appl. Catal., B* **2003,** *42* (4), 319-335.

22.   Fujishima, A.; Zhang, X., *C. R. Chim.* **2006,** *9* (5–6), 750-760.

23.   Chen, X.; Mao, S. S., *Chem. Rev.* **2007,** *107* (7), 2891-2959.

24.   Ni, M.; Leung, M. K. H.; Leung, D. Y. C.; Sumathy, K., *Renew, Sust. Energ. Rev.* **2007,** *11* (3), 401-425.

25.   Gaya, U. I.; Abdullah, A. H., *J. Photochem. Photobiol., C* **2008,** *9* (1), 1-12.

26.   Li Puma, G.; Bono, A.; Krishnaiah, D.; Collin, J. G., *J. Hazard. Mater.* **2008,** *157* (2–3), 209-219.

27.   Han, F.; Kambala, V. S. R.; Srinivasan, M.; Rajarathnam, D.; Naidu, R., *Appl. Catal., A* **2009,** *359* (1–2), 25-40.

28.   Shan, A. Y.; Ghazi, T. I. M.; Rashid, S. A., *Appl. Catal., A* **2010,** *389* (1–2), 1-8.

29.   Pelaez, M.; Nolan, N. T.; Pillai, S. C.; Seery, M. K.; Falaras, P.; Kontos, A. G.; Dunlop, P. S. M.; Hamilton, J. W. J.; Byrne, J. A.; O'Shea, K.; Entezari, M. H.; Dionysiou, D. D., *Appl. Catal., B* **2012,** *125*, 331-349.

30.   Ni, M.; Leung, M. K. H.; Leung, D. Y. C.; Sumathy, K., *Renew, Sust. Energ. Rev.* **2007,** *11* (3), 401-425.

31.   Di Paola, A.; Bellardita, M.; Ceccato, R.; Palmisano, L.; Parrino, F., *J. Phys. Chem. C* **2009,** *113* (34), 15166-15174.

32.   Li, J.-G.; Ishigaki, T.; Sun, X., *J. Phys. Chem. C* **2007,** *111* (13), 4969-4976.

33.   Frederick, J. E.; Snell, H. E.; Haywood, E. K., *Photochem. Photobiol.* **1989,** *50* (4), 443-450.

34.   Izumi, Y.; Itoi, T.; Peng, S.; Oka, K.; Shibata, Y., *J. Phys. Chem. C* **2009,** *113* (16), 6706-6718.

35.   Czoska, A. M.; Livraghi, S.; Chiesa, M.; Giamello, E.; Agnoli, S.; Granozzi, G.; Finazzi, E.; Valentin, C. D.; Pacchioni, G., *J. Phys. Chem. C* **2008,** *112* (24), 8951-8956.

36.   Irie, H.; Watanabe, Y.; Hashimoto, K., *Chem. Lett.* **2003,** *32* (8), 772-773.

37.   Periyat, P.; Pillai, S. C.; McCormack, D. E.; Colreavy, J.; Hinder, S. J., *J. Phys. Chem. C* **2008,** *112* (20), 7644-7652.

38.   Choi, W.; Termin, A.; Hoffmann, M. R., *J. Phys. Chem.* **1994,** *98* (51), 13669-13679.

39.   Morikawa, T.; Irokawa, Y.; Ohwaki, T., *Appl. Catal., A* **2006,** *314* (1), 123-127.

40.   Kamat, P. V., *J. Phys. Chem. C* **2008,** *112* (48), 18737-18753.

41.   Wu, T.; Liu, G.; Zhao, J.; Hidaka, H.; Serpone, N., *J. Phys. Chem. B* **1998,** *102* (30), 5845-5851.

42.   Wu, T.; Lin, T.; Zhao, J.; Hidaka, H.; Serpone, N., *Environ. Sci. Technol.* **1999,** *33* (9), 1379-1387.

43.   Cho, Y.; Choi, W.; Lee, C.-H.; Hyeon, T.; Lee, H.-I., *Environ. Sci. Technol.* **2001,** *35* (5), 966-970.

44.   Xu, Y.; Langford, C. H., *Langmuir* **2001,** *17* (3), 897-902.

45.   O'Regan, B.; Gratzel, M., *Nature* **1991,** *353* (6346), 737-740.

46.   Park, N.-G., *J. Phys. Chem. Lett.* **2013,** *4* (15), 2423-2429.

47.   Kazim, S.; Nazeeruddin, M. K.; Grätzel, M.; Ahmad, S., *Angew. Chem. Int. Ed.* **2014,** *53* (11), 2812-2824.

48.   Grätzel, M., *J. Photochem. Photobiol., C* **2003,** *4* (2), 145-153.

49.   Archer, S.; Weinstein, J. A., *Coord. Chem. Rev.* **2012,** *256* (21), 2530-2561.

50.   Islam, A.; Sugihara, H.; Hara, K.; Singh, L. P.; Katoh, R.; Yanagida, M.; Takahashi, Y.; Murata, S.; Arakawa, H., *New J. Chem.* **2000,** *24* (6), 343-345.

51.   Geary, E. A. M.; McCall, K. L.; Turner, A.; Murray, P. R.; McInnes, E. J. L.; Jack, L. A.; Yellowlees, L. J.; Robertson, N., *Dalton Trans.* **2008,** (28), 3701-3708.

52.   Gillaizeau-Gauthier, I.; Odobel, F.; Alebbi, M.; Argazzi, R.; Costa, E.; Bignozzi, C. A.; Qu, P.; Meyer, G. J., *Inorg. Chem.* **2001,** *40* (23), 6073-6079.

53.   Geary, E. A. M.; Yellowlees, L. J.; Jack, L. A.; Oswald, I. D. H.; Parsons, S.; Hirata, N.; Durrant, J. R.; Robertson, N., *Inorg. Chem.* **2005,** *44* (2), 242-250.

54.   Geary, E. A. M.; Hirata, N.; Clifford, J.; Durrant, J. R.; Parsons, S.; Dawson, A.; Yellowlees, L. J.; Robertson, N., *Dalton Trans.* **2003,** (19), 3757-3762.

55.   Zhang, Y.; Galoppini, E., *ChemSusChem* **2010,** *3* (4), 410-428.

56.   Kwok, E. C.-H.; Chan, M.-Y.; Wong, K. M.-C.; Lam, W. H.; Yam, V. W.-W., *Chem. Eur. J.* **2010,** *16* (40), 12244-12254.

57.   Nazeeruddin, M. K.; Péchy, P.; Renouard, T.; Zakeeruddin, S. M.; Humphry-Baker, R.; Comte, P.; Liska, P.; Cevey, L.; Costa, E.; Shklover, V.; Spiccia, L.; Deacon, G. B.; Bignozzi, C. A.; Grätzel, M., *J. Am. Chem. Soc.* **2001,** *123* (8), 1613-1624.

58.   Carmo, M.; Fritz, D. L.; Mergel, J.; Stolten, D., *Int. J. Hydrogen Energy* **2013,** *38* (12), 4901-4934.

59.   Kalyanasundaram, K.; Kiwi, J.; Grätzel, M., *Helv. Chim. Acta* **1978,** *61* (7), 2720-2730.

60.   Kiwi, J.; Gratzel, M., *Nature* **1979,** *281* (5733), 657-658.

61.   Goldsmith, J. I.; Hudson, W. R.; Lowry, M. S.; Anderson, T. H.; Bernhard, S., *J. Am. Chem. Soc.* **2005,** *127* (20), 7502-7510.

62.   DiSalle, B. F.; Bernhard, S., *J. Am. Chem. Soc.* **2011,** *133* (31), 11819-11821.

63.   Metz, S.; Bernhard, S., *Chem. Commun.* **2010,** *46* (40), 7551-7553.

64.   Curtin, P. N.; Tinker, L. L.; Burgess, C. M.; Cline, E. D.; Bernhard, S., *Inorg. Chem.* **2009,** *48* (22), 10498-10506.

65.   Tinker, L. L.; McDaniel, N. D.; Curtin, P. N.; Smith, C. K.; Ireland, M. J.; Bernhard, S., *Chem. Eur. J.* **2007,** *13* (31), 8726-8732.

66.   Wang, C.; deKrafft, K. E.; Lin, W., *J. Am. Chem. Soc.* **2012,** *134* (17), 7211-7214.

67.   Singh, A.; Spiccia, L., *Coord. Chem. Rev.* **2013,** *257* (17), 2607-2622.

68.   Duan, L.; Bozoglian, F.; Mandal, S.; Stewart, B.; Privalov, T.; Llobet, A.; Sun, L., *Nat. Chem.* **2012,** *4* (5), 418-423.

69.   Ananyev, G.; Dismukes, G. C., *Photosynth. Res.* **2005,** *84* (1), 355-365.

70.   Tard, C.; Pickett, C. J., *Chem. Rev.* **2009,** *109* (6), 2245-2274.

71.   Lubitz, W.; Ogata, H.; Rüdiger, O.; Reijerse, E., *Chem. Rev.* **2014,** *114* (8), 4081-4148.

72.   Vignais, P. M.; Billoud, B., *Chem. Rev.* **2007,** *107* (10), 4206-4272.

73.   Evans, D. J.; Pickett, C. J., *Chem. Soc. Rev.* **2003,** *32* (5), 268-275.

74.   De Lacey, A. L.; Fernández, V. M.; Rousset, M.; Cammack, R., *Chem. Rev.* **2007,** *107* (10), 4304-4330.

75.   Fontecilla-Camps, J. C.; Volbeda, A.; Cavazza, C.; Nicolet, Y., *Chem. Rev.* **2007,** *107* (10), 4273-4303.

76.   Liu, X.; Ibrahim, S. K.; Tard, C.; Pickett, C. J., *Coord. Chem. Rev.* **2005,** *249* (15), 1641-1652.

77.   Capon, J.-F.; Gloaguen, F.; Pétillon, F. Y.; Schollhammer, P.; Talarmin, J., *Coord. Chem. Rev.* **2009,** *253* (9), 1476-1494.

78.   Artero, V.; Berggren, G.; Atta, M.; Caserta, G.; Roy, S.; Pecqueur, L.; Fontecave, M., *Acc. Chem. Res.* **2015,** *48* (8), 2380-2387.

79.   Caserta, G.; Roy, S.; Atta, M.; Artero, V.; Fontecave, M., *Curr. Opin. Chem. Biol.* **2015,** *25*, 36-47.

80.   Rauchfuss, T. B., *Acc. Chem. Res.* **2015,** *48* (7), 2107-2116.

81.   Ott, S.; Kritikos, M.; Åkermark, B.; Sun, L., *Angew. Chem. Int. Ed.* **2003,** *42* (28), 3285-3288.

82.   Wolpher, H.; Borgström, M.; Hammarström, L.; Bergquist, J.; Sundström, V.; Styring, S.; Sun, L.; Åkermark, B., *Inorg. Chem. Commun.* **2003,** *6* (8), 989-991.

83.   Ott, S.; Borgström, M.; Kritikos, M.; Lomoth, R.; Bergquist, J.; Åkermark, B.; Hammarström, L.; Sun, L., *Inorg. Chem.* **2004,** *43* (15), 4683-4692.

84.   Ekstrom, J.; Abrahamsson, M.; Olson, C.; Bergquist, J.; Kaynak, F. B.; Eriksson, L.; Sun, L.; Becker, H.-C.; Akermark, B.; Hammarstrom, L.; Ott, S., *Dalton Trans.* **2006,** *0* (38), 4599-4606.

85.   Wang, F.; Wang, W.-G.; Wang, H.-Y.; Si, G.; Tung, C.-H.; Wu, L.-Z., *ACS Catal.* **2012,** *2* (3), 407-416.

86.   Wang, W.-G.; Wang, F.; Wang, H.-Y.; Si, G.; Tung, C.-H.; Wu, L.-Z., *Chem. Asian J.* **2010,** *5* (8), 1796-1803.

87.   Wang, H.-Y.; Si, G.; Cao, W.-N.; Wang, W.-G.; Li, Z.-J.; Wang, F.; Tung, C.-H.; Wu, L.-Z., *Chem. Commun.* **2011,** *47* (29), 8406-8408.

88.   Song, L.-C.; Tang, M.-Y.; Su, F.-H.; Hu, Q.-M., *Angew. Chem. Int. Ed.* **2006,** *45* (7), 1130-1133.

89.   Song, L.-C.; Tang, M.-Y.; Mei, S.-Z.; Huang, J.-H.; Hu, Q.-M., *Organometallics* **2007,** *26* (7), 1575-1577.

90.   Li, X.; Wang, M.; Zhang, S.; Pan, J.; Na, Y.; Liu, J.; Åkermark, B. r.; Sun, L., *J. Phys. Chem. B* **2008,** *112* (27), 8198-8202.

91.   Kluwer, A. M.; Kapre, R.; Hartl, F.; Lutz, M.; Spek, A. L.; Brouwer, A. M.; van Leeuwen, P. W. N. M.; Reek, J. N. H., *Proc. Natl. Acad. Sci. U.S.A.* **2009,** *106* (26), 10460-10465.

92.   Samuel, A. P. S.; Co, D. T.; Stern, C. L.; Wasielewski, M. R., *J. Am. Chem. Soc.* **2010,** *132* (26), 8813-8815.

93.   Scattergood, P. A.; Delor, M.; Sazanovich, I. V.; Bouganov, O. V.; Tikhomirov, S. A.; Stasheuski, A. S.; Parker, A. W.; Greetham, G. M.; Towrie, M.; Davies, E. S.; Meijer, A. J. H. M.; Weinstein, J. A., *Dalton Trans.* **2014,** *43* (47), 17677-17693.

94.   Li, P.; Amirjalayer, S.; Hartl, F.; Lutz, M.; Bruin, B. d.; Becker, R.; Woutersen, S.; Reek, J. N. H., *Inorg. Chem.* **2014,** *53* (10), 5373-5383.

95.   Cui, H.-h.; Hu, M.-q.; Wen, H.-m.; Chai, G.-l.; Ma, C.-b.; Chen, H.; Chen, C.-n., *Dalton Trans.* **2012,** *41* (45), 13899-13907.

96.   Yu, T.; Zeng, Y.; Chen, J.; Li, Y.-Y.; Yang, G.; Li, Y., *Angew. Chem. Int. Ed.* **2013,** *52* (21), 5631-5635.

97.   Wang, W.; Yu, T.; Zeng, Y.; Chen, J.; Yang, G.; Li, Y., *Photochem. Photobiol. Sci.* **2014,** *13* (11), 1590-1597.

98.   Borg, S. J.; Behrsing, T.; Best, S. P.; Razavet, M.; Liu, X.; Pickett, C. J., *J. Am. Chem. Soc.* **2004,** *126* (51), 16988-16999.

99.   Na, Y.; Pan, J.; Wang, M.; Sun, L., *Inorg. Chem.* **2007,** *46* (10), 3813-3815.

100.   Li, X.; Wang, M.; Zhang, S.; Pan, J.; Na, Y.; Liu, J.; Åkermark, B.; Sun, L., *J. Phys. Chem. B* **2008,** *112* (27), 8198-8202.

101.   Na, Y.; Wang, M.; Pan, J.; Zhang, P.; Åkermark, B.; Sun, L., *Inorg. Chem.* **2008,** *47* (7), 2805-2810.

102.   Ridley, A. R.; Stewart, A. I.; Adamczyk, K.; Ghosh, H. N.; Kerkeni, B.; Guo, Z. X.; Nibbering, E. T. J.; Pickett, C. J.; Hunt, N. T., *Inorg. Chem.* **2008,** *47* (17), 7453-7455.

103.   Kaziannis, S.; Santabarbara, S.; Wright, J. A.; Greetham, G. M.; Towrie, M.; Parker, A. W.; Pickett, C. J.; Hunt, N. T., *J. Phys. Chem. B* **2010,** *114* (46), 15370-15379.

104.   Bingaman, J. L.; Kohnhorst, C. L.; Van Meter, G. A.; McElroy, B. A.; Rakowski, E. A.; Caplins, B. W.; Gutowski, T. A.; Stromberg, C. J.; Webster, C. E.; Heilweil, E. J., *J. Phys. Chem. A* **2012,** *116* (27), 7261-7271.

105.   Johnson, M.; Thuman, J.; Letterman, R. G.; Stromberg, C. J.; Webster, C. E.; Heilweil, E. J., *J. Phys. Chem. B* **2013,** *117* (49), 15792-15803.

106.   Kania, R.; Frederix, P. W. J. M.; Wright, J. A.; Ulijn, R. V.; Pickett, C. J.; Hunt, N. T., *J. Chem. Phys.* **2012,** *136* (4), 044521.

107.   Caplins, B. W.; Lomont, J. P.; Nguyen, S. C.; Harris, C. B., *J. Phys. Chem. A* **2014,** *118* (49), 11529-11540.

108.   Hunt, N. T.; Wright, J. A.; Pickett, C., *Inorg. Chem.* **2016,** *55* (2), 399-410.

109.   Whittle, C. E.; Weinstein, J. A.; George, M. W.; Schanze, K. S., *Inorg. Chem.* **2001,** *40* (16), 4053-4062.

110.   Hissler, M.; McGarrah, J. E.; Connick, W. B.; Geiger, D. K.; Cummings, S. D.; Eisenberg, R., *Coord. Chem. Rev.* **2000,** *208* (1), 115-137.

111.   Chan, C.-W.; Cheng, L.-K.; Che, C.-M., *Coord. Chem. Rev.* **1994,** *132*, 87-97.

112.   Hissler, M.; Connick, W. B.; Geiger, D. K.; McGarrah, J. E.; Lipa, D.; Lachicotte, R. J.; Eisenberg, R., *Inorg. Chem.* **2000,** *39* (3), 447-457.

113.   Delor, M.; Archer, S. A.; Keane, T.; Meijer, A. J. H. M.; Sazanovich, I. V.; Greetham, G. M.; Towrie, M.; Weinstein, J. A., *Nat. Chem.* **2017,** *9*, 1099.

114.   Delor, M.; Keane, T.; Scattergood, P. A.; Sazanovich, I. V.; Greetham, G. M.; Towrie, M.; Meijer, A. J. H. M.; Weinstein, J. A., *Nat. Chem.* **2015,** *7* (9), 689-695.

2. Methodology

SYNTHESIS

Starting materials and solvents that were commercially available were purchased from Sigma Aldrich, Fluorochem, Alfa Aesa, VWR UK and Johnson Matthey. These materials were used as received without further purification. Deaeration of solvents was performed by freeze-pump-thaw cycles or purging the solvent with bubbling argon. All synthetic techniques were performed under standard Schlenk line procedures with an argon atmosphere. Column chromatography was performed on 60 Å mesh silica gel.

ANALYSIS OF PRODUCTS

NMR

All ^{1}H and ^{13}C NMR spectra were recorded at either 400 or 250 MHz on Bruker Avance 400, Bruker Avance III 400 HD, Bruker DPX-400 and Bruker Avance 250 spectrometers. ^{31}P NMR spectra were recorded on either a 250 MHz Bruker Avance 250 or 400 MHz Bruker DPX-400 spectrometer, with carrier frequencies for phosphorus nuclei of 101.1 MHz and 161.9 MHz respectively. ^{1}H COSY spectra were recorded at 400 MHz on a Bruker 400 Avance III HD spectrometer. Deuterated solvents were purchased from Sigma-Aldrich and were of spectroscopic grade. All chemical shifts are quoted in parts per million (ppm), with ^{1}H NMR spectra being calibrated relative to the residual solvent signal (CHCl$_3$ 7.26, DMSO 2.50, Acetone 2.05, CH$_2$Cl$_2$ 5.32).[1]

Mass Spectrometry

Positive electrospray (ES) mass spectra were recorded via a Waters LCT time-of-flight (TOF) mass analyser and electron ionisation (EI) spectra through the use of a VG AutoSpec magnetic sector instrument. Analysis of material in the solid state was collected through an atmospheric solids analysis probe (ASAP). All experiments were carried out by the University of Sheffield mass spectrometry service.

X-Ray Crystallography

X-Ray diffraction data were collected on a Bruker SMART CCD (charge coupled device) area detector with an Oxford Cryosystems low temperature system. The typical experimental temperature was 100 K, with an X-Ray wavelength of 0.71073 Å. Crystal structures were solved by direct methods and refined by full-matrix least-squares on F^2. All diffraction experiments and structural determination was carried out by Mr. Harry Adams of the University of Sheffield X-Ray crystallography service.

PHOTOPHYSICAL MEASUREMENTS

Cyclic Voltammetry (CV)

Cyclic voltammograms were measured using an Autolab Potentiostat 100 with General Purpose Electrochemical Software (GPES). Analyte solutions were prepared using nitrogen saturated dry dichloromethane obtained from a Grubbs solvent purification system. All measurements were conducted at room temperature under a stream of dry nitrogen at potential scan rates ranging from 25 to 400 mV s^{-1}. NBu$_4$PF$_6$ was used as a supporting electrolyte, previously recrystallised from ethanol and oven dried prior to use, with a typical solution concentration of 0.1 mol dm^{-3}. The working electrode was a glassy carbon disc. Platinum wire was utilised as the counter electrode. The reference electrode was Ag/AgCl, being chemically isolated from the analyte solution by an electrolyte containing bridge tube tipped with a porous frit. Ferrocene was utilised as an internal reference, with all potentials being quoted relative to the Fc/Fc$^+$ couple. The linear relationship between the maximum detected current and the square root of the

applied potential was utilised to check whether electrochemical processes were diffusion controlled across a range of scan rates.

Steady state FTIR and UV/vis spectrometry

Solution phase infrared spectra were recorded using a Perkin Elmer Spectrum One Spectrometer at 2 cm^{-1} resolution in dichloromethane solution, unless otherwise stated. Solid state spectra were recorded using a diamond ATR attachment on Perkin Elmer Spectrum One spectrometer. All electronic absorption spectra were recorded in dichloromethane solution. Spectra were recorded on either a Cary 50 Bio or Cary 5000 spectrometer.

Emission Spectra and Lifetimes

Emission spectra were recorded on a Horiba Jobin Yvon Fluoromax4 controlled by FluorEssence software. Spectra for analyte solutions were recorded anaerobically and under atmospheric conditions. Anaerobic conditions were achieved by either freeze pump thaw degassing or purging with argon gas. Analyte solutions were adjusted to a concentration whereby the solution has optical density of 0.1 at the excitation wavelength used. Lifetime data were recorded using a single photon counting method on an Edinburgh Instruments mini-tau using a 410 nm pulsed diode laser with a pulse length of 75 ps. Data points were fit to exponential functions using Origin 8.5 software to extract the values of the emission lifetimes. Quantum yields of emission were recorded in deaerated dichloromethane solution and referenced to $[Ru(bpy)_3]Cl_2$ in deaerated water, $\Phi = 0.063$.[2]

Transient absorption

Picosecond transient absorption experiments were performed on a home-built pump-probe setup.[3] The fundamental output (1064 nm, 20 ps, 10 Hz, 3 mJ) of a mode-locked Nd:YAG laser was passed through a computer controlled optical delay line and focused into a 10 cm length cell filled with D_2O to generate a continuum probe light source. The broadband supercontinuum was then split into both signal and reference beams, being detected by a spectrograph (home-modified monochromator) fitted with a CCD camera. The sample was excited with the output 450 - 580 nm from a dual stage optical parametric oscillator-optical parametric amplifier (OPO-OPA), itself pumped with the third harmonic (355 nm, 10 Hz, 6 mJ) of the aforementioned laser. The typically energy of the pump was 1.5-2.0 mJ per pulse with a repetition rate of 10 Hz. The instrumental response of the setup is estimated to be ca. 25 ps. Analyte solutions were contained within 2 mm pathlength quartz cuvettes, with the solution being flowed during data acquisition. All experiments were conducted with the assistance of George A Farrow and Simon E Greenough. Data processing of transient absorption data and spectra was performed using Glotaran software.

Time Resolved InfraRed (TRIR) Spectroscopy

TRIR studies were performed at the Rutherford Appleton Laboratory using the ULTRA facility, details of which have been published previously.[3-5] In these experiments a 65 MHz, 40 fs Titanium Sapphire laser is used to pump a range of optical parametric amplifiers (OPAs). The pump beam (400 nm) is generated from the second harmonic of the Ti:Sapph laser, whilst another portion of the initial laser beam is used to generate tuneable mid-IR probe light with a 400 cm^{-1} bandwidth. The pump energy is typically 1.0-1.5 µJ per pulse. Changes in IR absorbance are determined via three HgCdTe linear IR-array detectors. All analyte solutions were contained within Harrick cells with 2 mm thick CaF_2 windows with a typical pathlength of 500 µm. Sample solutions were flowed and the cells rastered during the experiments to minimise photo-decomposition. Fitting of the exponential decays was performed using Origin 8.5 logarithmic fitting functions of the output of a single pixel for individual band and by combining the individual bands using a global fit method to obtain the lifetimes of processes.

Quenching experiments

Quenching experiments were performed by making a (1 – 4) x10^{-5} mol dm^{-3} solution of PS in dichloromethane that was then purged with bubbling argon. The initial lifetime was measured using these solutions in a 1 cm pathlength, septum capped, fluorescence cell on an Edinburgh Instruments mini-τ single photon counting spectrophotometer excited by a pulsed 410 nm diode, single exponential fits were performed using Origin 8.5 software. Emission spectra were recorded using a Jobin Yvon Fluoromax 4 and UV/Vis absorption spectra were recorded on a Cary 50 Bio spectrometer. Quenching of this initial emission then proceeded by titrating in 10-500 μL of a 1-4x10^{-2} mol dm^{-3} solution of quencher and further lifetimes were recorded.

COMPUTATIONAL METHODS

All calculations were carried out by Theo Keane at the University of Sheffield, using the Gaussian 09 software package, version C.01.[6] Gaussian was compiled using the Portland compiler v 8.0-2 on an EMT64 architecture using Gaussian-supplied versions of BLAS and ATLAS.[7-8] All calculations utilized the B3LYP functional.[9] The 6-311G** basis set[10-11] was employed for all elements except platinum, for which a Stuttgart-Dresden pseudo-potential was instead used.[12] This combination of basis sets has been found to provide a reasonably accurate description of the properties and behaviour of transition-metal complexes in our previous work.[13] In all calculations, the solvent was described using the polarizable continuum model (PCM), as implemented in Gaussian.[14-15] For all calculations, ultrafine integrals were used and no symmetry constraints were applied. All optimized geometries were confirmed as local minima by the absence of imaginary frequencies in their calculated vibrational spectra, within the harmonic approximation.

REFERENCES

1.   Gottlieb, H. E.; Kotlyar, V.; Nudelman, A., *J. Org. Chem.* **1997,** *62* (21), 7512-7515.

2.   Suzuki, K.; Kobayashi, A.; Kaneko, S.; Takehira, K.; Yoshihara, T.; Ishida, H.; Shiina, Y.; Oishi, S.; Tobita, S., *PCCP* **2009,** *11* (42), 9850-9860.

3.   Best, J.; Sazanovich, I. V.; Adams, H.; Bennett, R. D.; Davies, E. S.; Meijer, A. J. H. M.; Towrie, M.; Tikhomirov, S. A.; Bouganov, O. V.; Ward, M. D.; Weinstein, J. A., *Inorg. Chem.* **2010,** *49* (21), 10041-10056.

4.   Kania, R.; Stewart, A. I.; Clark, I. P.; Greetham, G. M.; Parker, A. W.; Towrie, M.; Hunt, N. T., *PCCP* **2010,** *12* (5), 1051-1063.

5.   Greetham, G. M.; Burgos, P.; Cao, Q.; Clark, I. P.; Codd, P. S.; Farrow, R. C.; George, M. W.; Kogimtzis, M.; Matousek, P.; Parker, A. W.; Pollard, M. R.; Robinson, D. A.; Xin, Z.-J.; Towrie, M., *Appl. Spectrosc.* **2010,** *64* (12), 1311-1319.

6.   Frisch, M. J.; Trucks, G. W.; Schlegel, H. B.; Scuseria, G. E.; Robb, M. A.; Cheeseman, J. R.; Scalmani, G.; Barone, V.; Mennucci, B.; Petersson, G. A.; Nakatsuji, H.; Caricato, M.; Li, X.; Hratchian, H. P.; Izmaylov, A. F.; Bloino, J.; Zheng, G.; Sonnenberg, J. L.; Hada, M.; Ehara, M.; Toyota, K.; Fukuda, R.; Hasegawa, J.; Ishida, M.; Nakajima, T.; Honda, Y.; Kitao, O.; Nakai, H.; Vreven, T.; Montgomery Jr., J. A.; Peralta, J. E.; Ogliaro, F.; Bearpark, M. J.; Heyd, J.; Brothers, E. N.; Kudin, K. N.; Staroverov, V. N.; Kobayashi, R.; Normand, J.; Raghavachari, K.; Rendell, A. P.; Burant, J. C.; Iyengar, S. S.; Tomasi, J.; Cossi, M.; Rega, N.; Millam, N. J.; Klene, M.; Knox, J. E.; Cross, J. B.; Bakken, V.; Adamo, C.; Jaramillo, J.; Gomperts, R.; Stratmann, R. E.; Yazyev, O.; Austin, A. J.; Cammi, R.; Pomelli, C.; Ochterski, J. W.; Martin, R. L.; Morokuma, K.; Zakrzewski, V. G.; Voth, G. A.; Salvador, P.; Dannenberg, J. J.; Dapprich, S.; Daniels, A. D.; Farkas, Ö.; Foresman, J. B.; Ortiz, J. V.; Cioslowski, J.; Fox, D. J. *Gaussian 09*, Gaussian, Inc.: Wallingford, CT, USA, 2009.

7.   Clint Whaley, R.; Petitet, A.; Dongarra, J. J., *Parallel Computing* **2001,** *27* (1–2), 3-35.

8.   Whaley, R. C.; Petitet, A., *Software: Practice and Experience* **2005,** *35* (2), 101-121.

9.   Becke, A. D., *J. Chem. Phys.* **1993,** *98* (7), 5648-5652.

10.   Krishnan, R.; Binkley, J. S.; Seeger, R.; Pople, J. A., *J. Chem. Phys.* **1980,** *72* (1), 650-654.

11.   McLean, A. D.; Chandler, G. S., *J. Chem. Phys.* **1980,** *72* (10), 5639-5648.

12.   Andrae, D.; Häußermann, U.; Dolg, M.; Stoll, H.; Preuß, H., *Theor. Chim. Acta* **1990,** *77* (2), 123-141.

13.   Foxon, S. P.; Green, C.; Walker, M. G.; Wragg, A.; Adams, H.; Weinstein, J. A.; Parker, S. C.; Meijer, A. J. H. M.; Thomas, J. A., *Inorg. Chem.* **2012,** *51* (1), 463-471.

14.   Mennucci, B.; Tomasi, J., *J. Chem. Phys.* **1997,** *106* (12), 5151-5158.

15.   Cossi, M.; Barone, V.; Mennucci, B.; Tomasi, J., *Chem. Phys. Lett.* **1998,** *286* (3–4), 253-260.

3. Synthesis and Characterisation of a PS – [FeFe] Dyad Featuring a Cyclometalated Platinum Luminophore

INTRODUCTION

Molecular hydrogen (H_2) may be considered the ideal fuel.[1-3] Hydrogen is the most abundant element in the universe and the use of hydrogen in fuel cells produces no harmful greenhouse gases, only water. The use of hydrogen as a fuel would also allow it to replace oil, coal and gas in processes requiring combustion. Its use as a fuel could reverse the problems faced by humanity from the greenhouse effect and continued use of fossil fuels. Unfortunately, these distinct advantages of hydrogen fuel are currently outweighed by several large hurdles.

The hydrogen economy would require advances in storage, transport and production in order to be a viable energy vector. Currently there is no attractive method for storing hydrogen; liquefying hydrogen requires temperatures of -253°C, bottling it requires very high pressures of up to 700 bar that must be contained by heavy or expensive pressure vessels and storing it chemically reduces its energy density to the point where it is not a useful source of energy compared to more available alternatives.[3-4] Hydrogen scarcely exists naturally as molecular hydrogen on earth; it must be manufactured and is therefore a secondary energy source. This makes hydrogen a renewable energy store only where renewable energy is used to produce the hydrogen fuel.

Hydrogen can be produced through a multitude of chemical systems. As of 2007, 95% of hydrogen production is from fossil fuels, typically steam-methane reforming, and 5% comes from the electrolysis of water using renewable energy.[5] Electrolysis is not viable for expansion; its high cost prevents it from being a competitor to steam reforming of fossil fuels. Instead new technologies relying on the use of renewable energy sources, such as solar and wind, must be developed. The use of biologically inspired, hydrogenase enzyme mimics coupled to photosensitizers may be able to achieve this goal.[6]

Hydrogenase enzymes can be classified into three categories, depending on the character of the active site in each. These are a [Ni-Fe] metal cluster, a Fe single site cluster or a bridged [Fe-Fe] cluster, all of which show promising electrocatalytic behaviour with regard to reducing protons to hydrogen.

As stated in the introduction, this work concentrates on the diiron [Fe-Fe] type clusters.[7] This enzyme species has been shown to electrochemically catalyse hydrogen evolution at a rate of 0.55 mol min^{-1} mg^{-1}.[8] The diiron hydrogenase active site features two iron atoms bridged by an azadithiolate, with four carbonyls and two cyanides filling the remaining ligand coordination sites (Figure 1). The structure has been modelled synthetically by many complexes featuring the diiron disulfide butterfly functionality at the core of this form of hydrogenase. These complexes may feature an all-carbon or heteroatom alkyl bridge, a conjugated aryl bridge, no bridge at all, cyanides replaced by carbonyls, phosphines or N-heterocyclic carbenes or pendant groups designed to stabilise the loss of a carbonyl from the structure.[7]
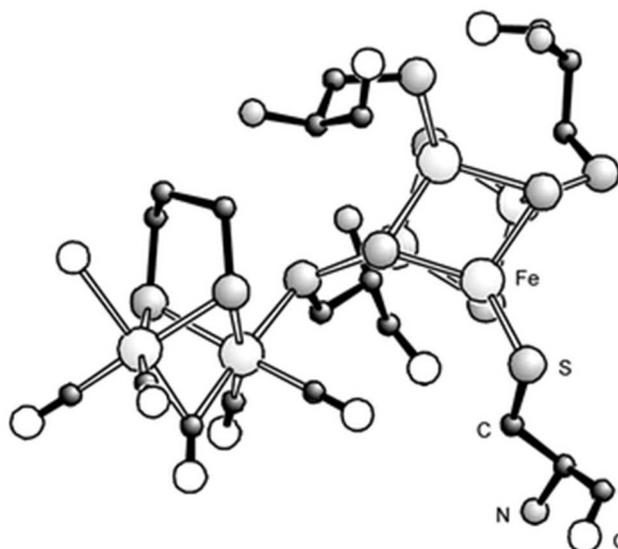
Figure 1 A composite structure of the H-centre of [FeFe] hydrogenase constructed from the crystal structures of hydrogenases isolated from D. desulfuricans and C. pasteurianum and FTIR data from D. vulgaris.[6]

To achieve photocatalytic hydrogen production using these molecules, a photosensitizer (PS) must be attached, to harvest light and provide a source of photoelectrons. In order to efficiently transfer an electron from PS to catalyst the two have been covalently or supramolecularly linked in many systems, to reduce the time required for charge separation to occur. This has been achieved by attaching the catalyst to PS by ester, amide, conjugated and pyridyl linkers with the use of primarily five kinds of metal photosensitizers; $[Ru(bpy)_3]^{2+}$, metal porphyrins, $[Re(bpy)(CO)_3X]$ type complexes, cyclometalated iridum(III) and cyclometalted platinum(II) complexes.[9]

Shortfalls of reported PS – [FeFe] dyads

Complexity of synthesis

The incorporation of a diiron hydrogenase mimic into a dyad with a photosensitizing moiety requires that a chemical link is formed between the two functional centres. This link can be covalent,[10-13] coordinative[14-16] or supramolecular.[17-19] These types of bonding all feature in the reported PS-[FeFe] dyads, with each displaying strengths and weaknesses in their use to link the two functional moieties, and each have corresponding complexities to their synthesis.

Dyads primarily featuring zinc porphyrin PS complexes often make use of supramolecular interactions to make the link between PS and catalyst functionalities, due to well understood and reliable supramolecular interactions between Zn porphyrins and pyridine based ligands. Although these links are easy to form, requiring only a pyridine bearing [FeFe] complex and a Zn porphyrin photosensitizer, the bonding is not permanent and an excess of catalyst is required to ensure coordination. These links can also facilitate delayed charge recombination, despite slowed charge separation, which may be useful in propagating the catalytic cycle.[20] The supramolecular interactions may be used to rapidly form libraries of possibly catalytic dyads, but this happens at the expense of more targeted synthetic options.[19]

Coordination bonds are utilised where the electron transfer is designed to be directed to one of the iron centres of the [FeFe] moiety.[14-15, 21] Despite this configuration being more similar to the accepted biological configuration of the diiron hydrogenase enzyme family, dyads featuring this connection still show low catalytic activities with no advantage in terms of reducing synthetic complexity. They require extensive modification to PS ligands to include isonitrile[15] or phosphine[14, 16] functionality to allow coordination to the iron centres. These modifications

35

require careful consideration to prevent coordination of these to PS metal centres, which may result in significant loss of synthetic yields; this is a problem when considering the abundance of the PS metal centres, which are typically platinum group metals, such as iridium, ruthenium or rhodium.

A large number of dyads reported to date feature a covalent linker between the ligands of the PS and the dithiolate bridge of the [FeFe] functionality.[10-13] This arrangement is not ideal, as the distance between electron donor and acceptor centres can be quite long and these linkers are not fully conjugated, weakening electron transfer ability along these pathways. These types of linkers benefit from using well understood and reliable synthons, utilising coupling reactions to link the two centres using reliable synthetic methods, including but not limited to palladium catalysed cross couplings, peptide coupling reactions, and esterifications. Methods such as these offer the option of targeted synthesis using reliable and understood reaction pathways.
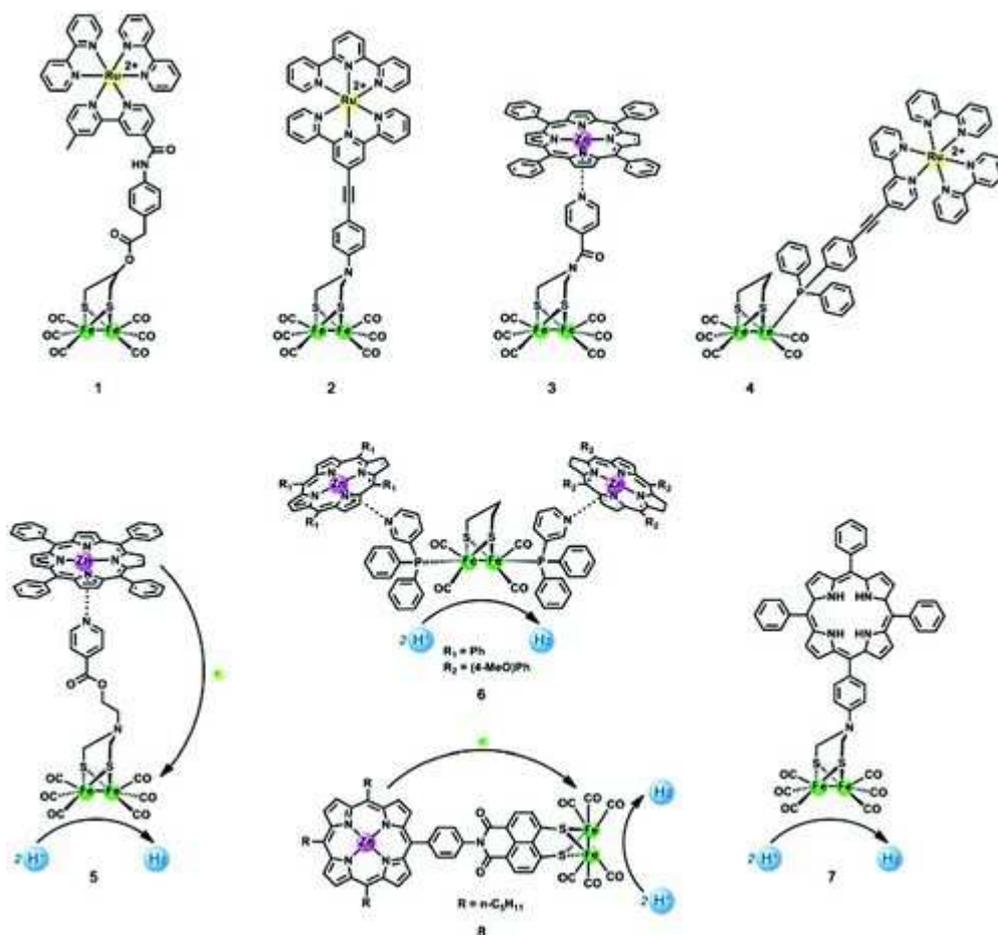
Figure 2 Structures of previously reported PS – [FeFe] dyads, featuring ruthenium and porphyrin PS moieties.[9]

With this understanding in mind, this work will focus on a covalent link between PS and [FeFe] moieties, in order to maximise the opportunity for creating a directional electron transfer and reduce the electron transfer distance as much as possible.

Evidence of electron transfer

Stronger evidence is required to support the occurrence of electron transfers in PS–[FeFe] dyads, as only limited investigations into the excited state of these complexes has taken place.[10, 16, 22] Comparing the spectroelectrochemical and transient spectroscopic data obtained independently for reduced forms and for excited states of diiron hydrogenase mimics to the observation made for the dyad complexes reveals that the interactions between PS and [FeFe] centres are not well understood.

The mono-reduced state of $[Fe_2(\mu\text{-pdt})(CO)_6]$ has been well characterized through the use of spectroelectrochemical methods in both the UV/vis domain and the infra-red domain, the latter due to the presence of strongly absorbing metal carbonyl groups.[23] These studies revealed characteristic signals for both domains, with characteristic sub 1950 cm^{-1} peaks in the IR spectrum, and bands at 400, 550 and 700 nm in the UV/vis spectrum of the monoreduced species. Observation of these signals in transient spectroscopy of dyads should be indicative of a monoreduced state located on the [FeFe] moiety of the dyad.

Although the UV/vis bands characteristic of a monoreduced state of [FeFe] moiety have been observed in TA studies of zinc and ruthenium based dyads[10] and bimolecular systems,[24] these measurements are not useful for understanding the structural changes that take place during the formation and decay of the transiently reduced species.[20]
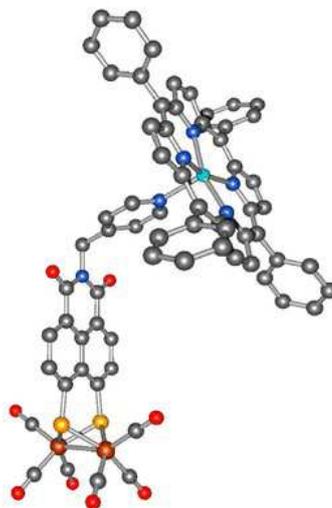
Figure 3 DFT optimized structure of the zinc porphyrin – [FeFe] dyad studied by TRIR spectroscopy.[20]

The study in question, a TRIR study of a zinc porphyrin complex supramolecularly bound to a NMI bearing diiron hydrogenase mimic (Figure 3), does not report the TRIR transient signals expected of a monoreduced diiron hydrogenase mimic. Instead, only a small amount of red shifting is seen, with no change in band structure, indicating that any charge transfer does not involve the diiron centres. The authors rationalize this findings by attributing this charge separated state to a reduced NMI moiety, with only a small amount of electron density present on the iron centres. Their postulation is supported by DFT modelling, which indicates a LUMO with only a small amount of electron density placed in the Fe − Fe antibonding orbitals. This state is unable to progress through the catalytic cycle.[20]

The transient signals observed in the aforementioned dyad study closely resemble those seen in TRIR investigations of multiple diiron hydrogenase mimics.[25] Diiron hexacarbonyls featuring ethyl,[26] propyl[26-31] and aryl[32] organic bridging ligands have undergone study, revealing the nature of the unsensitized [FeFe] in its excited state. These studies reveal that [FeFe] complexes, after excitation, undergo rapid electronic decay to the ground electronic state, followed by various vibrational state decays, including intramolecular vibrational energy redistribution (IVR), vibrational cooling (VC), and decay of vibrationally excited carbonyl modes. Some signals have also been attributed to states involving a lengthened Fe − Fe bond, which may or may not be associated with a longer lived electronically excited state. All studies show the presence of a long lived carbonyl loss photoproduct after excitation.

Although the reduced state of the enzyme mimic is well characterized, this has not allowed the study of dyads to produce a detailed characterization of the excited state. TA spectra recorded for the dyads do not have the resolution possible in TRIR spectroscopy to understand geometry

and structural changes, understood to be important in the catalytic cycle of diiron hydrogenase enzymes.

Stability

Despite promising evidence that some of the reported dyads are capable of catalytic activity, these have been unable to produce sustained catalytic activity due to a lack of stability.

The most successful catalytic systems in terms of activity have been based on iridium photosensitizers. Despite the ability to reach hundreds of turnover numbers in linked dyadic and bimolecular systems, these show a lack of stability of the iridium PS functionalities. This behaviour was confirmed by the return of catalytic activity upon refreshing the PS component of the system, after activity loss.[14]

Photocatalytic hydrogen production should not be limited by the expensive component of the system, which would compromise the desired reduction of environmentally harmful emissions in producing the hydrogen fuel. A successful system will need a stable PS complex attached to the catalytic centre. Although the instability has been partially overcome by encapsulating the dyad, ideally the dyad should be inherently stable to decomposition.[21]

Aims

The shortcomings of the aforementioned dyads highlight the required properties a successful dyad will have. The dyad must be produced through a simple and reliable synthetic method to maximise synthetic efficiency. There must be an excited state in the PS long lived enough to transfer an electron to the catalyst and the electron must be placed into an excited state that may be used to progress the catalytic cycle. After electron transfer, the catalyst must be able to use the electron transferred, and this requires identification of further steps, such as carbonyl loss. Dyads where the PS or catalyst is unstable are not feasible. In summary, any dyad synthesized must be readily synthetically accessible, with a long lived electron transfer in the excited state and must remain stable throughout the catalytic cycle.

The designed and synthesized dyad must be assessed. Assessing the electron transfer performance of a dyad will take place using the following method:

- First, the light absorbing capabilities of the dyad are measured using UV/vis and FTIR absorption spectroscopy. Cyclic voltammetry is used to identify the positions of electronic energy levels.
- Secondly, the excited state behaviour of the dyad is examined by emission spectroscopy. The results are compared to model PS compounds to identify quenching of the excited state by the presence of diiron species.
- Thirdly, in cases where there is quenching, the excited state is characterized using transient absorption methods. Observation of the characteristic signals in UV/vis TA for diiron anions can be compared to IR TA to help understand transient structural and electronic changes.

The aim of this study is to synthesize a platinum PS – diiron hydrogenase dyad that is structurally capable of linear electron transfer, characterize its ground and excited state electronic properties and attempt to observe the electron transfer experimentally with transient absorption methods. The characterization of the dyad's excited state will be compared to the reported excited state properties of relevant diiron hydrogenase mimics and DFT modelling to determine the identity of excited states and the pathway to the ground state after excitation.

SYNTHESIS OF A DYAD FEATURING AN ESTER LINKER BETWEEN PS AND HYDROGENASE MODEL

Due to the limitations of a long multi-step synthesis, a design philosophy promoting high yielding reactions with few side products was chosen. This involves a reactive group on the bipyridyl portion of the Pt N^N^C photosensitizer (PS) being used to connect a diiron hydrogenase mimic. The route does not involve a palladium catalysed cross coupling, as any route to the platinum species with an aryl iodide, available for cross coupling, is long and the yields of these reactions are low. These considerations led to choosing a target that connected the PS and diiron moiety through an ester or amide linker, as this type of coupling had been used previously to successfully link zinc, ruthenium and iridium photosensitizers to hydrogenase mimics.[12, 14, 33] Ester or amide coupling of a diiron unit required that a carboxylic acid or activated ester bearing Pt N^N^C compound was developed first.

Route to a Pt (NNC) compound amenable to esterification

Synthesis of an acid bearing platinum complex

The first route to **PtACID** (Figure 4) considered hydrolysing the ester of **PtESTER**. **PtESTER** was synthesised according to literature procedures.[34] This platinum compound however was unstable under strong acidic or basic conditions, precluding the use of either for the hydrolysis. A less harsh route to the carboxylic acid was considered, in which the ester group is hydrolysed at room temperature by potassium trimethylsilanolate.[35] Although this route is not typically recommended for pyridine derivatives, it has been successfully applied previously to platinum bipyridine complexes.[36]

The method was applied herein by dissolving the **PtESTER** in THF, adding a tenfold excess of 2M potassium trimethylsilanolate solution and stirring the mixture for 3 hours at r.t. (Figure 4). This route was successful, producing **PtACID** in 31% yield. The reaction produced a wet precipitate that was found to be difficult to dry and insoluble in most organic solvents. Although this route was successful, it was later discarded in favour of a simpler method, described below.
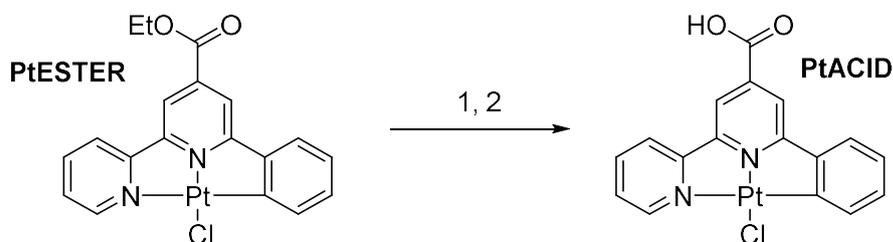
Figure 4 Method for hydrolyzing the PtESTER by potassium trimethylsilanolate. This method is less harsh than using strong bases, for example potassium hydroxide. 1. KOSiMe$_3$ (10 equiv.), THF, 3h, RT. 2. 1M HCl (aq.), 30 mins, RT.
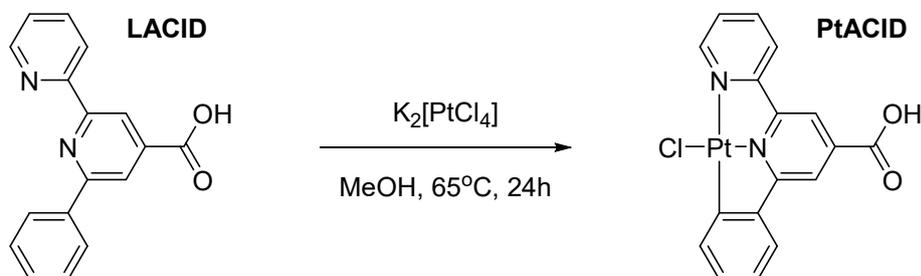
Figure 5 Reaction scheme representing a simpler route to accessing a carboxylic acid derivatized platinum complex, PtACID.

The simpler method involved synthesizing **LACID**, by literature procedures,[37] and then complexing it to platinum directly, in a method reminiscent of one used for the analogous

palladium compound (Figure 5).[37] Briefly, a suspension of Pt(DMSO)$_2$Cl$_2$ and **LACID** were suspended in MeOH and the mixture was heated to reflux for 24 hours. This produced a bright orange precipitate that could be separated by centrifugation and washed with methanol, acetone and ether to yield a pure, dry product. In comparison to the synthesis of palladium analogues, no benzene was required to solubilize the platinum starting material as the reaction proceeded as a suspension; acetone was used to wash the products, as one of the impurities was found to be especially soluble in acetone; and a longer reaction time was required, due to the lower reaction temperature and lower lability of platinum compared to palladium. With a yield of 47%, this method improves upon the yield of the potassium silanolate method and was also preferable due to simpler purification procedures. The complex was more easily dried, as it had not come into contact with significant amounts of water at any point in the synthesis or purification, and the use of low viscosity solvents allowed for better separation by centrifugation than by filtration from water.

Synthesis of a platinum NNC complex bearing an activated ester

Development of an activated ester was a continuation of producing the **PtACID**. In case the acid proved unreactive to esterification of an iron compound, a pentafluorophenol bearing ester was synthesized to produce a reactive carbonyl for nucleophilic attack by an alcohol or amine group (**LActEst**).
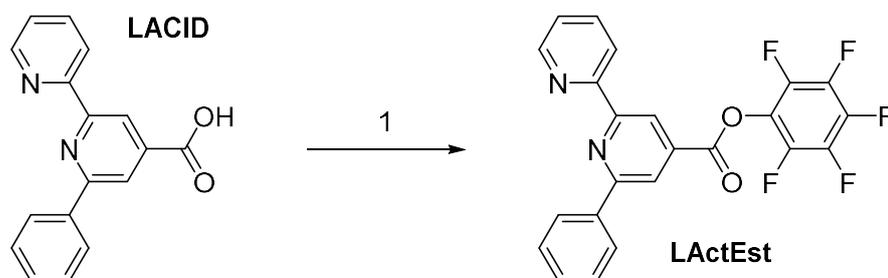
Figure 6 Attachment of the pentafluorophenol activated leaving group using modified Steglich esterification procedures. 1. HOC$_6$F$_5$, DCC, CH$_2$Cl$_2$, 4h, RT.

Synthesis of the activated ester NNC ligand, **LActEst**, proceeded by a modified Steglich esterification typical for producing these activated esters (Figure 6). Synthesis proceeded by adding N.N'-Dicyclohexylcarbodiimide and pentafluorophenol to **LACID** in DCM solution and allowed to react at room temperature for 4 hours. The product was easily separated by column chromatography on silica producing a white crystalline solid that fluoresces under UV light. This product could be used to attempt coupling of a hydrogenase mimic before complexation of the NNC moiety to platinum.

Attempts to complex platinum to **LActEst** were unsuccessful. The reaction between Pt(DMSO)$_2$Cl$_2$ and the ligand was performed at reflux in THF for 18 hours, producing an orange precipitate. The precipitate appeared to be two different compounds by NMR suggesting either incomplete complexation or two different products forming. Separation of the two compounds by column chromatography on silica or alumina was not possible as the compounds co-eluted.

In order to ensure the success of the cyclometalation step, a higher reaction temperature was required. This was achieved by using a microwave reactor with pressurized reaction vessels. The activated ester ligand and Pt(DMSO)$_2$Cl$_2$ were placed in a sealed 35mL microwave vial with 15mL of acetic acid. The reaction mixture was heated to 150°C at 4 bar of pressure for 10 minutes producing an orange precipitate. After centrifugation to separate the precipitate, and washing with diethyl ether, again two products were detected by NMR in a 2:1 ratio compared to the 1:10 ratio obtained at lower temperatures. These ratios were compared for ^{19}F NMR as ^{1}H NMR was not readily assignable for the lower temperature reaction. Despite these promising results

in attempting to form one product only, repeating the microwave reaction at 160°C produced only a black precipitate in green solution, likely to be decomposition products. The difficulty of producing the precursor was judged to outweigh its usefulness and the synthesis of **PtActEst** by complexation of **LActEst** to platinum was abandoned.

Attaching a diiron hydrogenase mimic

This part of work was performed in collaboration with Professor Christopher Pickett's group of the University of East Anglia, the leading experts in the field of diiron hydrogenases. Two hydroxyl functionalised diiron compounds were considered which would allow for coupling with either an activated ester or Steglich esterification, Figure 7. The ethyl bridged diiron compound (**BAL**) was selected for its ease of synthesis, whilst the propyl bridged diiron compound (**PDT-OH**) was selected for it closer structural resemblance to hydrogenase mimics. The preparation of the propyl bridged diiron compound is described in work by the Pickett Group[38] and its electrochemical behaviour has been described.[39] The ethyl bridged diiron compound is well studied; the one step synthesis, spectroscopic and crystallographic properties and catalytic activity have been published.[40-44]

The variety of precursors prepared allowed for multiple synthetic routes to be assessed. These are outlined below in Figure 7. Routes involving nucleophilic substitution at the carbonyl were promoted by either loss of a pentafluorophenyl group or through the addition of N,N'-dicyclohexylcarbodiimide and subsequent elimination of N,N'-dicyclohexylurea. Steglich esterification could be attempted for both **PtACID** and **LACID**; however there is only an activated ester of the free NNC ligand, **LActEst**, to compare to.

Due to the Pickett group's experience with using activated esters these reaction conditions were attempted first, to attempt to form a dyad. When **LActEst** and either of the two iron compounds were dissolved in dichloromethane containing triethylamine, no reaction appeared to have occurred over the course of 6h at room temperature, when the reaction mixture composition was monitored by TLC (Figure 7). The lack of reaction was confirmed by NMR and IR spectroscopic data. Neither increasing reaction times from 6 hours to 48 hours, nor increasing the temperature from room temperature to 30°C led to reaction between the components. This lack of reactivity may be attributed to the considerable electron donating effect of the bipyridine moiety, which decreased the electrophilic strength of the carbonyl group. As this reaction scheme seemed to be ineffective, it was discounted as a route to a dyad.

Steglich esterification was then used to attempt to form the ester bond both pre and post platinum complexation. In these attempts **LACID** or **PtACID** were dissolved in the minimum amount of dichloromethane and 1 equivalent of either iron compound was added along with 1 equivalent N-N'-dicyclohexylcarbodiimide and 0.1 equivalents of N,N-dimethyl -4-aminopyridine (Figure 7). This reaction proceeded over 72 hours. After this time it could be seen that mixtures containing either propyl bridged diiron complex or the NNC acid ligand had not reacted. In most cases the diiron reactant was recovered by column chromatography. The acid ligand and complex could not be recovered with column chromatography due its strong adherence to silica.
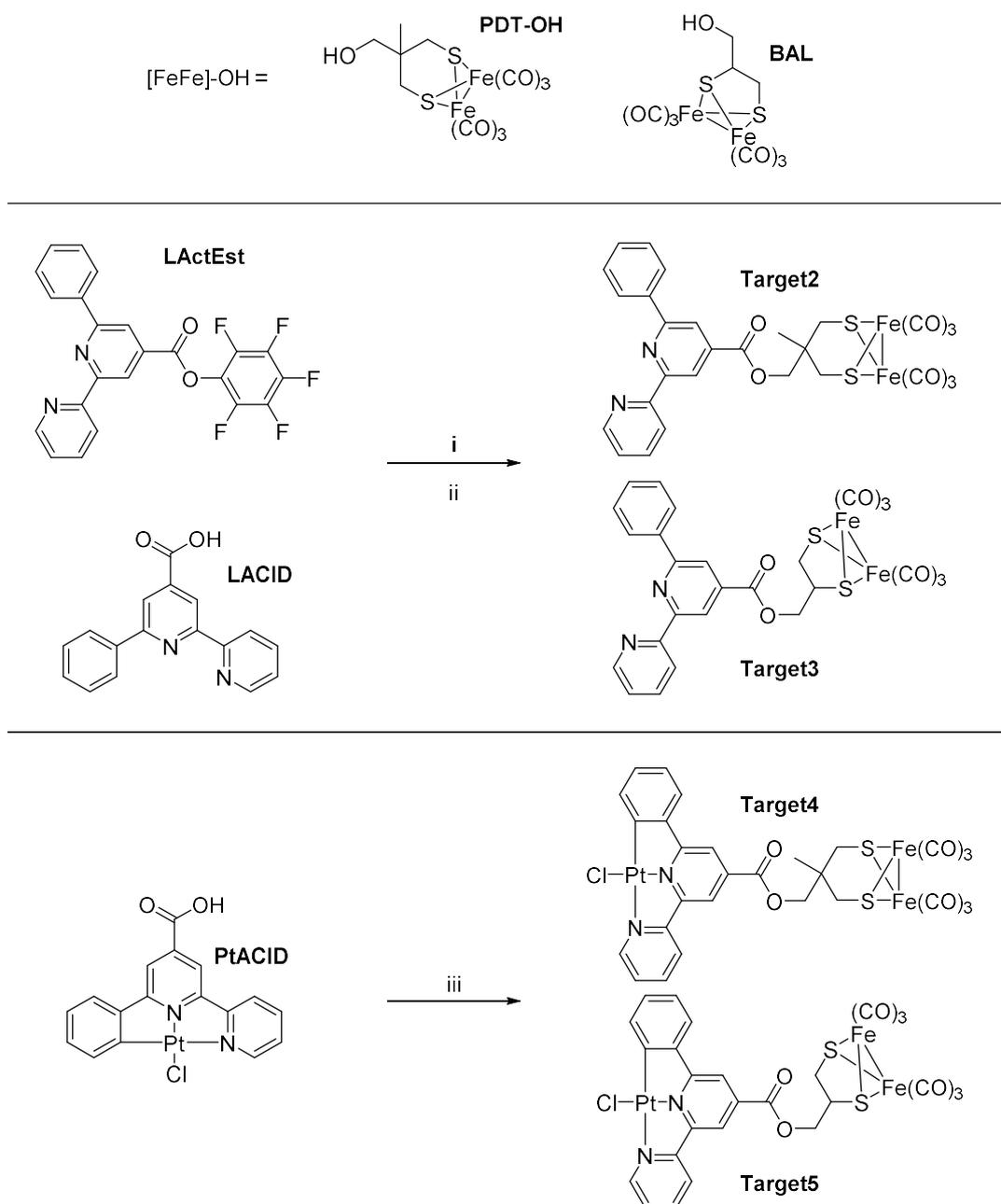
Figure 7 Three planned routes to forming dyads with two different hydrogenase mimics. Route i uses the LActEst to reach Target2 and Target3 with conditions: [FeFe]-OH, CH₂Cl₂/TEA 10:1, RT, 6-48h. Route ii uses LACID with conditions: CH₂Cl₂, [FeFe]-OH (1 equiv.), DCC (1.1 equiv.), DMAP (10 mg), 24h, RT. Route iii uses PtACID with the conditions: CH₂Cl₂, [FeFe]-OH (1-3 equiv.), DCC (1.1 equiv.), DMAP (10 mg), 4 - 24h, RT.
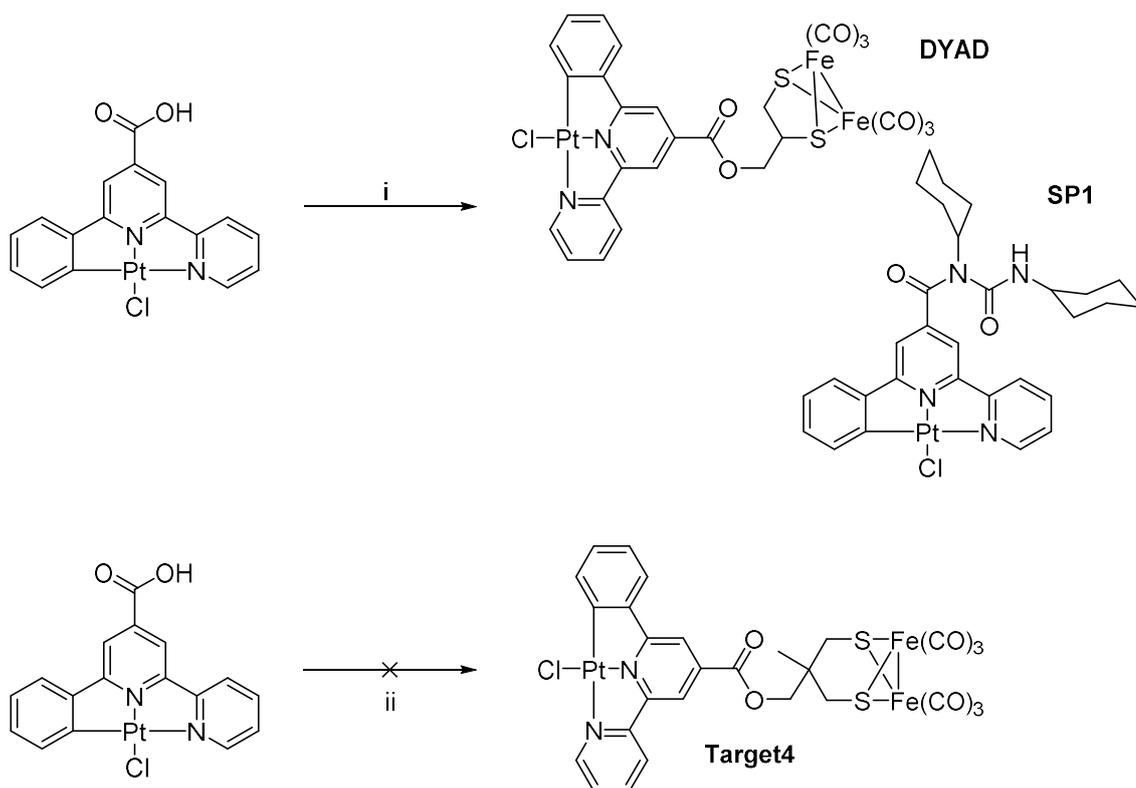
Figure 8 Steglich esterification proved successful in synthesizing a dyad, DYAD, and an amide side product, SP1. The reaction did not proceed for PDT-OH with PtACID. i) CH_2Cl_2, [FeFe]-OH (3 equiv.), DCC (1.1 equiv.), DMAP (10 mg), 4h, RT. ii) CH_2Cl_2, [FeFe]-OH (1 equiv.), DCC (1.1 equiv.), DMAP (10 mg), 24h, RT.

Despite no reaction taking place between the free **LACID** and **BAL**, the **PtACID** complex successfully reacted with **BAL** and formed the dyad, **DYAD** (Figure 8) under the same conditions. In comparison to the other 3 Steglich reactions performed, where after tracking the reactions by TLC for 3 days no changes in the reaction mixture composition were detected, the TLC plates of the reaction mixture **PtACID/BAL** displayed two new spots at higher and lower R_f than the diiron reactant. After separation by column chromatography, these two spots were found to be a side product **SP1** (Figure 8), with functionality commonly seen when a Steglich esterification does not complete, and **DYAD**.

DYAD was recovered in low yields of <20%. Once separated this compound was found to be insoluble in most solvents, except dichloromethane, in which it exhibited sparing solubility. Although modern procedures for esterification between organic acids and alcohols call for stoichiometric acid to alcohol ratio, the original procedure required a 2-4 equivalent excess of alcohol except where the alcohol is difficult to remove. As the FeFe-alcohol in this case is a readily available compound, [FeFe](BAL), which can also be easily separated from the desired product by washing with acetonitrile, further reactions used a 3 equivalent excess of [FeFe](BAL) over **PtACID**. The amount of solvent used for the reaction was also decreased, owing to the fact that a competing side product was found. This side product, **SP1**, is formed when the elimination step to form the intended product of the reaction competes with a rearrangement. With a lowered solvent volume, concentration of the iron reactant was much higher, increasing the rate of elimination of dicylcohexylurea and suppressing formation of **SP1**, as well as increasing reaction rate and allowing the reaction to reach completion quicker. These two modifications to the procedure improved yields from <20% to 78%, completely prevented formation of **SP1** and decreased reaction times from 72 hours to 4 hours.

43

Confirmation of Dyad Identity

Although TLC indicated the formation of new products from the reaction of the **PtACID** and **BAL**, there was the possibility that none of the products are the intended dyad. Several methods have been used as assurance that the dyad has been formed, including FTIR & ^{1}H NMR spectroscopy and mass spectrometry. These methods in combination have been used to demonstrate the identity of the product, **DYAD**.

The formation of a covalently linked dyad was initially confirmed using infra-red spectroscopy, due to the strongly absorbing metal carbonyl handles that can be used to identify the presence of a diiron hydrogenase mimic moiety. The platinum complex bears an ester group that has a characteristic ν(CO) stretching vibration that does not overlap with the vibrational spectrum of the diiron hydrogenase mimic. The infra-red spectra of the starting materials and dyad have been compared to the spectrum of the dyad.

The infra-red spectrum of **DYAD** (Figure 10) displays both metal carbonyl and ester ν(CO) stretches, at 1920 – 2100 cm^{-1} and 1734 cm^{-1}. The metal carbonyl stretches are comparable to those seen in the **BAL** starting material, and the ester ν(CO) stretch is 6 cm^{-1} higher in energy than that of the **PtESTER** model (used as the nearest soluble analog of **PtACID**). Due to **PtACID**'s insolubility, no solution FTIR spectrum could be obtained and **PtESTER** should be considered a suitable model for comparison. The shifting of the ester frequency to higher wavenumber indicates the presence of a functional group that is more electron withdrawing than an ethyl fragment, consistent with the presence of an electron withdrawing diiron complex. There is also a consistent shift in frequencies for metal carbonyl stretches in **DYAD** to higher wavenumber compared to **BAL**, indicating a change in electronic environment that could be caused by the formation of a dyad.

These results indicate the formation of a compound that features both the diiron hexacarbonyl moiety and also an ester, which provides strong evidence for the formation of a dyad featuring an ester linker between PS and diiron moieties.

The ^{1}H NMR can be used to support the possible formation of an ester linked dyad (Figure 9). The hydroxy proton of the **BAL** starting material exists in a portion of the spectrum that features no other chemical shifts for either **BAL** or the **PtESTER** model complex. This can be used as an indicator that an ester has been formed, as it will no longer be observed in the region 4.5 – 6.0 ppm after ester formation. The ^{1}H NMR spectra of **DYAD**, **BAL** and **PtESTER** in D$_6$-DMSO have been compared to show that there are changes in the electronic environment for the diiron moiety of the dyad, indicating formation of an ester linker.

The integrations of aryl and alkyl peaks recorded for the dyad in deuterated DMSO are in proportion, indicating that there is one PS moiety for every diiron moiety present in the sample. This supports the hypothesis that a dyad has formed through the formation of a covalent linker between PS and diiron unit. Additionally, the peak associated with the hydroxyl of **BAL** can no longer be seen in the spectrum, and is accompanied by the splitting of other peaks that represent the alkyl bridge of the diiron hydrogenase model. This is confirmation of formation of the ester and structural changes close to the bridge. The aromatic region shows little change between **DYAD** and **PtESTER**, including retention of platinum satellite peaks that are typically seen for Pt complexes with bipyridine ligands. This reveals that the ester linker acts as an insulator of each subunit from electronic effects in the other.

The absence of a peak associated with the **BAL** hydroxy in the spectrum of **DYAD** indicates the formation of an ester link. There has been little change in the aromatic peaks, associated with the cyclometalated platinum moiety, indicating that the link has formed between intact Pt PS

and diiron complexes. The integrals of the peaks shows a 1:1 ratio of PS to diiron complexes and supports the hypothesis that this is a dyad.
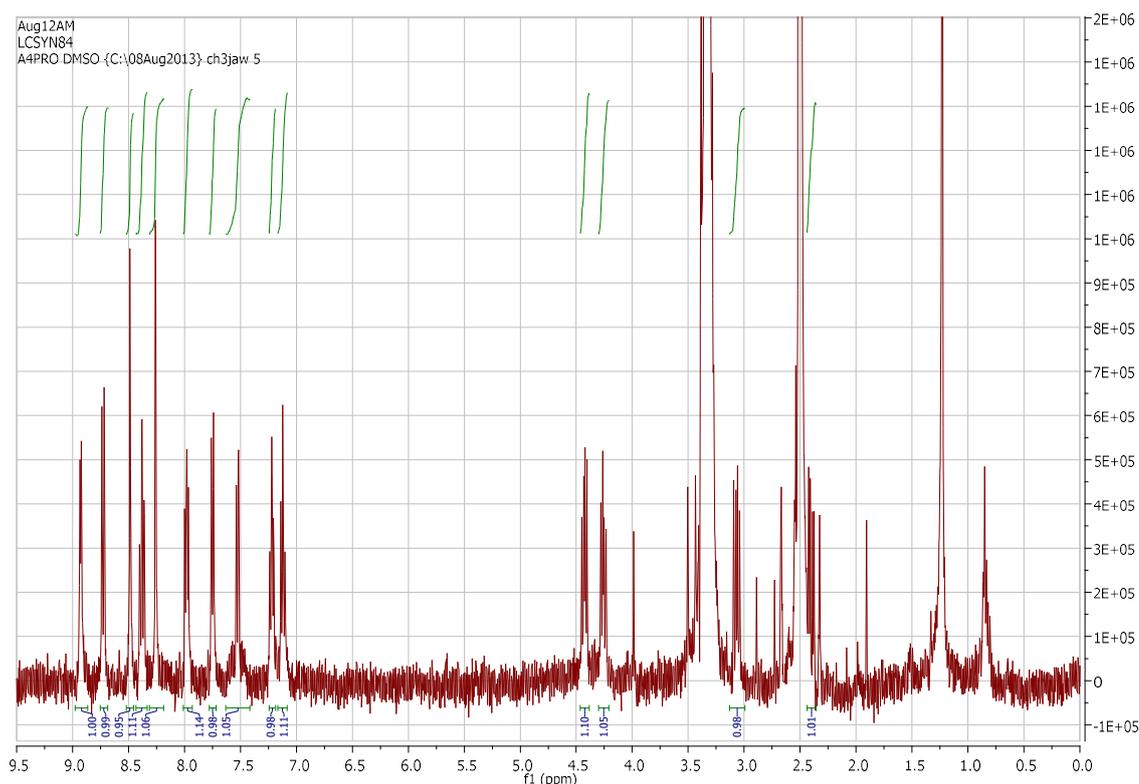
Figure 9 400 MHz ^{1}H NMR spectrum of DYAD recorded in d$_6$-DMSO. Peaks ssoicated with aryl protons on the PS moiety and alkyl protons on the [FeFe] moiety show integrations in correct proportion indicating they are likely to be on the same molecule. The spectrum is missing an expected alkyl proton peak; this is most likely obscured by the peaks associated with residual DMSO (2.5 ppm) and water (3.3 ppm).

A technique that can be used in combination with the above to demonstrate the presence of the dyad is mass spectrometry. Due to the dyad's very high mass compared to either of the starting materials, the presence of high mass species that coincide with **DYAD** or its decomposition products can be used as indication of the presence of a new dyad species. Fast atom bombardment time of flight (FAB TOF) mass spectrometry has been used to analyse the product of the reaction between **PtACID** and **BAL** to this effect.

The spectrometric results show a result of m/z = 833. Although this is not consistent with the mass of an intact **DYAD** residue, which would have an m/z of 889 for a singly charged ion, it is indicative of the dyad after it has lost two carbonyl ligands. The oxidised or reduced diiron hydrogenase model complexes are known to liberate carbonyl ligands after accepting or losing an electron; therefore, this is acceptable corroborating evidence that **DYAD** has formed.

The combination of FTIR & ^{1}H NMR spectroscopies and mass spectrometry has shown beyond doubt the presence of a dyad featuring a cyclometalated PS linked through an ester to a diiron hydrogenase model complex that has the same core structure as **BAL**.

CHARACTERIZATION OF THE NEW DYAD

The new dyad has been characterised using FTIR, UV/vis and NMR spectroscopies and cyclic voltammetry in the ground state and emission spectroscopy in the excited state to characterise its response to light and attempts to affect its charge. The characteristic signals shown by the model compounds **PtESTER** and **BAL** can be compared to **DYAD** to reveal how the two metal centres have been affected by their linking through an ester.

Infra-red absorption spectroscopy
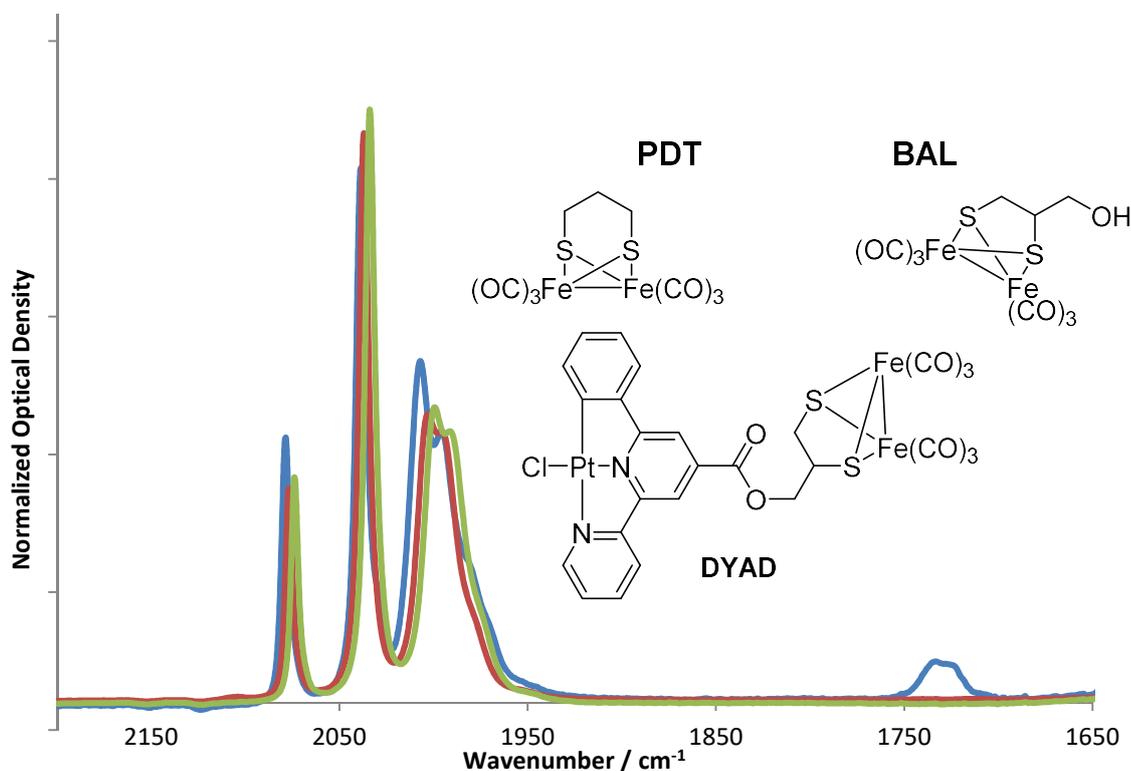
Figure 10 Solution phase IR spectra for diiron carbonyl compounds in DCM: DYAD (blue), BAL (red) and PDT (green) between 2200 and 1650 cm^{-1}. The optical densities have been normalized for comparison.

 Solution phase IR absorption spectroscopy, recorded in dichloromethane solvent, was used to confirm the presence of the diiron carbonyl functionality, by observation of ν_{CO} bands between 2200 and 1900 cm^{-1}. In the spectrum of each of the compounds, 4 distinct bands have been detected in this region, with a shoulder present on the band with lowest wavenumber (Figure 10).

Compound	$\nu(C\equiv O)$ / cm^{-1}	$\nu(R_2C=O)$ / cm^{-1}
PDT	2074, 2034, 2000, 1991	
BAL	2077, 2037, 2003, 1996	
DYAD	2079, 2039, 2007, 1996	1730

Table 1 The key IR absorption bands for the diiron carbonyl containing complexes recorded in dichloromethane solution.

The positions of the bands have been summarized in Table 1. There are slight shifts in the band positions between 2100 and 1900 cm^{-1} of less than 10 cm^{-1}, indicating that the alkyl groups of the disulfide ligand have only small effects on the electron density at the metal centre. Diiron carbonyls with disulfide ligands that contain more electron withdrawing substituents have $\nu(CO)$ bands at higher wavenumber, reflecting lower electron density at the iron centers, weaker back-bonding and stronger carbonyl C≡O bonds with less populated π* orbitals.

46

Using solution phase IR, confirmation of the formation of the dyad was achieved by comparing the entire v_{CO} region from 1700 – 2200 cm^{-1} for **PtESTER** and **DYAD**. The new v_{CO} band at ≈1730 cm^{-1} is typical of an ester carbonyl stretch and the appearance of the bands between 1900 and 2200 cm^{-1} indicate metal carbonyls are now present.

Direct comparison of **PtACID** and the dyad formed is not possible using solution phase infra-red spectroscopy as both complexes are not soluble in the same solvent where spectra can be obtained. This comparison was achieved using diamond ATR measurements to compare bands below 1900 cm^{-1}. Diamond ATR IR spectroscopy was used to characterize acyl groups and aryl ring stretches, but could not be used to characterize metal carbonyls, as there is no transparency to infra-red light with wavenumber between 2200 and 1900 cm^{-1} in diamond (Figure 11). This comparison reveals that ring breathing modes associated with the N^N^C ligand in **DYAD** are largely unaffected by the presence of a diiron moiety. There are very small shifts between the ring breathing modes observed for **PtACID** and **DYAD** of 1 – 4 cm^{-1} (Table 2). This indicates that there is a negligible amount of coupling between the two functional centres and that the ground state properties for both moieties should reflect their associated model compounds.
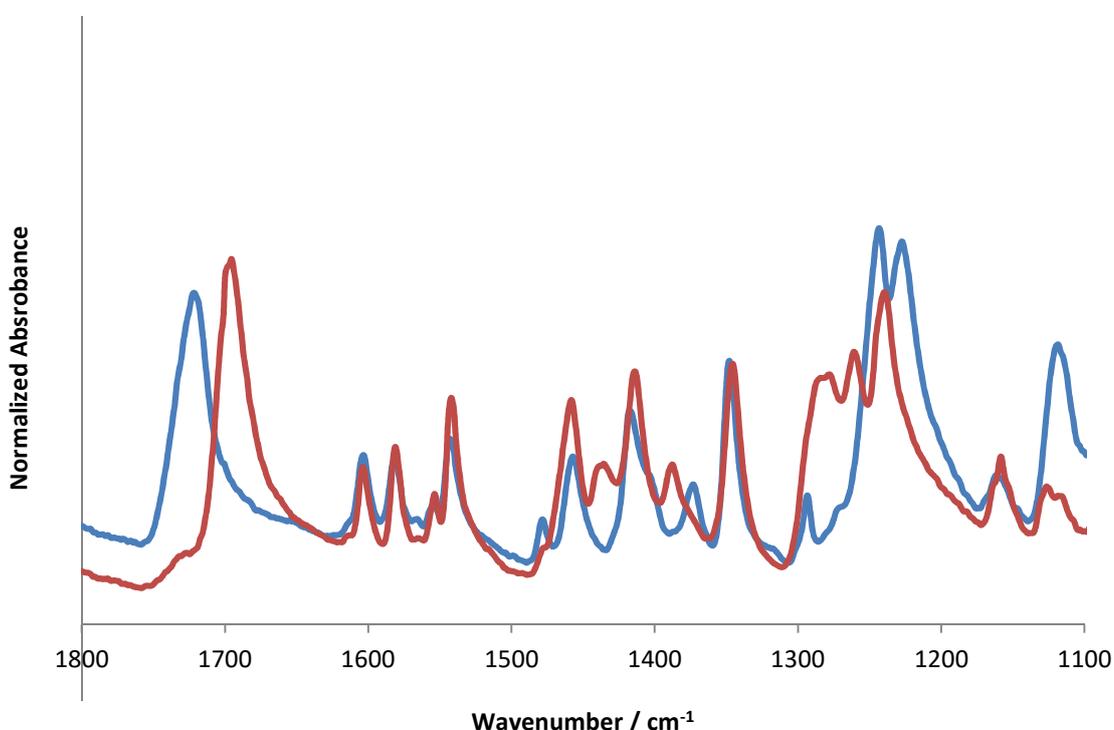
Figure 11 Overlaid diamond ATR FTIR spectra of DYAD (blue) and PtACID (red) in the range of aromatic ring vibrations ("Aryl" in Table 2), and the ester groups stretching vibration, –C(O)=O ("acyl" in Table 2).

Compound	v_{CO} (acyl) / cm^{-1}	v (aryl) / cm^{-1}
DYAD	1724	1604, 1582, 1543, 1458, 1418, 1348
PtACID	1697	1604, 1581, 1542, 1459, 1414, 1346

Table 2 Selected absorption bands from the diamond ATR IR spectra of DYAD and PtACID.

The use of FTIR spectroscopy has been used to confirm the presence of both a carbonyl associated with the ester present on the PS moiety and the carbonyls of a diiron hydrogenase model, as discussed in the confirmation of the formation of a dyad, above. FTIR has also been used to show that there is a negligible amount of interaction electronically between the two centres in the ground state, which is reflected in other ground state properties, seen below.

UV/vis Electronic Absorption Spectroscopy

UV/vis spectroscopy has been used to understand how **DYAD** reacts to light and compare its electronic properties to the model components, **PtESTER** and **BAL**. These comparisons allow for an understanding of the energies required to promote an electronic transition in the molecules and the position of bands in the **DYAD** spectrum compared to its models allows an understanding of the electronic influence each metal centre has on the other. Comparison to **SP1** has been included to demonstrate that replacement of the ester with an amide has greater effect on the Pt-center than incorporation of a diiron moiety.

All electronic absorption spectra were recorded in dichloromethane solution. Spectra of the cyclometalated platinum chloride compounds show a peak associated with the mixed metal-ligand to ligand charge transfer (MMLL'CT) transition, with a shoulder at higher wavelengths and a tail at lower wavelengths, between 400 and 600 nm. At higher energies several transitions occur at around 380, 340 and 280 nm; these are observed in all of the studied cyclometalated N^N^C compounds and can be attributed to intraligand π/π^* transitions. In **DYAD**, a transition at around 325 nm is observed; this is also seen in the UV/vis spectra for the hydroxyl containing diiron compound. This is attributed to a MLCT transition that leads to the loss of a CO ligand. The iron compound also features a broad band between 410 and 550 nm, which has previously been attributed to activation of the Fe-Fe bond resulting in a change in geometry.[26]
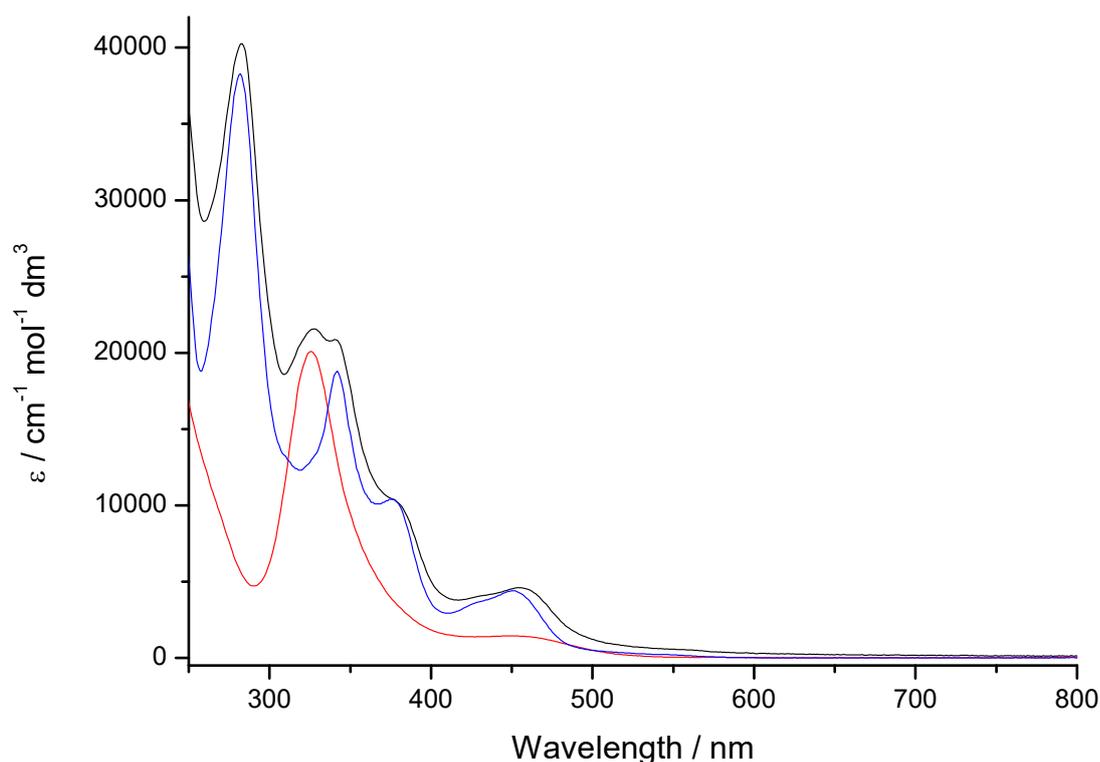
Figure 12 A comparison of the electronic absorption spectra of DYAD (black), PtESTER (blue) and BAL (red) recorded in dichloromethane solution revealing a lack of coupling between the diiron centers and the platinum center.

When the spectra of the **DYAD**, **PtESTER** and **BAL** are compared, it can be seen that the dyad's spectrum is similar to the spectra of the two constituent moieties, with no extra bands (Figure 12). This could be a sign of the lack of coupling between the platinum metal centre and the diiron metal centres. A lack of coupling between one metal centre and the other two would inhibit both forward and backward electron transfer, if electron transfer is possible.

Comparison of the MMLL'CT bands of the cyclometalated platinum complexes reveals how the LUMO is affected by changes in substituent at the 4 position on the cyclometalating ligand (Table 3). More electron withdrawing carbonyl groups stabilize the LUMO and this is reflected in lower energy absorptions. There is a relatively small difference of 3 nm between the two esters, **DYAD** and **PtESTER**, compared to the amide, **SP1**. The coplanarity of the extended π system allows the amide to reduce the electrophilicity of the carbonyl by electron donation from the nitrogen, destabilizing the LUMO and raising the energy required to access it. Compared to the ethyl ester, the dyad contains an extra electron withdrawing group in the diiron moiety that allows stabilization of the LUMO through inductive effects. These properties are also reflected in the emission spectroscopy results, described in the section on emission spectroscopy, below.

Compound	ML/ILCT λ_{max} / nm (ε / mol^{-1}dm^{3}cm^{-1})	π/π* λ / nm
SP1	444 (2300)	373, 338, 282
PtESTER	451 (3200)	375, 342, 282
DYAD	454 (4600)	377(sh), 342, 328, 281

Table 3 Electronic absorption spectra recorded in dichloromethane solution for cyclometalated N^N^C platinum chloride complexes; DYAD, PtESTER and SP1.

UV/vis spectroscopy has shown that the electronic transitions of each moiety of **DYAD** are barely affected by the other, as is demonstrated by only small changes in the peak positions and in the values of extinction coefficients for the observed electronic transitions. This shows that the each moiety is insulated from electronic changes in the other, most likely by the ester linker. This supports the observations made by FTIR spectroscopy and indicates that there is no coupling of the iron and platinum centres in the ground state. Any electron transfer would have to take place in an excited state.

Cyclic Voltammetry

Electrochemistry can be used to determine the energy at which a molecule becomes oxidised or reduced; this is useful for estimating the relative energies of the HOMO and LUMO molecular orbitals. Cyclic voltammograms were recorded for each of the platinum complexes to determine the energies of HOMO and LUMO levels. Experiments were performed in a dichloromethane solution of tetrabutylammonium hexafluorophosphate electrolyte (0.2 M) purged with nitrogen. The working electrode was a glassy carbon disc, the counter electrode was a platinum wire and the reference electrode was Ag/AgCl. All values are quoted vs. $Fc^{0/+}$.

Compound	$E_{1/2}$ / V	$E_{1/2}$ / V	E_{pa} / V	E_{pa} / V
DYAD	-1.72 (0.11)	-1.50 (0.08)	+0.51	+0.72
PtESTER	-	-1.55 (0.08)	+0.52	-
SP1	-1.95 (0.10)	-1.58 (0.08)	+0.63	-

Table 4 Cyclic voltammetric data for PtESTER, DYAD and SP1 with their ½ cell potentials of reduction and peak anode potential of oxidation vs Fc/Fc$^+$ ($\Delta(E_{p,a}-E_{p,c})$= 95 mV). Numbers in brackets represent separation between anodic and cathodic peak potentials.

The three cyclometalated complexes all possess an electrochemically reversible first reduction process between -1.50 and -1.58 V, attributable to the bpy/bpy$^-$ reduction. Reversibility was confirmed by the linear correlation of current amplitude against the square root of the scan rate. These processes occur at more negative potentials than usually seen for platinum-coordinated bipyridyl ligands, which can be explained by the destabilization of the LUMOs for each case by an electron withdrawing group on the central bipyridyl ring. This behaviour has been seen for multiple platinum bipyridne species with pendant ester groups.[45-46] An irreversible oxidation process between +0.5 and +0.63 V is also present in each case, attributable to an oxidation of the phenyl-platinum moiety. Complex **SP1** also has a second reversible reduction process at -1.95 V that can be ascribed to the second reduction of the bipyridyl group (bpy$^-$/bpy^{2-}). This second reduction process of bpy$^-$/bpy^{2-} cannot be characterized in the other two compounds as it appears to take place at potentials more negative than -2 V vs Fc/Fc$^+$ where the solvent is undergoing electrolytic breakdown.

The dyad's CV consists of two reversible reduction, and two irreversible oxidation processes. This is consistent with the dyad comprising two redox active moieties within the molecule. The first reversible reduction process occurs at a potential of -1.50 V and this is consistent with carboxylate-bpy ligand reduction . The 50 mV anodic shift observed with regard to the first reduction process of the PtESTER model is consistent with the slight stabilization of the LUMO also manifested by the slightly red shifted emission and ML/ILCT band of **DYAD**, compared to the ethyl ester reference, **PtESTER**. The second reversible reduction process at $E_{1/2}$ = -1.72 V is likely to be the first reduction of the diiron part of the molecule. This value is comparable to the value of the first reduction potential of **PDT**, for which $E_{1/2}$ = -1.67 V in MeCN. The two reduction processes recorded for the dyad have a separation of 220 mV. This small energy gap could lead to thermal population of the higher excited state.

The two irreversible oxidation processes, at +0.51 V and +0.72 V, of **DYAD** are assignable to the Pt-Ph oxidation and the [Fe^{I}Fe^I]/[Fe^{I}Fe^{II}] oxidation, respectively. The +0.51V oxidation is also seen in the voltammogram for **PtESTER** at almost the same potential of +0.52 V. The +0.72 V oxidation potential is comparable to the oxidation potential of **PDT**, which has an oxidation potential of +0.70 V in propylene carbonate.[47] The oxidation potential of the starting material **BAL** is 200 mV higher than that of the DYAD, at +0.90 V.

The small changes in reduction potentials for **DYAD** compared to both the **PtESTER** and **PDT** model further shows the lack of interaction the metal centres of the dyad, but also reveal that they have similar reduction potentials. With a separation of only 220 mV, and considering that

when in the excited state, the orbital associated with the Dyad's first reduction potential at -1.50 V will be filled, there is a possibility for electron transfer in the excited state, if there is enough thermal energy to allow the promoted electron to reach the higher excited state at -1.72 V. The oxidation potentials for the two moieties are also separated by only 210 mV, which means that the Dyad may see exchange between the singly occupied HOMO on the excited state platinum moiety and the filled HOMO of the ground state diiron hydrogenase model moiety. Transfer of electron density from the excited state platinum moiety can be confirmed by observing quenching of **DYAD**'s emission relative to the model PS compound, **PtESTER**.

Emission spectroscopy

Emission spectroscopy has been used to investigate the properties of **DYAD** in its excited state. If electron transfer from the platinum to iron moiety occurs in the excited state, this should be observed in quenching of the emission of **DYAD** relative to its model complex, **PtESTER**, seen as a drop in emission intensity and observed lifetime.
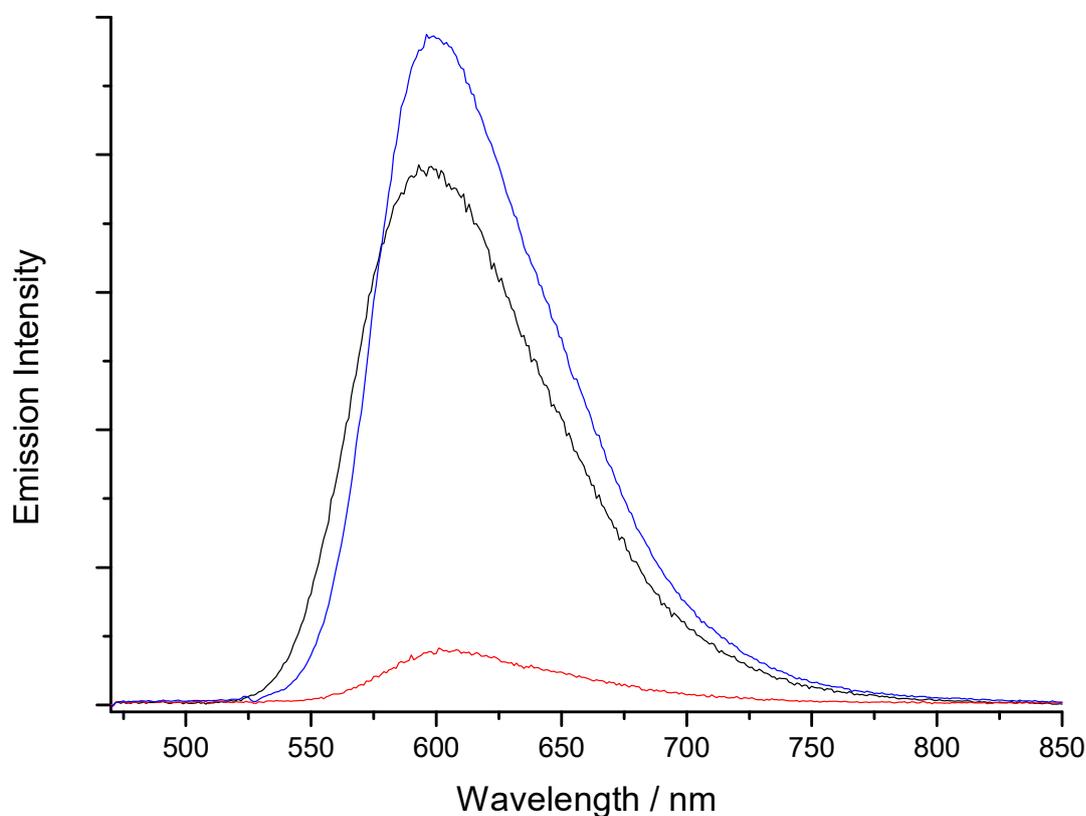
Figure 13 Emission spectra of the DYAD (red), SP1 (black) and PtESTER (blue), in CH$_2$Cl$_2$ solution when excited by light of 455 nm at OD 0.1 (1 cm pathlength cell).

Emission spectra were recorded on a Horbia Jobin Yvon Fluoromax4 controlled by FluorEssence software. Analyte solutions were recorded anaerobically and under atmospheric conditions. Anaerobic conditions were achieved by either freeze pump thaw degassing or purging with argon gas. Analyte solutions were adjusted to a concentration whereby the solution has optical density of 0.1 at the excitation wavelength used. Lifetime data were recorded using a single photon counting method on an Edinburgh Instruments mini-tau using a 410 nm pulsed diode laser with a pulse length of 75 ps. Data points were fit to exponential functions using Origin 8.5 software to extract the values of the emission lifetimes.

Compound	Emission λ_{max} / nm	Emission energy / eV	Lifetime / ns (%)
DYAD	604	2.05	297 (5), 26 (95)
PtESTER	608	2.04	335
SP1	618	2.01	276

Table 5 Emission data for the three cyclometalated platinum chloride complexes, DYAD, PtESTER and SP1, obtained in CH$_2$Cl$_2$ solution.

The dyad, PtNNC ester and NNC amide side product are all emissive when excited using 455 nm light (Figure 13). All three have a single broad, featureless emission band between 550 nm and 820 nm with a peak at around 600 nm. The intensities of these emissions are reduced by the presence of oxygen, suggesting emission from a triplet state. There is a large shift for each of

the compounds between the absorption maximum and the emission maximum, further indicative of a triplet state emission.

The compounds each have a λ_max of emission between 600 and 620 nm. This is equivalent to emission energies of 2.01 to 2.05 eV, consistent with the difference between HOMO and LUMO energies obtained from cyclic voltammetry measurements. These differences can be attributed to the change in ester or amide environment on the bipyridyl ring changing the energy of the LUMO, as the environment where HOMO electron density is found remains unchanged between the molecules. The relative intensity of the emission of **DYAD** is much lower compared to **PtESTER**, indicating quenching of the emission by the diiron moiety. This is likely due to the effect of energy or electron transfer, as the origin of emission in **DYAD** is unchanged from the Phbipy based emission of **PtESTER** and there is little electronic coupling from the diiron moiety.

Emission Lifetimes
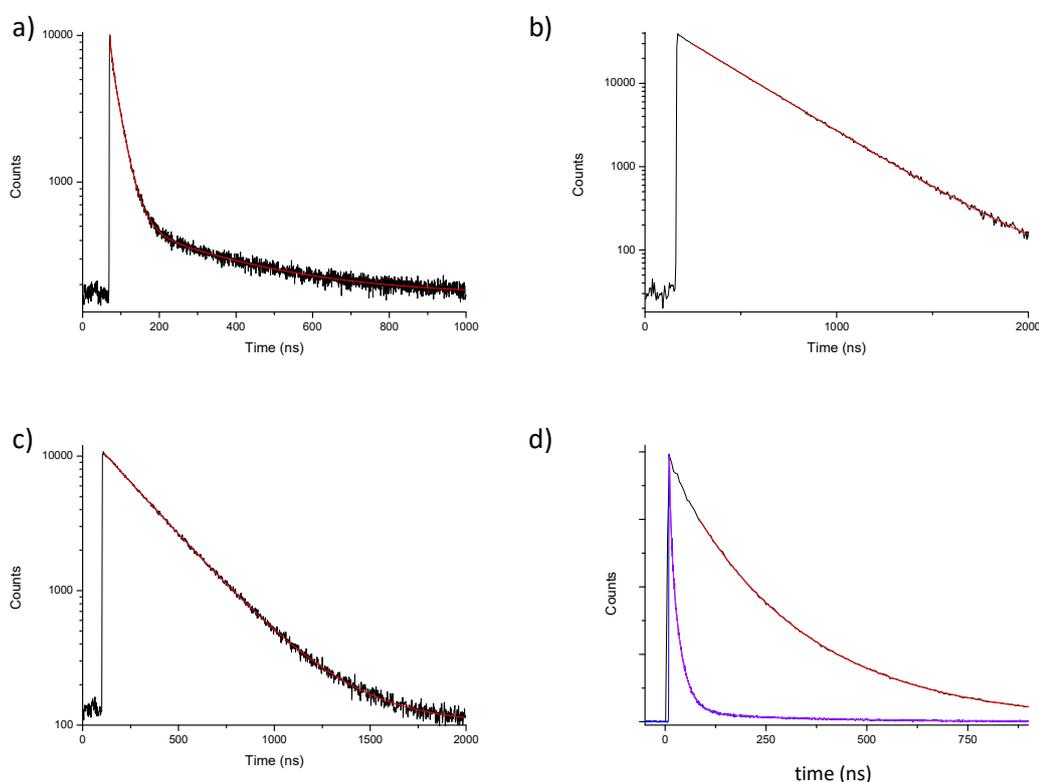
Figure 14a) Decay curve with biexponential fit for DYAD after exciting with 100 fs pulsed 410 nm LED. b) Decay curve (black) with exponential fit (red) for PtESTER after exciting with 100 ps pulsed 410 nm LED. c) Decay curve with exponential fit for SP1 after exciting with 100 fs pulsed 410 nm LED. d) Comparison of decay traces and fits for PtESTER (red and black) and DYAD (blue and purple) on a linear plot. Quenching of the dyad's excited state results in a much shorter lifetime than those observed for PtESTER.

Emission decay kinetics were recorded using the same sample concentrations as used to record emission spectra, as the optical densities are lower at the 410 nm probe wavelength, and there are therefore no issues with self-quenching or aggregation effects. All three have a long lifetime component of around 300 ns. The dyad has a second lifetime component of 26 ns that accounts for most the radiative decay of its excited state. A lifetime of several hundred nanoseconds confirms that the emission of these complexes is from triplet excited states. The shorter emission lifetime of the dyad could be for one of several different reasons; either the radiative triplet excited state has been quenched with a resultant shortening of its apparent (experimentally detected) lifetime, a new radiative singlet excited state has formed with a lifetime slightly longer than those typical for fluorescence or there is a new populated radiative

excited state that is located on either the iron or platinum centre and has a much shorter lifetime.

The formation of a radiative singlet state is unlikely. Intersystem crossing in platinum (II) complexes is known to be on the sub-ps timescale[48-49] hence population of a singlet state located on the Pt-subunit is unlikely and, when tested, the diiron hexacarbonyl model was non-emissive. The possibility of a new emissive excited state located on the iron or platinum moieties of the dyad is also unlikely. There is no coupling between the two metal centres; the UV/vis spectrum for DYAD reveals that the spectrum is a combination of the spectra of the two model complexes. The model iron complex has no emissive excited state and therefore will not have an iron-localized emissive excited state in the dyad. There are no new transitions in the UV/vis spectrum of the dyad associated with the platinum moiety, this indicates there is no new excited state after covalently attaching the diiron moiety.

Energy or electron transfer to iron from platinum once excited by light could account for quenching and therefore, quenching of the radiative triplet excited state by the presence of the diiron centres is most likely. The reduction in lifetime for **DYAD** compared to the PS model, **PtESTER** by around 90% is comparable with a 90% reduction in the luminescence quantum yield. This quenching exists despite a lack of ground state coupling, indicating a bimolecular process or an excited state that is more coupled, allowing energy or electron transfer.

The reason for the long lifetime component of the emission is not apparent, however it accounts for less than 5% of the decay and is therefore not one of the main mechanisms through which the dyad recovers to the ground state.

Investigation of the dyad's emissions properties and comparison to its model complexes shows that there is a possibility of electron transfer from the PS moiety to the diiron moiety on excitation using visible light. Reductions in both emission intensity and emission lifetime for **DYAD**, compared to **PtESTER** reveal the presence of either an energy or electron transfer mechanism reducing the available excited state population for an emission mechanism. Due to the complicated nature of the close lying electronic state, revealed by cyclic voltammetry, and the possibility of an electron transfer mechanism, as revealed by emission spectroscopy, time-resolved infra-red spectroscopy has been used to investigate structural and electronic changes in the excited state. TRIR can be used to identify electron transfer products and the mechanisms of interconversion between excited state species.

Time Resolved InfraRed (TRIR) Spectroscopy

In order to confirm or disprove photoinduced electron transfer between the components of the dyad, time resolved infrared (TRIR) spectroscopy was applied. TRIR can be used to observe structural and electronic changes in the excited state. The set-up employed in this research can detect such changes on the timescale from approximately 0.5 ps to 3 ns. This would allow for the observation of a very short lived electron transfer state as well as vibrational cooling processes. This is a powerful technique for observing the excited state of molecules, especially when there are strong handles for identifying species, such as v_{CO} stretches of metal carbonyl complexes.

TRIR studies were performed at the Rutherford Appleton Laboratory using the ULTRA facility, details of which have been published previously.[50-52] In these experiments a 65 MHz, 40 fs Titanium Sapphire laser is used to pump a range of optical parametric amplifiers (OPAs). The pump beam (400 nm) is generated from the second harmonic of the Ti:Sapph laser, whilst another portion of the initial laser beam is used to generate tuneable mid-IR probe light with a 400 cm^{-1} bandwidth. The pump energy is typically 1.0-1.5 μJ per pulse. Changes in IR absorbance are determined via three HgCdTe linear IR-array detectors. All analyte solutions were contained within Harrick cells with 2 mm thick CaF_2 windows with a typical pathlength of 500 μm. Sample solutions were flowed and the cells rastered during the experiments to minimise photo-decomposition. Data analysis was performed by global fit analysis using Glotaran 1.5.1 software.[53]

The signals recorded by this method account for a 3 ns time window after excitation. By examining how the difference spectrum develops over these three nanoseconds, it was hoped that the electron transfer state could be observed and characterised using the medium time period data. To provide context for any observation made about the dyad's excited state, it has been compared to the TRIR spectra for **BAL** and **PtESTER**. Differences between the spectra of the dyad and its models can be used to support the assignment of an electron transfer mechanism or rule it out.

Global fitting of TRIR data using Glotaran software allows the plotting of evolution and decay associated spectra (EAS and DAS). EAS and DAS can be used to visualise the changes associated with different decay periods and allow the decay lifetimes fitted to be associated with spectra, which can then be used to identify different processes. Evolution associated spectra show how the whole spectrum changes over time, associated a time slice with the start of each decay period. These can be used to identify solvent effects as peaks shift over time.

PtESTER TRIR spectroscopy

PtESTER is a model for the PS moiety of the dyad, by examining its TRIR spectra in the 1500 – 1800 cm^{-1} and characterizing its decay dynamics, it can be compared to the TRIR spectra for DYAD to identify the decay pathways associated with the PS half of the complex. TRIR spectroscopy has been performed on **PtESTER**, exciting with a 50 fs 400 nm pulse of light, followed by a TRIR probe, for the region 1500 to 1780 cm^{-1} with delays of 1 ps to 2800 ps after excitation.
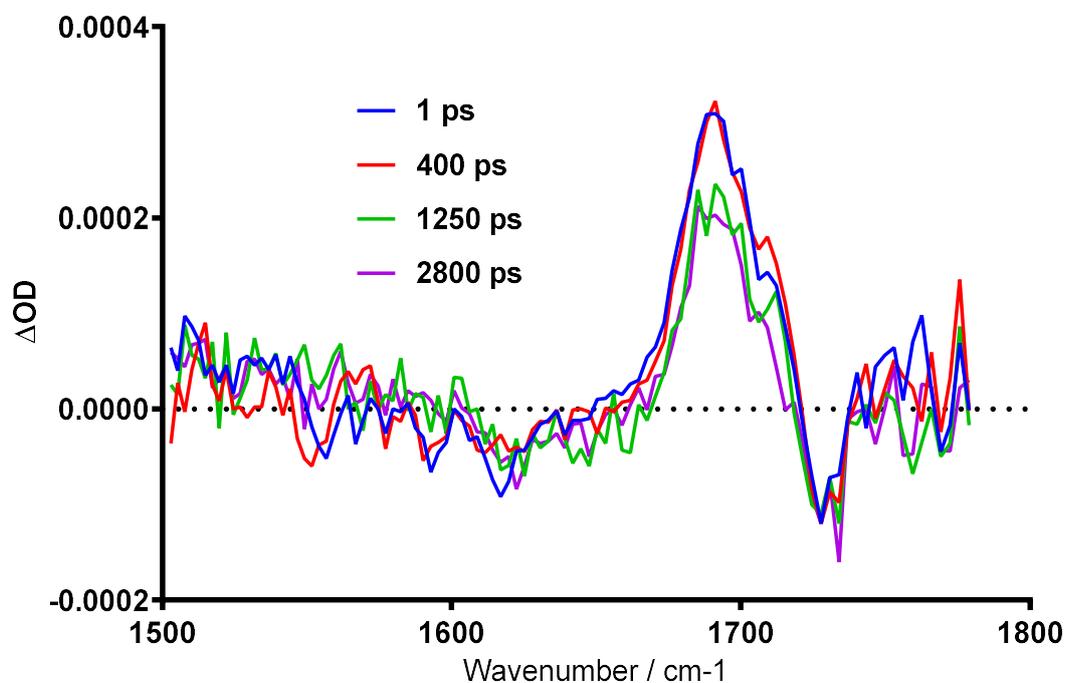
Figure 15 Selected time slices from the TRIR spectra recorded for PtESTER solution in DCM, following 400 nm, ~40 fs excitation, between 1500 and 1800 cm^{-1}.

In the TRIR spectra of **PtESTER**, immediately after excitation, transient and bleach peaks form at 1691 cm^{-1} and 1731 cm^{-1}, respectively (Figure 15). These signals both decay monoexponentially, with a lifetime of 6.6 ± 0.7 ns, implying that the excited state decays to the ground state. Although this lifetime is much shorter than the lifetime found using the fits of data from single photon counting methods, it is important to note that due to the short time period examined in these TRIR experiments, the lifetime cannot be accurately obtained. Additionally, although the bleach, associated with loss of the ground state, is not at 1725 cm^{-1} as expected, this is likely due to the associated, overlapping transient obscuring the true bleach peak. These associated signals are likely due to the presence of the long lived, luminescent, triplet excited of **PtESTER** and no vibrational cooling of this state is seen in the date presented. The lack of cooling is most likely due to a lack of temporal resolution in the collected data failing to capture a very rapid cooling process, as the amount of energy added by the 400 nm pump pulse far exceeds the expected energy required to directly excite the complex to its lowest excited state.

These data display the characteristic rapid formation of a triplet excited state for a cyclometalated platinum complex. As DYAD also populates a luminescent state upon excitation with visible light, similar signals and decay lifetimes can be expected to be seen in data captured for the same region of the mid-IR spectrum.

DYAD Ester TRIR spectroscopy

A comparison of the TRIR spectra to DYAD's TRIR spectra in the same region reveals both similarities and difference that indicate the presence of extra decay processes, associated with the inclusion of a diiron hydrogenase model moiety. TRIR spectroscopy has been performed on **DYAD**, exciting with a 50 fs 400 nm pulse of light, followed by a TRIR probe, for the region 1500 to 1800 cm^{-1} with delays of 1 ps to 3000 ps after excitation.

Similar to **PtESTER**, upon excitation **DYAD** displays transient and bleach peaks at 1692 and 1736 cm^{-1} (Figure 16). Again the bleach peak is displaced relative to the ground state absorption for the bridging ester, most likely due to overlapping bleach and transient signals. The transient signals seen for **DYAD** are broader than for **PtESTER**, with a shoulder decaying with shorter lifetime than the main band. Global fitting analysis reveals that the transient and bleach signals decay with common lifetimes of 17 ± 2 ps and 5.8 ± 0.6 ns. The longer lifetime is consistent with the lifetime found for **PtESTER** by analysis of TRIR spectra, but the shorter lifetime is only seen in **DYAD**. This shorter lifetime is consistent with a vibrational cooling process, matching the lifetimes of vibrational cooling in other reported platinum complexes – however, it was not observed in the model PtESTER, and therefore cannot be attributed to cooling of the PtESTER-localised state (unless the data quality were much higher in the studies of the DYAD).

Indeed, EAS and DAS reveal that the spectrum is not typical of a vibrational cooling process despite the expected narrowing of transient bands, as EAS shows that the transient shifts from high (1710 cm^{-1}) to low energy (1692 cm^{-1}) (Figure 16). DAS shows that this process is associated with the decay of a transient peak at this energy, as well as the higher energy portion of the bleach peak. As such, this peak should be considered to be due to the influence of the [FeFe] moiety rather than a vibrational cooling process.

If the process associated with the decay lifetime of 17 ps is due to a [FeFe] influenced process, then this should also be seen in both the TRIR spectra of the model diiron hydrogenase mimic, **BAL** and the dyad. This is the case, with vibrational cooling lifetimes of **BAL** proceeding over similar timescales.

Due to the small signals observed and the presence of only one band in this region, direct comparison of just the ester vCO TRIR spectra does not reveal much about the excited state of the dyad, beyond the presence of a fast component that was not observed in the **PtESTER** model compound. Although this reveal there may be some interaction between the metal centres in the excited state, more information is contained with the metal carbonyl vCO TRIR spectra for **DYAD** and its comparison with the model complex, **BAL**.
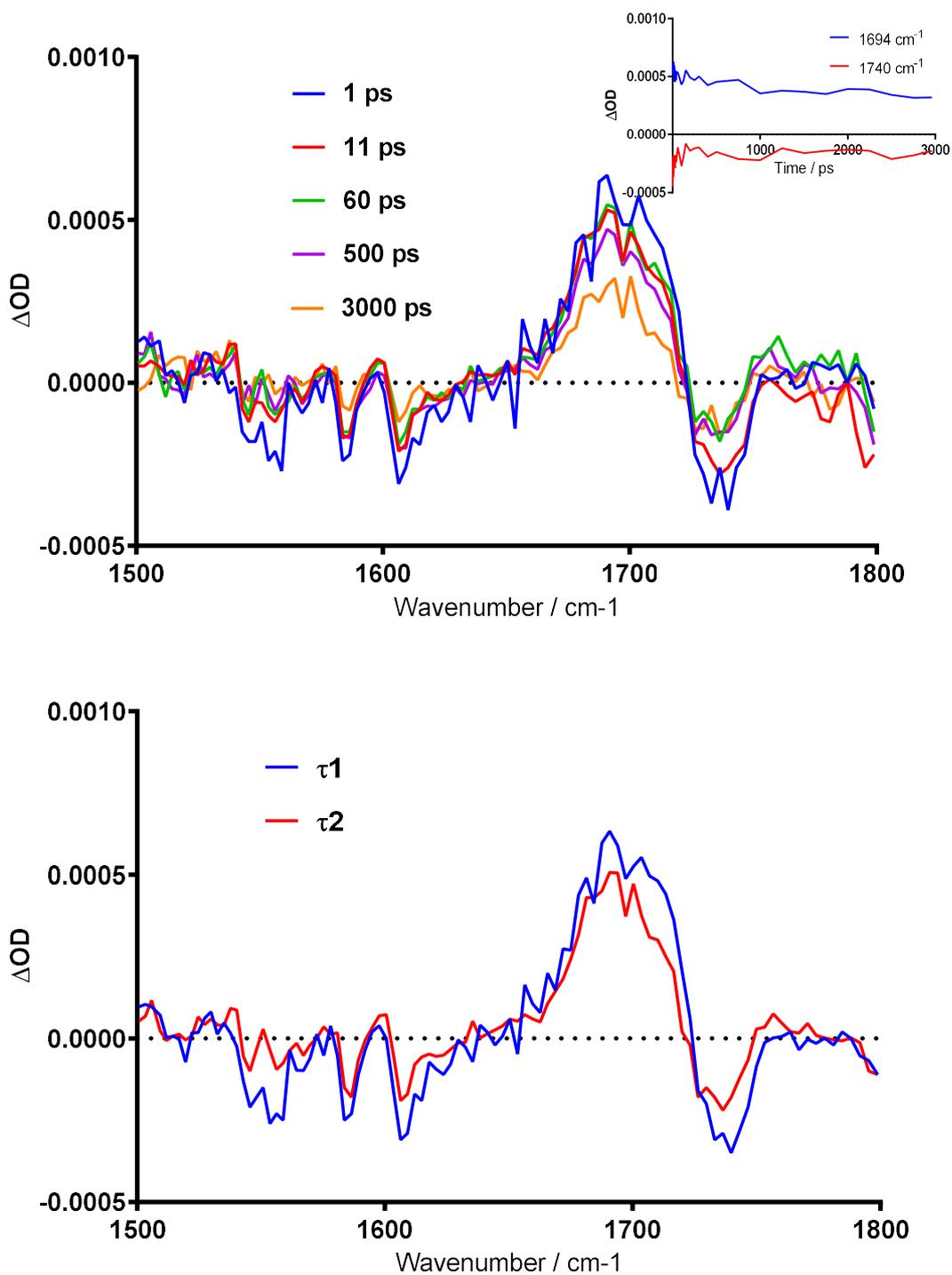
Figure 16 top) Selected time slices from the TRIR spectra recorded for DYAD in DCM solution, following excitation with 400 nm, 50 fs laser pulse, between 1500 and 1800 cm^{-1}. **Bottom)** EAS spectra of DYAD showing the evolution of the spectrum over the two lifetime associated processes. Each spectrum represents the appearance of the difference spectrum at the beginning of the lifetime associated change.

BAL metal carbonyl TRIR spectroscopy

The TRIR spectra in the region 1900 – 2100 cm^{-1} of **BAL** act as an important analogue for any data recorded for **DYAD**, as they are functionally similar, with an ethyl bridged dithiolate linker and a pendant group featuring an oxygen atom. Differences in the dynamics of **BAL** and **DYAD** for this spectral region allow for confirmation or rejection of an electron transfer occurring in the photoexcited state. TRIR spectra for **BAL** have been recorded where **BAL** is excited with a 400 nm pump beam and examined using a 1900 cm^{-1} to 2100 cm^{-1} probe pulse, over a time period of 1 ps to 3000 ps (Figure 19). This data has been fit to a decay model using Glotaran (Figure 20).

The TRIR spectra have been fit to a multiexponential decay model with 5 sequential exponential decay lifetimes, incorporating a pseudostatic component. After initial excitation, transient peaks at 1970, 2022 and 2057 cm^{-1} and bleach peaks at 2000, 2036 and 2075 cm^{-1} appear, associated with formation of an excited state species and depletion of the ground state, respectively. Over the course of 100 ps, the transient peaks shift from the initial peak positions to higher energy at 1981, 2029 and 2068 cm^{-1}, with only a small recovery in bleach peaks, associated with now overlapping transient and bleach peaks. This is followed by an almost total recovery of the ground state, within 2000 ps, and the formation of a new pseudostatic state, with transient peaks at 1938, 1970, 1988 and 2049 cm^{-1}.
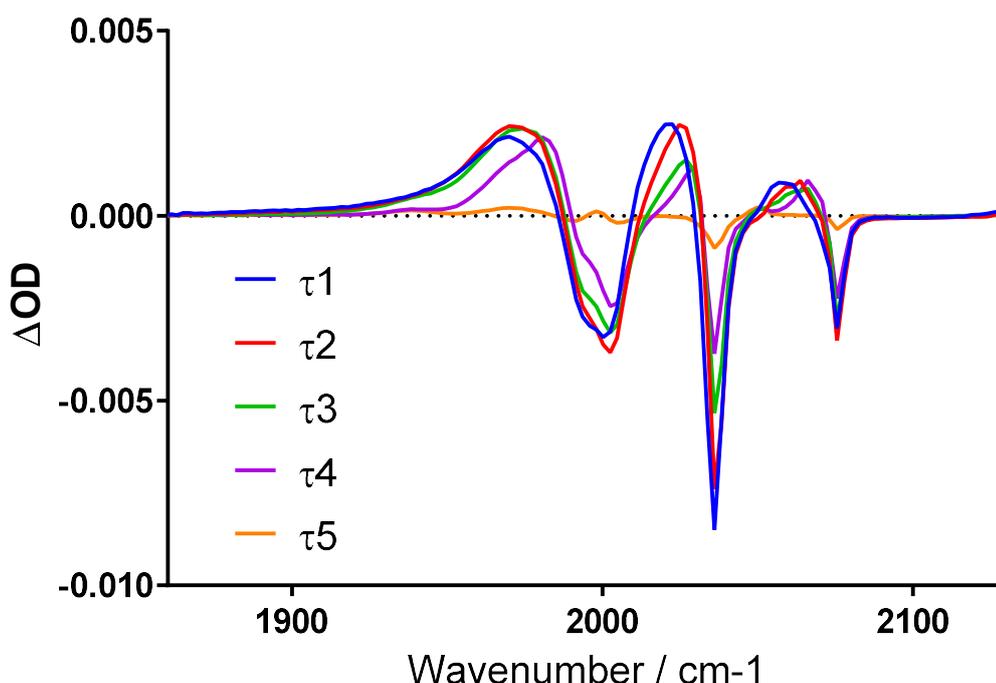
Figure 17 EAS spectra of BAL showing the evolution of the spectrum over the five lifetime associated processes. Each spectrum represents the appearance of the difference spectrum at the beginning of the lifetime associated change. These spectra display a blue shift and narrowing of the spectra across proccesses τ1, τ2 and τ3, followed by spectra associated with the τ4 decay of an electronically excited state and the carbonyl loss photoproduct, which does not decay on the timescale of the experiment.

This blue shift of IR band positions followed by decay to the ground state can be traced most easily by studying the associated evolution associated spectra (EAS) (Figure 17). The EAS show the difference spectrum that is apparent at the beginning of each associated decay lifetime. It can be seen that for each of the three shorter decay lifetimes (τ1, τ2, τ3) there is a more blue shifted transient spectrum, the second longest decay lifetime (τ4) represents a recovery of the

ground state and the pseudostatic component (τ5) represents the formation of a photoproduct. The lifetimes associated with each evolution of the spectrum are summarized in Table 6.

These results are consistent for those seen in the study of other hydrogenase models using TRIR spectroscopy; the shorter lifetimes associated with intramolecular vibrational energy redistribution, vibrational cooling and relaxation of metal carbonyl modes has been seen for the constrained $[Fe_2(\mu\text{-bdt})(CO)_6]$ complex, and additionally the carbonyl loss photoproduct has been seen in studies of $[Fe_2(\mu\text{-pdt})(CO)_6]$. The BAL complex does show a different behaviour in its relaxation to the ground state compared to these complexes however, in that process associated with τ4 has a lifetime is twice as long as would be expected in dichloromethane solvent and that it exists past the end of a process that can be ascribed to the decay of carbonyl vibrational modes (τ3). This process most strongly resembles behaviour seen in the TRIR studies of a diiron hydrogenase model supramolecularly linked to a porphyrin PS, in that it is longer lived than processes associated with vibration mode decay, displays a spectrum representing no change in geometry and has a constrained Fe-Fe bond due to the shortened linker. The excited state of the supramolecularly linked dyad produces TRIR spectra associated with a lengthened Fe-Fe bond, which often precedes the loss of a carbonyl where the metal carbonyl electronic transition is not directly excited.

Process	Transient Peaks (cm^{-1})	Lifetime (ps)
Ground	1996, 2003, 2037, 2077	
τ1	1970, 2022, 2057	2.23 ± 0.2
τ2	1970, 2025, 2064	12.1 ± 1.2
τ3	1974, 2027, 2066	149 ± 15
τ4	1981, 2029, 2068	311 ± 31
τ5	1938, 1970, 1988, 2049	-

Table 6 List of decay lifetimes and their associated peaks for BAL that are present in the spectrum at the start of each lifetime, as observed in the EAS. See Figure 17.

This state could be promoted by the hydroxyl pendant group that is not present in any of the other studied molecules. The hydroxyl group is too far away from either of the iron centres in the ground state to interact, but if the distance between the iron centres increases after excitation, then this would pull the dithiolate sulfur atoms apart, bringing the hydroxyl within reach of one of the iron centres and stabilising the lengthened Fe-Fe bond (Figure 18). This would account for the small shifts in peak position of $9 - 15$ cm^{-1} without significant changes in the structure of the transient peaks compared to the ground state peaks, as the electronic environment has changed, but the structural environment has not. Due to the stabilising effect of the pendant hydroxyl carbonyl loss products, which would normally form earlier after excitation, are not produced until later. This would be an extremely weak interaction, that would be easily disrupted by solvent interaction, leading to the typical pseudostatic signals associated with carbonyl loss photoproduct with coordinated solvent and recovery of ground and excited state signals indicating a recovery to the ground state.
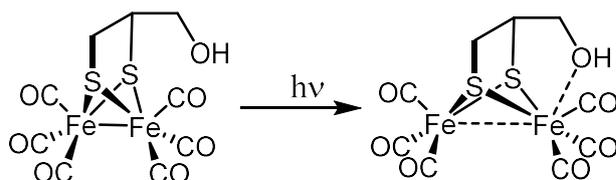
Figure 18 Possible stabilisation of the lengthened Fe-Fe bond state by weak electron donation from pendant hydroxyl group.

Thus, **BAL** can be characterized as undergoing the following processes after excitation, on its route to the ground state. There is an initial intramolecular vibrational energy redistribution with

a lifetime of a couple of picoseconds, followed by vibrational cooling with a lifetime of 12.1 ± 1.2 ps. This is followed by decay of the excited vibration modes of the carbonyls with a lifetime of 149 ± 15 ps, then decay of a state associated with a lengthened Fe-Fe bond within 1 ns to the ground state and a carbonyl loss photoproduct.
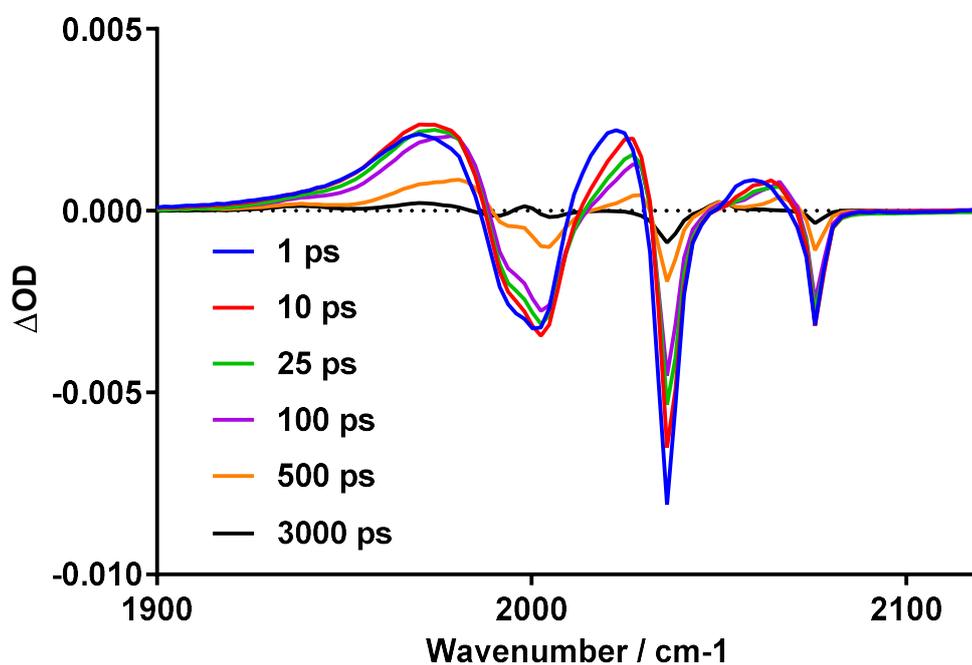
Figure 19 Selected time slices from the TRIR spectra recorded for BAL in DCM solution, following excitation with 400 nm, 50 fs laser pulse, between 1900 and 1920 cm^{-1}.
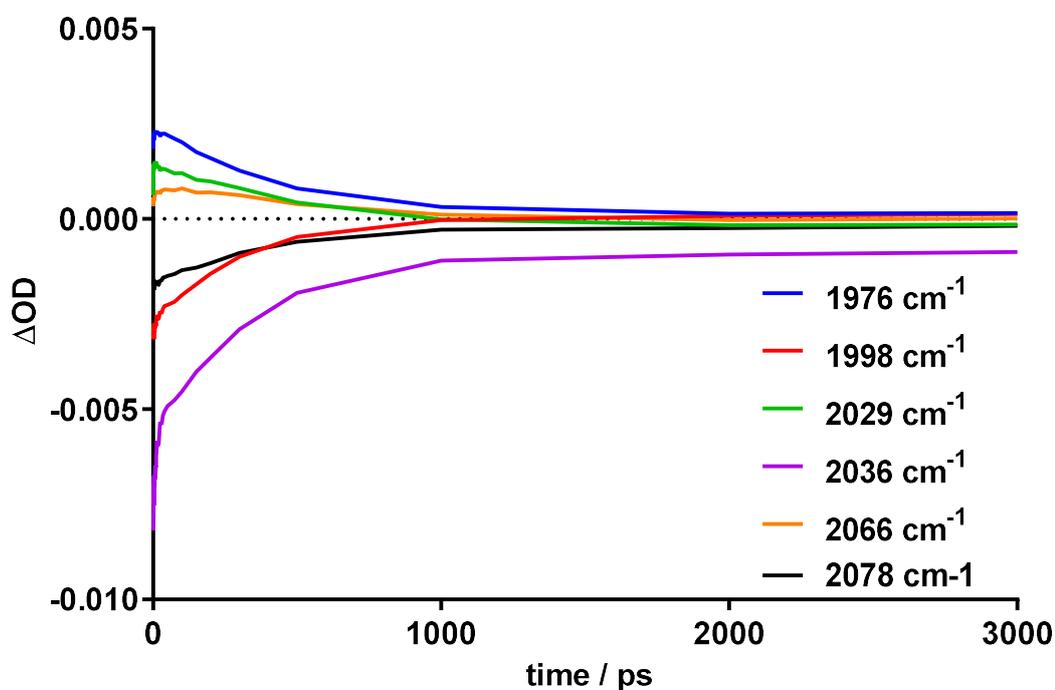
Figure 20 Amplitude traces for selected wavenumber signals, from the TRIR spectra of BAL recorded in DCM solution, following excitation with 400 nm, 50 fs laser pulse.

DYAD metal carbonyl TRIR spectroscopy

The TRIR spectra for DYAD can reveal important details about its route to ground state after excitation, including likely excited state intermediates. These can be compared to the spectra for the PS and diiron moieties to reveal if there are new processes not present in the decay mechanisms of the individual models. Similarly to **BAL**, TRIR spectra for **DYAD** have been recorded where **DYAD** is excited with a 400 nm pump beam and examined using a 1900 cm^{-1} to 2100 cm^{-1} probe pulse, over a time period of 0.25 ps to 3000 ps (Figure 23). This data has been fit to a decay model using Glotaran (Figure 24). Again, the TRIR spectra have been fit to a multiexponential decay model with 5 sequential exponential decay lifetimes, incorporating a pseudostatic component (Figure 21). These have been assigned with the help of spectra developed from DFT modelling of the ground and excited state of the dyad and decay associated spectra. Apart from the 5th pseudostatic state, all others are assumed to be sequential, allowing the use of decay associated spectra for characterising decay associated species.
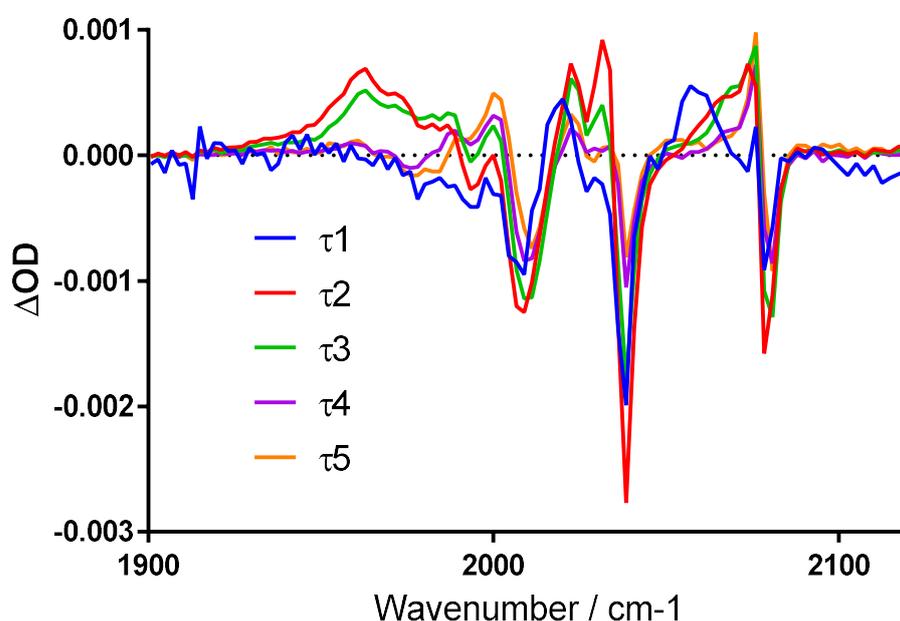
Figure 21 EAS of DYAD for changes in the spectrum that develop over the course of the 5 fitted lifetimes. These have been summarized in the table below.

Process	Transient Peaks (cm^{-1})	Lifetime (ps)
Ground	1993, 2009, 2038, 2078	
$\tau 1$	2022, 2057	0.5 ± 0.2
$\tau 2$	1961, 2022, 2066, 2076	43.7 ± 4.4
$\tau 3$	1961, 1982, 1989, 2022, 2076	247 ± 25
$\tau 4$	1986, 2000, 2022, 2076	3010 ± 300
$\tau 5$	1986, 2000, 2022, 2076	-
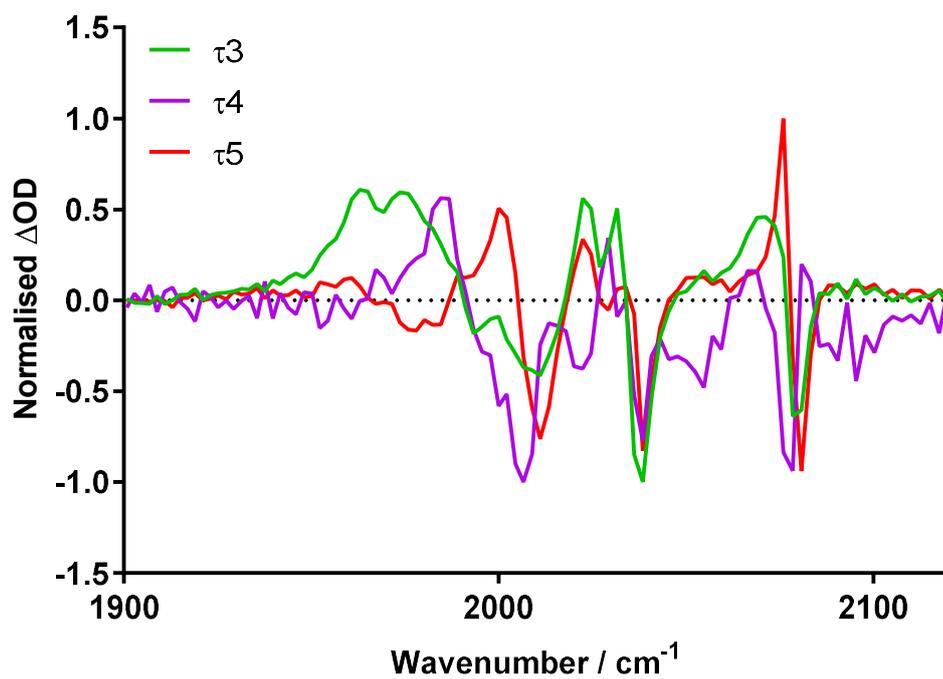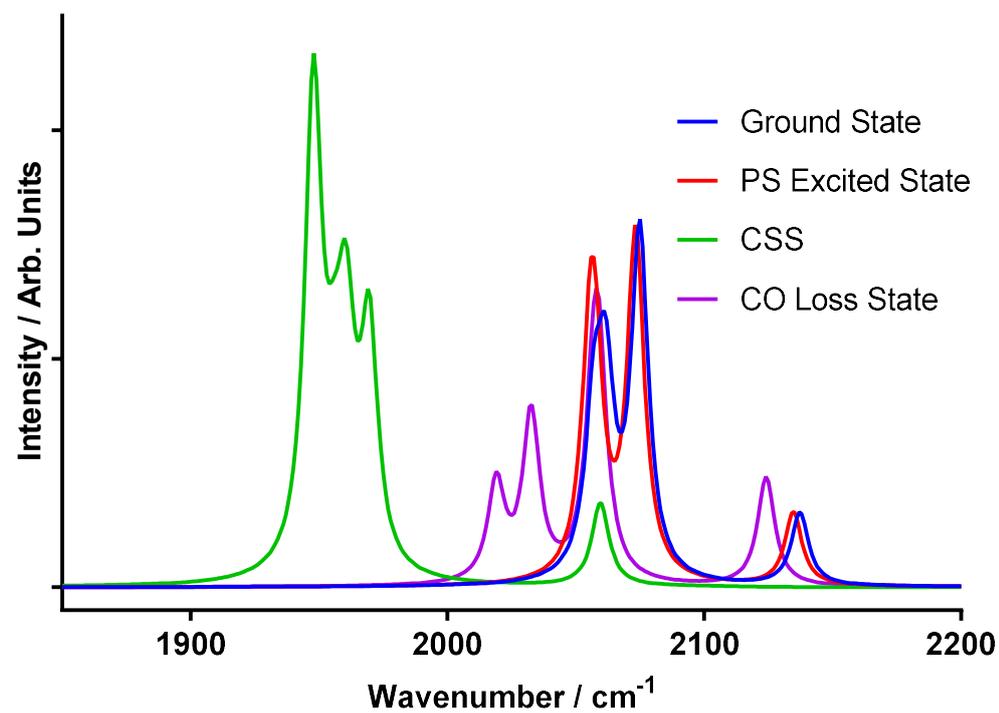
Figure 22 A comparison of IR spectra for DYAD modelled by DFT calculations (top), where the DYAD is in the ground state and CO loss state, and analogues for the excited state, charge separated state, and the DAS for DYAD for processes τ3, τ4 and τ5. The DAS represent the spectra of species associated with the decay lifetime they represent, and can be used to compare modelled and recorded IR spectra.
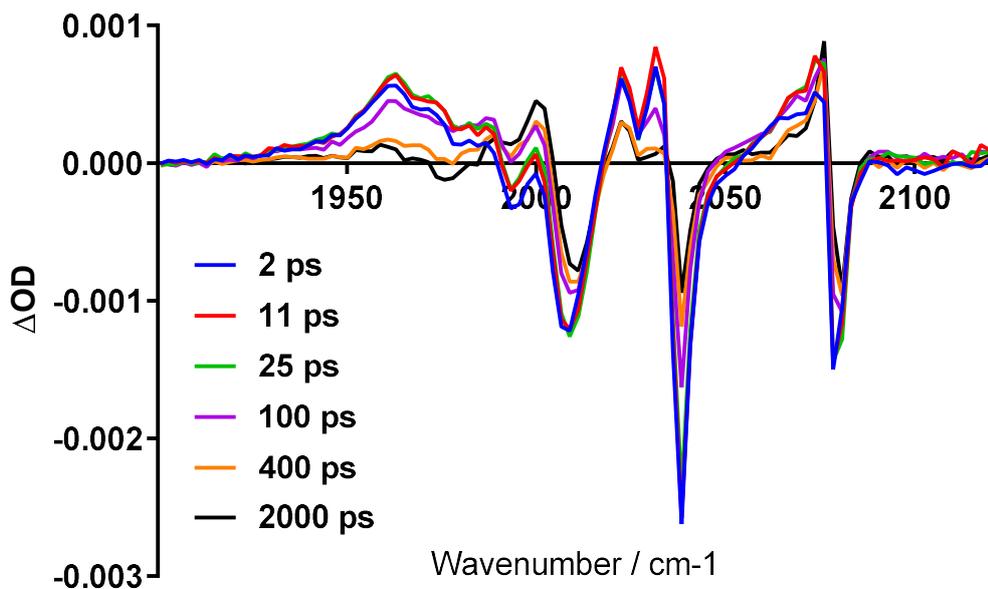
Figure 23 Selected time slices from the TRIR spectra recorded for DYAD in DCM solution, following excitation with 400 nm, 50 fs laser pulse, between 1900 and 1920 cm^{-1}.
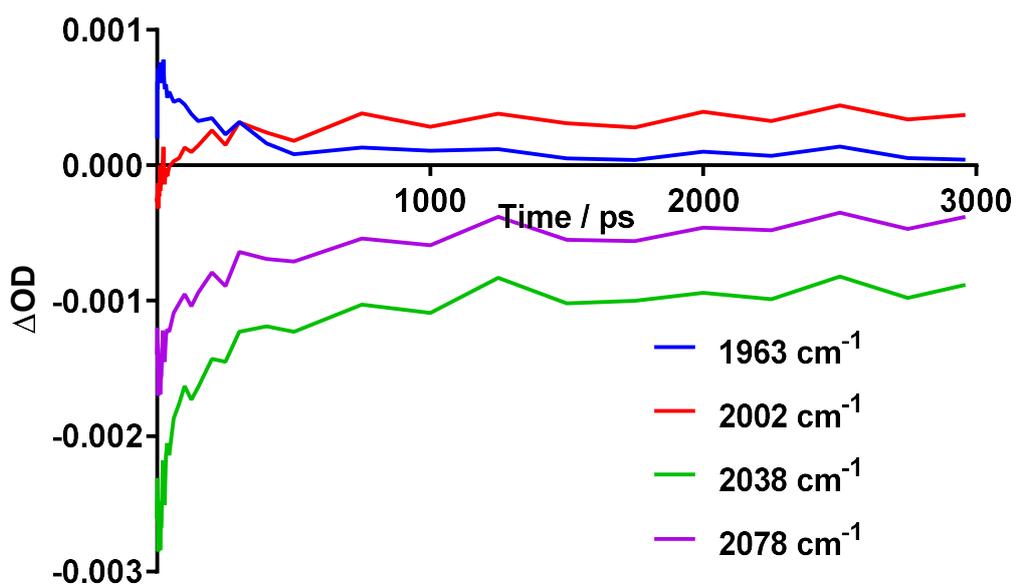
Figure 24 Amplitude traces for selected wavenumber signals, from the TRIR spectra of DYAD recorded in DCM solution, following excitation with 400 nm, 50 fs laser pulse.

After excitation, the difference spectrum shows bleach peaks, associated with the ground state spectrum of **DYAD**. Accompanying these bleaches, the modelled spectra show the same initial transients as **BAL**, associated with an intramolecular vibration energy redistribution with a sub-ps lifetime, followed by a vibrational cooling process. However, the vibrational cooling takes place over a longer time than **BAL**, with a lifetime of 43.7 ± 4.4 ps compared to just 12.1 ± 1.2 ps. These processes are followed by a state with a lifetime of 247 ± 25 ps, which exhibits no blue shifting over time indicating that this is not similar to the mid-lifetime carbonyl mode vibrational relaxation in **BAL**. This is proposed to be a charge separated state, with an electron from the excited PS moiety donated to FeFe moiety. This charge separated state decays to the state associated with lifetime of 3.01 ± 0.3 ns, the carbonyl loss state, and the ground state. The pseudo static state is the luminescent excited state associated with the lowest triplet excited state of the PS moiety of the dyad, which is seen in emission spectroscopy with a lifetime of 26 ns. The assignment of these states using DFT derived spectra will be described below. The DFT spectra are unscaled; although the peak structure and relative positioning is considered accurate, absolute positions of the bands are not (Figure 22).

The charge separated state, associated with decay $\tau 3$, has the most red shifted signals compared to the transient signals of other excited states, due to the extra electron density placed over the iron centres back bonding into the metal carbonyl bonds, weakening the carbonyl bond structure. It's peak structuring as seen in the DAS for the $\tau 3$ decay is very similar to DFT modelled spectra, but with a single extra band. This is likely a failure of DFT to accurately model the reduced state of the FeFe moiety, as comparison to work by Pickett et al. shows that the 4 band structure seen in the DAS is also seen in the spectroelectrochemical study of $[Fe_2(\mu\text{-pdt})(CO)_6]$. The relative red shifting of the lower energy bands is not as large in the real TRIR spectra compared to the DFT model spectra, as the constrained nature of the ethyl bridge does not allow as much separation of the iron centres as the DFT model suggests, leading to a smaller red shift of the lowest energy transients. The lifetime of this state is comparable to a similar charge separated state seen in a supramolecularly bound zinc porphyrin – FeFe dyad.

The DAS for $\tau 4$ bears most resemblance to signals seen in other studies and DFT modelling to a carbonyl loss photoproduct where one of the iron centres has lost its axial carbonyl. Although the characteristic peak at around 1940 cm^{-1} is missing, likely due to being lost beneath the noise associated with the TRIR measurement, the other distinguishing peaks at around 1980, 2030 and 2070 cm^{-1} are present. This species accounts for only a small amount of the full decay mechanism and as such, features a large amount of noise.

DAS for the species associated with $\tau 5$ have been assigned to the excited state where the PS moiety is in its lowest triplet excited state, with no electron density transfer to the FeFe moiety. This is characterised by transient peaks, which heavily overlap with ground state bleach peaks, distorting their appearance and a pseudostatic lifetime consistent with the 26 ns lifetime of the luminescent state.

As a result of these TRIR studies, it can be seen that upon photoexcitation, **DYAD** forms a charge separated state with a lifetime consistent with the only other dyad that has been studied by this method. The decay mechanism for this complex precedes through initial IVR ($\tau < 1$ ps) and VC ($\tau = 43.7 \pm 4.4$ ps) to the CSS ($\tau = 247 \pm 25$ ps), followed by recovery directly to the ground state, and through the PS localized triplet excited state ($\tau = 26$ ns) and a carbonyl loss photoproduct ($\tau = 3.01 \pm 0.3$ ns). The instability of the dyad complex suggests that the carbonyl loss photoproduct is persistent.

Decay mechanisms for diiron hydrogenase mimic containing species; DYAD and BAL

Having characterized the decay dynamics of BAL and DYAD, it can be seen that they follow different pathways from the their initial excited states to the ground state. The difference in pathways can be accounted for by assuming that when in the excited state, the FeFe and PS moieties interact more strongly than in the ground state. This can be seen when comparing the vibrational cooling times of **PtESTER**, **BAL** and **DYAD**, and when comparing the different transient states.

The vibrational cooling for **PtESTER** cannot be seen in the TRIR spectra recorded for the complex, whereas the dyad's spectra in the $1650 - 1750$ cm^{-1} displays a process with short lifetime ($v = 17.0 \pm 1.7$ ps) that could be attributed to interaction with the [FeFe] center. This lifetime has a counterpart in the spectra of **DYAD**, however it is longer at 43.7 ± 4.4 ps. This difference in lifetime for the same process is likely due to inaccuracies when fitting the data, due to noise and poor signal quality.

Comparing the vibrational cooling lifetimes of **DYAD** and **BAL** shows that there is a difference in the vibrational cooling process for the two. The vibrational cooling lifetime is almost 3 times longer in the DYAD than in BAL in the same solvent. This indicates that DYAD maintains its vibrationally hot state for longer, which could be due to a large amount of excess energy produced when the platinum performs rapid ISC from the singlet to triplet states. This energy is entirely dumped to the solvent bath and is not used to produce vibrationally excited carbonyl modes. This is why this process of **BAL**'s mechanism is not seen for the **DYAD**. This large amount of excess energy, as heat, could be used to populate the LUMO of the FeFe moiety from the PS LUMO, leading to a rapid deactivation of the luminescent state due to the faster recovery to the ground state of the CSS (Figure 25).

A comparison of vibrational cooling lifetimes and possible pathways for **PtESTER**, **BAL** and **DYAD** show that the PS and FeFe centres only interact in the excited state and this interaction disrupts the typical pathways to the ground state that **BAL** experiences without an attached PS. The energy produced from singlet-triplet ISC is used to promote a CSS, which diminishes the quantum yield of the luminescent platinum triplet excited state.

In summary, characterization of the excited state of **PtESTER**, **BAL** and **DYAD** has been achieved using TRIR spectroscopy. Observation and modelling of **BAL** has shown that its decay mechanism is more complex than some other diiron hydrogenase models, likely because of its pendant hydroxyl group. There is strong evidence for the formation of a CSS by **DYAD**, which ideally would be able to be confirmed using a second technique, such as time-resolved 2D infra-red spectroscopy (T2D-IR) spectroscopy. Unfortunately, due to the lack of solubility and stability of the dyad, T2D-IR spectra could not be obtained. Developing a more soluble dyad, to achieve stronger transient absorption signals is a priority. Attempts were made using platinum ligated acetylide ligands, but unfortunately this led to a more insoluble product.
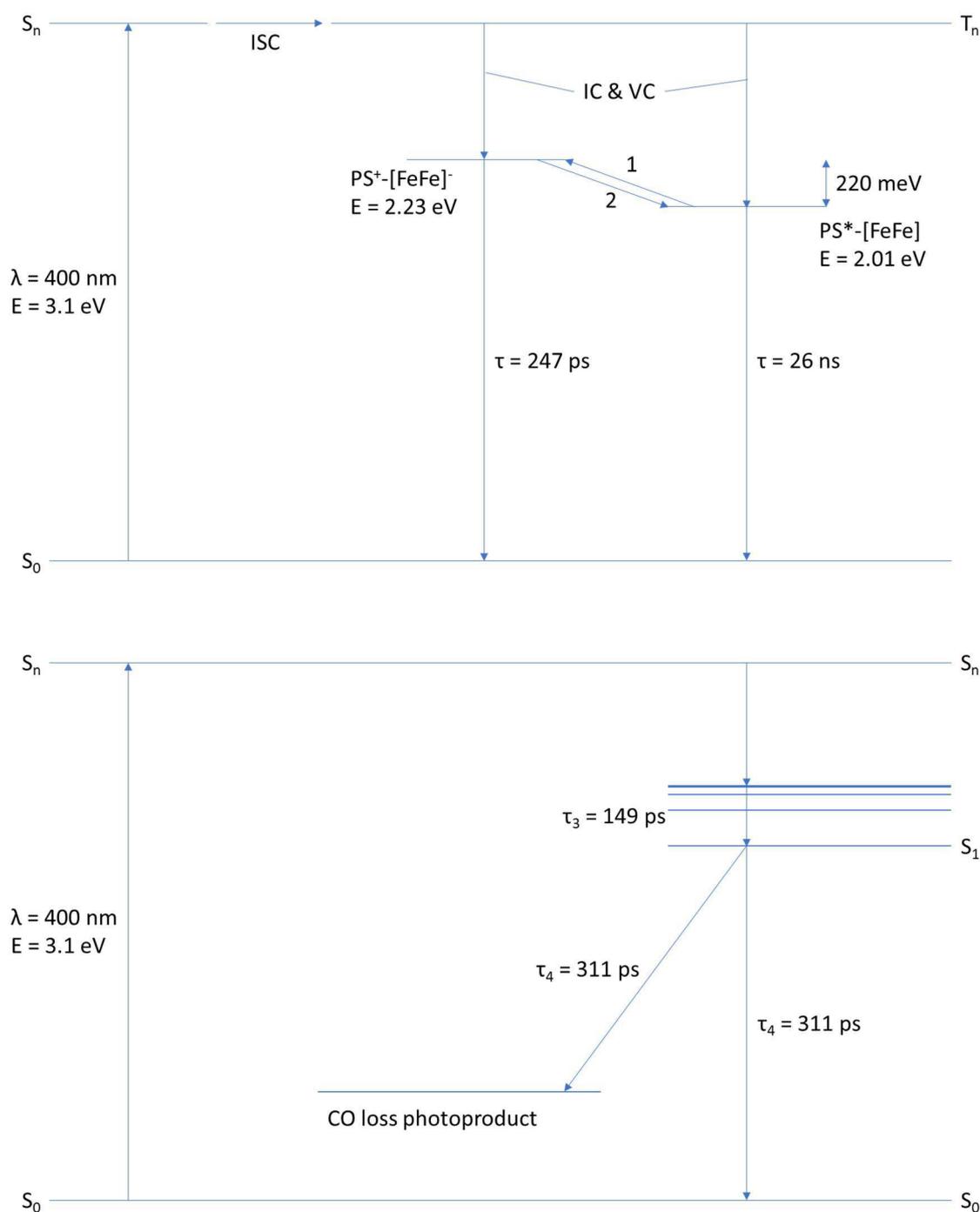
Figure 25 Jablonski diagrams detailing the excited state decay pathways for DYAD (top) and BAL (bottom). The top Jablonski diagram has the two excited states, PS*-[FeFe] and PS+-[FeFe]- interacting through pathways 1 and 2. Pathway 1 is only active whilst the molecule is vibrationally hot after excitation and leads to quenching of the excited state through the faster decaying CSS.

CONCLUSIONS

This is the first example of investigation of a covalently linked PS – FeFe dyad using time resolved infra-red spectroscopy. This builds on work from the literature, which investigates the excited state interaction between a supramolecularly bonded PS – FeFe dyad, featuring a Zn porphyrin dyad. The work in this chapter shows synthesis of a new covalently linked dyad and the investigation of its excited state decay using TRIR spectroscopy. These results are compared to model complexes to demonstrate the existence of a photoinduced charge separated state in the dyad.

To synthesize the dyad, reliant and efficient coupling methods for forming an ester from a carboxylic acid and hydroxyl residue have been used. Steglich esterification methods successfully linked an acid bearing PS complex and a hydroxyl bearing diiron hydrogenase model. The confirmation that a dyad has been synthesized was provided by FTIR & NMR spectroscopy and mass spectrometry. Early attempts at this method produced a side product characteristic of a failure of the Steglich esterification due to a slow elimination step, this was corrected in later attempts using adapted reaction conditions. Although this method was successful for a single diiron hydrogenase model, similar results could not be replicated for other hydroxyl bearing models, indicating that this method is not suitable in all cases.

The ground state properties of this dyad have been characterized using FTIR, UV/vis and NMR spectroscopy, indicating small changes to the environments of carbonyl residues of the dyad compared to model complexes. There is no strong evidence of strong coupling between the metal centres of the PS and hydrogenase centres in the ground state, bolstered by UV/vis spectroscopy, which shows that no new electronic transitions are present in the dyad, compared to the PS and diiron hydrogenase models.

Examination of the excited state revealed quenching of the emission of the dyad relative to its PS model complex, indicating the possibility of transfer of energy from the PS to the FeFe moiety. This was confirmed as an electron transfer process using TRIR spectroscopy, using comparison to published spectroelectrochemical studies of [FeFe] models and model spectra generated using DFT modelling. This CSS exists with a lifetime of just 247 ± 25 ps, indicating that without immediate electron injection from a sacrificial donor, this state unlikely to be useful in completing a catalytic cycle.

Although this work demonstrates the existence of a CSS for this dyad, it is unlikely to be considered a useful state. There is no proton shuttle, as there would be on a nitrogen bearing diiron hydrogenase mimic and the photoinduced CSS would need to be supported by a supramolecularly linked sacrificial donor. This would be possible to develop with the above methods, as peptide coupling methods are functionally identical to Steglich esterification for producing amide bonds and the platinum photosensitizer has a functionally unused coordination site; the chloride could be replaced with a mounting point for a sacrificial electron donor. This needs to be supported by improvements to the complex's solubility.

EXPERIMENTAL

Dichlorobis(dimethyl-sulfoxide)platinum(II)[54], [bis(1-ethynyl-4-heptylbenzene)platinum(4, 4'-ethylcarboxy-2,2'-bipyridine)], 2-(4-iodophenyl)-1,3-diethyl propanoate[55], 2-pyridinecarboximidic acid[56], 5-phenyl-3-(2-pyridinyl)-1,2,4-Triazine[57], 6-phenyl-4-(tributylstannyl)-2,2'-bipyridine[34], 4,4'-diethoxycarbonyl-2,2'-bipyridine[58], 6-phenyl-2,2'-bipyridine[59], 3-benzoyl acrylic acid[60], 2-acetylpyridylpyridine iodide[60], 4-carboxylic acid-6-phenyl-2,2'-bipyridine[60], 4-ethoxycarbonyl-6-phenyl-2,2'-bipyridine[61], [(6-phenyl-2,2'-bipyridyl) platinum chloride][62], μ-(propanedithiolate)diironhexacarbonyl[63] and 4- 2-phenyl-pyridinecarboxylic acid[64], were prepared by literature methods. [(4-ethylcarboxyl-6-phenyl-2,2'-bipyridyl) platinum chloride][34] and μ-(1,2-dimercaptopropan-3-ol) diiron hexacarbonyl[65] were prepared by modified literature methods.

Dichlorobis(dimethylsulfoxide)platinum(II)

To 100 mL round bottom flask; potassium tetrachloroplatinate (626 mg, 1.51 mmol) dissolved in water (10 mL) was added. To this solution, DMSO was added and was then stirred for 15 hours. The precipitate formed was filtered off and washed with water (3 x 5 mL) and acetone (3 x 5 mL) to leave a yellow crystalline powder (494 mg, 1.17 mmol). Yield: 78%

3-benzoyl acrylic acid[60]

To a two necked flask fitted with a reflux condenser, maleic anhydride (211 mg, 2.15 mmol) and anhydrous aluminium chloride (640 mg, 4.80 mmol) were added, followed by anhydrous benzene (30 mL). A colour change from yellow to red was observed and the resulting mixture was heated to reflux and stirred for 3 hours. The mixture was then allowed to cool to room temperature before being poured into ice water (150 mL). Concentrated hydrochloric acid (15 mL) was added and the resulting precipitate was taken up in ethyl acetate (100 mL). The organic layer was separated and extracted using two further portions of ethyl acetate (2 x 50 mL). The extract was washed with brine (3 x 50 mL) and then dried over magnesium sulfate. The magnesium sulfate was filtered off and removal of the solvent in vacuo afforded a yellow solid (157 mg, 0.89 mmol) Yield: 41%, 1H NMR (400 MHz, CDCl3): δ 8.04 – 7.96 (m, 3H), 7.68 – 7.61 (m, 1H), 7.57 – 7.50 (m, 2H), 6.90 (d, J = 15.6 Hz, 1H).

2-acetylpyridylpyridine iodide[60]

To a two necked flask fitted with a reflux condenser, iodine (5g, 19.7 mmol) was added and then dissolved in anhydrous pyridine (20 mL). 2-acetyl pyridine (1 mL, 8.93 mmol) was then added to the iodine solution by syringe and the mixture heated to reflux with stirring for 3 hours. The solution was then cooled to -18°C and allowed to stand overnight. The resulting precipitate was filtered and washed with ice cold pyridine (3 x 50 mL). The precipitate was then dissolved in a 4:1 mixture of ethanol and water and charcoal (100 mg) was added. This suspension was heated to reflux with stirring for one hour. The charcoal was filtered off and the filtrate reduced *in vacuo* to produce a grey solid. The solid was recrystallized from hot water and ethanol and washed with ice cold ethanol to give yellow crystals (701 mg, 2.14 mmol). Yield: 24%, ^{1}H NMR (250 MHz, DMSO): δ 9.01 (d, *J* = 5.5 Hz, 2H), 8.88 (ddd, *J* = 4.7, 1.5, 1.0 Hz, 1H), 8.80 – 8.68 (m, 1H), 8.28 (dd, *J* = 7.6, 6.7 Hz, 2H), 8.21 – 8.04 (m, 2H), 7.84 (ddd, *J* = 7.2, 4.7, 1.6 Hz, 1H).

4-carboxylic acid-6-phenyl-2,2'-bipyridine[60]

To a two necked flask fitted with a reflux condenser; 3-benzoyl acrylic acid (0.92 g, 5.23 mmol), 2-acetylpyridylpyridine iodide (2.47 g, 7.55 mmol) and ammonium acetate (6.0 g, 77.9 mmol) were added. Ethanol (40 mL) was added to dissolve the mixture and the solution was heated to reflux with stirring for 4 hours. The mixture was cooled to 0°C and acidified with 2M hydrochloric acid to pH 3 to precipitate the crude product. The ethanol was removed *in vacuo* and then the precipitate was filtered off, washed with water (3 x 20 mL) and dried *in vacuo* to leave a grey powder (1.101 g, 3.99 mmol) Yield: 76%, ^{1}H NMR (400 MHz, DMSO): δ 8.79 (d, *J* = 1.3 Hz, 1H),

8.76 (ddd, J = 4.7, 1.7, 0.9 Hz, 1H), 8.62 (d, J = 7.9 Hz, 1H), 8.36 (d, J = 1.3 Hz, 1H), 8.32 − 8.26 (m, 2H), 8.04 (td, J = 7.7, 1.8 Hz, 1H), 7.62 − 7.49 (m, 4H).

4-ethylcarboxy-6-phenyl-2,2'-bipyridine[61]

To a two necked flask fitted with a reflux condenser; 3-benzoyl acrylic acid (110 mg, 0.62 mmol), 2-acetylpyridylpyridine iodide (194 mg, 0.59 mmol) and ammonium acetate (443 mg, 5.75 mmol) were added. Ethanol (20 mL) was added to dissolve the mixture and the solution was heated to reflux with stirring for 15 hours. The solution was allowed to cool to room temperature and concentrated 0sulfuric acid was added (1 mL). The mixture was then heated to reflux with stirring for 2.5 hours before being cooled to 0°C and neutralized with 50% w/v potassium hydroxide solution. The product was extracted with ethyl acetate (3 x 50 mL) and washed with water (3 x 50 mL) and brine (3 x 50 mL) and dried over magnesium sulfate. The magnesium sulfate was filtered off and solvent removed *in vacuo*. The product was columned on silica using an eluant of ethyl acetate (R_f = 0.65) to leave a crystalline powder (80 mg, 0.26 mmol). Yield: 44%, ^{1}H NMR (400 MHz, CDCl$_3$): δ 8.90 (d, J = 1.3 Hz, 1H), 8.74 (ddd, J = 4.8, 1.7, 0.9 Hz, 1H), 8.65 (dt, J = 8.0, 1.0 Hz, 1H), 8.36 (d, J = 1.3 Hz, 1H), 8.24 − 8.19 (m, 2H), 7.87 (td, J = 7.7, 1.8 Hz, 1H), 7.56 − 7.45 (m, 3H), 7.37 (ddd, J = 7.5, 4.8, 1.2 Hz, 1H), 4.48 (q, J = 7.1 Hz, 2H), 1.47 (t, J = 7.1 Hz, 3H).

4-pentafluorophenylcarboxy-6-phenyl-2,2'-bipyridine

To 100 mL round bottom flask; 4-carboxyl-6-phenyl-2,2'-bipyridine (542 mg, 1.96 mmol), pentafluorophenol (399 mg, 2.17 mmol) and N,N'-dicyclohexylcarbodiimide (416 mg, 2.02 mmol) were added and suspended in dichloromethane (40 mL). The suspension was stirred for 4 hours before being filtered. Removal of the filtrate solvent *in vacuo* produced a light pink solid. This solid was subjected to column chromatography on silica and eluted with ethyl acetate/hexane 1:6 to isolate 4-pentafluorophenylcarboxy-6-phenyl-2,2'-bipyridine as a white solid (R_f = 0.50, 517 mg, 1.17 mmol). Yield = 59%, ^{1}H NMR (400 MHz, CDCl$_3$): δ 9.07 (d, J = 1.4 Hz, 1H), 8.75 (ddd, J = 4.8, 1.7, 0.9 Hz, 1H), 8.67 (dt, J = 8.0, 1.0 Hz, 1H), 8.45 (d, J = 1.4 Hz, 1H), 8.25 − 8.19 (m, 2H), 7.91 (td, J = 7.8, 1.8 Hz, 1H), 7.60 − 7.48 (m, 3H), 7.41 (ddd, J = 7.5, 4.8, 1.2 Hz, 1H), ^{19}F NMR (376 MHz, CDCl$_3$): δ -151.88 − -152.15 (m, J = 17.4 Hz), -156.93 (t, J = 21.7 Hz), -161.38 − -161.91 (m, J = 21.6, 17.5 Hz).

6-phenyl-2, 2'-bipyridine[59]

To a two necked flask fitted with a reflux condenser; 2,2'-bipyridine (1.1120g, 7.13 mmol) was added and dissolved in toluene (20 mL). The solution was cooled to 0°C and 1.8M phenyl lithium in dibutyl ether solution (4 mL, 7.2 mmol). This mixture was then heated to reflux with stirring for 18 hours. The mixture was then transferred to a separating funnel, washed with brine and extracted with dichloromethane (3 x 15 mL). The toluene solution was dried with magnesium sulfate. The solvent was removed *in vacuo* and the crude mixture subjected to column chromatography on silica eluted on a gradient from diethyl ether/hexane 3:7 to 8:2. The third fraction (R_f = 0.54 in 8:2) was retained and 6-phenyl-2, 2'-bipyridine (0.2902g, 1.25 mmol) was isolated after removal of the solvent *in vacuo*. Yield: 17%, ^{1}H NMR (400 MHz, CDCl$_3$) δ 8.71 (ddd, J = 4.8, 1.6, 0.8 Hz, 1H), 8.66 (d, J = 8.0 Hz, 1H), 8.40 (d, J = 7.8 Hz, 1H), 8.18 − 8.14 (m, 2H), 7.90 (t, J = 7.8 Hz, 1H), 7.87 (td, J = 7.8, 1.8 Hz, 1H), 7.79 (dd, J = 7.8, 0.9 Hz, 1H), 7.54 − 7.42 (m, 3H), 7.35 (ddd, J = 7.4, 4.8, 1.1 Hz, 1H).

PtESTER [(4-ethylcarboxy-6-phenyl-2, 2'-bipyridyl) platinum chloride][34]

To a two necked flask fitted with a reflux condenser; potassium tetrachloroplatinate (155 mg, 0.37 mmol) and 4-ethoxycarbonyl-6-phenyl-2,2'-bipyridine (112 mg, 0.37 mmol) were added and suspended in a 1:1 mixture of water and acetonitrile (20 mL). The suspension was heated to reflux with stirring for 18 hours. The resulting suspension was cooled to room temperature and the precipitate formed was filtered off and washed with water (3 x 10 mL) to leave an orange crystalline powder (148 mg, 0.27 mmol). Yield: 75%, ^{1}H NMR (400 MHz, CD$_2$Cl$_2$): δ 9.00 (ddd, J =

5.3, 1.5, 0.7 Hz, 1H), 8.14 (td, J = 7.9, 1.6 Hz, 1H), 8.09 – 8.03 (m, 2H), 8.01 – 7.95 (m, 1H), 7.71 (ddd, J = 7.5, 5.3, 1.3 Hz, 1H), 7.60 (dd, J = 7.6, 1.0 Hz, 1H), 7.43 (dd, J = 7.7, 1.3 Hz, 1H), 7.23 (td, J = 7.4, 1.4 Hz, 1H), 7.12 (td, J = 7.5, 1.3 Hz, 1H), 4.47 (q, J = 7.1 Hz, 2H), 1.47 (t, J = 7.1 Hz, 3H), ASAP MS: m/z = 534 (M$^+$). FTIR (in DCM, r.t.): ν(CO) at 1734 cm^{-1}.

PtACID [(4-carboxylic acid-6-phenyl-2, 2′-bipyridyl) platinum chloride]

To a two necked flask fitted with a reflux condenser; dichlorobis(dimethyl sulfoxide)platinum (438 mg, 1.15 mmol) and 4-carboxyl-6-phenyl-2,2'-bipyridine (318 mg, 1.15 mmol) were added and suspended in methanol (20 mL). The suspension was heated to reflux with stirring for 24 hours. The resulting suspension was cooled to room temperature and the precipitate formed was filtered off, washed with methanol (3 x 10 mL), acetone (3 x 20 mL) and diethyl ether (3 x 10 mL) to leave an orange crystalline powder (275 mg, 0.55 mmol). Yield: 48%, ^{1}H NMR (400 MHz, DMSO): δ 8.92 (dd, J = 5.2, 0.8 Hz, 1H), 8.72 (d, J = 8.1 Hz, 1H), 8.48 (d, J = 1.0 Hz, 1H), 8.35 (td, J = 7.9, 1.6 Hz, 1H), 8.23 (d, J = 1.0 Hz, 1H), 7.96 (ddd, J = 7.5, 5.3, 0.8 Hz, 1H), 7.72 (d, J = 7.2 Hz, 1H), 7.52 (dd, J = 7.5, 0.8 Hz, 1H), 7.20 (td, J = 7.4, 1.2 Hz, 1H), 7.10 (td, J = 7.6, 1.1 Hz, 1H), EI MS: m/z = 506 (MH$^+$), 462 (M – CO$_2$H), 426 (M – (Cl)(CO$_2$H)), 230 (M – (PtCl)(CO$_2$H)), EI-MS: m/z = 506 (MH$^+$), 462 (M$^+$-(COOH)), 426 (M$^+$-(Cl)(COOH)), 232 (M$^+$-(PtCl)(COOH)).

PDT μ-(propanedithiolate) diiron hexacarbonyl[63]

To a two necked flask fitted with a reflux condenser; triiron dodecacarbonyl (4.24 g, 8.41 mmol) and 1,3-dimercaptopropane (0.9 mL, 8.98 mmol) were added. Toluene (40 mL) was then added and the solution heated to reflux with stirring until the mixture had changed colour from green to red-brown. The reaction mixture was then cooled to room temperature and the solvent removed *in vacuo*. The oily residue was loaded onto a silica (60 mesh) column and eluted with dichloromethane/hexane 3:1 (R$_f$ = 0.48). After removal of the solvent *in vacuo*, the red crystalline powder was redissolved in the minimum amount of hexane and placed in the freezer at -18°C to crystallize. The red crystals formed were filtered off and washed with ice cold hexane, to leave μ-(propanedithiolate) diiron hexacarbonyl (1.136g, 2.05 mmol). Yield: 24%, ^{1}H NMR (400 MHz, Acetone-d$_6$): δ 2.31 – 2.23 (m, 4H), 1.92 – 1.82 (m, 2H), ^{13}C NMR (101 MHz, Acetone-d$_6$): δ 209.01 (s), 31.23 (s), 23.63 (s).

BAL μ-(1,2-dimercaptopropan-3-ol) diiron hexacarbonyl[65]

To a two necked flask fitted with a reflux condenser; triiron dodecacarbonyl (1.5 g, 3.0 mmol) and 1,2-dimercaptopropan-2-ol (0.35 mL, 3.5 mmol) were added. Toluene (100 mL) was then added and the solution heated to reflux with stirring for one hour. The reaction mixture was then cooled to room temperature and the solvent removed *in vacuo*. The oily residue was loaded onto a silica column and eluted with ethyl acetate/hexane 1:3 (R$_f$ = 0.32). The solvent was removed *in vacuo* to leave a red crystalline powder (1.2 g, 2.1 mmol). Yield: 70%, ^{1}H NMR (400 MHz, CDCl$_3$): δ 3.64 (s, 1H), 3.58 – 3.47 (m, 1H), 2.90 – 2.76 (m, 1H), 2.67 (dd, J = 12.9, 7.8 Hz, 1H), 1.92 (dd, J = 13.3, 5.1 Hz, 1H), 1.86 (s, 1H).

DYAD [(4-carboxy(μ-(1,2-dimercaptopropane) diiron hexacarbonyl)-6-phenyl-2, 2′-bipyridyl) platinum chloride]

To a two necked flask; [(4-carboxyl-6-phenyl-2, 2'-bipyridyl) platinum chloride] (195 mg, 0.39 mmol), μ-(1,2-dimercaptopropan-3-ol) diiron hexacarbonyl (634 mg, 1.11 mmol), N,N'-dicyclohexyl-carbodiimide (98 mg, 0.48 mmol) and N,N'-dimethylaminopyridine (10 mg, 0.08mmol) were added and suspended in dichloromethane (40 mL) added by cannula transfer at 0°C. This suspension was allowed to warm to room temperature and allowed to stir for 11 days whilst being monitored by TLC for appearance of the product (silica plate, dichloromethane/ethyl acetate 9:1, R$_f$ = 0.95). Once the reaction appeared to proceed no further the solvent was removed *in vacuo*, and the remaining solid washed with acetonitrile (3 x 50 mL) to remove excess μ-(1,2-dimercaptopropan-3-ol) diiron hexacarbonyl. The solid was then subjected to column chromatography on silica using dichloromethane/ethyl acetate 9:1 to

isolate an orange crystalline powder (Rf = 0.95, 76 mg, 0.09 mmol). Yield: 23%, ^{1}H NMR (400 MHz, DMSO): δ 8.93 (dd, *J* = 4.7, 0.6 Hz, 1H), 8.73 (d, *J* = 8.0 Hz, 1H), 8.49 (d, *J* = 0.9 Hz, 1H), 8.38 (td, *J* = 7.7, 1.3 Hz, 1H), 8.26 (d, *J* = 0.7 Hz, 1H), 7.98 (ddd, *J* = 7.6, 5.7, 0.9 Hz, 1H), 7.75 (dd, *J* = 7.7, 0.5 Hz, 1H), 7.53 (dd, *J* = 7.9, 0.8 Hz, 1H), 7.22 (td, *J* = 7.2, 0.9 Hz, 1H), 7.12 (td, *J* = 7.7, 0.8 Hz, 1H), 4.43 (dd, *J* = 11.3, 7.3 Hz, 1H), 4.26 (dd, *J* = 11.4, 7.1 Hz, 1H), 3.07 (dd, *J* = 13.5, 7.5 Hz, 1H), 2.50 – 2.36 (m, 2H). FAB TOF MS: m/z = 833 (MH$^+$ - 2(CO)).

SP1 [(4-carboxy(dicyclohexylurea)-6-phenyl-2, 2′-bipyridyl) platinum chloride]

To a two necked flask; [(4-carboxyl-6-phenyl-2, 2′-bipyridyl) platinum chloride] (118 mg, 0.23 mmol), μ-(1,2-dimercaptopropan-3-ol) diiron hexacarbonyl (95 mg, 0.24 mmol), N,N′-dicyclohexylcarbodiimide (59 mg, 0.29 mmol) and N,N′-dimethylaminopyridine (2 mg, 0.02 mmol) were added and suspended in dichloromethane (70 mL). This suspension was stirred for 18 hours whilst being monitored by TLC (silica plate, dichloromethane/ ethyl acetate 9:1, R$_f$ = 0.95). Once the reaction appeared to proceed no further the solvent was removed *in vacuo*, leaving a crude product as a solid. The compound isolated by column chromatography on silica, eluted by dichloromethane/ ethyl acetate 9:1(R$_f$ = 0.4), as a purple crystalline solid (103 mg, 0.14 mmol). Yield: 61%, ^{1}H NMR (400 MHz, DMSO-d$_6$): δ 8.92 (d, *J* = 5.0 Hz, 1H), 8.48 (d, *J* = 8.0 Hz, 1H), 8.38 (td, *J* = 7.9, 1.4 Hz, 1H), 8.33 (d, *J* = 7.9 Hz, 1H), 8.11 (s, 1H), 8.02 – 7.93 (m, 1H), 7.89 (s, 1H), 7.55 (d, *J* = 7.4 Hz, 1H), 7.51 (d, *J* = 7.5 Hz, 1H), 7.20 (td, *J* = 7.4, 1.0 Hz, 1H), 7.12 (td, *J* = 7.4, 0.8 Hz, 1H), 4.26 – 4.10 (m, 1H), 3.21 (dd, *J* = 17.5, 9.9 Hz, 1H), 1.92 (d, *J* = 11.8 Hz, 2H), 1.81 (d, *J* = 12.9 Hz, 2H), 1.63 (qd, *J* = 12.6, 3.0 Hz, 3H), 1.36 (t, *J* = 13.1 Hz, 7H), 1.13 – 0.85 (m, 6H).

REFERENCES

1.   Crabtree, G. W.; Dresselhaus, M. S.; Buchanan, M. V., *Phys. Today* **2004,** *57* (12), 39-44.
2.   Armaroli, N.; Balzani, V., *Angew. Chem. Int. Ed.* **2007,** *46* (1-2), 52-66.
3.   Coontz, R.; Hanson, B., *Science* **2004,** *305* (5686), 957-957.
4.   Sakintuna, B.; Lamari-Darkrim, F.; Hirscher, M., *Int. J. Hydrogen Energy* **2007,** *32* (9), 1121-1140.
5.   Ni, M.; Leung, M. K. H.; Leung, D. Y. C.; Sumathy, K., *Renew, Sust. Energ. Rev.* **2007,** *11* (3), 401-425.
6.   Evans, D. J.; Pickett, C. J., *Chem. Soc. Rev.* **2003,** *32* (5), 268-275.
7.   Tard, C.; Pickett, C. J., *Chem. Rev.* **2009,** *109* (6), 2245-2274.
8.   Adams, M. W. W., *BBA - Bioenergetics* **1990,** *1020* (2), 115-145.
9.   Wang, F.; Wang, W.-G.; Wang, H.-Y.; Si, G.; Tung, C.-H.; Wu, L.-Z., *ACS Catal.* **2012,** *2* (3), 407-416.
10.   Samuel, A. P. S.; Co, D. T.; Stern, C. L.; Wasielewski, M. R., *J. Am. Chem. Soc.* **2010,** *132* (26), 8813-8815.
11.   Ott, S.; Kritikos, M.; Åkermark, B.; Sun, L., *Angew. Chem. Int. Ed.* **2003,** *42* (28), 3285-3288.
12.   Wolpher, H.; Borgström, M.; Hammarström, L.; Bergquist, J.; Sundström, V.; Styring, S.; Sun, L.; Åkermark, B., *Inorg. Chem. Commun.* **2003,** *6* (8), 989-991.
13.   Ott, S.; Borgström, M.; Kritikos, M.; Lomoth, R.; Bergquist, J.; Åkermark, B.; Hammarström, L.; Sun, L., *Inorg. Chem.* **2004,** *43* (15), 4683-4692.
14.   Cui, H.-h.; Hu, M.-q.; Wen, H.-m.; Chai, G.-l.; Ma, C.-b.; Chen, H.; Chen, C.-n., *Dalton Trans.* **2012,** *41* (45), 13899-13907.
15.   Wang, W.-G.; Wang, F.; Wang, H.-Y.; Tung, C.-H.; Wu, L.-Z., *Dalton Trans.* **2012,** *41* (8), 2420-2426.
16.   Ekstrom, J.; Abrahamsson, M.; Olson, C.; Bergquist, J.; Kaynak, F. B.; Eriksson, L.; Sun, L.; Becker, H.-C.; Akermark, B.; Hammarstrom, L.; Ott, S., *Dalton Trans.* **2006,** *0* (38), 4599-4606.
17.   Song, L.-C.; Tang, M.-Y.; Mei, S.-Z.; Huang, J.-H.; Hu, Q.-M., *Organometallics* **2007,** *26* (7), 1575-1577.
18.   Li, X.; Wang, M.; Zhang, S.; Pan, J.; Na, Y.; Liu, J.; Åkermark, B.; Sun, L., *J. Phys. Chem. B* **2008,** *112* (27), 8198-8202.
19.   Kluwer, A. M.; Kapre, R.; Hartl, F.; Lutz, M.; Spek, A. L.; Brouwer, A. M.; van Leeuwen, P. W. N. M.; Reek, J. N. H., *Proc. Natl. Acad. Sci. U.S.A.* **2009,** *106* (26), 10460-10465.
20.   Li, P.; Amirjalayer, S.; Hartl, F.; Lutz, M.; Bruin, B. d.; Becker, R.; Woutersen, S.; Reek, J. N. H., *Inorg. Chem.* **2014,** *53* (10), 5373-5383.
21.   Wang, W.; Yu, T.; Zeng, Y.; Chen, J.; Yang, G.; Li, Y., *Photochem. Photobiol. Sci.* **2014,** *13* (11), 1590-1597.
22.   Li, P.; Amirjalayer, S.; Hartl, F.; Lutz, M.; de Bruin, B.; Becker, R.; Woutersen, S.; Reek, J. N. H., *Inorg. Chem.* **2014,** *53* (10), 5373-5383.
23.   Borg, S. J.; Behrsing, T.; Best, S. P.; Razavet, M.; Liu, X.; Pickett, C. J., *J. Am. Chem. Soc.* **2004,** *126* (51), 16988-16999.
24.   Na, Y.; Pan, J.; Wang, M.; Sun, L., *Inorg. Chem.* **2007,** *46* (10), 3813-3815.
25.   Hunt, N. T.; Wright, J. A.; Pickett, C., *Inorg. Chem.* **2016,** *55* (2), 399-410.
26.   Bingaman, J. L.; Kohnhorst, C. L.; Van Meter, G. A.; McElroy, B. A.; Rakowski, E. A.; Caplins, B. W.; Gutowski, T. A.; Stromberg, C. J.; Webster, C. E.; Heilweil, E. J., *J. Phys. Chem. A* **2012,** *116* (27), 7261-7271.
27.   Stewart, A. I.; Clark, I. P.; Towrie, M.; Ibrahim, S. K.; Parker, A. W.; Pickett, C. J.; Hunt, N. T., *J. Phys. Chem. B* **2008,** *112* (32), 10023-10032.
28.   Ridley, A. R.; Stewart, A. I.; Adamczyk, K.; Ghosh, H. N.; Kerkeni, B.; Guo, Z. X.; Nibbering, E. T. J.; Pickett, C. J.; Hunt, N. T., *Inorg. Chem.* **2008,** *47* (17), 7453-7455.
29.   Kaziannis, S.; Santabarbara, S.; Wright, J. A.; Greetham, G. M.; Towrie, M.; Parker, A. W.; Pickett, C. J.; Hunt, N. T., *J. Phys. Chem. B* **2010,** *114* (46), 15370-15379.

30.   Kania, R.; Frederix, P. W. J. M.; Wright, J. A.; Ulijn, R. V.; Pickett, C. J.; Hunt, N. T., *J. Chem. Phys.* **2012,** *136* (4), 044521.

31.   Johnson, M.; Thuman, J.; Letterman, R. G.; Stromberg, C. J.; Webster, C. E.; Heilweil, E. J., *J. Phys. Chem. B* **2013,** *117* (49), 15792-15803.

32.   Caplins, B. W.; Lomont, J. P.; Nguyen, S. C.; Harris, C. B., *J. Phys. Chem. A* **2014,** *118* (49), 11529-11540.

33.   Li, X.; Wang, M.; Zhang, S.; Pan, J.; Na, Y.; Liu, J.; Åkermark, B. r.; Sun, L., *J. Phys. Chem. B* **2008,** *112* (27), 8198-8202.

34.   Lu, W.; Chan, M. C. W.; Zhu, N.; Che, C.-M.; Li, C.; Hui, Z., *J. Am. Chem. Soc.* **2004,** *126* (24), 7639-7651.

35.   Marija, L.; Ivica, C.; Mladen, L.; Anamarija, B.; Vladimir, V., *Croat. Chem. Acta* **2007,** *80* (1), 109-115.

36.   Archer, S. A. The Synthesis and Photophysical Properties of Light-Harvesting Platinum (II) Diimine Acetylides. University of Sheffield, 2015.

37.   Neve, F.; Crispini, A.; Di Pietro, C.; Campagna, S., *Organometallics* **2002,** *21* (17), 3511-3518.

38.   Xu, F.; Tard, C.; Wang, X.; Ibrahim, S. K.; Hughes, D. L.; Zhong, W.; Zeng, X.; Luo, Q.; Liu, X.; Pickett, C. J., *Chem. Commun.* **2008,** (5), 606-608.

39.   Wang, Y.; Li, Z.; Zeng, X.; Wang, X.; Zhan, C.; Liu, Y.; Zeng, X.; Luo, Q.; Liu, X., *New J. Chem.* **2009,** *33* (8), 1780-1789.

40.   Donovan, E. S.; Nichol, G. S.; Felton, G. A. N., *J. Organomet. Chem.* **2013,** *726*, 9-13.

41.   Jiang, X.; Long, L.; Wang, H.; Chen, L.; Liu, X., *Dalton Trans.* **2014,** *43* (26), 9968-9975.

42.   Le Cloirec, A.; Davies, S. C.; Evans, D. J.; Hughes, D. L.; Pickett, C. J.; Best, S. P.; Borg, S., *Chem. Commun.* **1999,** (22), 2285-2286.

43.   Razavet, M.; Le Cloirec, A.; Davies, S. C.; Hughes, D. L.; Pickett, C. J., *J. Chem. Soc., Dalton Trans.* **2001,** (24), 3551-3552.

44.   Zhu, D.; Xiao, Z.; Liu, X., *Int. J. Hydrogen Energy* **2015,** *40* (15), 5081-5091.

45.   Sazanovich, I. V.; Best, J.; Scattergood, P. A.; Towrie, M.; Tikhomirov, S. A.; Bouganov, O. V.; Meijer, A. J. H. M.; Weinstein, J. A., *PCCP* **2014,** *16* (47), 25775-25788.

46.   Hissler, M.; Connick, W. B.; Geiger, D. K.; McGarrah, J. E.; Lipa, D.; Lachicotte, R. J.; Eisenberg, R., *Inorg. Chem.* **2000,** *39* (3), 447-457.

47.   Mathieu, R.; Poilblanc, R.; Lemoine, P.; Gross, M., *J. Organomet. Chem.* **1979,** *165* (2), 243-252.

48.   Ramakrishna, G.; Goodson, T.; Rogers-Haley, J. E.; Cooper, T. M.; McLean, D. G.; Urbas, A., *J. Phys. Chem. C* **2009,** *113* (3), 1060-1066.

49.   Rogers, J. E.; Slagle, J. E.; Krein, D. M.; Burke, A. R.; Hall, B. C.; Fratini, A.; McLean, D. G.; Fleitz, P. A.; Cooper, T. M.; Drobizhev, M.; Makarov, N. S.; Rebane, A.; Kim, K.-Y.; Farley, R.; Schanze, K. S., *Inorg. Chem.* **2007,** *46* (16), 6483-6494.

50.   Greetham, G. M.; Burgos, P.; Cao, Q.; Clark, I. P.; Codd, P. S.; Farrow, R. C.; George, M. W.; Kogimtzis, M.; Matousek, P.; Parker, A. W.; Pollard, M. R.; Robinson, D. A.; Xin, Z.-J.; Towrie, M., *Appl. Spectrosc.* **2010,** *64* (12), 1311-1319.

51.   Kania, R.; Stewart, A. I.; Clark, I. P.; Greetham, G. M.; Parker, A. W.; Towrie, M.; Hunt, N. T., *PCCP* **2010,** *12* (5), 1051-1063.

52.   Best, J.; Sazanovich, I. V.; Adams, H.; Bennett, R. D.; Davies, E. S.; Meijer, A. J. H. M.; Towrie, M.; Tikhomirov, S. A.; Bouganov, O. V.; Ward, M. D.; Weinstein, J. A., *Inorg. Chem.* **2010,** *49* (21), 10041-10056.

53.   Snellenburg, J. J.; Laptenok, S. P.; Seger, R.; Mullen, K. M.; van Stokkum, I. H. M., *J. Stat. Softw.* **2012,** *49* (3), 1-22.

54.   Price, J. H.; Williamson, A. N.; Schramm, R. F.; Wayland, B. B., *Inorg. Chem.* **1972,** *11* (6), 1280-1284.

55.   Simoneau, B.; Deroy, P.; Fader, L.; Faucher, A. M.; Gagnon, A.; Grand-Maitre, C.; Kawai, S.; Landry, S.; Mercier, J. F.; Rancourt, J., *WO 2011100838 A1* **2011**.

56.   Orselli, E.; Kottas, G. S.; Konradsson, A. E.; Coppo, P.; Fröhlich, R.; De Cola, L.; van Dijken, A.; Büchel, M.; Börner, H., *Inorg. Chem.* **2007,** *46* (26), 11082-11093.

57.   Ye, L.; Haddadin, M. J.; Lodewyk, M. W.; Ferreira, A. J.; Fettinger, J. C.; Tantillo, D. J.; Kurth, M. J., *Org. Lett.* **2009,** *12* (1), 164-167.

58.   Gillaizeau-Gauthier, I.; Odobel, F.; Alebbi, M.; Argazzi, R.; Costa, E.; Bignozzi, C. A.; Qu, P.; Meyer, G. J., *Inorg. Chem.* **2001,** *40* (23), 6073-6079.

59.   Hebbe-Viton, V.; Desvergnes, V.; Jodry, J. J.; Dietrich-Buchecker, C.; Sauvage, J.-P.; Lacour, J., *Dalton Trans.* **2006,** (17), 2058-2065.

60.   Liu, Y.; Zai, Y.; Chang, X.; Guo, Y.; Meng, S.; Feng, F., *Anal. Chim. Acta* **2006,** *575* (2), 159-165.

61.   Lu, W.; Mi, B.-X.; Chan, M. C. W.; Hui, Z.; Che, C.-M.; Zhu, N.; Lee, S.-T., *J. Am. Chem. Soc.* **2004,** *126* (15), 4958-4971.

62.   Constable, E. C.; Henney, R. P. G.; Leese, T. A.; Tocher, D. A., *J. Chem. Soc., Chem. Commun.* **1990,** (6), 513-515.

63.   Lyon, E. J.; Georgakaki, I. P.; Reibenspies, J. H.; Darensbourg, M. Y., *J. Am. Chem. Soc.* **2001,** *123* (14), 3268-3278.

64.   Bomben, P. G.; Robson, K. C. D.; Sedach, P. A.; Berlinguette, C. P., *Inorg. Chem.* **2009,** *48* (20), 9631-9643.

65.   Donovan, E. S.; Nichol, G. S.; Felton, G. A. N., *Journal of Organometallic Chemistry* **2013,** *726*, 9-13.

4. Optimizing Photosensitizer Properties and Understanding Decay Mechanisms by Exploiting the Hammett Equation

INTRODUCTION

In order to develop a global sustainable society, there must be more effective utilisation of solar energy. Meeting the predicted world energy demand of up to 43 TW by 2050, whilst reducing the predicted, unsustainably high CO_2 levels requires new methods of harnessing the 17000 TW of solar energy hitting the earth's surface.[1-3] Approaches to harnessing this energy include, but are not limited to; converting solar energy into electrical energy, converting CO_2 into usable fuels, replicating natural processes to split water and converting solar energy into thermal energy.[4-8] Excluding converting light into heat, the heart of these processes lies in using a photon to transfer an electron; forming a charge separated state, separating charge carriers or inducing a redox reaction. These processes are loosely defined as "artificial photosynthesis".[9] Making this process as efficient as possible requires us to find the best possible light absorbing compounds, by finding the compounds with the best combinations of properties; broad spectrum absorption, high extinction coefficients and high quantum yields of useable excited states.

Designing a better light absorber

Dye sensitized solar cells (DSSCs) are a prominent method for converting solar energy into electrical energy using transition metal photosensitizers. These rely on the use of a transition metal photosensitizers (PS) to broaden the spectrum of light that a semiconductor may use to promote an electron into its conduction band. The use of a broadly absorbing ruthenium dye was shown to produce a photoelectrochemical cell capable of a conversion efficiency of 7.1%, leading to the development of new photosensitizers that may be used to harvest light for DSSCs and form charge separated states (CSS).[10-13]

Despite promising results from the use of ruthenium photosensitizers, the efficiency of the cell is still limited by the ability of the PS to harvest light. In order to harvest more light, convert more energy and make the cells economically viable, better light harvesting compounds are required. DSSCs featuring solid state PS in the form of perovskites have been found to have efficiencies of 15.0%.[14] Platinum PS complexes have also been considered,[13, 15-19] due to highly solvatochromic, intense charge transfer transitions in visible range and high tunability of light-harvesting properties of such complexes through molecular design. These properties also make them viable for other photochemical reactions, including artificial photosynthesis and light driven proton conversion to hydrogen.[20]

Developing platinum complexes with the capabilities required for these uses requires that their properties are predictable, to guide further research, and this requires an understanding of the history of square planar platinum luminophores. Initially, investigations probed the emission properties of complexes of the form; Pt(diimine)X_2.[21-23] These compounds displayed emission in alcoholic solution after absorption of visible light and showed how the properties of the PS are sensitive to its counter ion. Adapting these compounds to have more useful luminescent properties, to harvest and utilise light, took place through replacing the monodentate, anionic, X type ligands with chelating dithiolates.[24]
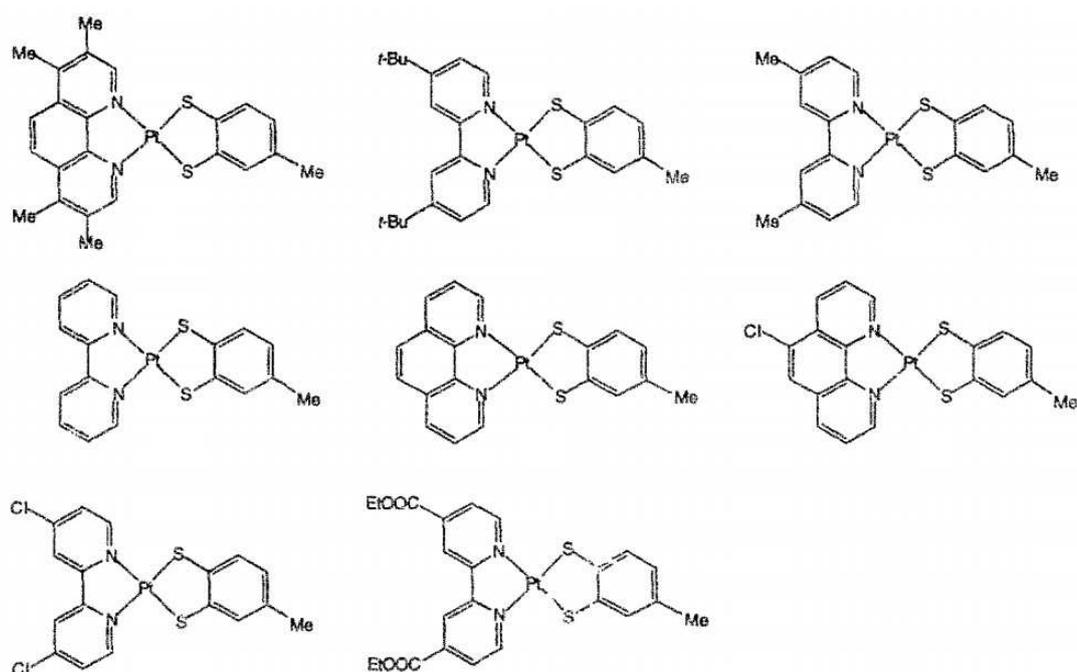
Figure 1 Complexes of the type, Pt(diimine)(dithiolate), adapted from the work of Paw et Al.[25]

Luminescence from solution phase Pt(diimine)(maleonitriledithiolato) at room temperature was reported in 1990.[26] Following this discovery, many Pt(diimine)(dithiolate) PS complexes (Figure 1) were discovered to have similar luminescence properties.[24] These properties include a moderately intense solvatochromic visible light absorption band (ε = 5000 – 10000 M^{-1} cm, 450 – 700 nm) from an MMLL'CT transition, broad unstructured solution luminescence and extremely tuneable excited state properties. Systematic variation of diimine and dithiolate ligands led to variance in the excited state energy of up to 1 eV, ϕ_{Em} between < 10^{-5} and 6.4 x 10^{-3} and τ_{Em} between 1 ns and > 1 μs.[27] Spectroscopic and spectroelectrochemical studies further revealed that the LUMO is located on the bipyridine ligand whilst the HOMO is located on the dithiolate ligand.[28] These complexes also feature important directional charge transfer, enhancing their candidacy for use in light driven electron transfer reactions, as this promotes effective solar energy use.[25]

Finding how to tune the ground and excited state electronic properties of platinum diimines required that similar but contrasting ligand sets be used to tune the HOMO electronic levels. The implementation of acetylide ligands fulfils the requirement for a similar, tunable ligand system, whilst also providing high quantum yields of emission, long emissive lifetimes and shifting the HOMO to an orbital with more metal character.[29-30] However this ligand set change leads to a smaller change in excited state properties, between members of the series studied, than seen in the dithiolates.
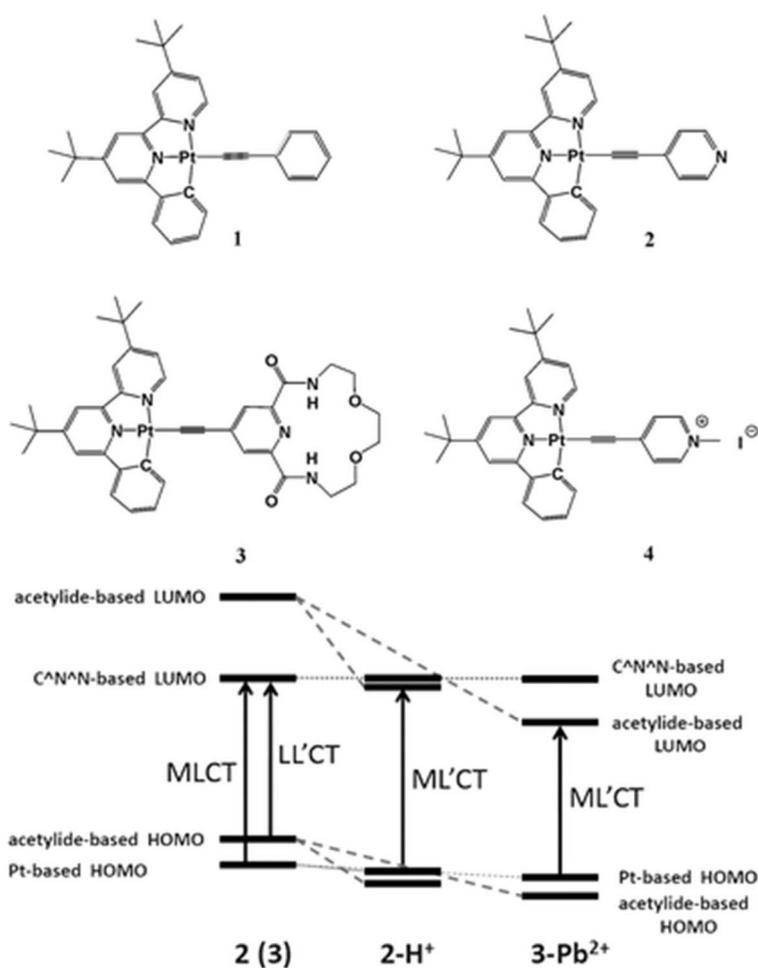
Figure 2 Proposed qualitative energetic scheme for the switching of the low-lying excited states of 2 upon protonation and of 3 upon addition of Pb2+ cations.[31]

Investigations of platinum diimine bisarylacetylide behaviour led to the study of cyclometaled Pt(N^N^C) arylacetylide systems and their luminescent properties,[32] as cyclometalated platinum complexes show stronger emission and lifetimes than their diimine counterparts, useful for complexes that may be used in electroluminescent devices.[33] The excited state character in these compounds is dominated by the Pt d, cyclometalating ligand π^* and arylacetylide π orbitals, with the HOMO located primarily in metal centred orbitals with contribution from the arylacetylide and the LUMO located on the bipyridine moiety. The effect of protonation of the arylacetylide on excited state properties has been investigated in order to observe a LUMO switch from N^N^C character to arylacetylide character (Figure 2).[31]

Structure activity relationships and property modelling

Despite the extensive study of square planar platinum complex excited states, their properties are still not very easy to predict. There are often multiple competing low-lying excited states, where ligand and metal orbitals combine to provide many different pathways to the ground state. Several techniques have been used to attempt to predict the excited state properties, including expensive computational methods such as DFT and TD-DFT and less expensive empirical methods.[31, 34-35]

The primary empirical method for analysing how these systems' properties are affected by electronic perturbation is Hammett theory.[36-38] Use of Hammett theory to describe platinum compounds' properties has been restricted to describing LUMO acceptor behaviour of diimine complexes in the ground state.[39-40] These studies demonstrate that the properties of the

complex correlate well with empirical Hammett parameters and may be used to screen complexes for suitable excited state behaviour.

The Hammett equation is a linear free energy relationship that relates reaction rates and equilibrium rates to empirically derived constants that describe the electrophilicity of a substituent.[41] Through this relationship it can be determined how dependent a reaction is upon the electrophilicity of a substituent and also how the mechanism for the reaction proceeds. Despite the age and simplicity of the relationship, it is still considered a viable part of structure-activity and structure-property analyses to this day.[42-44] The Hammett constant relates the difference between a reaction rate (k_D) and a normalized reaction rate (k_H) to reaction constant (ρ) and a substituent constant (σ), according to equation:

$$\log \left(\frac{k_D}{k_H} \right) = \rho\sigma \qquad \textbf{Eq.1}$$

Plotting a range of these relationships for substituents with differing values of σ allows the extraction of information about the mechanism of the reaction and its dependence on the non-innocent substituent. A positive gradient to this relationship means that there is an increase in negative partial charge or loss in positive partial charge in the transition state stabilised by more electron withdrawing substituents. A negative gradient means there is an increase in positive partial charge or decrease in negative partial charge in the transition state stabilised by the substituent. Zero gradient indicates the substituent has no effect on reaction rate. Where there is a non-constant gradient or a discontinuity, a change in reaction mechanism with changing electron demand is implied. The gradient change or discontinuity contains important information about the nature of the mechanism change based on the relationships described above.

Correlation between Hammett σ constants and the physical properties of emissive platinum complexes has been demonstrated before, where the HOMO-LUMO gap has been correlated for a series of Pt(diimine)(X_2) complexes with electronically non-innocent substituents substituted onto the diimine. This has been demonstrated by Eisenberg et al. to be due to the effect the diimine substituents have on the electronics of the LUMO, significantly changing its energy relative to the HOMO, whilst not having any significant effect on the HOMO, conclusively revealing that the LUMO has overwhelmingly diimine character.[45]
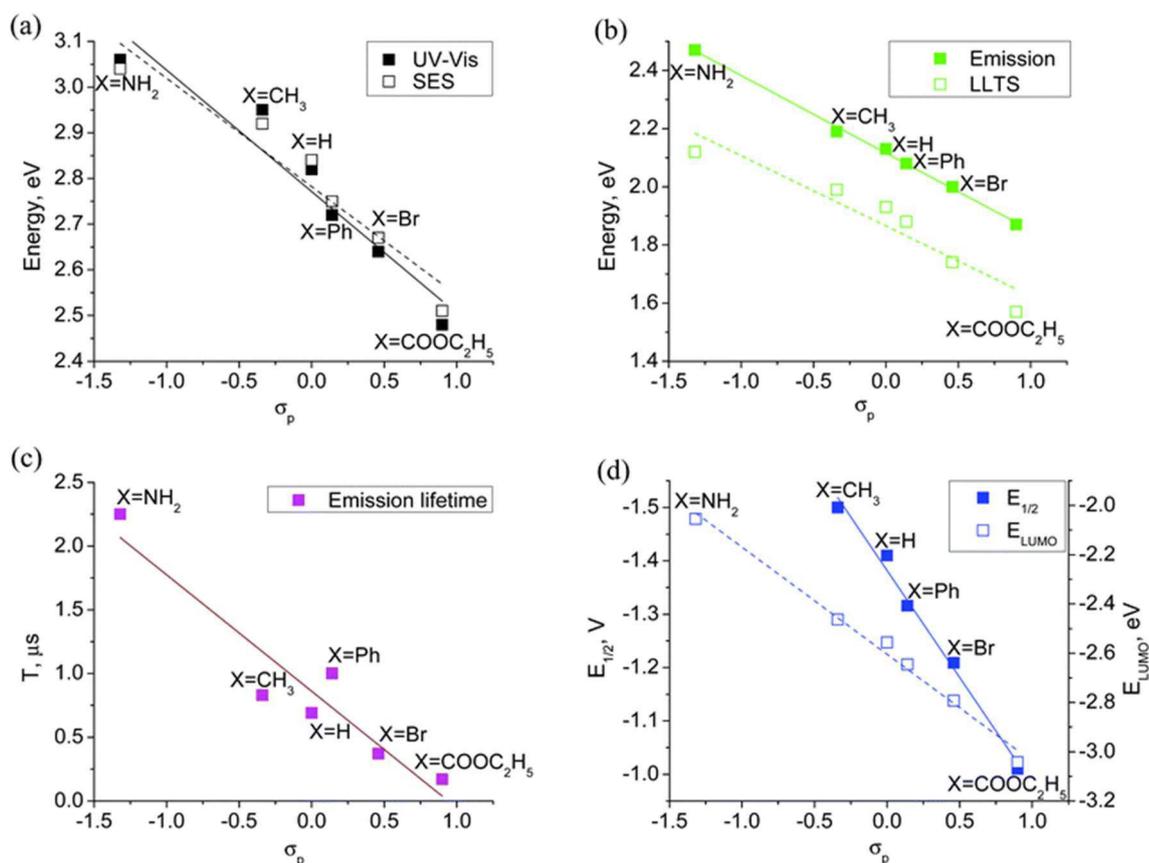
Figure 3 From the work of Rillema et al.; experimental UV-Vis absorption and calculated 1MLLCT state energies vs. σp (a), experimental emission and calculated LLTS energies vs. σp (b), experimental emission lifetime vs. σp (c), and electrochemical reduction potential E1/2red and ELUMOvs. σp(d) for the Pt(bph)(4,4'-X2bpy) complexes.[40] These are examples of the strong correlations between electronic modelling parameters and photophysical properties.

This effect was further examined in a study by Rillema et Al.[40] This study reveals the strength of using Hammett σ constants for modelling multiple properties of luminescent platinum complexes. Strong correlations of σ to ground and excited properties are made, revealing how predictable modifying the diimine and LUMO electronics can be (Figure 3). These studies only represent modification of the diimine, as it can be used to raise or lower the energy stored in the excited state. No similar comparisons have been made for the HOMO bearing ligands, which may also have an influence on the excited state behaviour of complexes.

How can predictions of which light absorbers are most effective be made?

From the last chapter, it could be seen that photosensitized hydrogen production can only take place where there is an effective and long lived charge separation. This investigation will attempt to answer the question of, "can Hammett theory be used to accurately describe the excited state behaviour of a series of cyclometalated platinum complexes?" The aims of this chapter are to synthesize a range of chromophores where the properties have been tuned by the use of substituted acetylide ligands. The ground and excited state properties of these photosensitizers have been investigated experimentally and computationally. The Hammett equation has been used to investigate the mechanisms of excited state relaxations and how predictable the photophysical properties of the complexes are, and the Hammett equation has been used to probe the mechanism of decay to the ground state.

RESULTS AND DISCUSSION

Synthesis

Cyclometalated platinum chromophores, of the type [Pt(N^N^C)X] were selected, for comparability to the dyad already described in the previous chapter. [Pt(N^N^C)X] type photosensitizers have a site available for coordination of a ligand that may be used to tune the electronic properties. The ligand classes available to achieve this include thiophenolates, isocyanides, substituted phenyls or acetylides.[33, 46-48]
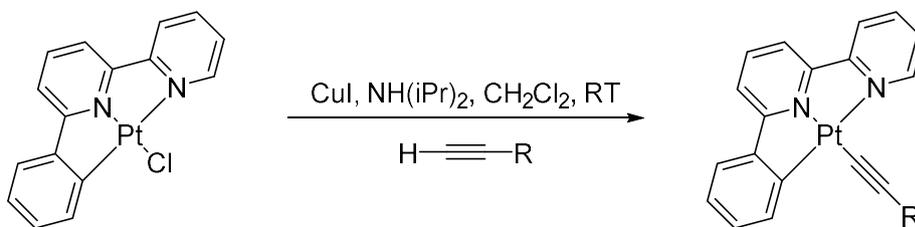
Figure 4 Generalized reaction conditions for the substitution of a chloride for an acetylide ligand. A mixture of the cyclometalated platinum chloride, copper chloride and diisopropylamine were stirred with a substituted acetylene at room temperature.

Acetylide ligands were selected in our work for their simple substitution reactions, using modified Sonogashira reaction conditions to replace the chloride (Figure 4).[49] The other reason to use these acetylides was to afford the ability to tune the electronics, through introducing substituents into phenyl group. This approach will be used in conjunction with Hammett theory to elucidate excited state decay mechanisms. A wide range of substituted phenyl acetylides are available commercially allowing simple derivatization of the cyclometalated platinum core structure. The common structure of the photosensitizers synthesized is given below (Figure 5), with the specific examples described.

The wide range of donor and acceptor substituents on the phenylacetylide cover a wide range of sigma values (Figure 5),[50] allowing a full comparison to be made between properties and donating nature. Ligands of both electron withdrawing and electron donating natures were selected for substitution onto the core complex, to allow a full examination of how the properties of these complexes react to a change in donor electronics.

The compounds above were all synthesized using the same procedure from two stock [Pt(N^N^C)Cl] complexes and the appropriate acetylene, using a copper iodide catalyst and diisopropylamine base in dichloromethane. Reactions took between 1 and 24 hours to complete, with more withdrawing acetylides, such as the bis-trifluoromethyl and nitrile bearing phenylacetylides, taking longer. Due to lack of starting material solubility, reaction progress can be determined by clarity of solution; as more soluble product forms, the suspension clarifies. Colour change occurs as electronic structure of the platinum species changes, influenced by the new donor ligand. Compounds were purified by column chromatography on silica. Compounds were characterized by ^{1}H NMR, FTIR, UV/Vis & Emission spectroscopies, mass spectrometry and X-ray crystallography.
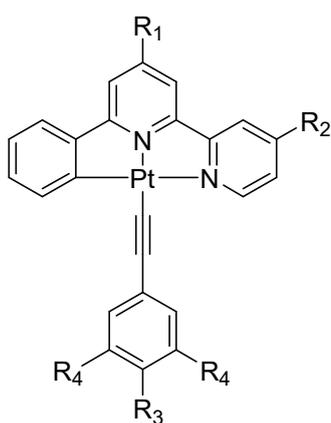
R₁ = R₂ = ᵗBu

R₁ = COOEt
R₂ = H

R₄ = H
R₃ =

1	CN
2	COOMe
3	Cl
4	H

R₃ = H
R₄ =

| 5 | CF₃ |

R₄ = H
R₃ =

6	CN
7	COOMe
8	Cl
9	F
10	H
11	Me
12	OMe
13	NH₂
14	NMe₂

R₃ = H
R₄ =

| 15 | CF₃ |

Figure 5 General structure of synthesized cyclometalated Pt(N^N^C) acetylides with substituent sites defined. σ^+ values for the substituted phenyl acetylide ligands given below. * Value represents double the σ_{meta} for CF₃, as two are present on the phenyl acetylide ligand.[50]

Complex	14	13	12	11	10	9	8	7	6	15
R₃ or R₄	NMe₂	NH₂	OMe	Me	H	F	Cl	CO₂Me	CN	CF₃
σ^+	-1.7	-1.3	-0.778	-0.311	0	-0.073	0.114	0.489	0.659	1.224*

Electrochemistry

As ligands with very different electronic demands were introduced to the complexes, cyclic voltammetry was performed to determine the energies of accessible molecular orbitals in the ground state of complexes **1 – 15**. Cyclic voltammetry was performed in a nitrogen purged dichloromethane solution of 0.1 M tetrabutylammonium hexafluorophosphate, recorded using a glassy carbon working electrode, platinum wire counter electrode and a silver/silver chloride reference electrode. Ferrocene was used as internal standard for each set of measurements. These measurements allow for an estimation of HOMO and LUMO energies, which may then be compared against similar properties calculated by DFT methods, and plotted against Hammett sigma constants for an analysis of their conformity to a simple SAR model.

Table 1 Redox potentials determined for complexes 1 – 15 by cyclic voltammetry in CH$_2$Cl$_2$ solvent with 0.1 M [NBu$_4$][PF$_6$] supporting electrolyte, the values are reproted against a Fc/Fc$^+$ reference.

COMPLEX	$E_{RED}^{1/2}$ / V	E_{OX}^{PA} / V
1	-1.89	0.49, 0.83
2	-1.89	0.45, 0.78
3	-1.91	0.39, 0.72
4	-1.91	0.35, 0.73
5	-1.88	0.59, 0.90
6	-1.57	0.19, 0.53, 0.91
7	-1.57	0.18, 0.46, 0.84
8	-1.59	0.13, 0.42, 0.84
9	-1.60	0.12, 0.39, 0.82
10	-1.60	0.09, 0.36, 0.75
11	-1.60	0.13, 0.36, 0.91
12	-1.60	0.03, 0.26, 0.88
13	-1.61	0.00, 0.19
14	-1.62	-0.08, 0.03, 0.78
15	-1.56	0.31, 0.56, 0.94

The 15 cyclometalated complexes all possess an electrochemically reversible one electron first reduction process between -1.56 and -1.91 V vs. Fc/Fc+, attributable to the bpy/bpy⁻ reduction.[45, 51] These values are typical of platinum (II) N^N^C complexes. Complexes **1 - 5** all feature more negative first reduction potentials (-1.91 V - -1.88 V) than complexes **6 – 15** (-1.62 V - -1.58 V). This is indicative of the donating butyl groups stabilising the LUMO by induction, where the MO is located on the bipyridine moiety, with values similar to those seen in platinum bipyridyl acetylide complexes in the literature.[16, 19, 28, 32-33, 39-40, 45, 47, 49, 51-53] Modifying the donor group has little effect on the reduction potential of the complex; for the entire range of ester bearing complexes there is only a 60 mV change and in the butyl bearing complexes there is only a 30 mV change. This is less than the separation of anodic and cathodic peak potentials for the reduction processes in question and is therefore considered a negligible shift in reduction potential for each set of complexes. Therefore, it can be inferred that electron density in the orbitals of the phenyl acetylene ligand do not interfere strongly with the electronics of the bipyridine moiety of the N^N^C ligand.

Cyclic voltammograms of **6 – 15** each feature 3 irreversible oxidation processes, except **13**, which has two. In each, the first oxidation process occurs in the range between -0.08 and 0.31 V, the second between 0.03 and 0.56 V and the third between 0.75 and 0.94 V (Table 1). The first and second oxidation processes are assigned to phenyl acetylide ligand localized oxidations whilst

the third oxidation is assigned to oxidation of the phenyl moiety of the N^N^C ligand. These assignments are supported by DFT modelling. The presence of three different close lying oxidations from two different structural locations of the complex suggest that any charge transfer behaviour the complexes possess will be complex.

The cyclic voltammetry of complexes **1** –**5** features two irreversible reduction potentials for all cases. The first oxidation potential ranges between 0.35 and 0.59 V and the second between 0.73 and 0.90 V (Table 1). The second oxidation process is assigned to an acetylide localized oxidation, whilst the first oxidation is assigned to oxidation of the phenyl moiety of the N^N^C ligand. The oxidations seen in these complexes are more clearly separated and defined than in complexes **6** – **15** and therefore can be expected to display more straightforward charge transfer behaviour (CV traces located in Annex B).

As excited state properties and charge transfer behaviours are quite often strongly associated with the redox potentials of a complex, by applying Hammett theory to the complexes electrochemical potentials and searching for conformity to the model, it may be possible to determine and predict ground and excited state photophysical behaviours.

Correlation between electrochemical potentials and Hammett parameters for substituents R in reduction and oxidation potentials

Energy Gap (Ered-Eox) vs. Hammett parameters for R-substituents on the acetylide ligand

For comparison to Hammett plots of absorption energies, plots of σ^+ against the series of energy gaps derived from electrochemistry were made. Although strong correlations can be seen for the energy gaps associated with the two least positive oxidation potentials, there is not a strong correlation with the redox gap from the most positive series of oxidation potentials. This can be seen for the narrowest two redox energy gaps, which display a positive correlation when the energy gap is plotted against sigma constant (Figure 6).
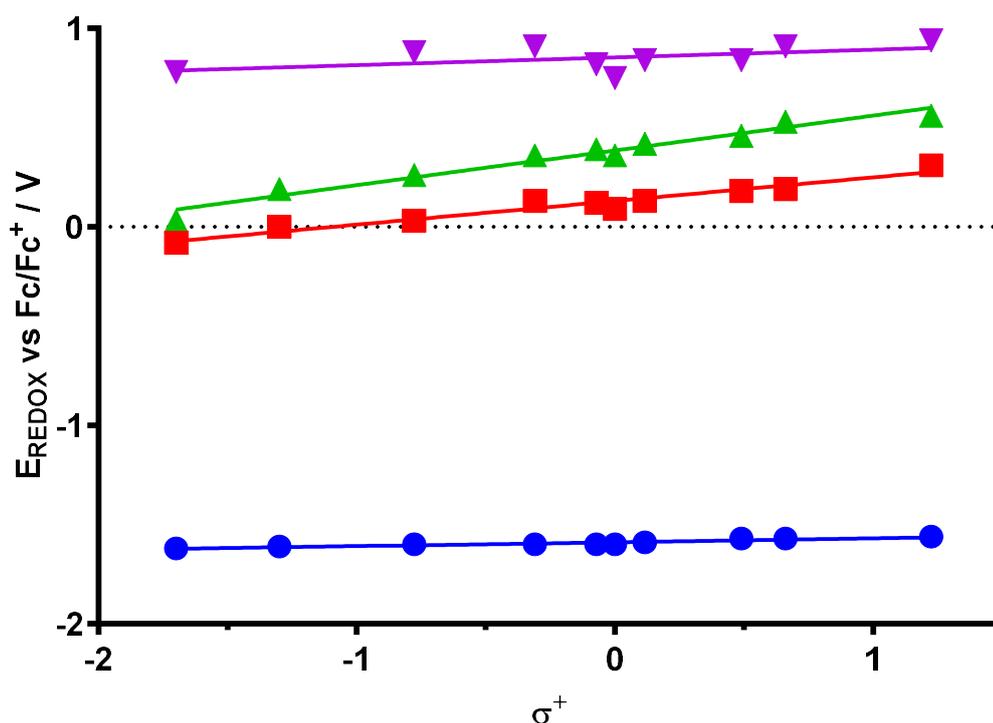
Figure 6 Plot of Redox potentials from CV experiments against Hammett σ^+ constant for the complexes 6 - 15. 1st reduction (blue circles, gradient = 0.02, r^2 = 0.87), 1st oxidation (red squares, gradient = 0.12, , r^2 = 0.95) and 2nd oxidation (green triangles, gradient = 0.18, r^2 = 0.96) show strong correlation between σ^+ and redox potential. 3rd oxidation (purple v, gradient = 0.04, r^2 = 0.27) does not.

These correlations reveal that for redox reactions associated with the phenyl acetylide moiety of the complexes, which involve the two less positive oxidation potentials, there is strong correlation to the electron withdrawing or donating nature of the R substituent. For the redox potentials associated with distant moieties this is less the case. This strengthens the assignments made for the oxidation potentials, as a redox process with little, or no, involvement from the phenyl acetylide will show little dependence on the electron demand of the determining R group. Additionally, it can be seen that one of the redox potential series is affected more by the presence of the interfering R group than the other, suggesting a greater involvement of the R group in the molecular orbitals associated with the oxidation. This will be further investigated using visualization of the calculated MOs from DFT modelling.

Oxidation Potentials

A closer look at the oxidation potentials confirms the observations made above. A plot of oxidation potentials for complexes **6 - 15** against σ^+ reveals the significant affect donor

substituents have on the first and second oxidation potentials (Figure 6). There is no correlation with the third oxidation potential. This effect is reflected in the gradient of the line fitted per σ^+ unit. The smaller effect in the first oxidation potential could be indicative of a mixing of character between the more stable, planar contribution from the acetylide and N^N^C ligand oxidations. The equations derived from these plots could be used to predict how the HOMO energies will be affected by acetylide donors. The fitted line does not stay within the measurement error of ±10 mV for the oxidation potentials measured by cyclic voltammetry; this greater variance despite strong correlation indicates that contribution from some other effects. The value of the third oxidation potential cannot be correlated with Hammett constants of the substituents. It is likely that this oxidation is localised on the N^N^C ligand and unrelated to the substituted R groups.
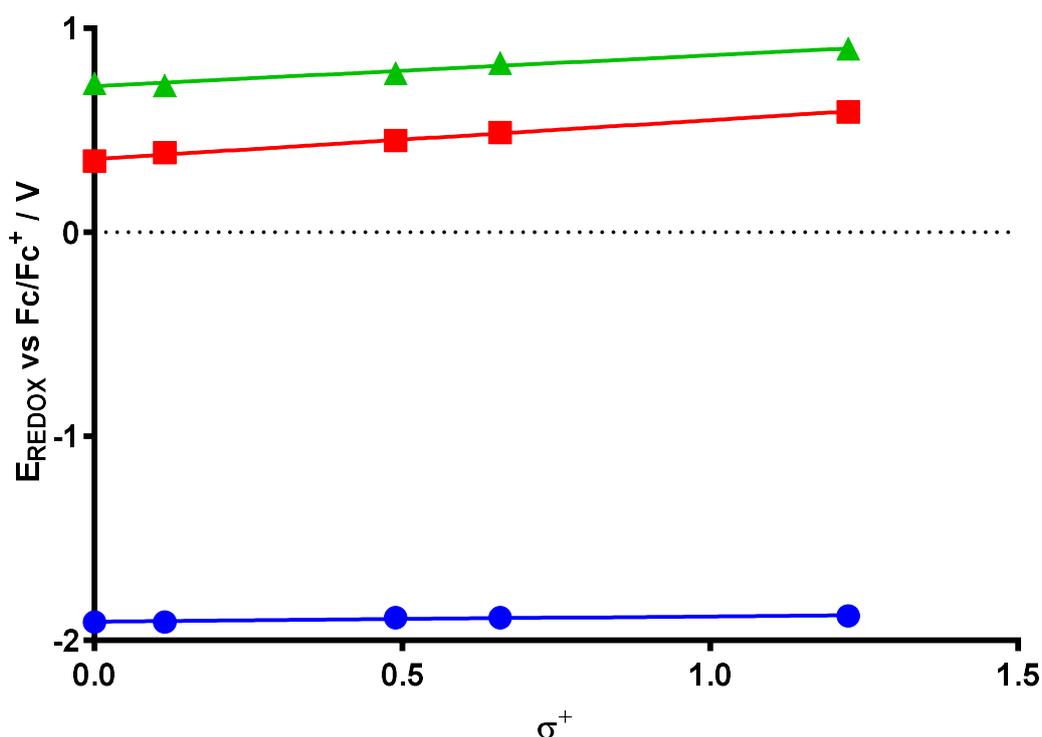
Figure 7 Plot of Redox potentials from CV experiments against Hammett σ^+ constant for the complexes 1 - 5. 1st reduction (blue circles, gradient = 0.03, r^2 = 0.91), 1st oxidation (red squares, gradient = 0.19, r^2 = 0.99) and 2nd oxidation (green triangles, gradient = 0.15, r^2 = 0.97) show strong correlation between σ^+ and redox potential.

A plot of oxidation potentials for complexes **1 – 5** against σ+ reveals the significant affect donor substituents have on the reduction potentials. This effect is consistent across both sets of oxidation potentials with a smaller effect in the more positive oxidation potential for each, reflected in the gradient of the line fitted per σ^+ unit. This smaller effect in the upper oxidation potential could be indicative of a mixing of character between the acetylide and phenyl bipyridine ligand oxidations. The equations derived from these plots could be used for predictions on the behaviour of HOMO energies where affected by acetylide donors as the prediction stays within the measurement error of ±10 mV for the oxidation potentials measured by cyclic voltammetry.

Reduction potentials

A plot of σ^+ against the first reduction potential for both sets of complexes reveals the small affect donor substituents have on the reduction potentials. There is only a 20 mV change in reduction per σ^+ unit for the ester compounds, **6 – 15**, and a 26 mV change per σ^+ unit for the ^{t}Bu compounds, **1 – 5**. This indicates how changing the acetylide has very little effect in tuning

LUMO levels, decoupling effects on the HOMO, and confirms that modification of donor ligands can be used for enhanced fine tuning of photosensitive complex electronics.

DFT calculations

Prediction of electronic energy levels can be performed using density functional theory modelling techniques. This allows comparison of modelled and measured energy levels, although it should be noted that neither DFT modelled energy levels nor redox potentials from electrochemical techniques are fully representative of excited electronic states. However, DFT calculated orbital energies and electron densities can be used to investigate processes not adequately described by ground state methods. For example, although CV can give the relative energy required to oxidise or reduce a species, this is not always expressive of the relative energies of the orbitals involved in electronic transitions after absorbing a photon, due to the presence of hot excited states. Comparing these two techniques can strengthen analysis of excited state behaviour with respect to the series of complex's electronics.

Density Functional Theory (DFT) and Time-Dependent DFT (TD-DFT) calculations were performed using the Gaussian 09 software suite, revision D.01.[54] In all calculations the exchange-correlation functional B3LYP was used.[55-56] Dunning's correlation consistent basis set of triple-ζ quality (cc-pVTZ) was used for all atoms, specifically the valence set with relativistic pseudopotential (-PP) variant for platinum[57] and all-electron basis sets for other elements.[58-59] Dichloromethane solvent was included implicitly using the Integral Equation Formalism of the Polarizable Continuum Method (IEFPCM), as implemented in Gaussian.[52, 60-61] An 'ultrafine' integral grid, as defined by Gaussian, was utilised in all calculations. Geometries were optimised and confirmed as minima by vibrational frequency analysis.

Comparing calculated MO energies to Redox energies
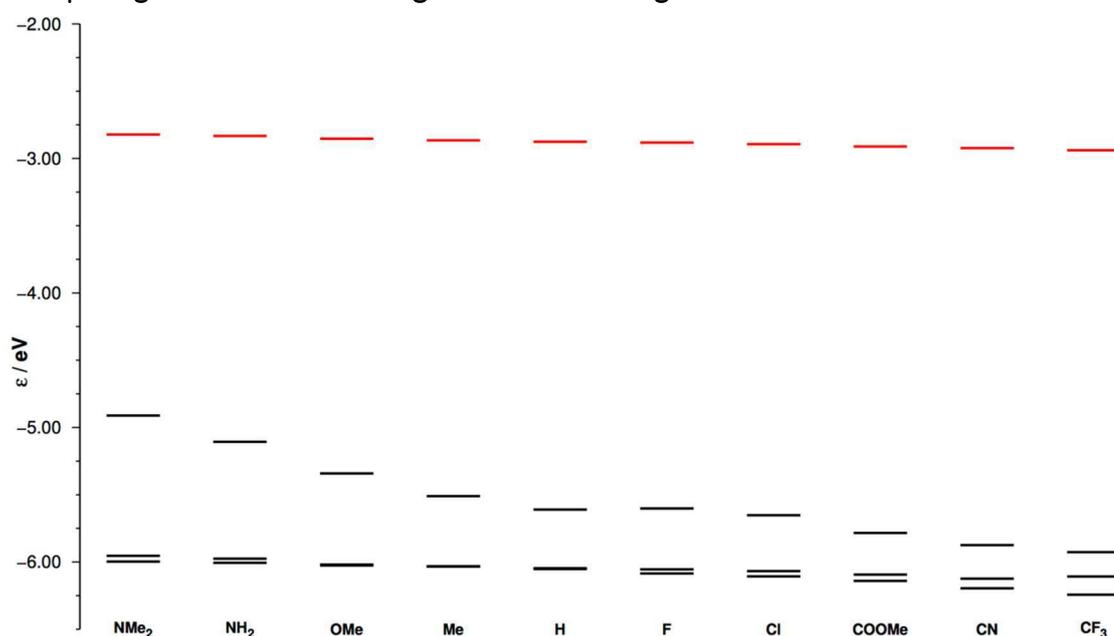
Figure 8 MO energy levels calculated by DFT methods for complexes 6 – 15. LUMO energy levels are given in red, HOMO energy levels are given in black. Complexes 6 – 15 are labelled by their R group.

For the ester complexes **6 – 15**, LUMO energies are largely unaffected by donor potential, (Figure 8) consistent with the oxidation potentials recorded in cyclic voltammetry. The HOMO energies, however, can be seen to diverge from the HOMO-1 and HOMO-2 energies as more donating phenyl acetylides are ligated. Visualizations of MOs (Table 2) show that;

- The HOMO is located mostly over the phenyl acetylide and substituent with some Pt d character and phenyl acetylide R group character.
- HOMO-1 and HOMO-2 contain no significant electron density on the 4-substituent or benzene ring of the phenyl acetylide.

As orbitals HOMO-1 and HOMO-2 have effectively no influence from the non-innocent R groups of the phenyl acetylide ligand, they experience less of a shift as more electron donating R groups are substituted onto the phenyl acetylide. This contrasts with the electrochemical behaviour of the series where both the series of first and second oxidations diverge from the third series, representing the oxidations associated with the phenyl acetylide moiety diverging from the oxidation associated with the N^N^C phenyl moiety.

HOMO-1 and HOMO-2 also experience a change in character across the series; as the lowest energy of the two switches from an MO concentrated on the acetylide to N^N^C benzene ring, as the R group becomes more electron withdrawing. HOMO-1 has mostly acetylide π character in complexes with more donating phenyl acetylides, and mostly N^N^C phenyl π character in complexes with more withdrawing phenyl acetylides. This is consistent with observations of electronic transitions by spectroscopic methods, discussed later, where complexes with the largest divergence show the largest separation of absorption bands.
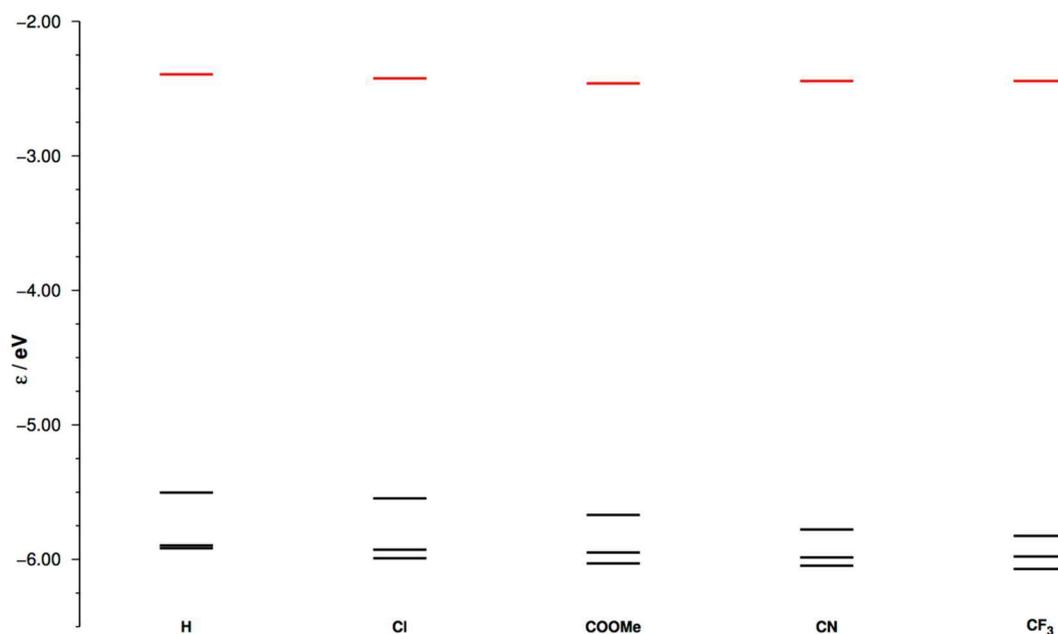
Figure 9 MO energy levels calculated by DFT methods for complexes 1 – 5. LUMO energy levels are given in red, HOMO energy levels are given in black. Complexes 1 – 5 are labelled by their R group.

Butyl complexes **1 – 5** only have two observable oxidation potentials, measured by CV and within the solvent window, contrasting the 3 close lying HOMOs calculated by DFT (Figure 9). The DFT calculated HOMOs and the LUMOs mirror the behaviour of the ester HOMOs and LUMOs closely, so this may be due to two isoenergetic oxidation states appearing as one in the cyclic voltammetry. Despite the similarities of the two species' number of calculated HOMO signatures (3), only the ester bearing complexes display three separated oxidation potentials by cyclic voltammetry. The butyl bearing complexes display only two oxidations but this may be due to isoenergetic oxidations associated with the phenyl acetylide MOs. The beginning of a divergence, similar to that seen in complexes **6 – 15**, can be seen in DFT calculated energy levels. As only the start of a divergence can be seen, it is impossible to infer that there may be a crossing of energy levels with different character in these complexes and any anomalous effects are unlikely to be seen.

Use of DFT to characterize MOs

Character of MOs can be visualised by DFT, revealing where likely charge movement stem from and go to. Optimised structures of modelled compounds were based on crystal structure data for complexes **8** (Figure 10) and **14** (Annex B). Calculated MO representations are in Annex B. Examination of electron density maps for the HOMOs and LUMOs of optimised structures can reveal how electron density is redistributed when transitions between different excited states take place. In all complexes, **1** − **15**, the first LUMO calculated is characterised by a significant portion of the electron density residing in the π* orbitals of the bipy moiety. This is where excited state energy will move back from, to reach the ground state.

Table 2 Singlet LUMO, HOMO, HOMO-1 and HOMO-2 MOs for complexes 6, 11 and 14 visualizing electron density. Further MOs for complexes in this chapter in Annex B
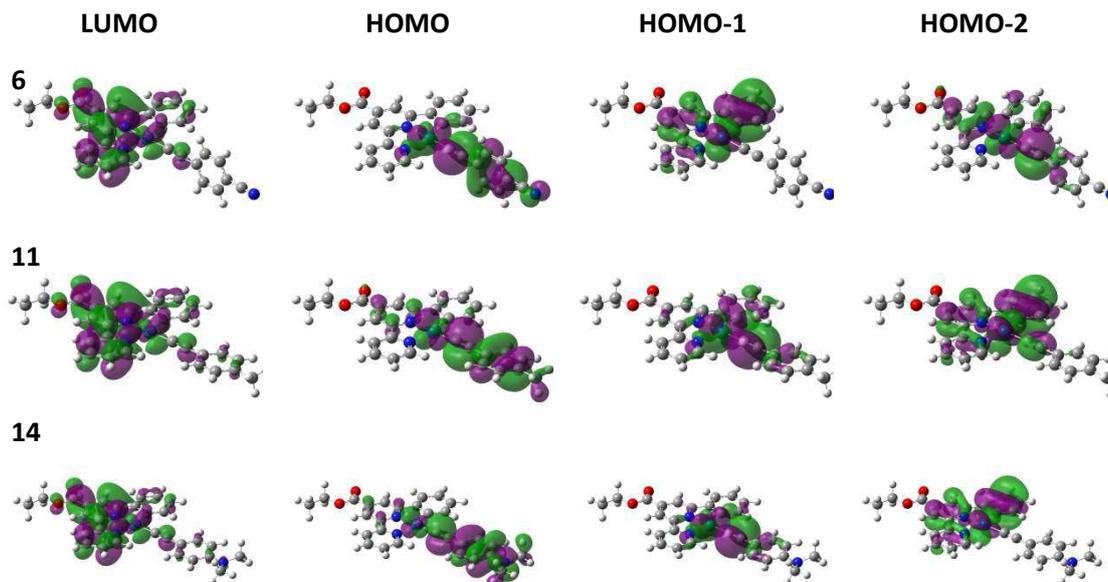
The HOMO in all cases is located in the phenyl acetylide π orbital systems incorporating substituent orbitals. The character of each MO is not identical in all cases however. All of the butyl complexes display strong anti-planarity of the phenyl acetylide to the N^N^C ligand, but the ester complexes have planar phenyl acetylide ligands. Due to the nature of alkynyl bonds and the highly conjugated structure of the system, these ligands will not rotate, fixing the structures in either a planar or anti-planar configuration. As alkynyl bonds have two sets of π bonding orbitals which are orthogonal to each, one of the two occupied MO contributions exists in plane with the bipy while the other is not. Being in plane with bipy increases orbital overlap and therefore will enhance relaxation rates. This may explain the highly emissive states of the butyl complexes, where the HOMO is out of plane with the bipy, compared to the ester complexes, where the HOMO is in plane with bipy for these weak emissive complexes.

In both sets of complexes cases there are isoenergetic states for some complexes. HOMO-1 and HOMO-2 are effectively isoenergetic for complexes, **4** and **9** − **12**. As the redox energy gap of the lowest excited state for the ester complexes is not large enough to account for the emission energies, emission must be from one or both of these isoenergetic states. If these states interact then enhanced non-radiative rates can be expected as more non-radiative pathways to the ground state are available. This has implications for the mechanism of excited state decay as further discussed, with the use of the Hammett equation, below.
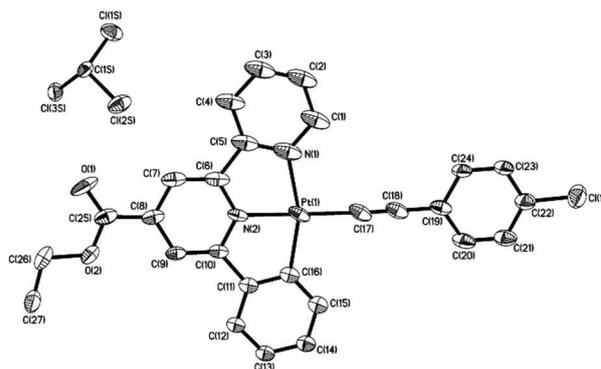
Figure 10 Ellipsoid plot of solved structure for complex 8 with ellipsodis at 50% thermal probability.

UV/Vis spectroscopy

Electronic absorption spectra for compounds **6 – 15** were recorded in CH$_2$Cl$_2$ at 298K between 230 and 700 nm (Figure 11a&b). These compounds display low energy transition bands between 400 and 720 nm, which are mixed metal ligand to ligand charge transfer (MMLL'CT) in nature,[33] consistent with behaviour seen in the butyl N^N^C complexes below and similar published complexes. The highly conjugated nitrile complex, **6**, has much higher intensity absorptions in MMLL'CT region. The ester bearing complex, **7**, does not display this behaviour despite also allowing resonance stabilisation of the phenyl acetylide, suggesting a relatively lower state of overall conjugation than **6**. There is a systematic red shift of bands at low energy that occurs in the presence of more donating phenyl acetylides, which will be examined further using Hammett theory.

The bands observed between 300 and 400 nm are ILCT in nature, primarily localised on the phenyl bipyridine ligand, evidenced by the negligible shift in band position with different donor acetylides. The intensity of bands at 310 nm in the two more conjugated complexes, **6** and **7**, suggest an ILCT state located within the conjugated phenyl acetylide in each.

Electronic absorption spectra for compounds **1 – 5** were recorded in CH$_2$Cl$_2$ at 298K between 230 and 700 nm (Figure 11c). These compounds display low energy transition bands between 400 and 550 nm, which are mixed metal ligand to ligand charge transfer (MMLL'CT) in nature.[33,46] More conjugated compounds, such as the ester phenyl acetylide, **2**, and nitrile phenyl acetylide, **1**, have greater intensity absorptions in MMLL'CT region whilst the bis CF$_3$ phenyl acetylide, **5**, is less intense, reflecting how highly conjugated systems absorb more strongly. There is a systematic red shifting of bands at low energy that occurs in the presence of more donating phenylacetylides, in the order **4** > **3** > **2** > **1** > **5**, where **4** is most red shifted and **5** is least red shifted. These transitions occur at much higher energy than for ester bearing complexes, consistent with the wider band gap seen in the redox differences seen in cyclic voltammetry data.

Bands observed between 300 and 400 nm are ILCT in nature, mainly localised on the phenyl bipyridine moiety. This is evidenced by the negligible shift in band position when different donor acetylides are ligated. The intensity and asymmetry of bands at 320 nm in the two more conjugated complexes, **1** and **2**, suggest an ILCT state located on the conjugated phenyl acetylide in each, adding constructively to the underlying absorption bands.
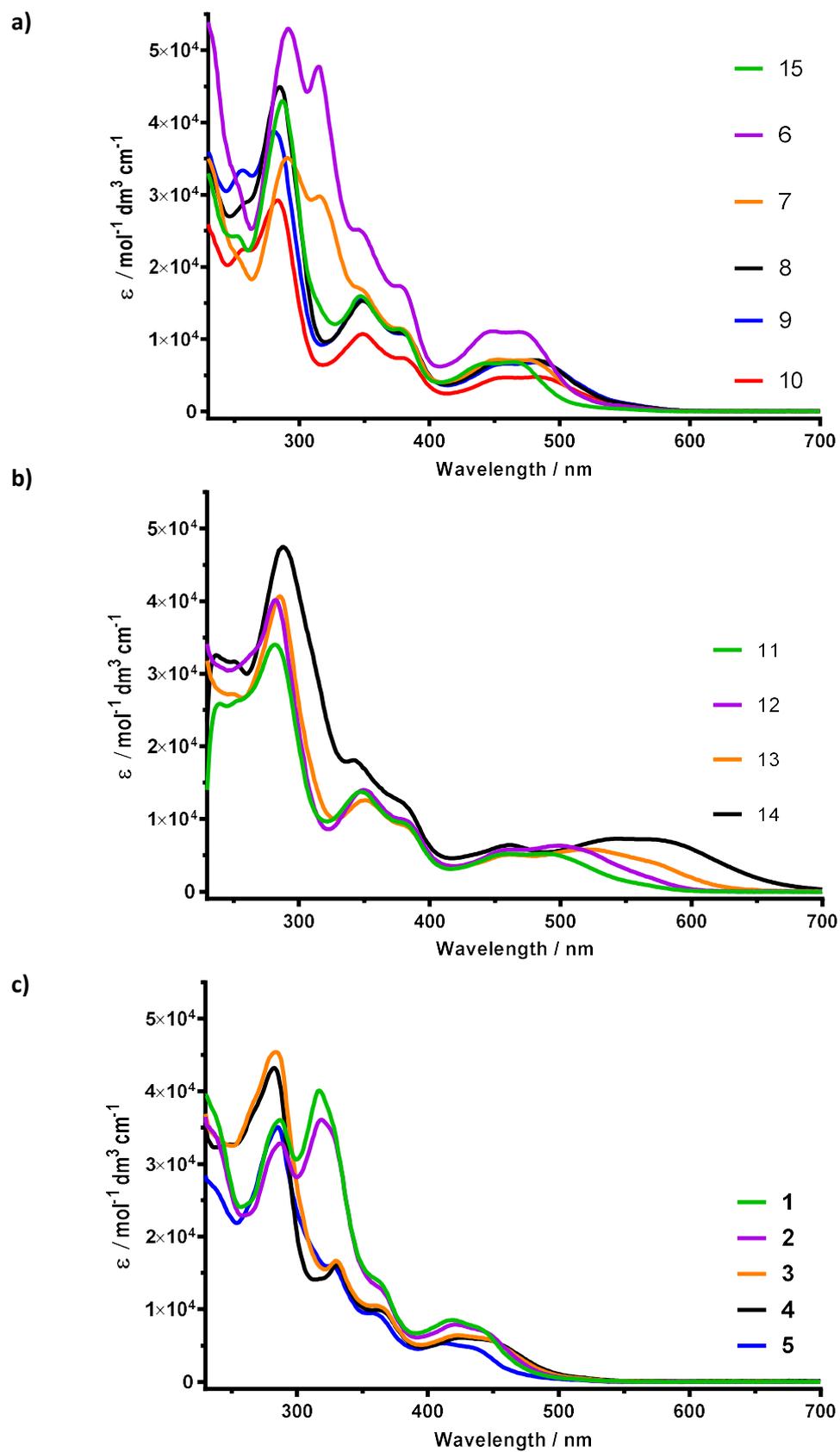
Figure 11 UV/vis electronic absorption spectra recorded for complexes 1 – 15 in dichloromethane between 230 and 700 nm. Data plotted with molar extinction coefficient on the y axis for comparison.

Solvatochromism of the absorption spectra

Three of the ester complexes display well separated transitions in UV/vis spectra. These three compounds, **12**, **13**, **14**, have been used to investigate the charge transfer nature of the electronic transitions using solvatochromism. Complexes were dissolved in five solvents; toluene, tetrahydrofuran, dichloromethane, acetonitrile and methanol, and absorption spectra were recorded for the 400 – 800 nm window (Figure 12). All three compounds display a shift in absorption bands in different solvents indicating these have charge transfer character. Three absorption bands are apparent in **13** and **14** while complex **12** displays 2. This colour change is exemplified by the change from pink to yellow for **12** in solvents ranging in polarity between toluene and methanol.

Plotting energy of transitions against solvent polarity parameter Z gives positive linear relationships indicative of negative solvatochromsism. Negative solvatochromism is observed in compounds with a highly polar ground state that exhibits a loss in, or reversal of the dipole moment in the exited state. This behaviour is consistent with other Pt N^N^C complexes and also observed in other Pt diimines.[33, 45, 53]

Table 3 Solvatochromic shift values of the complexes, 12, 13, 14 for the lowest energy, visible light transitions, where CT1 is the lowest energy transition, CT2 the next lowest and CT3 is the highest energy transition.

	Solvatochromic Shift / eV^{-1}			Z scale Solvatochromic Shift / cm^{-1}		
Compound	CT1	CT2	CT3	CT1	CT2	CT3
12	0.21	0.23		80	91	
13	0.21	0.34	0.32	57	101	109
14	0.25	0.2	0.28	63	83	106

Plotting transition energy against Z and Eisenberg solvent polarity scales can quantify the strength of a dipole change, allowing comparison between absorption bands and other complexes featuring charge transfer transitions (Table 3).[46] A comparison of the values shows that the lowest energy absorption band displays the largest change in dipole while the highest energy visible light absorption shows the least. This allows transitions to be separated using less polar solvents and supports the MO transitions suggested by DFT modelling. The gradient of this relationship can reveal the strength of dipole transitions, indicating how much charge is transferred or the nature of the excited state.

Plotting the transition energies against the solvent polarity coefficient described by Eisenberg gives strong correlations for each transition in each complex examined. The gradient of these linear correlations gives a solvatochromic shift of 0.20 – 0.34 eV^{-1} for each case. This is very comparable to values for cyclometalated platinum thiolates and unbridged dithiolate platinum diimines, which have values of 0.18 – 0.20 eV^{-1} and about 0.35 eV^{-1},[46, 53] respectively, which display strong charge transfer behaviour. These values are all lower than those for the bridged dithiolate diimine complexes, which have solvatochromic shift values greater than 0.40 eV^{-1}.[45] The solvatochromic shift is higher for transitions related to the acetylide π to bipy π* charge transfer. Furthermore, the NH$_2$ bearing complex, which can participate in hydrogen bonding, has the highest solvatochromic shift values, indicating that the electron demand of the phenyl acetylide ligand has a strong effect on charge transfer transitions. Although the values of solvatochromic shift for the complexes presented are indicative of a charge transfer, however the change in dipole at the transition is less pronounced than in bridged dithiolate platinum diimines.
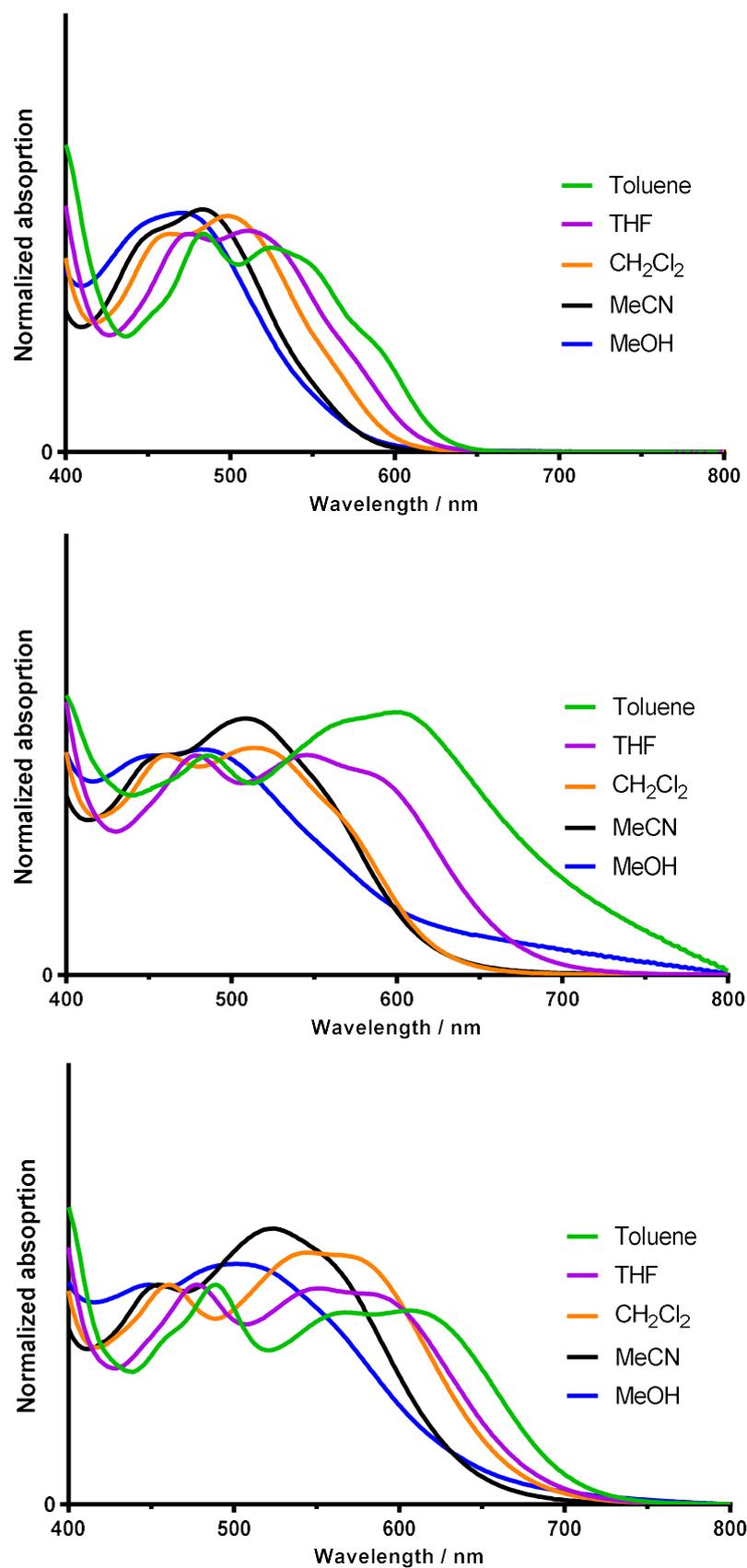
Figure 12 Solvatochromism studies for complexes 12 (top), 13 (middle), 14 (bottom) in five solvents: toluene, THF, CH$_2$Cl$_2$, MeCN and MeOH. Spectra in the visible region have been normalized to the highest energy absorption for comparison.

Electronic Absorption Maxima and their correlation with Hammett Parameters

The consistency of electronic levels within a Hammett equation model suggest that the UV/vis absorptions of electronic spectroscopy should also be able to be modelled using the Hammett equation. However, plotting σ^+ against ^{1}MMLL'CT absorption energy in wavenumbers for complexes **6 – 15** reveals a complicated relationship between R group electron demand and transition energy (Figure 13).
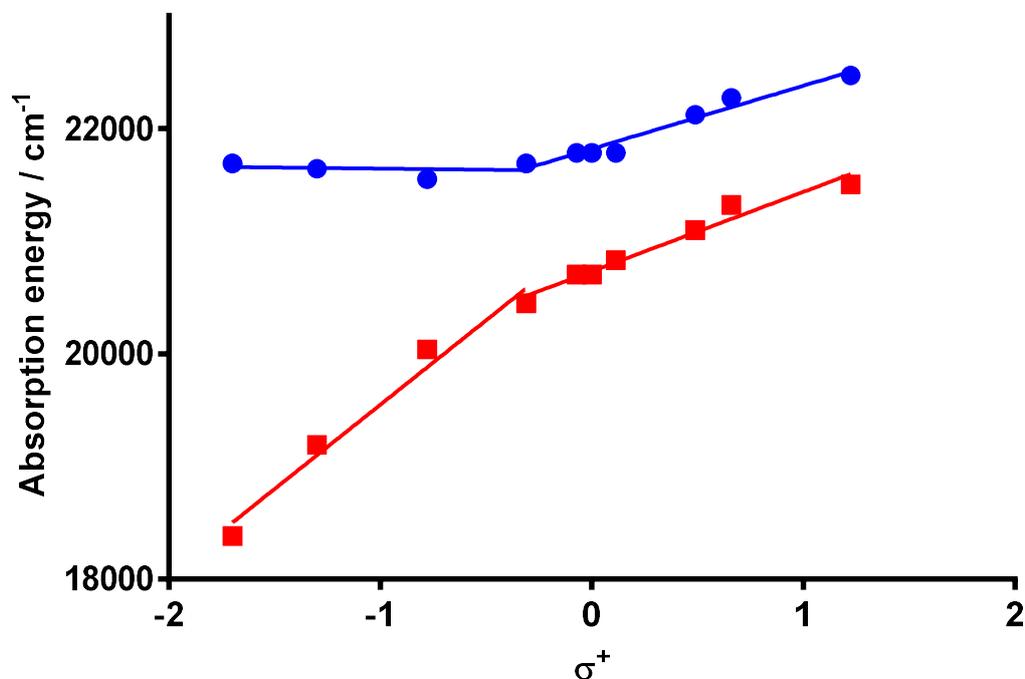
Figure 13 Electronic absorption transition energies for 6 - 15 plotted against σ^+ with two straight line fits for each transition. Each straight line fit represents a different regime, where the electronics of the phenyl acetylide affect the electronic transitions to varying degrees.

Above σ^+ values of 0, there are two slopes of approximately of around 600 cm^{-1}, this implies there is an effect on absorption energies propagated by a change in the donor potential of the acetylide. Correlation with DFT singlet LUMO and HOMO to HOMO-2 MOs suggest these two transitions are a combination of charge transfer from both phenyl acetylide and N^N^C phenyl moiety to bipy. At σ^+ values less than 0, a different behaviour dominates; the two absorptions diverge, the low energy MLCT absorption shows a greater reliance upon donor potential than the high energy absorption. The high energy transition now has effectively zero gradient, whilst the low energy absorption has a slope double that seen at positive σ^+. This is indicative of a breakdown in the mixed behaviour of the absorptions into more discrete transitions, unaffected by each other. The behaviour is suggestive of one transition that is unaffected by the electronic properties of the phenyl acetylide R group at low σ^+ values, and another transition that is more affected by the R group moving from positive to negative σ^+ values, similar to how the oxidations associated with the N^N^C phenyl moiety were unaffected by phenyl acetylide electrophilicity in contrast to the phenyl acetylide ligand oxidations.

This behaviour demonstrates that the two charge transfer transitions are decoupled when more donating phenyl acetylides, characterized by low σ^+ values, increase the energy gap between the two electronically excited states; this produces a higher energy absorption barely affected by substitutions on the phenyl acetylide and a lower energy absorption directly affected by the substitutions on the phenyl acetylide substituent. This behaviour is supported by the diverging energy gaps predicted by electrochemical methods; more donating phenyl acetylides also

display a diverging set of two lower and one higher band gaps, from oxidation and reduction process values.

The effect also reveals itself in solvatochromic effects in complexes **12**, **13**, **14.** Larger solvatochromic shifts are evident in the lower energy, phenyl acetylide associated ^{1}MMLL'CT absorptions, as these have a greater level of charge separation associated with them than the N^N^C localized, higher energy ^{1}MMLL'CT transition. This behaviour is noticeable in complexes **12**, **13** and **14**, as the transitions have been separated and the more polar excited state shows greater dependence on the electron density demand of the phenyl acetylide.

Plotting ^{1}MMLL'CT absorption energy against σ^+ in wavenumbers for complexes **1 − 5** also produces a linear relationship. Gradient values of around 600 cm^{-1} imply there is an effect on absorption energies propagated by a change in the donor potential of the acetylide. Correlation with DFT singlet LUMO and HOMO to HOMO-2 MOs suggest these two transitions are a combination of charge transfer from both phenyl acetylide and N^N^C phenyl moiety to bipy. Considering this information regarding the transitions, a gradient of around 600 cm^{-1} could be considered indicative of a mixed transition including strong and weak charge transfer character. This is consistent with behaviour for ester bearing N^N^C complexes where $\sigma^+ > 0$, as seen above.

Emission spectroscopy

Emission spectra for compounds **6 – 15** were recorded in degassed CH_2Cl_2 solution at 298 K (Figure 14b&c). Compounds were excited at 455 nm in the MMLL'CT bands observed in electronic absorption spectra. All 9 complexes display a broad featureless emission between 500 and 800 nm, with emission maxima between 594 and 644 nm; a 1306 cm^{-1} energy difference, and quantum yields between 0.002 and 0.13. The emissive states have lifetimes of between 63 and 710 ns. There is a red shift of emission maxima with the increase in the electron donating ability of the acetylide ligand for **6 – 11** and **15**.

An extreme red shift and broadening of the emission band is observed for the tolylacetylide complex, **11**, (Table 1). The trend is reversed for the next three compounds in the series, **12 – 14**, with an extreme blue shift from **11** to **12** (863 cm^{-1}) and a smaller shift from **12** to **14** (218 cm^{-1}). For the complexes, **6 – 15** the energy gap law is not conserved, however there is a loose correlation between emission energy maxima and $ln(k_{nr})$. These compounds display a wide range of quantum yields and lifetimes (Table 5), suggesting non-consistent radiative excited states across the complexes studied, and hence more than one mechanism of non-radiative deactivation.

Table 4 Emissive properties of complexes 6 – 15, including both λMAX of emission and the the full width at half maximum in wavenumbers.

Complex	λMAX / cm^{-1}	FWHM / cm^{-1}
15	16800	2140
6	16700	2120
7	16600	2200
8	16300	2430
9	16000	2500
10	16100	2500
11	15500	2890
12	16400	2400
13	16500	2400
14	16600	2400

Emission spectra for compounds **1 – 5** were recorded in degassed CH_2Cl_2 solution at 298 K. Compounds were excited in the MMLL'CT bands at the wavelengths identified by electronic absorption spectroscopy (Figure 14a). All 5 complexes display a broad featureless emission between 500 and 750 nm, with emission maxima between 552 and 572 nm; a 633 cm^{-1} energy difference and quantum yields between 0.18 and 0.27. The emissive states have lifetimes of between 630 and 720 ns. There is a red shift of emission maxima with the increase in donating ability of the acetylide ligand. The energy gap law is observed in the case of all the compounds except for the bis-CF_3 acetylide complex, **5**. This compound has an anomalously high rate of non-radiative deactivation for the energy of the emissive state, likely related to additional deactivation channels, due to vibrational deactivation through the trifluoromethyl groups.
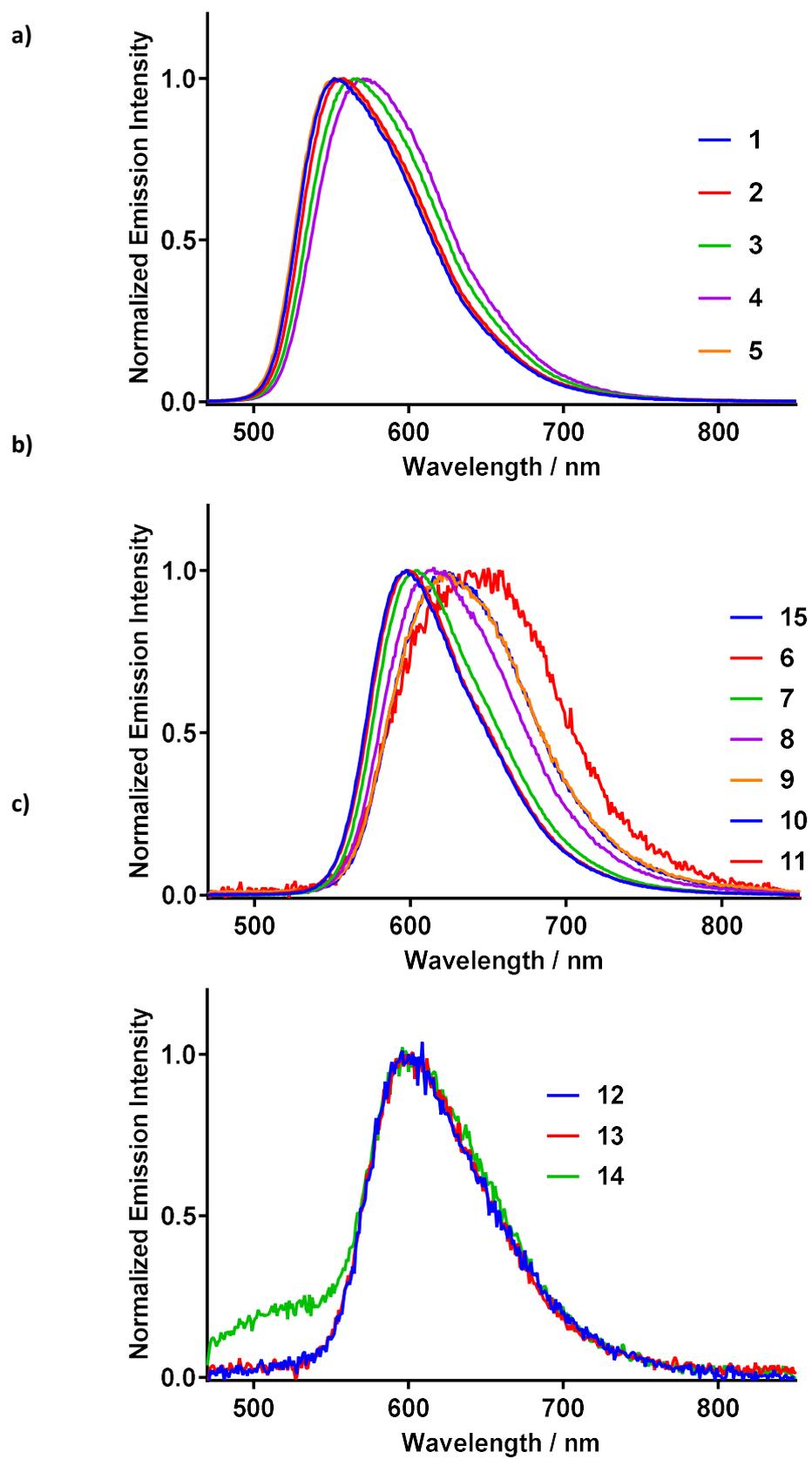
Figure 14 Emission spectra recorded for complexes 1 - 15 in deaerated CH_2Cl_2.

Application of Hammett Theory to Emission spectroscopy

The ground state properties of complexes **6** – **15** are well modelled by the Hammett SAR, with strong correlations between the electronics of the phenyl acetylide ligand and ground state properties. This predictability is not seen in the excited state, where more complex comparisons show that excited state behaviour cannot be modelled so easily.

Figure 15a is a plot of emission energy in wavenumbers against σ^+, allowing comparison of the energy gap between excited state and ground state against influencing electronic factors. The plot shows that emission energy is at a minimum for complex **11**, with σ^+ value of -0.311. Emission energy increase with both increasing and decreasing σ^+ values centred around -0.311. In comparison to electronic transition energies seen above in Figure 13, emission energy reaches a minimum, similar in behaviour to the higher energy visible light transition and shows two regimes in relation to σ^+. This is not comparable to the lower energy transition in Figure 13, which continues to decrease with decreasing σ^+. This shows that excited state energy is not as modellable as ground state properties, which have been shown to follow behaviours expected in a simple SAR model.

This behaviour is also seen in a plot of emission lifetime against σ^+, which can be used to assess how electronic factors affect the rate of radiative relaxation. Again, there is minimum emission lifetime coincident with a σ^+ value of -0.311, with increasing emissive lifetimes either side of this value. There is a strong correlation of emission lifetime to σ^+ value within the constraints of -0.5 > σ^+ > 0.5. This behaviour demonstrates how the electronics of a ligand not directly involved in the emissive state nonetheless has an effect on radiative decay processes, and indicates the possibility of a more complex pathway to the ground state, where several close lying electronic excited states are present.

This correlation of an excited state property to σ^+ for intermediate values, where -0.5 < σ^+ < 1.0, is also seen in a plot of quantum yield of emission against σ^+. In this plot, at increasing σ^+ values, greater than -0.3, there is an increase in quantum yield that reaches a maximum before σ^+ = 1.0. This behaviour indicates that the electronics of the ligand that is not directly participating in the emissive excited state influences how populated the emissive excited state is. This behaviour indicates an interaction between dark and excited states for intermediate σ^+ values and further highlights the complex behaviour of this series of complexes in the excited state.

The indication that there are correlations with some excited state properties but not all suggests that the pathways from a generic high lying excited state, after excitation using < 450 nm light, to the ground state are not straightforward. The molecular orbitals of the phenyl acetylide ligand are interfering with the route to the ground state, this behaviour has been further examined below.
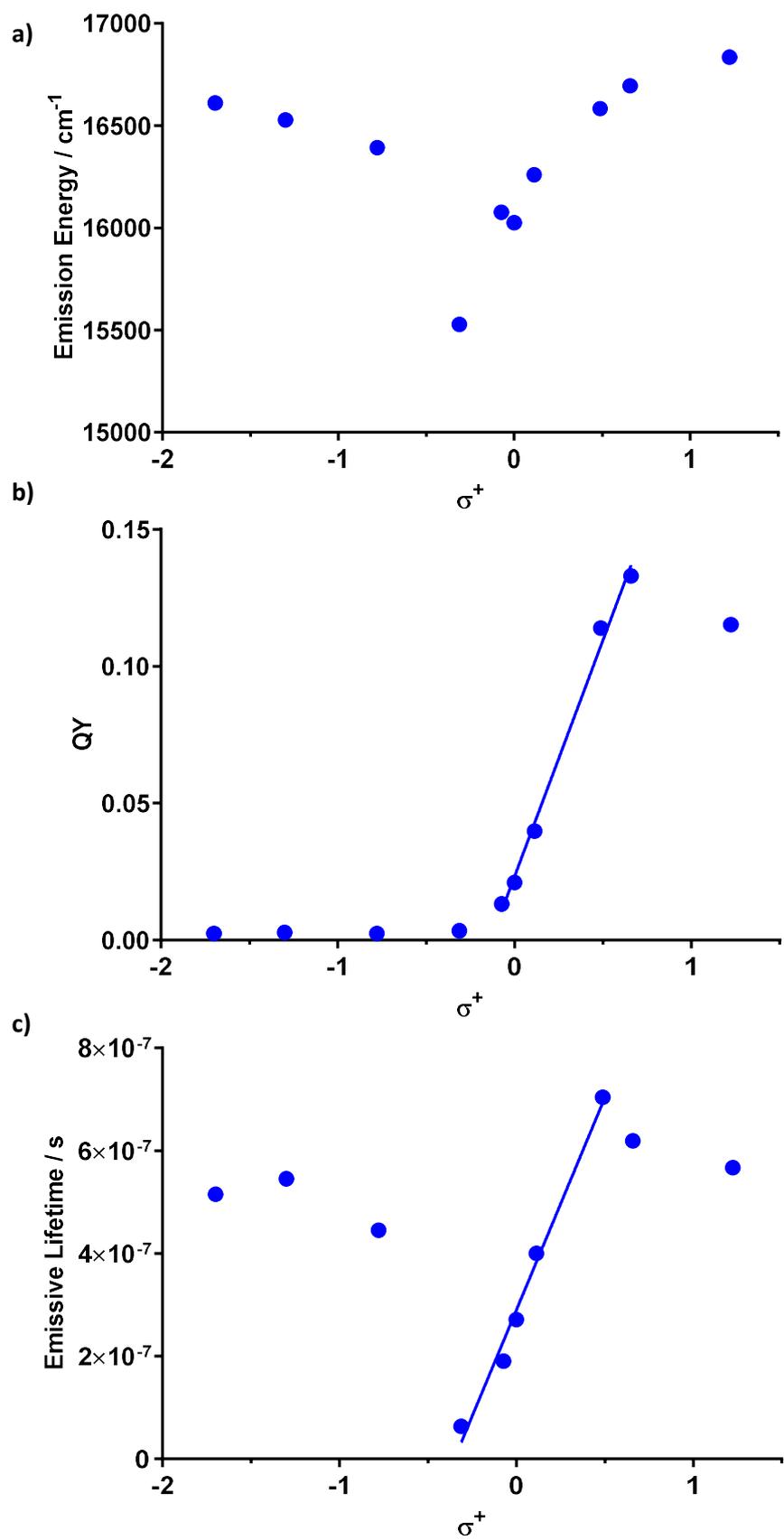
Figure 15 A plot of emission energy in wavenumbers (a), quantum yield (b) and emissive lifetime (c) against σ⁺ for complexes 6 – 15, revealing the effect donor ligand electronics have on excited state properties.

Application of the Hammett equation to excited state decay rates

Using the above comparisons of various properties of complexes **1 – 15** against their Hammett σ constants reveals that ground state properties are consistent within the Hammett equation, but excited properties are not. This disconnect between ground state and excited properties indicates that in the process of the molecule being promoted from the ground to the excited state, and then decaying back to the ground state, there are several different routes that can be taken for these complexes.

$$k_r = \frac{\Phi}{\tau}$$

Eq. 2

$$k_{nr} = \frac{1-\Phi}{\tau}$$

Eq. 3

Using radiative and non-radiative decay rates, calculated using equations 2 and 3, where k_r is radiatve rate, k_{nr} is non-radiative rate, Φ is the emissive quantum yield and τ is the lifetime of the emissive state, in the Hammett equation model allows a fuller picture of the mechanism for these routes, indicating the identities of the transition states for sets of complexes and revealing the mechanism of deactivation for the complexes with anomalously low activity emissive behaviours.
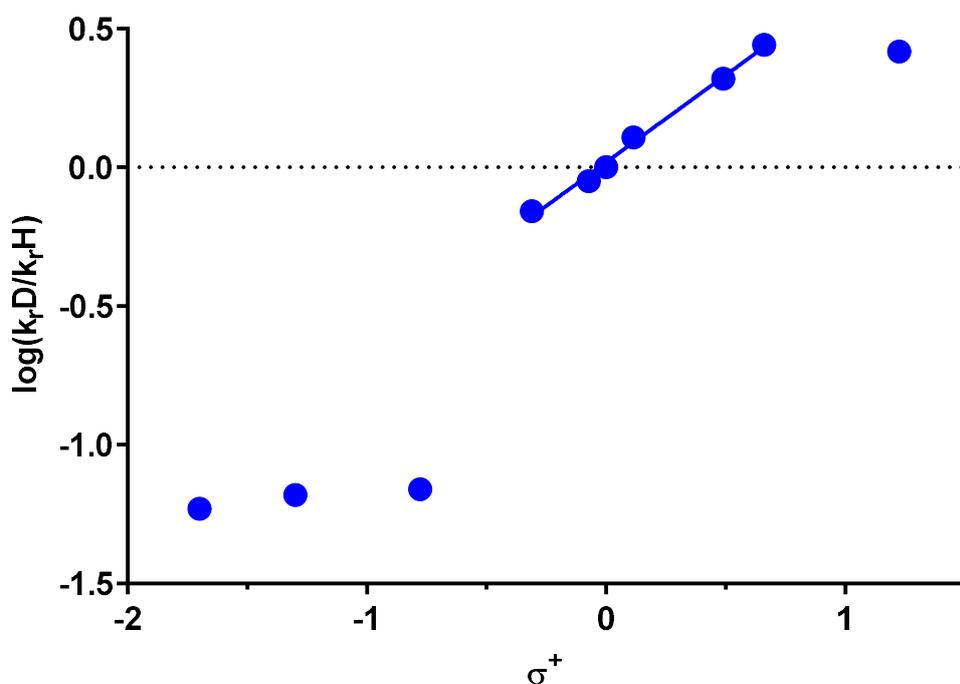
Figure 16 Radiative rates Hammett plot for complexes 6 – 15. The straight line indicates a region affected by donor properties. Between two unaffected areas, indicating a change in radiative mechanism. The correlation shown has a gradient of 0.63, r^2 = 0.99.

The plot above (Figure 16) is of σ⁺ against log(kD/kH) where kD is the radiative rate constant for complexes **6 – 15** and kH is the radiative rate constant for complex **10**. This plot shows that the acetylide substituent affects the radiative rate constant in six of the ten compounds and has no effect in the other four. In the four unaffected complexes (**12 - 15**), a gradient of effectively zero indicates no change in charge for the radiative transition state when changing the phenyl acetylide substituent. The mechanism of emission is unaffected by the change in donating group for these complexes.

The gradient of the plotted relationship has a value of 0.63 for complexes **6** - **15**. This unitless value is the reaction constant (ρ, **Eq. 1**); its positive value, less than one, suggests that the rate determining step of the reaction, to radiatively relax to the ground state, involves a decrease in positive charge or increase in negative charge in the transition state, near to the associated R group. The change in gradient over the course of moving from an σ^+ value of -1.7 to 1.224 indicates a change in reaction mechanism, however as the gradient returns to zero, the effects of the R group on mechanism become null again and the original mechanism is also re-established. Although the gradient returns to zero, the values for radiative rate are higher at large σ^+ and the plotted graph is continuous. This plotted behaviour indicates that where there is an R group located on the phenyl acetylide, which is more electron donating than a methyl group, radiative rate drops by around to around 1/100 of the maximum. Furthermore, the radiative rate is permanently affected by a more donating phenyl acetylide, indicating that the change in electronics has changed the dominant route for decay to the ground state.

It can be assumed, based on the properties of the emissive excited state that it is similar in nature to that of the cyclometalated platinum chloride complex, (**PtESTER**), featured in the previous chapter. The transition state of the decay to the ground state for this complex has the partial negative charge located over the bipy moiety of the N^N^C ligand and the partial positive charge located over the phenyl moiety of the N^N^C ligand (Figure 18a). A decrease in positive charge from this transition state in the phenyl acetylide substituted complexes would see migration of the positive charge from the phenyl moiety of the N^N^C ligand to the phenyl acetylide ligand (Figure 18b), with donation from phenyl acetylide π system electron density into the N^N^C ligand in the excited state, as this is the closest in energy MO. This is the most likely outcome where the emissive and charge separated states have enough overlap in energy to exchange. This behaviour is further reflected in the Hammett plot for non-radiative decay rates.
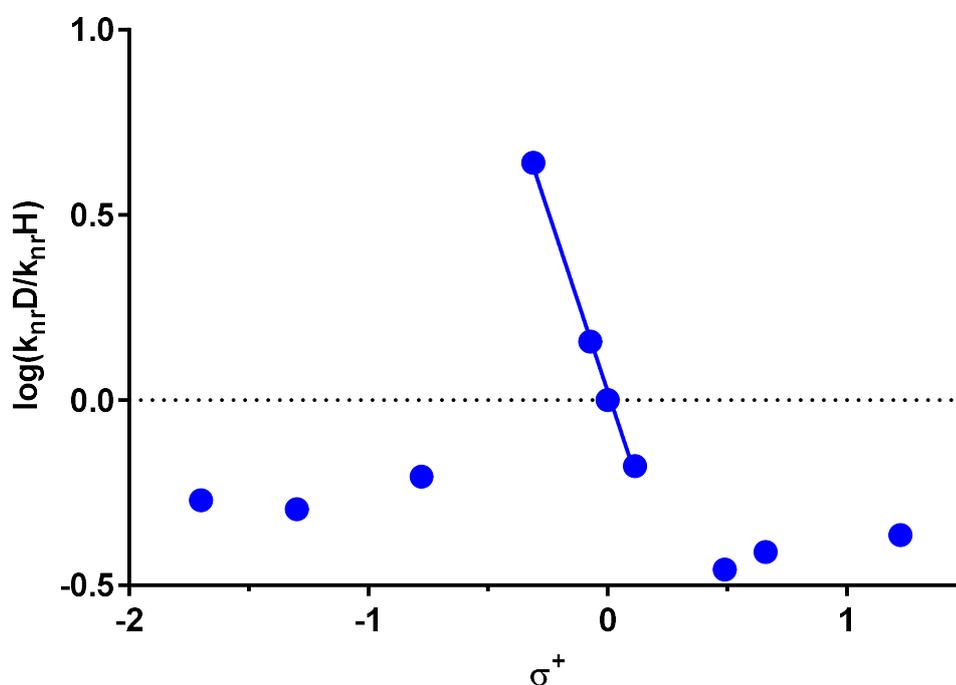
Figure 17 Non-radiative rates Hammett plot for complexes 6 – 15. The straight line indicates a region affected by donor properties. Between two unaffected areas, indicating a change in radiative mechanism. The gradient of the fitted line is -1.96, r^2 = 1.00.

Figure 17 is of σ^+ against $\log(k_{nr}D/k_{nr}H)$, where $k_{nr}D$ is the non-radiative rate constant for complexes **6 – 15** and $k_{nr}H$ is the non-radiative rate constant for complex **10**. This plot shows

that the acetylide substituent affects the non-radiative rate constant in four of the ten compounds and has no effect in the other six. In the six unaffected complexes (**6**, **7**, **12** - **15**), a gradient of effectively zero indicates no change in charge for the radiative transition state when changing the phenyl acetylide substituent for these complexes. The gradient of the plotted relationship has a value of -1.96 for complexes **8** - **11**. This reaction constant has a negative value, of magnitude greater than one, suggesting that the transition state of the reaction to non-radiatively relax to the ground state involves an increase in positive charge or decrease in decrease charge. There is only a gradient for complexes **8** – **11**, with a discontinuity between complexes **12** and **11**, at σ^+ values of -0.778 and -0.311 respectively. This discontinuity combined with a large gradient for very few complexes indicates that the non-radiative rate only has a transition state influenced by the electronics of the phenyl acetylide for a narrow range of R group σ^+ values.

The increase in positive charge, indicated by the >(-1) gradient of the Hammett plot, is on the phenyl-acetylide (Figure 18c). The amount of positive charge located on the phenyl-acetylide increases as donor groups with more electron donating potential bring the oxidized N^N^C phenyl and oxidized phenyl-acetylide energies closer (Figure 19). This is very sensitive to change in donor potential of the phenyl acetylide as this change in charge takes place on the acetylide and is directly influenced by the electronic effects of the donor group.

When considering the excited state of these molecules, predictions cannot be made using Hammett plots about the radiative or non-radiative relaxation rates, due to the non-linearity of the plots. This non-linearity is seen in all excited state properties; emission energy, quantum yield, emission lifetime and relaxation rates. The non-linearity is discontinuous in some plots, while continuous in others, but it is always characterized by two distinct gradients, coincident with complexes represented by sigma values -0.5 to 0.5. This Hammett plot behaviour suggests a change in mechanism, the character of which can be determined by inference from the difference in the two gradients, seen in each of the plots.
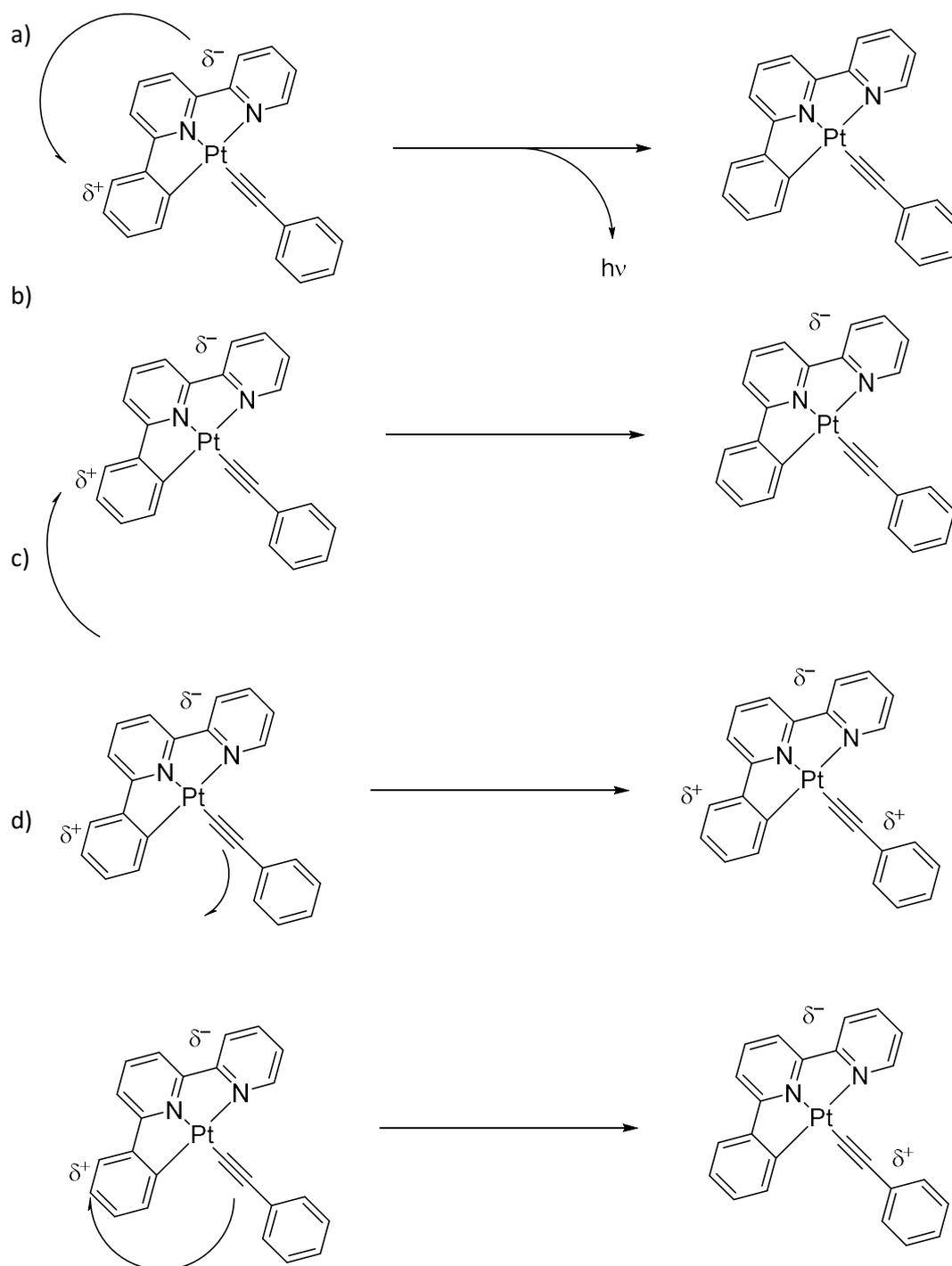
Figure 18 Representative eletron movements for the processes indicated by analysis of the Hammett equation for complexes 6 – 15. a) is a representation of the electron movement required to undergo an emissive (radiative) decay to the ground state. b) represents the loss in positive charge seen for intermediate σ⁺ values, in the Hammett plot for radiative decay rates, for the phenyl moiety of the N^N^C ligand. c) represents the gain in positive charge seen for intermediate σ⁺ values, in the Hammett plot for non-radiative decay rates, for the phenyl acetylide ligand. d) represents the logical electron transfer movement in the intermediate σ⁺ region, as indicated by the combination of radiative and non-radiative rate analysis. The electron moves from HOMO to HOMO-1 when these two MOs h ave sufficient overlap.

The plot for the non-radiative relaxation shows a linear relationship that is unaffected by the donor properties, with a discontinuity where the non-radiative rate is strongly affected by the donor. There is a very negative gradient displayed in the plot, which shows that the change in mechanism, associated with the increase in rate of non-radiative relaxation, involves an increase in positive charge at the phenyl acetylide (Figure 18c).

This prediction is reflected in the change in gradient seen for the radiative relaxation rate plot, with a continuous positive correlation between two areas with no gradient, indicating a change in reaction mechanism where there is a loss in positive charge at the transition state, which is less sensitive to phenyl acetylide donor character (Figure 18b). The gradient in the comparison of radiative rate and σ^+ is less steep, indicating that the phenyl acetylide donor has a greater effect on the non-radiative rates, than the radiative rates.
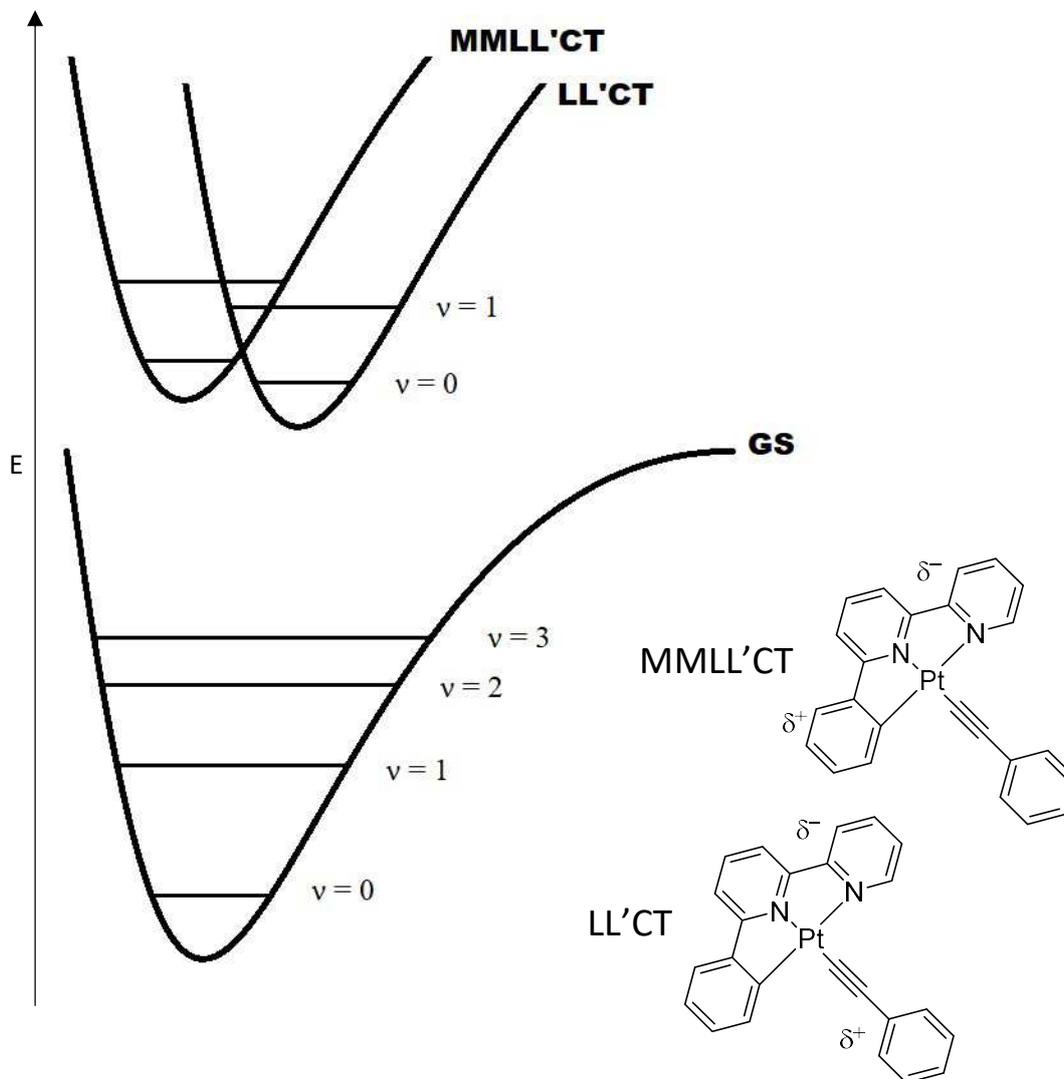
Figure 19 Representative potential energy curves, not to scale, for the excited state of complexes 6 – 15. Where the MMLL'CT and LL'CT states are close in energy, there is a possibility to populate the LL'CT state from the MMLL'CT state, resulting in a transfer of energy from N^N^C Ph moiety to phenyl acetylide ligand.

These two results combined suggest that the decrease in the quantum yield and emission lifetime upon increasing electron donating ability of the phenyl acetylide is due to electron density transfer from the initially populated emissive N^N^C localised intraligand $\pi\pi^*$ state to a non-emissive, lower in energy phenylacetylide π to bipy π^* state, when they have similar energies (Figure 18d). Despite an inability to predict the excited state properties, the ability to investigate relaxation mechanisms is very promising. This mechanism could not be inferred from ground state electrochemical properties or from observation of excited state phenomena, with partial rationalisation of the mechanism only possible through the aid of DFT modelling methods. This method for the investigation of relaxation mechanism allows the findings associated with the use DFT data to be corroborated, whilst also allowing the extreme,

unpredicted shortening of emissive lifetimes to be justified. This has provided a justification of unusual results presented by computer modelling of electronic states and structure.
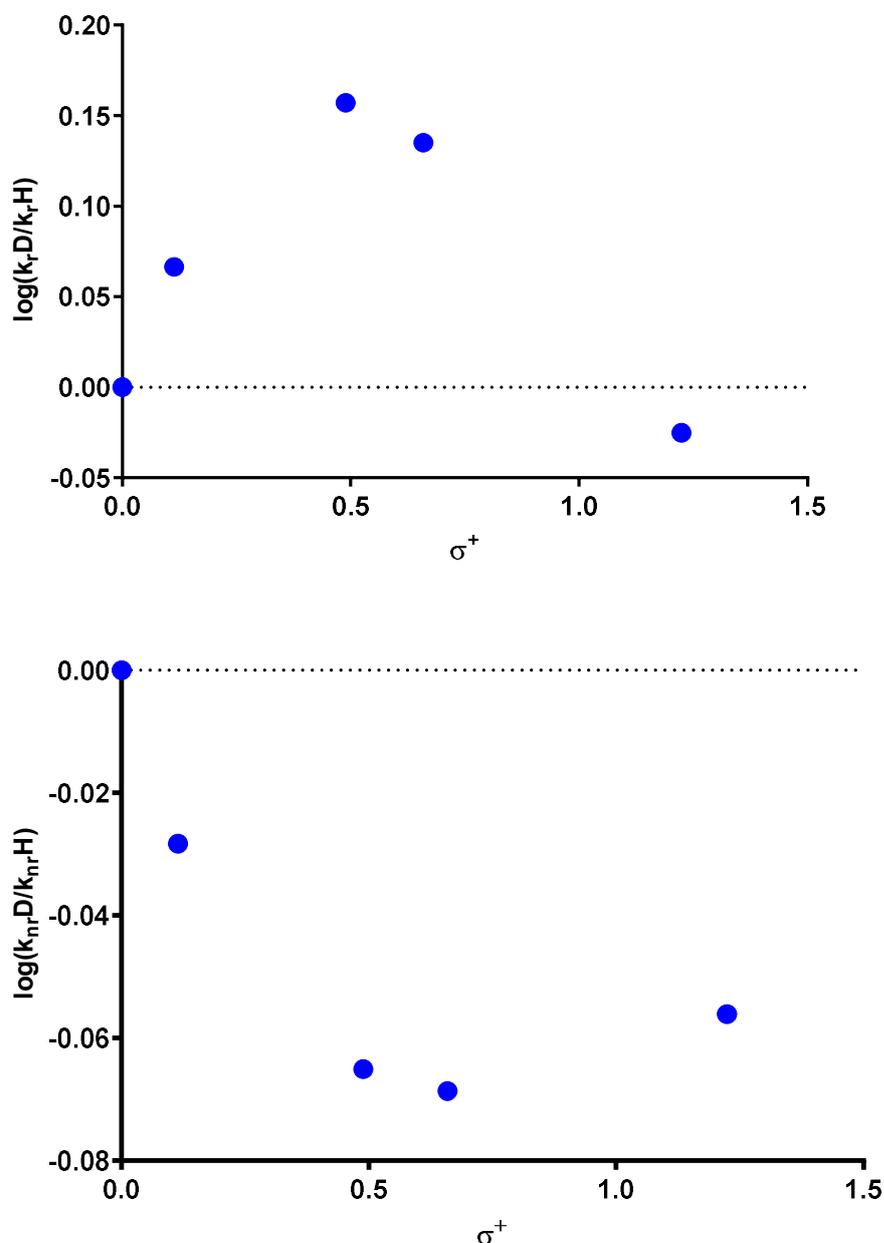
Figure 20a) A semilog plot of relative radiative rate against σ⁺ for complexes 1 – 5. Figure18b) A semilog plot of relative non-radiative rate against σ⁺ for complexes 1 – 5.

Hammett plots for the radiative and non-radiative relaxation rate constants of the butyl complexes show no correlation. DFT modelling indicates there is little coupling between N^N^C and phenyl acetylide moieties in the ground or excited state. The lowest excited state is a charge transfer from the non-planar phenyl acetylide π to bipy π* and excited state properties correlate strongly with planarization of the phenyl acetylide ligand, shown above by DFT modelling. This strongly implies that for complexes **1 – 5** excited state behaviour is dominated by geometric, not electronic, properties. Quantum yields for these complexes are high (0.18 – 0.27) whereas quantum yields for complexes **6 – 15** are low (0.002 – 0.13), suggesting a different mechanism of relaxation to the ground state for these two sets of complexes. Extension of the series may

help to show a further trend, as this series may have a step change in excited state properties, like ester bearing complexes.

The use of the Hammett equation to investigate the ground and excited state properties of complexes with complex decay pathways

The results demonstrated here show that even when complexes conform to the Hammett equation in their ground state properties, they may not in their excited state properties. This is revealed by how modellable the ground state properties are, with most observable redox potentials and ground state spectroscopic properties conforming to a simple linear relationship with σ^+, despite more complex relationships with excited state properties. These more complex relationships revealed that where complexes **6 – 15** have an intermediate σ^+ substituent on the R group, there is a complex mechanism for excitation followed by emissive decay to ground state; this is in contrast to a simple mechanism where, after excitation, a complex emits from its lowest accessible excited state.

The results here indicate that this more complex mechanism involves ligand to ligand charge transfer (LL'CT) across the complex, deactivating the light emitting mechanism in the process. This result was obtained through the use of a comparison of a wide series of cyclometalated platinum complexes with differing phenyl acetylide ligands, representing a significant change in electronics. Without this wide range of complexes, it may not have been possible to identify this behaviour, as has been seen with complexes **1 – 5**, where no discernible trend is obvious. These results would not be able to be obtained through a computationally inexpensive method from DFT, despite the strong characterisation of MO potential energies and character provided. The benefits of this method are easier to recognise with a series of easily functionalised complexes, which can quickly be modified to produce a suitable series.

CONCLUSIONS

In this chapter, the synthesis and characterization of new cyclometalated platinum acetylides has been presented, synthesized by previously published methods. The optical properties of these compounds have been studied and transitions assigned based on the assignments of previous studies and molecular modelling. Investigation using DFT revealed close lying electronic excited states that may interact with one another. Investigating these mechanisms would have been extremely computationally expensive so an empirical structure activity relationship based on the Hammett equation was used instead.

Their properties suggested predictable ground state behaviour but very unpredictable excited state behaviour. The optical and electronic properties of the complexes have been compared to Hammett constants for the donor substituents of the complexes. Ground state properties correlate well with σ^+ values, while excited state properties, radiative and non-radiative rates do not. The energy gap law, typically useful for predicting emission lifetimes and quantum yields, does not provide useful information. Instead, Hammett theory is used to rationalize changes of mechanism implied by the unexpected excited state properties.

The anomalous excited state behaviours of the ester complexes were further examined using Hammett theory and mechanisms of radiative and non-radiative relaxation changes proposed based on these studies. The lowering of lifetimes and quantum yields coincides with a change in non-radiative and radiative relaxation mechanisms for some complexes. This has been proposed to be coupling between an emissive and a dark state causing the quenching of the emissive excited state by electron density transfer to the dark state.

Investigation using a Hammett theory regime allowed mechanistic data to be determined from a series of structurally related compounds. This is not computationally expensive but it can be

time intensive and when using SARs the benefits of synthesis vs computation must be assessed. The mechanisms proposed by the SARs cannot be directly corroborated using time resolved visible light techniques. The next chapter will detail how time-resolved infra-red techniques have been used to enhance the investigation posed here.

Experimental

Materials

$K_2[PtCl_4]$, substituted phenyl acetylides, CuI and diisopropylamine were used as received from commercial sources (Johnson Matthey, Sigma-Aldrich, VWR UK and Fluorochem) without further purification. Pt(N^N^C)Cl precursor complexes were prepared according to literature procedures.[33, 62]

Methods

NMR spectra were recorded on a Bruker Avance HD3 400MHz spectrometer. UV/vis spectra were recorded on a Cary 50 Bio spectrometer or a Cary 5000 spectrometer. Luminescence spectra were recorded on a Jobin Yvon Fluormax 4 spectrometer. Lifetimes were obtained using a single photon counting method on an Edinburgh Instruments mini-τ. Emission decay curves were fit using multiexponential functions in Origin 8.0 data processing software. Cyclic Voltammetry was performed using an Autolab PGSTAT100 under nitrogen atmosphere.

Platinum(N^N^C)phenylacetylide general method

In a two-necked round bottom flask under argon atmosphere the relevant Pt(N^N^C)Cl, 1.1 equivalents of phenyl acetylide, and a catalytic amount of CuI (<5 mg) were suspended in dichloromethane (10 mL), then diisopropylamine (1 mL) was added. The suspension was stirred for 2 – 24 hours, after which period the solvent was removed under vacuum. The solid residue was redissolved in dichloromethane (200 mL) and washed with 1% aqueous acetic acid (100 mL), 1% aqueous ammonia (100 mL) and deionized water (100 mL). The solvent was removed under vacuum and the residue subjected to column chromatography on silica to give analytically pure complex.

The products were characterised by ^1H NMR, ^{19}F NMR where appropriate, 2D NMR in some cases, and mass spectrometry. Complexes **8** and **11** have been characterised by X-ray crystallography.

4 *(6-phenyl-(4-4'-ditertiarybutyl-2,2'bipyridine))(ethynylbenzene)platinum(II)*
Reaction time: 4 h. Yield: 64% ^1H NMR (400 MHz, DMSO) δ 8.94 (d, J = 6.1 Hz, 1H), 8.57 (d, J = 1.5 Hz, 1H), 8.35 (d, J = 1.4 Hz, 1H), 7.95 (d, J = 1.2 Hz, 1H), 7.86 (dd, J = 5.7, 1.9 Hz, 1H), 7.80 – 7.70 (m, 1H), 7.36 (d, J = 7.0 Hz, 2H), 7.31 – 7.24 (m, 2H), 7.19 – 7.14 (m, 1H), 7.11 (td, J = 7.3, 1.6 Hz, 1H), 7.06 (td, J = 7.3, 1.2 Hz, 1H), 1.46 (s, 9H), 1.43 (s, 9H). TOF MS ES+ m/z 640 (M$^+$)

3 *(6-phenyl-(4-4'ditertiarybutyl-2,2'bipyridine))(4-chloro-1-ethynylbenzene)platinum(II)*
Reaction time: 4 h. Yield: 68% ^1H NMR (400 MHz, DMSO) δ 8.92 (d, J = 5.8 Hz, 1H), 8.57 (d, J = 1.5 Hz, 1H), 8.35 (d, J = 1.3 Hz, 1H), 7.95 (d, J = 1.2 Hz, 1H), 7.85 (dd, J = 5.8, 2.0 Hz, 1H), 7.77 (dd, J = 7.8, 1.1 Hz, 1H), 7.71 (dd, J = 7.3, 1.3 Hz, 1H), 7.40 – 7.27 (m, 4H), 7.11 (td, J = 7.3, 1.4 Hz, 1H), 7.06 (td, J = 7.5, 1.5 Hz, 1H), 1.46 (s, 9H), 1.43 (s, 9H). TOF MS ES+ m/z 675 (M$^+$)

2 *(6-phenyl-(4-4'ditertiarybutyl-2,2'bipyridine))(4-methylcarboxy-1-ethynylbenzene)platinum(II)*
Reaction time: 4 h. Yield: 82% ^1H NMR (400 MHz, DMSO) δ 8.91 (d, J = 5.7 Hz, 1H), 8.58 (d, J = 1.6 Hz, 1H), 8.36 (d, J = 1.3 Hz, 1H), 7.96 (d, J = 1.2 Hz, 1H), 7.91 – 7.82 (m, 3H), 7.78 (dd, J = 7.7, 1.4 Hz, 1H), 7.71 (dd, J = 7.3, 1.4 Hz, 1H), 7.51 – 7.38 (m, 2H), 7.12 (td, J = 7.4, 1.6 Hz, 1H), 7.06 (td, J = 7.3, 1.4 Hz, 1H), 3.85 (s, 3H), 1.46 (s, 9H), 1.43 (s, 9H). TOF MS ES+ m/z 698 (M$^+$)

1 *(6-phenyl-(4-4'ditertiarybutyl-2,2'bipyridine))(4-cyano-1-ethynylbenzene)platinum(II)*
Reaction time: 4 h. Yield: 69% ^{1}H NMR (400 MHz, DMSO) δ 8.89 (d, J = 6.0 Hz, 1H), 8.58 (d, J = 1.7 Hz, 1H), 8.36 (d, J = 1.2 Hz, 1H), 7.96 (d, J = 1.2 Hz, 1H), 7.84 (dd, J = 5.8, 2.0 Hz, 1H), 7.78 (dd, J = 7.3, 1.7 Hz, 1H), 7.74 − 7.70 (m, 2H), 7.69 (dd, J = 7.3, 1.3 Hz, 1H), 7.52 − 7.46 (m, 2H), 7.11 (td, J = 7.4, 1.7 Hz, 1H), 7.06 (td, J = 7.5, 1.6 Hz, 1H), 1.46 (s, 9H), 1.42 (s, 9H). TOF MS ES+ m/z 665 (M$^+$)

5 *(6-phenyl-(4-4'ditertiarybutyl-2,2'bipyridine))(3,5-bistrifluoromethyl-1-ethynylbenzene)platinum(II)*
Reaction time: 4 h. Yield: 83% ^{1}H NMR (400 MHz, DMSO) δ 8.95 (d, J = 5.7 Hz, 1H), 8.57 (d, J = 1.8 Hz, 1H), 8.36 (d, J = 1.1 Hz, 1H), 7.96 (d, J = 1.1 Hz, 1H), 7.94 (d, J = 0.9 Hz, 2H), 7.87 − 7.80 (m, 2H), 7.78 (d, J = 7.2 Hz, 1H), 7.71 (dd, J = 7.3, 1.3 Hz, 1H), 7.13 (td, J = 7.4, 1.5 Hz, 1H), 7.07 (td, J = 7.0, 0.8 Hz, 1H), 1.46 (s, 9H), 1.43 (s, 9H). ^{19}F NMR (376 MHz, DMSO) δ -61.44 (s). TOF MS ES+ m/z 776 (M$^+$)

14 *(6-phenyl-4-ethylcarboxy-2,2'-bipyridine))(4-dimethylamino-1-ethynylbenzene)platinum(II)*
Reaction time: 2 h. Yield: 65% ^{1}H NMR (400 MHz, CDCl$_3$) δ 9.24 (dd, J = 5.3, 0.8 Hz, 1H), 8.11 − 7.90 (m, 5H), 7.58 (ddd, J = 7.4, 5.3, 1.3 Hz, 1H), 7.48 − 7.41 (m, 3H), 7.21 (td, J = 7.4, 1.4 Hz, 1H), 7.09 (td, J = 7.5, 1.3 Hz, 1H), 6.74 − 6.65 (m, 2H), 4.47 (q, J = 7.1 Hz, 2H), 2.97 (s, 6H), 1.48 (t, J = 7.1 Hz, 3H). TOF MS ES+ m/z 642 (M$^+$)

13 *(6-phenyl-4-ethylcarboxy-2,2'-bipyridine))(4-amino-1-ethynylbenzene)platinum(II)*
Reaction time: 2 h. Yield: 69% ^{1}H NMR (400 MHz, CDCl$_3$) δ 9.23 (dd, J = 5.3, 0.8 Hz, 1H), 8.13 − 7.88 (m, 5H), 7.59 (ddd, J = 7.4, 5.3, 1.2 Hz, 1H), 7.44 (dd, J = 7.7, 1.1 Hz, 1H), 7.38 (d, J = 8.5 Hz, 2H), 7.21 (td, J = 7.4, 1.3 Hz, 1H), 7.09 (td, J = 7.5, 1.3 Hz, 1H), 6.69 − 6.59 (m, 2H), 4.48 (q, J = 7.1 Hz, 2H), 3.65 (s, 2H), 1.48 (t, J = 7.1 Hz, 3H). TOF MS ES+ m/z 615 (M$^+$)

12 *(6-phenyl-4-ethylcarboxy-2,2'-bipyridine))(4-methoxy-1-ethynylbenzene)platinum(II)*
Reaction time: 4 h. Yield: 68% ^{1}H NMR (400 MHz, CDCl$_3$) δ 9.23 (dd, J = 5.3, 0.8 Hz, 1H), 8.13 − 7.87 (m, 5H), 7.60 (ddd, J = 7.3, 5.3, 1.2 Hz, 1H), 7.53 − 7.47 (m, 2H), 7.44 (dd, J = 7.6, 0.9 Hz, 1H), 7.22 (td, J = 7.4, 1.2 Hz, 1H), 7.09 (td, J = 7.5, 1.2 Hz, 1H), 6.90 − 6.80 (m, 2H), 4.48 (q, J = 7.1 Hz, 2H), 3.83 (s, 3H), 1.48 (t, J = 7.1 Hz, 3H). TOF MS ES+ m/z 630 (M$^+$)

11 *(6-phenyl-4-ethylcarboxy-2,2'-bipyridine))(4-methyl-1-ethynylbenzene)platinum(II)*
Reaction time: 4 h. Yield: 65% ^{1}H NMR (400 MHz, CDCl$_3$) δ 9.18 (dd, J = 5.3, 0.8 Hz, 1H), 8.11 − 7.83 (m, 5H), 7.57 (ddd, J = 7.4, 5.3, 1.3 Hz, 1H), 7.47 − 7.44 (m, 2H), 7.42 (dd, J = 7.9, 1.3 Hz, 1H), 7.20 (td, J = 7.4, 1.4 Hz, 1H), 7.12 − 7.05 (m, 3H), 4.47 (q, J = 7.1 Hz, 2H), 2.36 (s, 3H), 1.48 (t, J = 7.1 Hz, 3H). TOF MS ES+ m/z 613 (M$^+$)

10 *(6-phenyl-4-ethylcarboxy-2,2'-bipyridine))(ethynylbenzene)platinum(II)*
Reaction time: 4 h. Yield: 81% ^{1}H NMR (400 MHz, CDCl$_3$) δ 9.11 (dd, J = 5.3, 0.8 Hz, 1H), 8.07 − 7.79 (m, 5H), 7.59 − 7.49 (m, 3H), 7.39 (dd, J = 7.7, 1.2 Hz, 1H), 7.34 − 7.27 (m, 2H), 7.22 − 7.13 (m, 2H), 7.07 (td, J = 7.5, 1.3 Hz, 1H), 4.46 (q, J = 7.1 Hz, 2H), 1.47 (t, J = 7.1 Hz, 3H). MS ES+ m/z 600 (M$^+$)

9 *(6-phenyl-4-ethylcarboxy-2,2'-bipyridine))(4-fluoro-1-ethynylbenzene)platinum(II)*
Reaction time: 4 h. Yield: 75% ^{1}H NMR (400 MHz, CDCl$_3$) δ 9.20 (dd, J = 5.3, 0.8 Hz, 1H), 8.13 − 7.84 (m, 5H), 7.60 (ddd, J = 7.5, 5.3, 1.3 Hz, 1H), 7.54 − 7.47 (m, 2H), 7.45 (dd, J = 7.7, 1.2 Hz, 1H), 7.22 (td, J = 7.4, 1.4 Hz, 1H), 7.10 (td, J = 7.5, 1.3 Hz, 1H), 7.03 − 6.93 (m, 2H), 4.48 (q, J = 7.1 Hz, 2H), 1.48 (t, J = 7.1 Hz, 3H). ^{19}F NMR (377 MHz, CDCl$_3$) δ -110.66 − -124.07 (m). MS ES+ m/z 618 (M$^+$)

8 *(6-phenyl-4-ethylcarboxy-2,2'-bipyridine))(4-chloro-1-ethynylbenzene)platinum(II)*

Reaction time: 6 h. Yield: 79% ^{1}H NMR (400 MHz, CDCl$_3$) δ 9.20 (dd, J = 5.3, 0.9 Hz, 1H), 8.14 – 7.81 (m, 5H), 7.61 (ddd, J = 7.4, 5.3, 1.2 Hz, 1H), 7.49 – 7.43 (m, 3H), 7.26 – 7.20 (m, 3H), 7.10 (td, J = 7.5, 1.3 Hz, 1H), 4.49 (q, J = 7.1 Hz, 2H), 1.48 (t, J = 7.1 Hz, 3H). MS ES+ m/z 635 (MH$^+$)

7 *(6-phenyl-4-ethylcarboxy-2,2'-bipyridine))(4-carboxymethyl-1-ethynylbenzene)platinum(II)*

Reaction time: 6 h. Yield: 41% ^{1}H NMR (400 MHz, CDCl$_3$) δ 9.21 (d, J = 5.1 Hz, 1H), 8.16 – 7.82 (m, 7H), 7.67 – 7.60 (m, 1H), 7.57 (d, J = 8.3 Hz, 2H), 7.47 (dd, J = 7.4, 0.7 Hz, 1H), 7.24 – 7.19 (m, 1H), 7.14 – 7.06 (m, 1H), 4.50 (q, J = 7.1 Hz, 2H), 3.92 (s, 3H), 1.48 (t, J = 7.1 Hz, 3H). MS ES+ m/z 680 (MNa$^+$)

6 *(6-phenyl-4-ethylcarboxy-2,2'-bipyridine))(4-cyano-1-ethynylbenzene)platinum(II)*

Reaction time: 8 h. Yield: 64% ^{1}H NMR (400 MHz, CDCl$_3$) δ 9.18 (dd, J = 5.3, 0.9 Hz, 1H), 8.17 – 8.01 (m, 4H), 7.90 (dd, J = 7.5, 1.0 Hz, 1H), 7.64 (ddd, J = 7.5, 5.3, 1.2 Hz, 1H), 7.60 – 7.53 (m, 4H), 7.48 (dd, J = 7.6, 1.3 Hz, 1H), 7.23 (td, J = 7.4, 1.4 Hz, 1H), 7.12 (td, J = 7.5, 1.3 Hz, 1H), 4.50 (q, J = 7.1 Hz, 2H), 1.49 (t, J = 7.1 Hz, 4H). MS ES+ m/z 624 (M$^+$)

15 *(6-phenyl-4-ethylcarboxy-2,2'-bipyridine))(3,5-bistrifluoromethyl-1-ethynylbenzene)platinum(II)*

Reaction time: 24 h. Yield: 64% ^{1}H NMR (400 MHz, CDCl$_3$) δ 9.08 (dd, J = 5.3, 0.9 Hz, 1H), 8.11 – 7.94 (m, 4H), 7.90 (s, 2H), 7.81 (dd, J = 7.5, 1.0 Hz, 1H), 7.64 (s, 1H), 7.61 (ddd, J = 7.5, 5.3, 1.2 Hz, 1H), 7.40 (dd, J = 7.7, 1.2 Hz, 1H), 7.20 (td, J = 7.4, 1.4 Hz, 1H), 7.08 (td, J = 7.5, 1.3 Hz, 1H), 4.47 (q, J = 7.1 Hz, 2H), 1.47 (t, J = 7.1 Hz, 3H). ^{19}F NMR (377 MHz, CDCl$_3$) δ -62.96 (s). MS ES+ m/z 736 (M$^+$)

Table 5 Photophysical data for complexes 1 – 15. a) Recorded in DCM with 0.1 M (^{t}Bu$_4$N)$^+$(PF$_6$)$^-$ electrolyte at a scan rate of 100 mVs^{-1} vs Fc$^{+/0}$ couple. b) Recorded in Ar purged DCM at an OD of 0.1. c) Compared to [Ru(bpy)$_3$]Cl$_2$ in water. OD = 0.063.[63]

Compound	$E_{RED1/2}$ / V[a]	E_{OXpa} / V[a]	$E_{RED} - E_{OX}$ / V	Emission / nm[b]	Emission / eV	Lifetime / ns[b]	QY[c]
4	-1.91	0.35, 0.73	2.26, 2.64	571	2.17	635	0.18
3	-1.91	0.39, 0.72	2.3, 2.63	565	2.19	649	0.22
2	-1.89	0.45, 0.78	2.34, 2.67	556	2.23	658	0.27
1	-1.89	0.48, 0.83	2.37, 2.72	554	2.24	671	0.26
5	-1.88	0.59, 0.90	2.47, 2.78	553	2.24	713	0.19
14	-1.62	-0.08, 0.03, 0.78	1.54, 1.65, 2.40	602	2.06	349	0.002
13	-1.61	0, 0.19	1.61, 1.80	605	2.05	286	0.003
12	-1.60	0.03, 0.26, 0.88	1.63, 1.86, 2.48	610	2.03	411	0.002
11	-1.60	0.13, 0.36, 0.91	1.73, 1.96, 2.51	644	1.93	63	0.003
9	-1.60	0.12, 0.39, 0.82	1.72, 1.99, 2.42	622	1.99	190	0.02
10	-1.60	0.09, 0.36, 0.75	1.69, 1.96, 2.35	624	1.99	271	0.01
8	-1.59	0.13, 0.42, 0.84	1.72, 2.01, 2.43	615	2.02	400	0.04
7	-1.57	0.18, 0.46, 0.84	1.75, 2.03, 2.41	603	2.06	704	0.11
6	-1.57	0.19, 0.53, 0.91	1.76, 2.10, 2.48	599	2.07	619	0.13
15	-1.56	0.31, 0.56, 0.94	1.87, 2.12, 2.50	594	2.09	567	0.12

REFERENCES

1.   Potočnik, J., *Science* **2007,** *315* (5813), 810-811.
2.   Service, R. F., *Science* **2005,** *309* (5734), 548-551.
3.   Schiermeier, Q.; Tollefson, J.; Scully, T.; Witze, A.; Morton, O., *Nature* **2008,** *454* (7206), 816-823.
4.   Armaroli, N.; Balzani, V., *Angew. Chem. Int. Ed.* **2007,** *46* (1-2), 52-66.
5.   Morris, A. J.; Meyer, G. J.; Fujita, E., *Acc. Chem. Res.* **2009,** *42* (12), 1983-1994.
6.   Meyer, T. J., *Acc. Chem. Res.* **1989,** *22* (5), 163-170.
7.   Wasielewski, M. R., *Chem. Rev.* **1992,** *92* (3), 435-461.
8.   Young, K. J.; Martini, L. A.; Milot, R. L.; Snoeberger Iii, R. C.; Batista, V. S.; Schmuttenmaer, C. A.; Crabtree, R. H.; Brudvig, G. W., *Coord. Chem. Rev.* **2012,** *256* (21–22), 2503-2520.
9.   Harriman, A., *Angew. Chem. Int. Ed.* **2004,** *43* (38), 4985-4987.
10.   Vlachopoulos, N.; Liska, P.; Augustynski, J.; Graetzel, M., *J. Am. Chem. Soc.* **1988,** *110* (4), 1216-1220.
11.   Grätzel, M., *J. Photochem. Photobiol., C* **2003,** *4* (2), 145-153.
12.   Hagfeldt, A.; Grätzel, M., *Acc. Chem. Res.* **2000,** *33* (5), 269-277.
13.   Hagfeldt, A.; Boschloo, G.; Sun, L.; Kloo, L.; Pettersson, H., *Chem. Rev.* **2010,** *110* (11), 6595-6663.
14.   Burschka, J.; Pellet, N.; Moon, S.-J.; Humphry-Baker, R.; Gao, P.; Nazeeruddin, M. K.; Gratzel, M., *Nature* **2013,** *499* (7458), 316-319.
15.   Islam, A.; Sugihara, H.; Hara, K.; Singh, L. P.; Katoh, R.; Yanagida, M.; Takahashi, Y.; Murata, S.; Arakawa, H.; Fujihashi, G., *Inorg. Chem.* **2001,** *40* (21), 5371-5380.
16.   Geary, E. A. M.; Yellowlees, L. J.; Jack, L. A.; Oswald, I. D. H.; Parsons, S.; Hirata, N.; Durrant, J. R.; Robertson, N., *Inorg. Chem.* **2005,** *44* (2), 242-250.
17.   Geary, E. A. M.; McCall, K. L.; Turner, A.; Murray, P. R.; McInnes, E. J. L.; Jack, L. A.; Yellowlees, L. J.; Robertson, N., *Dalton Trans.* **2008,** (28), 3701-3708.
18.   Geary, E. A. M.; Hirata, N.; Clifford, J.; Durrant, J. R.; Parsons, S.; Dawson, A.; Yellowlees, L. J.; Robertson, N., *Dalton Trans.* **2003,** (19), 3757-3762.
19.   Kwok, E. C.-H.; Chan, M.-Y.; Wong, K. M.-C.; Lam, W. H.; Yam, V. W.-W., *Chem. Eur. J.* **2010,** *16* (40), 12244-12254.
20.   Esswein, A. J.; Nocera, D. G., *Chem. Rev.* **2007,** *107* (10), 4022-4047.
21.   Webb, D. L.; Ancarani Rossiello, L., *Inorg. Chem.* **1971,** *10* (10), 2213-2218.
22.   Biedermann, J.; Wallfahrer, M.; Gliemann, G., *J. Lumin.* **1987,** *37* (6), 323-329.
23.   Diomedi Camassei, F.; Ancarani-Rossiello, L.; Castelli, F., *J. Lumin.* **1973,** *8* (1), 71-81.
24.   Cummings, S. D.; Eisenberg, R., Luminescence and Photochemistry of Metal Dithiolene Complexes. In *Dithiolene Chemistry*, John Wiley & Sons, Inc.: 2003; pp 315-367.
25.   Paw, W.; Cummings, S. D.; Adnan Mansour, M.; Connick, W. B.; Geiger, D. K.; Eisenberg, R., *Coord. Chem. Rev.* **1998,** *171*, 125-150.
26.   Zuleta, J. A.; Chesta, C. A.; Eisenberg, R., *J. Am. Chem. Soc.* **1989,** *111* (24), 8916-8917.
27.   Bevilacqua, J. M.; Eisenberg, R., *Inorg. Chem.* **1994,** *33* (9), 1886-1890.
28.   A. Weinstein, J.; N. Zheligovskaya, N.; Ya. Mel'nikov, M.; Hartl, F., *J. Chem. Soc., Dalton Trans.* **1998,** (15), 2459-2466.
29.   Chan, S.-C.; Chan, M. C. W.; Wang, Y.; Che, C.-M.; Cheung, K.-K.; Zhu, N., *Chem. Eur. J.* **2001,** *7* (19), 4180-4190.
30.   Archer, S.; Weinstein, J. A., *Coord. Chem. Rev.* **2012,** *256* (21), 2530-2561.
31.   Latouche, C.; Lanoe, P.-H.; Williams, J. A. G.; Guerchais, V.; Boucekkine, A.; Fillaut, J.-L., *New J. Chem.* **2011,** *35* (10), 2196-2202.
32.   Lu, W.; Mi, B.-X.; Chan, M. C. W.; Hui, Z.; Zhu, N.; Lee, S.-T.; Che, C.-M., *Chem. Commun.* **2002,** (3), 206-207.
33.   Lu, W.; Mi, B.-X.; Chan, M. C. W.; Hui, Z.; Che, C.-M.; Zhu, N.; Lee, S.-T., *J. Am. Chem. Soc.* **2004,** *126* (15), 4958-4971.

34. Mori, K.; Goumans, T. P. M.; van Lenthe, E.; Wang, F., *PCCP* **2014,** *16* (28), 14523-14530.

35. Tong, G. S.-M.; Che, C.-M., *Chem. Eur. J.* **2009,** *15* (29), 7225-7237.

36. Hino, J. K.; Della Ciana, L.; Dressick, W. J.; Sullivan, B. P., *Inorg. Chem.* **1992,** *31* (6), 1072-1080.

37. Laskar, I. R.; Chen, T.-M., *Chem. Mater.* **2004,** *16* (1), 111-117.

38. Maestri, M.; Armaroli, N.; Balzani, V.; Constable, E. C.; Thompson, A. M. W. C., *Inorg. Chem.* **1995,** *34* (10), 2759-2767.

39. J. L. McInnes, E.; D. Farley, R.; C. Rowlands, C.; J. Welch, A.; Rovatti, L.; J. Yellowlees, L., *J. Chem. Soc., Dalton Trans.* **1999,** (23), 4203-4208.

40. Rillema, D. P.; Stoyanov, S. R.; Cruz, A. J.; Nguyen, H.; Moore, C.; Huang, W.; Siam, K.; Jehan, A.; KomReddy, V., *Dalton Trans.* **2015,** *44* (39), 17075-17090.

41. Hammett, L. P., *J. Am. Chem. Soc.* **1937,** *59* (1), 96-103.

42. Karkas, M. D.; Liao, R.-Z.; Laine, T. M.; Akermark, T.; Ghanem, S.; Siegbahn, P. E. M.; Akermark, B., *Catalysis Science & Technology* **2016,** *6* (5), 1306-1319.

43. Salter-Blanc, A. J.; Bylaska, E. J.; Lyon, M. A.; Ness, S. C.; Tratnyek, P. G., *Environ. Sci. Technol.* **2016,** *50* (10), 5094-5102.

44. Eng, G., *Appl. Organomet. Chem.* **2017,** n/a-n/a.

45. Cummings, S. D.; Eisenberg, R., *J. Am. Chem. Soc.* **1996,** *118* (8), 1949-1960.

46. Schneider, J.; Du, P.; Wang, X.; Brennessel, W. W.; Eisenberg, R., *Inorg. Chem.* **2009,** *48* (4), 1498-1506.

47. Young, K. J. H.; Meier, S. K.; Gonzales, J. M.; Oxgaard, J.; Goddard, W. A.; Periana, R. A., *Organometallics* **2006,** *25* (20), 4734-4737.

48. Lai, S.-W.; Lam, H.-W.; Lu, W.; Cheung, K.-K.; Che, C.-M., *Organometallics* **2002,** *21* (1), 226-234.

49. James, S. L.; Younus, M.; Raithby, P. R.; Lewis, J., *J. Organomet. Chem.* **1997,** *543* (1), 233-235.

50. Hansch, C.; Leo, A.; Taft, R. W., *Chem. Rev.* **1991,** *91* (2), 165-195.

51. Hissler, M.; Connick, W. B.; Geiger, D. K.; McGarrah, J. E.; Lipa, D.; Lachicotte, R. J.; Eisenberg, R., *Inorg. Chem.* **2000,** *39* (3), 447-457.

52. Cancès, E.; Mennucci, B.; Tomasi, J., *J. Chem. Phys.* **1997,** *107* (8), 3032-3041.

53. Weinstein, J. A.; Tierney, M. T.; Davies, E. S.; Base, K.; Robeiro, A. A.; Grinstaff, M. W., *Inorg. Chem.* **2006,** *45* (11), 4544-4555.

54. Frisch, M. J.; Trucks, G. W.; Schlegel, H. B.; Scuseria, G. E.; Robb, M. A.; Cheeseman, J. R.; Scalmani, G.; Barone, V.; Mennucci, B.; Petersson, G. A.; Nakatsuji, H.; Caricato, M.; Li, X.; Hratchian, H. P.; Izmaylov, A. F.; Bloino, J.; Zheng, G.; Sonnenberg, J. L.; Hada, M.; Ehara, M.; Toyota, K.; Fukuda, R.; Hasegawa, J.; Ishida, M.; Nakajima, T.; Honda, Y.; Kitao, O.; Nakai, H.; Vreven, T.; Montgomery Jr., J. A.; Peralta, J. E.; Ogliaro, F.; Bearpark, M. J.; Heyd, J.; Brothers, E. N.; Kudin, K. N.; Staroverov, V. N.; Kobayashi, R.; Normand, J.; Raghavachari, K.; Rendell, A. P.; Burant, J. C.; Iyengar, S. S.; Tomasi, J.; Cossi, M.; Rega, N.; Millam, N. J.; Klene, M.; Knox, J. E.; Cross, J. B.; Bakken, V.; Adamo, C.; Jaramillo, J.; Gomperts, R.; Stratmann, R. E.; Yazyev, O.; Austin, A. J.; Cammi, R.; Pomelli, C.; Ochterski, J. W.; Martin, R. L.; Morokuma, K.; Zakrzewski, V. G.; Voth, G. A.; Salvador, P.; Dannenberg, J. J.; Dapprich, S.; Daniels, A. D.; Farkas, Ö.; Foresman, J. B.; Ortiz, J. V.; Cioslowski, J.; Fox, D. J., *Gaussian 09* **2009**.

55. Becke, A. D., *J. Chem. Phys.* **1993,** *98* (7), 5648-5652.

56. Lee, C.; Yang, W.; Parr, R. G., *Physical Review B* **1988,** *37* (2), 785-789.

57. Figgen, D.; Peterson, K. A.; Dolg, M.; Stoll, H., *J. Chem. Phys.* **2009,** *130* (16), 164108.

58. Dunning, T. H., *J. Chem. Phys.* **1989,** *90* (2), 1007-1023.

59. Dunning, T. H.; Peterson, K. A.; Wilson, A. K., *J. Chem. Phys.* **2001,** *114* (21), 9244-9253.

60. Cossi, M.; Barone, V., *J. Chem. Phys.* **2001,** *115* (10), 4708-4717.

61. Mennucci, B.; Cancès, E.; Tomasi, J., *J. Phys. Chem. B* **1997,** *101* (49), 10506-10517.

62. Lu, W.; Chan, M. C. W.; Zhu, N.; Che, C.-M.; Li, C.; Hui, Z., *J. Am. Chem. Soc.* **2004,** *126* (24), 7639-7651.

63.   Suzuki, K.; Kobayashi, A.; Kaneko, S.; Takehira, K.; Yoshihara, T.; Ishida, H.; Shiina, Y.; Oishi, S.; Tobita, S., *PCCP* **2009,** *11* (42), 9850-9860.

5. Time-Resolved Spectroscopy of Cyclometalated Platinum Acetylide Complexes

INTRODUCTION

The previous chapter provided evidence of the presence of several interacting electronic excited states. These states and the hypothesis will be further investigated in this chapter through the use of time resolved spectroscopies. The comparison of empirically derived Hammett parameters with the excited state properties of a range of cyclometalated platinum acetylide complexes revealed that for a selection of the compounds, close lying electronic excited states leads to quenching of the strong emission that is expected for these types of complexes. Time resolved spectroscopic studies can be used to examine the mechanisms of excited states decay, analogous to the work performed in the chapter examining the newly synthesised dyad.

The exploration of radiative and non-radiative mechanisms through spectroscopic methods requires ultrafast time resolution.[1-2] This is achieved by transient methods, also called "pump-probe" spectroscopy. These are the methods by which a compound is excited (pumped) by a short laser pulse, and its reaction is measured by a probe pulse at certain time intervals after this event.

Due to the nature of MLCT excited states, investigation of transition metal complex excited states and their sensitivity to their environment has become a widely studied area of research using time-resolved methods.[2-3] The most common method is that of transient electronic absorption spectroscopy, TA, that has consistently been used to elucidate excited state chemistry. More recently, the development of time resolved infra-red techniques has permitted wide-spread TRIR investigations of the structural, electronic and dynamic properties of excited states in transition metal complexes to be revealed.[4-9]
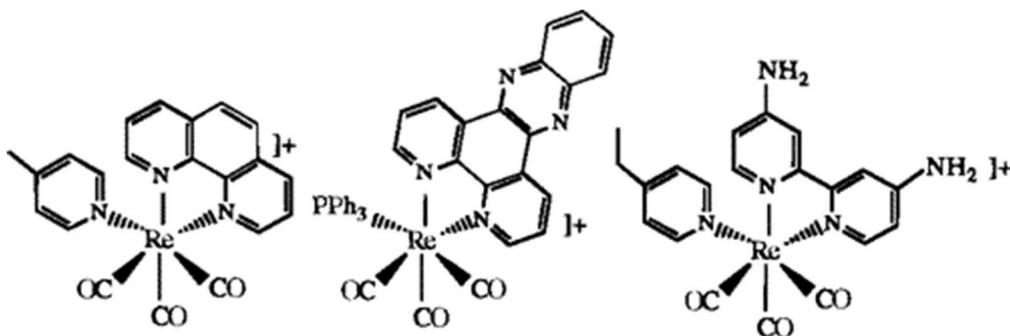
Figure 1 Rhenium complexes used to investigate MLCT and $\pi\pi^*$ excited states. These complexes displayed a shift of ν(CO) frequencies to the higher, or to the lower energies relative to the ground state depending on the nature of the excited state.[10]

In the context of using metal complexes as photosensitizers, early work concentrated on the investigation of rhenium diimine complexes featuring carbonyl ligands.[10-14] Molecules with these ligand sets were considered for study as the carbonyl ligand has strong oscillator strength and therefore strong sensitivity to infra-red probe light. These complexes had also already been exploited in sensing, chemiluminescence and light harvesting applications at the time of study. It was hoped that investigating the excited states of these species would allow the development of better photosensitizers.

Early studies of the rhenium complexes revealed the nature of the excited state; exposing electronic and structural changes associated with light absorption. The studies found that, consistent with MLCT excited state character, the complexes underwent a loss in π^* backbonding leading to raised carbonyl bond order causing a higher frequency transient signals compared to bleaches, shifting by $30 - 80$ cm^{-1}. No loss of carbonyl ligands was seen in the transient spectra, and the compounds were photostable. Other excited states, including dπ-π-

π* and π-π* states, were also investigated revealing subtle changes in the π systems upon excitation in these molecules, resulting in ~8 cm^{-1} downward shifts in frequencies. No structural changes could be seen in the excited state spectra, revealing the excited state structure is very similar to the ground state (Figure 1).[10, 12] Further developments in the techniques used to investigate excited state infra-red spectra allowed exploration of photophysical processes on the femtosecond timescale. The investigation of inter system crossing (ISC) rates in [Re(bpy)(CO)$_3$X] revealed a strong correlation between ISC times and the vibrational periods of the Re-L modes.[15]

The study of platinum CT states was furthered by using acetylide ligands opposite chelating bipy ligands, as functionality analogous to the metal carbonyls investigated in rhenium and osmium studies.[16-18] These molecules include the bipy acceptor ligand and the acetylide ligands, for which infra-red absorbancies associated with ν(C≡C) appear in the region of the spectrum uncomplicated by the signals of other functional groups, usually around 2000 cm^{-1}.[19] Combining these advantages with diimine ligands featuring ester carbonyl functionality allows the study of electron density redistribution across the molecules of.square-planar d^8 platinum complexes. Studying the movement of electron density across molecules allows the development of more efficient light harvesters and light-induced charge separators.[20]

1a : R$_1$ = CH$_3$

1b : R$_1$ CH$_3$)$_3$, R$_2$ = H

1c : R$_1$ O)NEt$_2$, R$_2$ = H

1d : R$_1$)$_2$Et, R$_2$ = H

2a : R = (

2b : R = I

2c : R = I

2d : R = (₃
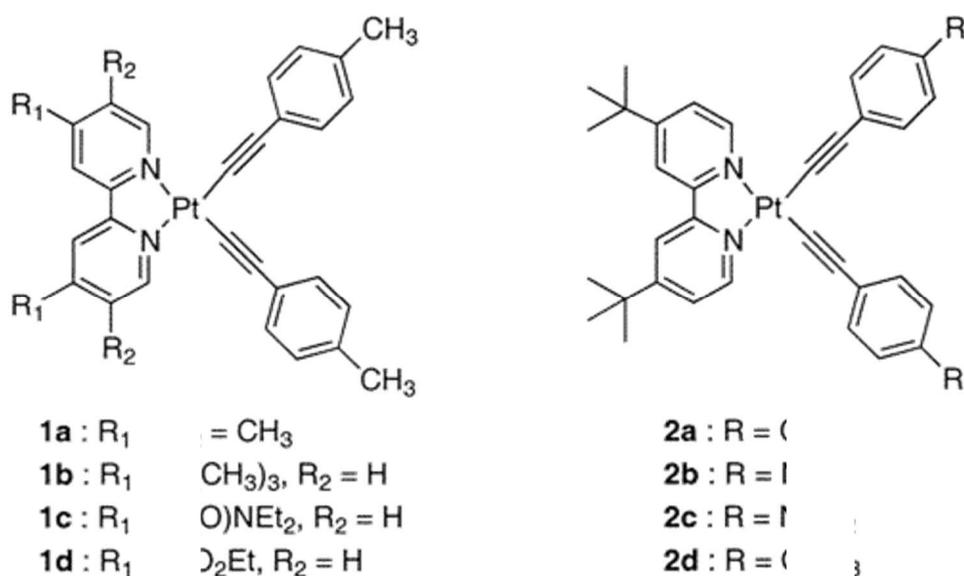
Figure 2 Platinum bipy bis-acetylide complexes used to study charge transfer states using step scan FTIR.[19]

Initial step-scan (s^2)FTIR of Pt(bipy)(CCPh)$_2$ compounds (Figure 2) revealed that upon excitation the signals associated with the energy of the acetylide CC stretching vibration moved to higher energy than the ground state vibration, from around 2115 cm^{-1} to around 2145 cm^{-1}. These results were consistent with a loss of dπ to π* back bonding character in the excited state, also seen in analogous rhenium compounds although the size of the shifts seen in Pt (II) complexes was much lower. This allowed the excited state of these molecules to be characterised as primarily MLCT/LLCT in nature. These studies only featured IR active reporters on the donor portion of the complexes, and only the region between 2000 and 2200 cm^{-1} has been investigated.[19]
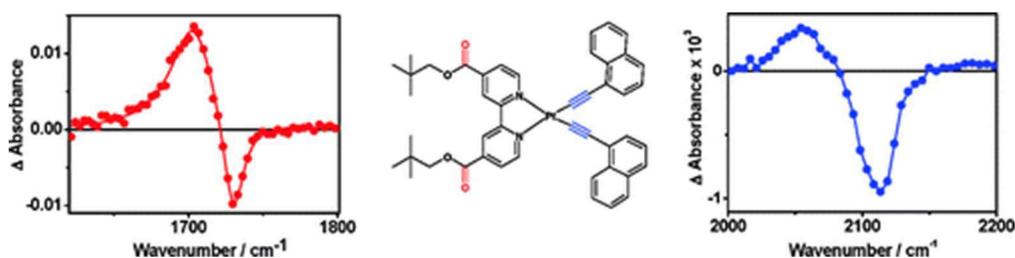
Figure 3 Studies on the propagation of charge transfer were undertaken on the complex show above. The left difference spectrum shows the signals associated with the ester at 50 ps delay and the right difference spectrum shows the signals associated with the acetylides at 50 ps delay.[20]

In order to investigate the dynamics of electron density shift across the molecule, ester groups were incorporated onto the bipy ligand, thus introducing IR reporters on both the donor (acetylide, >2000 cm^{-1}) and acceptor (ester group on the bipy, ~1720 cm^{-1}) which are well-separated not only in space, but also in energy (Figure 3). These studies revealed that the transfer of electron density from the acetylide to the ester upon excitation leads to the observed v(CO) signals for the excited species to be lower in frequency than the ground state for the ester by 30 cm^{-1}. This is also accompanied by a lowering in frequency of the excited state v(CC) signals compared to the ground state by 61 cm^{-1}. The lowering of v(CO) frequency in the excited state is expected as electron transfer to the bipy ester would populate the carbonyl antibonding orbitals, however the lowering of acetylide frequencies on entering an excited state is the opposite of previous TRIR studies. This behaviour was rationalised as a decrease of acetylide bond order as charge is transferred to the bipy as opposed to the previous study's interpretation that back bonding is reduced, therefore increasing acetylide bond order.[20]

The study of Pt(II) trans-acetylides in Donor-Bridge-Acceptor (DBA) arrangements, designed to facilitate light induced charge separation, has been enhanced by TRIR spectroscopy. The linear nature of trans-acetylides enhances CSS formation and the inclusion of naphthalene imide based acceptors includes other accessible triplet states.[14, 21-22]
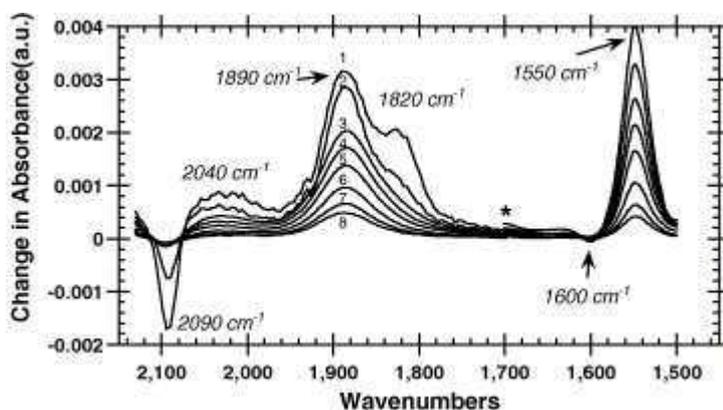
Figure 4 Difference TRIR spectra of a platinum trans-acetylide species 0 – 40 µs after excitation. The spectra were recorded in DCM solution purged with argon.[21]

Common signals in these compounds upon excitation include strong transients in the 1800 – 1900 cm^{-1} region of the IR spectrum. These have been attributed to allenic Pt=C=C=Ar moieties and are often indicative of a charge transfer from the Pt(CC) bridge to the acceptor. The large shift of up to 300 cm^{-1} was interpreted as a result of large changes in acetylide bond order upon accessing the excited state (Figure 4).[21]

Further investigation using T2DIR revealed that the pathways to the ground state could be manipulated using IR light pulses.[22-23] Typically, 2DIR & T2DIR is used to investigation coupling.[24-26] The time taken for vibrational changes to propagate due to Intramolecular Vibrational

122

Relaxation (IVR) and vibrational cooling can be investigated. Transient methods can give cooling times but also how infra-red pulses can affect the excited state. These studies revealed that IR light can be used for more than just assessing coupling and vibrational processes; it can also be used to adjust excited state populations.

A study of trans-acetylide Pt(II) DBA systems featuring phenothiazine (PTZ) donors and naphthalene monoimide (NMI) acceptors revealed that where branching decay pathway exist, excited state populations can be altered between pathways using IR light pulses. In this study, it was shown that by pumping the vibrational transitions of the acetylide bond, there was a suppression of the pathway leading to the formation of the CSS. This important finding leads the way to manipulating decay pathways in other compounds using pulsed IR excitation.[14, 22-23]

The aims of the work described in this chapter are to characterise the structure, electronics and dynamics of the excited states of [Pt(N^N^C)(CCPhR)] complexes using pump-probe methods. These characterizations will be compared to the literature regarding Pt(II) acetylides. The equilibrium dynamics described in chapter 4 will be more fully explored and further evidence for interacting states will be presented. Attempts to control the decay dynamics of a cyclometalated Pt(II) acetylide complex using IR light will also be undertaken.

RESULTS

Infra-red spectroscopy is a powerful tool for understanding the structure and electronic properties of compounds that feature infra-red handles, such as acetylides or esters. FTIR has been used to understand the ground state structure and electronic structure of complexes **6** – **15**. The information contained within the spectra have been used to understand the effect of electronic differences on bond strengths and how bond order is affected by donation from the substituted phenyl groups of these complexes into the acetylide.

Fourier Transform Infra-Red (FTIR) Spectroscopy

FTIR spectra for complexes **6** – **15** were recorded in dichloromethane at room temperature. Spectra with a range of 1650 to 2300 cm^{-1}, normalized to the intensity of the bipy-ester carbonyl stretching vibration v(CO) are shown to display ester carbonyl stretches, acetylide stretches and nitrile stretches (Figure 5). These bands are focussed on due to their positions on the accepting and donating moieties of the molecule. This allows comparison to time-resolved infra-red spectra in order to help assign excited states and dynamics.
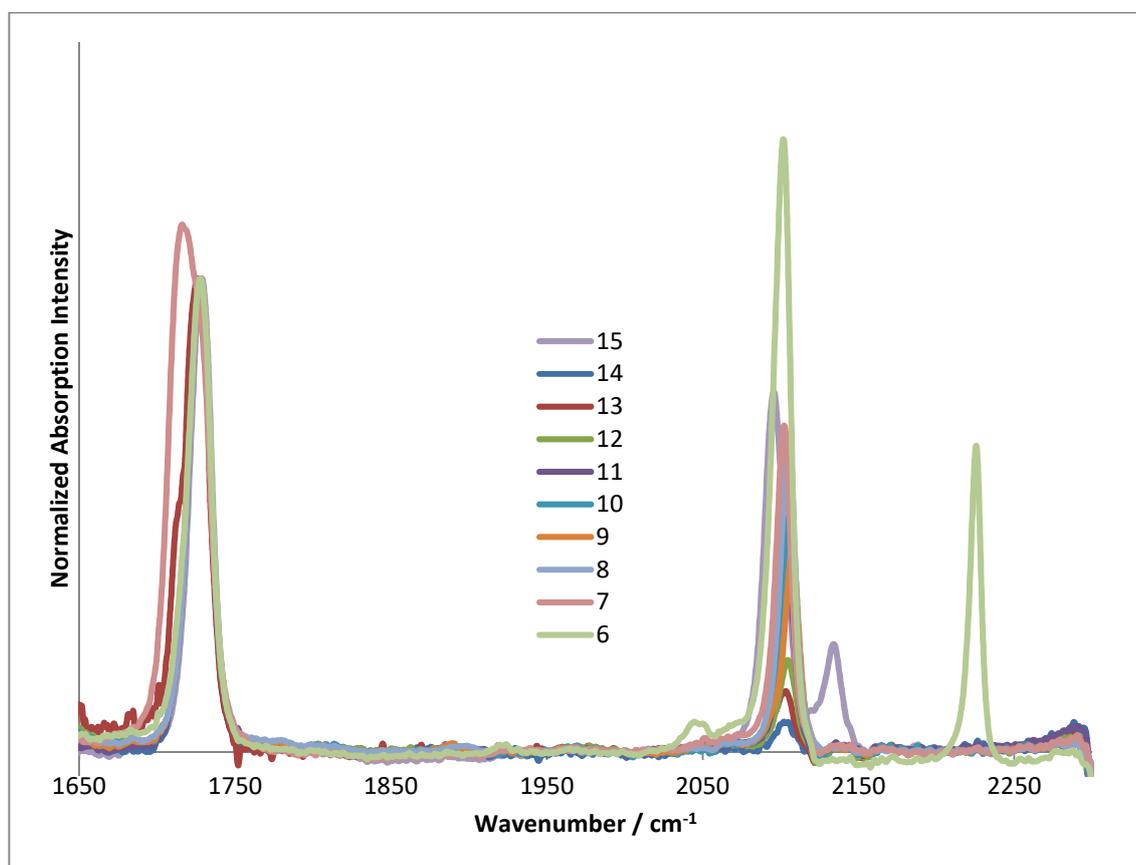
Figure 5 FTIR spectra recorded for complexes 6 – 15 in CH$_2$Cl$_2$ of the 1650 to 2300 cm^{-1} region of the IR spectrum. The absorptions are normalized against the bipy ester carbonyl signal in order to quantify the changing intensity of the acetylide v(CC) stretch.

The bipy ester carbonyl is located at around 1729 cm^{-1} in each compound. There is very little shift in the position of this band with changing acetylide donor, implying that the changing electronic effects of the donor does not affect the bpy ligand; the two ligands are not electronically coupled in the ground state. This could be due to the distance between donating and accepting groups or because the platinum atom acts as bottleneck to coupling. The lack of coupling seen is further supported by the small changes in first reduction potential, assigned to the bpy ester reduction, revealing that changes in donator electronics have little effect on

acceptor electronics. This effective insulation of acceptor against donor changes should reveal itself as very little difference for TRIR bands seen for all the complexes.

Small shifts in acetylide band of up to 10 cm^{-1} can be seen, which are larger than the 2 cm^{-1} shift detected for the ester ν(CO) bands. The more direct influence of a spatially close donor allows the differing donor character of the substituents to change the electron density over the acetylide, subtly changing bond order. The differing substituents also change the relative intensity of the acetylide ν(CC) bands. Assuming that bpy ester carbonyl bands do not change intensity, as there are no significant changes in acceptor electronics across these compounds, normalizing against these bands allows a comparison of the intensities of the acetylide bands relative to the unchanging carbonyl. This comparison shows a decreasing intensity with increased donating ability of the phenyl acetylide substituent, demonstrating how the dipole of the acetylide is disrupted by extra electron density being donated into the acetylide. A large change in bond order would result in a large shift in position of the band. The diminished intensity effect could be caused by extended conjugation, forming a Pt=C=C=Ar moiety. This suggestion may be supported by shifting peaks at around 1500 cm^{-1} as these could be due to conjugated double bonded C=C bands [please state the band shifts]. These peaks shift to higher energy with increasingly high donation into the acetylide by the donor group, suggesting that these bonds strengthen as their bond order increases.
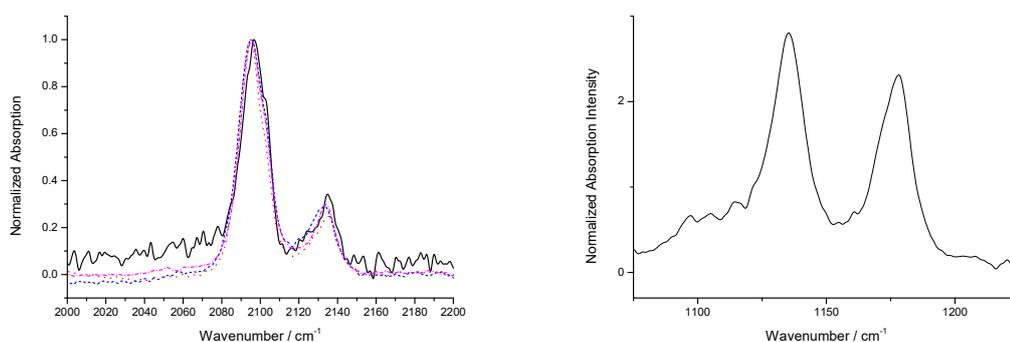
Figure 6 Left: The FTIR spectra of 15 in toluene (black), THF (red), CHCl$_3$ (blue) and CH$_2$Cl$_2$ (pink) between 2000 and 2200 cm^{-1}, normalized to the acetylide peak, displaying the acetylide νCC stretch peak and anomalous peaks. Right: FTIR spectrum of 15 in CH$_2$Cl$_2$ between 1075 and 1225 cm^{-1}, normalized to the acetylide νCC stretch peak, displaying high intensity CF$_3$ related bands.

Multiple ν(CC) acetylide peaks are apparent for complex **15** (Figure 6). This is unexpected as there is only one acetylide attached to the molecule. These bands could be due to combination bands intensity sharing with the acetylide or a solvent effect. In order to investigate solvent dependence, spectra were also obtained where the compound was solvated by chloroform, toluene and THF. These three solvents account for a broad polarity range. Chloroform can be a halogen bonder, THF can be a coordinating solvent and toluene can participate in the disruption of aggregation due to stacking effects.

The shoulder and extra peak are apparent across the four solvents. There is also very little shift in peak position. This suggests that the extra peaks are not related to the solvent and are inherent to complex **15**. Given the extremely strong Ph-CF$_3$ absorptions at around 1150 cm^{-1}, these extra peaks seen in the acetylide region are most likely combination bands, for example, of the 1135 cm^{-1} and 1178 cm^{-1} vibrations, with a vibration lost in the solvent background below 950 cm^{-1}. A spectrum showing frequencies that may form combination bands is in Annex C.

Time Resolved InfraRed (TRIR) Spectroscopy

Investigating how the excited states of these compounds interact and how this interaction changes with the nature of the acetylide requires a comparison of the time resolved characteristics of complexes **6 – 15**. For time-resolved infra-red spectra, comparing peak position and shape enables an analysis of where the excited state electron density has been moved from and to. The broadening seen in some spectra can be compared to analyse how the excited states of each compound interact and how acetylide donating ability changes this. Comparing dynamics can reveal quenching processes and displays how electron donating nature changes the lifetime of different excited states.
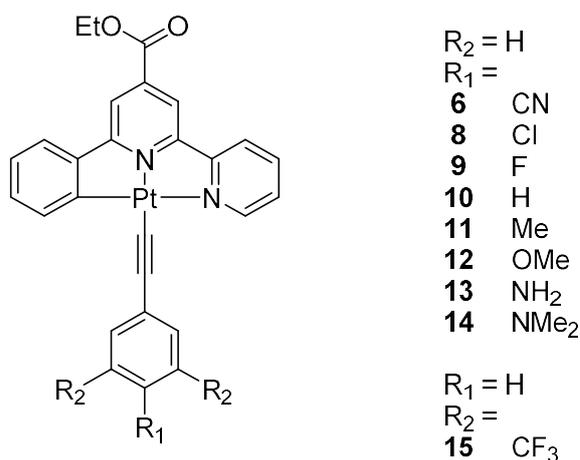
Figure 7 General structure and numbering diagram for the cyclometalated platinum (II) complexes studied using ultrafast spectroscopies in this chapter.

Time-resolved infra-red (TRIR) spectroscopy was performed for complexes **6** and **8 – 15** in CH_2Cl_2 solution at room temperature (Figure 7). Difference spectra at times between 1 and 3500 ps were recorded for the mid-IR $1644 – 2146$ cm^{-1} region. This region is characteristic for the IR absorbances of the carbonyl and ethynyl reporters based on the donor and acceptor portions of the complexes. The timescale allows characterization of processes not resolved by time-resolved emission measurements, which typically cannot be used to resolve lifetimes less than 2 ns reliably on the equipment that was available.

The time-resolved infra-red instrument used to record the data is the Rutherford Appleton Laboratories ULTRA setup. This instrument has been described in chapter 2.[27] The data from these experiments were processed using Glotaran software.[28]

Using the data obtained from these experiments and the lifetime values, evolution associated spectra and decay associated spectra from the Glotaran fits, the excited states of the Pt(N^N^C)acetylide complexes can be characterised. The sub nanosecond dynamics can be probed to reveal structural changes in the donor and acceptor moieties after excitation, as well as interactions between different excited states that may be accessible. The data presented herein will help to support the hypothesis that there are multiple interacting excited states for each molecule, which cause luminescence intensity and lifetime quenching. The shape and position of the peaks seen will allow structural changes required for these exchange processes to be explored.

There are three types of behaviour observed for the different cyclometalated platinum acetylide complexes, consistent with observations made using emission spectroscopy. These have been described below, highlighting the possible mechanisms that could explain the observed results.
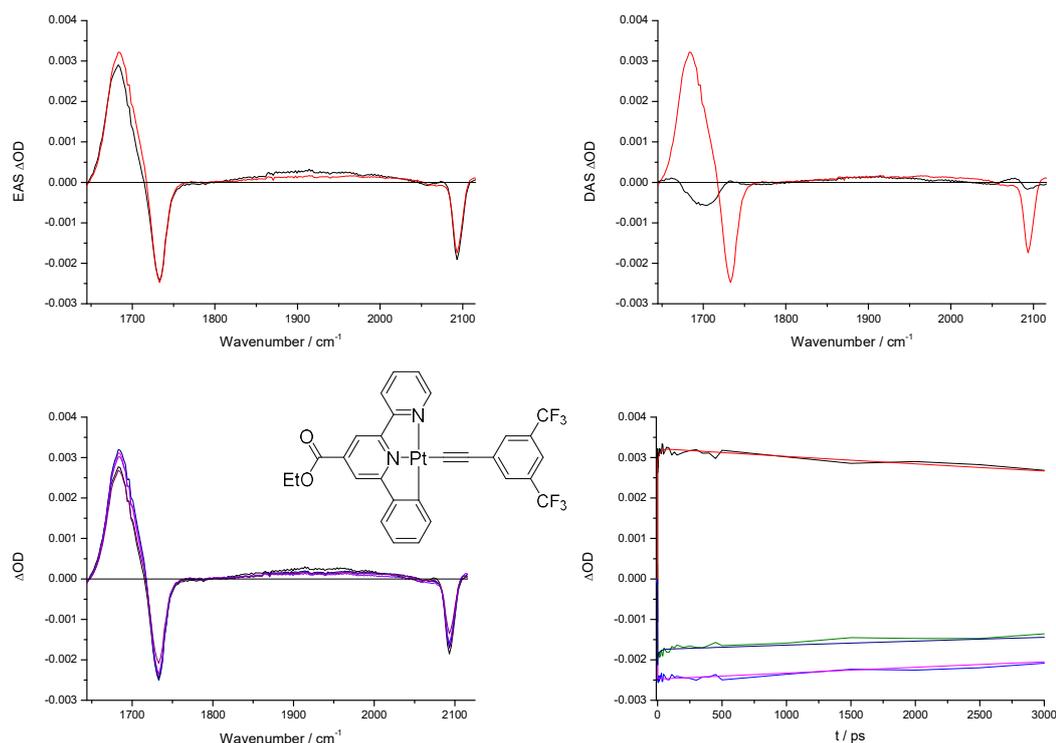
Figure 8a) Evolution Associated Spectra for τ_1 (black) and τ_2 (red) associated decays calculated for 15 between 1644 and 2115 cm^{-1}. b) Decay Associated Spectra for τ_1 (black) and τ_2 (red) associated decays calculated for 15 between 1644 and 2115 cm^{-1}. c) Spectra after excitation of 15 recorded in CH$_2$Cl$_2$ solution between 1 ps and 3000 ps. d) Decay traces with exponential fits recorded at selected wavenumbers; 1683 cm^{-1} (black and red), 1733 cm^{-1} (light blue and pink) and 2093 cm^{-1} (green and dark blue).

After exciting **15** with 50 fs, 400 nm laser pulse, measurements of the IR spectrum between 1644 and 2115 cm^{-1} at time delays between 0.25 ps and 3 ns have been performed. These spectra reveal that after excitation, transients and bleaches associated with the loss of ground state and formation of one or more excited states takes places. By monitoring the decay of these signals over time, the dynamics of these excited states can be assessed (Figure 8).

Signals associated with ester group appear as the transient at 1685 cm^{-1} and the bleach at 1733 cm^{-1}. The bleach maxima is displaced to lower energy compared to the FTIR spectrum absorbance maxima of 1728.5 cm^{-1} due to overlapping transient and bleach signals. The transient's shift to lower frequency than the bleach implies the loss of bond order consequent with population of the carbonyl π^* orbitals, this is consistent with the DFT results in the previous chapter suggesting electron density is transferred to the bipy ester ligand in the excited state.

A bleach signal associated with acetylide appears immediately after excitation at 2095 cm^{-1}. This signal strongly correlates with the signal seen at 2095.5 cm^{-1} in the ground state FTIR spectrum, especially as the resolution in the TRIR experiments was 4 cm^{-1}. This bleach is accompanied by an extremely broad, weak transient between 1800 cm^{-1} and 2050 cm^{-1}.

These signals decay by a biexponential process with lifetimes of τ_1 = 18.0 ± 0.70 ps and τ_2 = 15.8 ns. The value of τ_1 is higher than would usually be expected for vibrational cooling in platinum acetylides but similar to the vibrational cooling of a Pt(MesBIAN)(acetylide)$_2$ species, which displays a vibrational cooling time of 14 ps.[18, 29] This is much longer than would be seen in organic molecules but still shorter than most metal carbonyls. The longer decay lifetime is a model for the long lived excited state of the complex. This is not accurately modelled by measurement

over such a small time window and is included to more accurately model short-lived excited states; the lifetime of this state obtained from emission studies is 567 ns..

Comparing the decay associated spectra (DAS) to the evolution associated spectra (EAS) gives further evidence of vibrational cooling as the τ_1 associated decays in the DAS indicate where there is increasing intensity in the EAS. This makes the transfer of intensity from low frequency to high frequency for the ester transient more clearly seen, where there is no obvious narrowing of the peak in the EAS.

The lack of strong acetylide transients seen in **6** and **15** indicates that there is either a loss of acetylide character or dipole moment in the excited state of these complexes. This is accompanied by a single bleach peak associated with the ground state acetylide. MOs calculated by DFT suggest that excitation will lead to a loss of phenyl acetylide π character in the excited state. This could lead to a loss of acetylide character in the C-C bond as depopulation of the π orbitals would lead to a bond order less than 3. The small amount of transient signal seen almost completely decays with a lifetime of less than 10 ps. This indicates that any transient character comes from interaction between excited state formed of LUMO, HOMO, HOMO-1 and HOMO-2 whilst hot. This is supported by the calculated MOs suggesting the HOMO is orthogonal to the other states and cannot readily interact with them, due to limited orbital overlap. The extreme broadness of the band that exists to the end of data collection may be associated with a strong interaction of the molecule with solvent molecules, creating an ensemble of states.
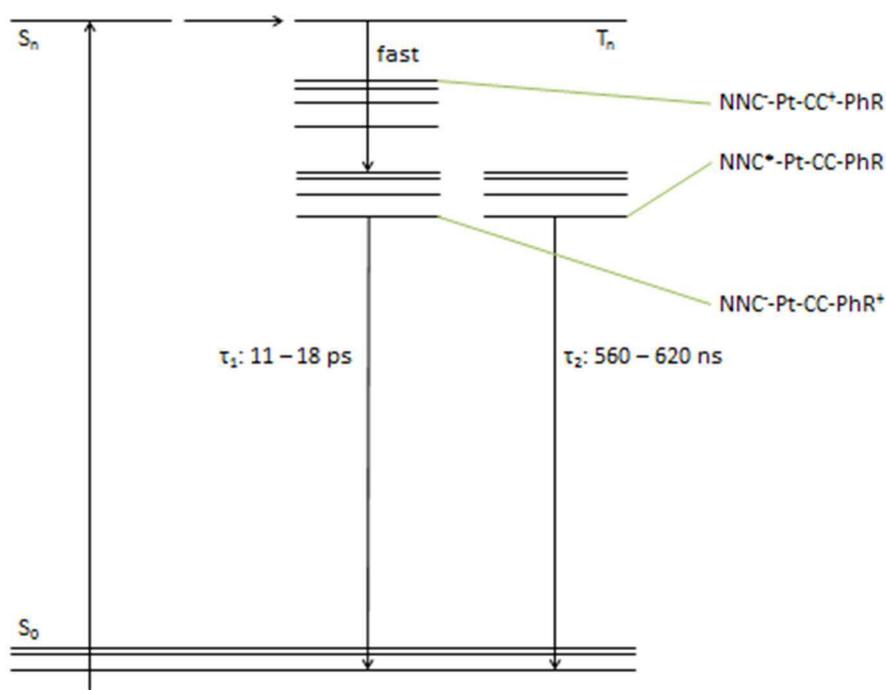
Figure 9 Jablonski diagram summarizing the decay pathways of complexes 6 and 15.

The first regime described (Figure 9) is that of complexes **6** and **15**. In this series of decays, there is a fast decay after intersystem crossing to the lowest two excited state which happen to be the N^N^C localised MMLL'CT state and the ^{3}ILCT state. There is no evidence that these two states interact and each decays to the ground state with characteristic lifetimes of 11 – 18 ps for the ^{3}ILCT state and 560 – 620 ns for the MMLL'CT. This is supported by the fitting of only two lifetimes to the TRIR spectra and the high emission quantum yields relative to the other complexes, suggesting no loss of luminescence quantum yield through a quenching pathway. These states are non-interacting and therefore cannot be controlled using IR light.

Complex 11 TRIR – Behaviour 2

After exciting **11** with a 50 fs, 400 nm laser pulse, measurements of the IR spectrum between 1628 and 2146 cm^{-1} at time delays between 0.25 ps and 3 ns have been recorded (Figure 10). Excited state signals associated with the ester appear between 1650 and 1750 cm^{-1}, with a bleach signal at 1733 cm^{-1} and a transient signal at 1685 cm^{-1}. The bleach maximum is displaced to lower energy compared to the FTIR spectrum absorbance maximum of 1727.5 cm^{-1} due to overlapping transient and bleach signals. These results are consistent with the DFT calculated LUMO being located on the bipy ester fragment. Asymmetry and broadening indicate multiple populated excited states.

Figure 10a) Evolution Associated Spectra for τ_1 (black), τ_2 (red) and τ_3 (blue) associated decays calculated for 11 between 1628 and 2146 cm^{-1}. b) Decay Associated Spectra for τ_1 (black), τ_2 (red) and τ_3 (blue) associated decays calculated for 11 between 1628 and 2146 cm^{-1}. c) Spectra after excitation recorded for 11 in CH$_2$Cl$_2$ solution between 1 ps and 3000 ps. d) Decay traces with exponential fits recorded for selected wavenumber signals; 1685 cm^{-1} (black and red), 1735 cm^{-1} (light blue and pink), 1903 cm^{-1} (green and dark blue) and 2107 cm^{-1} (light purple and dark purple).

A bleach signal associated with acetylide appears immediately after excitation at 2109 cm^{-1}. This signal strongly correlates with the signal seen at 2105 cm^{-1} in the ground state FTIR spectrum. This bleach is accompanied by an extremely broad transient between 1750 cm^{-1} and 2050 cm^{-1}, which narrows to a broad transient between 1800 cm^{-1} and 1980 cm^{-1} with the reveal of a small peak at 1996 cm^{-1}. This narrowing is attributed to vibrational cooling. There is no shift in transient peak maximum after vibrational cooling, as was seen in **8**.

These results indicate three processes with three lifetimes associated with them with values of τ_1 = 1.38 ± 0.03 ps, τ_2 = 17.5 ± 0.28 ps and τ_3 = 12.7 ns. As before, the value of τ_3 cannot be accurately modelled using a 3 ns data set and is included to improve the fitting of the shorter lifetimes. Using the EAS and DAS of these lifetimes it can be seen that the τ_1 DAS acetylide bleach is a mirror of the τ_3 acetylide transient, implying that τ_1 is the lifetime of a process that transfers population from one excited state to another. This supports the equilibrium hypothesis posed in the previous chapter as these results suggest that the vibrational cooling of the excited states transfers population from a short lived, higher lying excited state to a long lived, lower lying

129

excited state. This further supported by the DAS of τ_1 revealing there is no recovery of the ground state acetylide bleach and therefore no ground state recovery. In comparison τ_2 and τ_3 DAS show ground state acetylide bleach recovery, indicating τ_2 and τ_3 are decays to the ground state. The τ_2 process takes place independently of other processes. The EAS reveals these transitions are further separated energetically than in **8**, as indicated by the larger difference in EAS acetylide transient peaks maxima.

Complexes **8 – 12** display broad transient signals after excitation with 400 nm, 50 fs light pulses. These very broad transients accompany the acetylide bleach signal and both decay with a multi-exponential lifetime. At times greater than 20 ps, the asymmetry of the acetylide transient becomes obvious. This is accompanied by the reveal of a second transient acetylide peak after vibrational cooling. The reveal of two peaks, both decaying with the same kinetics, implies there are two excited states that are linked and decay together. The broad signals seen at 1850 – 1950 cm^{-1} are similar to those seen in the TRIR spectra of Pt(MesBIAN)(CC)$_2$ and Pt(II) trans-acetylides.[18] It is likely these broad signals are attributable to lowered bond order in the acetylide, comparable to the broad transient bands seen at 1820 cm^{-1} in Pt(MesBIAN)(CC)$_2$ attributed to the symmetric stretching mode. This could also be indicative of a Pt=C=C=Ar type allenic bonding regime, as suggested in some literature for Pt(II) trans acetylide compounds.[21]

The higher frequency narrower band seen in each is due to the strengthened trans effect of a partial charge transfer to the bipy compared to the ground state. This increases Pt-CC back bonding but less than the charge transfer away from the acetylide, reducing bond order less than a charge transfer from the acetylide, as an inductive effect has less influence than a direct loss of bond order. This effect is seen where charge separated states form in trans acetylide complexes.[23] A transient signal appears at around 2000 cm^{-1} where the acetylide bridge is influenced by the charge separation but bond order is unchanged.

This evidence further supports the hypothesis that the shortened lifetimes of complexes **8 – 12** are due to equilibrium between close lying excited states as shown by Hammett plots and DFT modelling; both excited states decay with the same bi-exponential parameters.
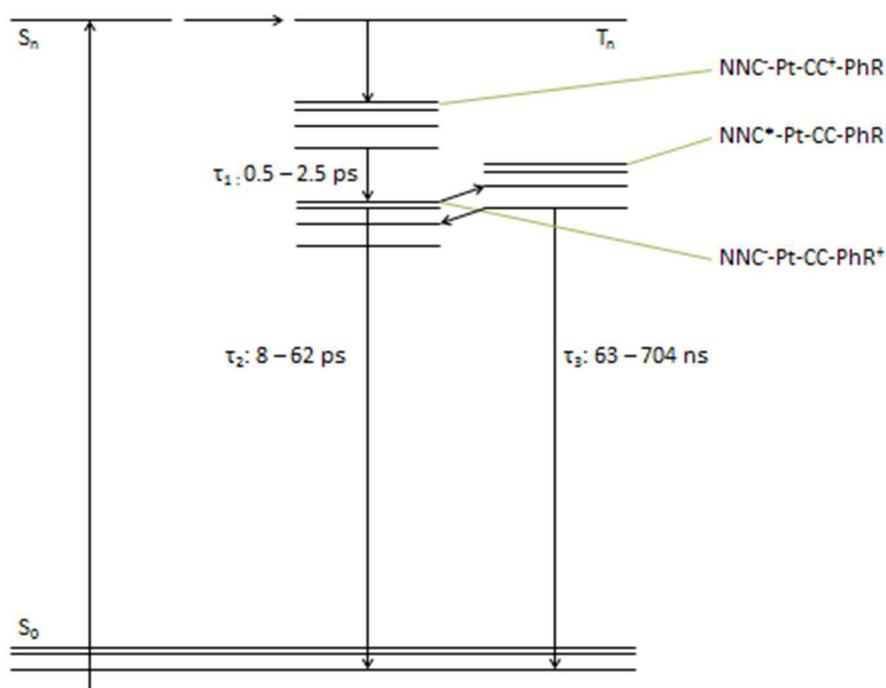
Figure 11 Jablonski diagram summarizing the decay pathways of complexes 8 – 12.

Complexes **8** – **12** have decay pathways determined by their equilibrating lowest excited states (Figure 11). These are quickly reached through the decay of the acetylide localized states to a further charge separated state and the emissive MMLL'CT state. This is supported by the DAS of τ_1 mirroring τ_3 suggesting the shortest lived state with allenic Pt=C=C=Ar character feeds two states with different localizations. The τ_2 decay represents the decay of a state with primarily Pt=C=C=Ar character whilst τ_3 features two bands, representing two states, with one decay for both. This suggests that the ^{3}ILCT state decays faster than the MMLL'CT state as would be expected but also that this decay pathway becomes less important the less populated the ^{3}ILCT is. This effect is accompanied by a lowering of emission quantum yield with shorter τ_2 values. This supports the hypothesis that emission intensity is quenched by population loss to a dark state. This behaviour suggests that even if a difference in relative populations was promoted using pulsed IR light, the equilibrium between the two lowest states would lead to no overall change in the long term population differences after fast vibrational cooling.

Complex 14 TRIR – Behaviour 3

After exciting **14** with a 50 fs, 400 nm laser pulse, measurements of the IR spectrum between 1625 and 2147 cm^{-1} at time delays between 0.25 ps and 3 ns have been recorded (Figure 12). Excited state signals associated with the ester appear between 1650 and 1750 cm^{-1}, with a bleach signal at 1733 cm^{-1} and a transient signal at 1678 cm^{-1}. The bleach maxima is displaced to lower energy compared to the FTIR spectrum absorbance maxima of 1725.5 cm^{-1} due to overlapping transient and bleach signals. These results are consistent with the DFT calculated LUMO being located on the bipy ester fragment. Asymmetry and broadening indicate multiple populated excited states.
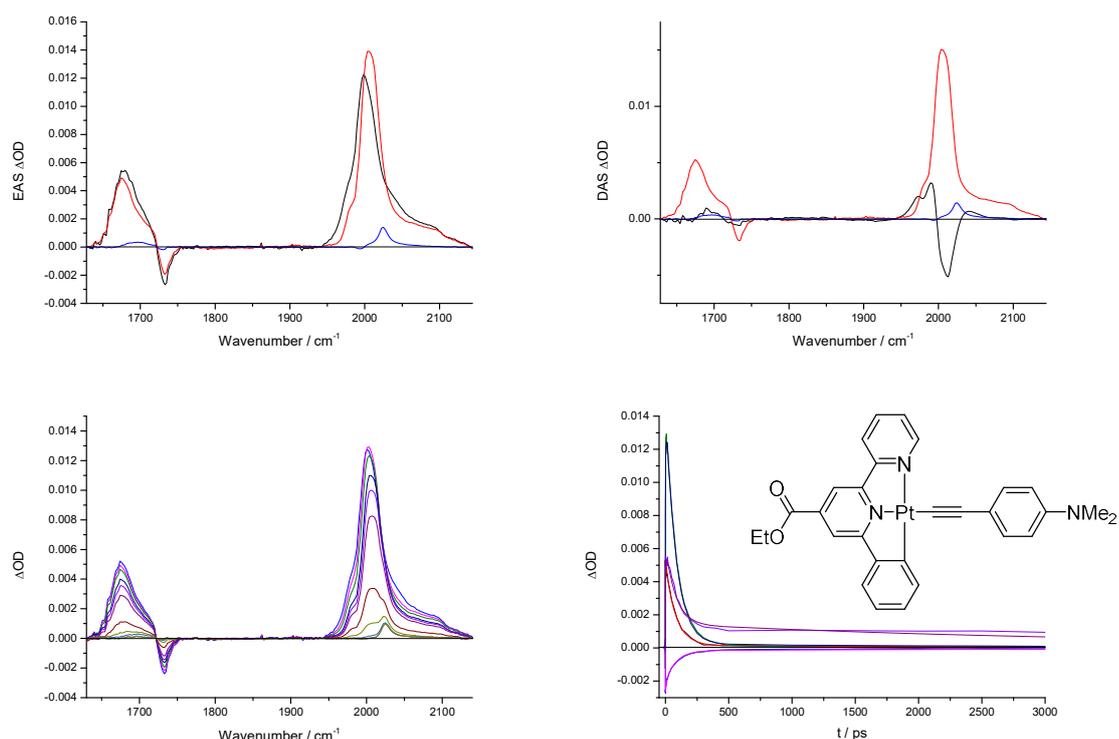
Figure 12a) Evolution Associated Spectra for τ_1 (black), τ_2 (red) and τ_3 (blue) associated decays calculated for 14 between 1628 and 2144 cm^{-1}. b) Decay Associated Spectra for τ_1 (black), τ_2 (red) and τ_3 (blue) associated decays calculated for 14 between 1628 and 2144 cm^{-1}. c) Spectra after excitation recorded for 14 in CH$_2$Cl$_2$ solution between 3 ps and 3000 ps. d) Decay traces with exponential fits recorded for selected wavenumber signals; 1678 cm^{-1} (black and red), 1733 cm^{-1} (light blue and pink), 2005 cm^{-1} (green and dark blue) and 2024 cm^{-1} (light purple and dark purple).

There is no apparent bleach signal associated with acetylide, as would be expected considering how weak the acetylide band is in FTIR spectra. After excitation, transients between 1975 cm^{-1} and 2094 cm^{-1} appear, no narrowing is apparent and at long time scales a small peak at 2026 cm^{-1} is revealed. The lack of peak narrowing suggest that vibrational cooling takes place faster than the instrument is able to resolve. These peaks are much narrower than those seen in the other compounds, suggesting a lack of equilibria or interconversion processes.

These results indicate three processes with three lifetimes associated with them with values of $\tau_1 = 7.14 \pm 0.13$ ps, $\tau_2 = 81 \pm 0.48$ ps and $\tau_3 = 3.93$ ns. As before, the long τ_3 cannot be accurately modelled using a 3 ns data set and is included to improve the fitting of the shorter lifetimes. Using the EAS and DAS of these lifetimes it can be seen that the τ_1 DAS acetylide bleach is a mirror of the τ_2 acetylide transient, implying that τ_1 is the lifetime of a process that transfers population from one excited state to another. This contrasts the other complexes that display transfer from the τ_1 associated state to the τ_3 associated state. The τ_3 decay is no longer

associated with either of the other two decays. This suggests that the long lived emissive state is no longer fed by the vibrational decay of the τ_1 associated excited state.

Complexes **13** and **14** display much narrower transient acetylide peaks than complexes **8 – 12**. The peaks seen for **13** and **14** are also at higher frequency than the equivalent peaks in the spectra of **8 – 12**. The higher frequency peaks suggest that charge transfer out of the acetylide is compensated by charge transfer in from another part of the molecule. In these cases the nitrogen on the phenyl acetylide can use its free lone pair to donate electron density in to the acetylide after excitation.

The τ_1 associated spectra of both these complexes shows no appreciable recovery of the ground state bleaches and therefore this process, with a lifetime of around 8 ps, is not a decay of the short lived excited state to the ground state. The τ_1 DAS does mirror the τ_2 DAS. This result suggests that the short lived excited state decays into a second excited state that lives several tens of picoseconds. The τ_2 DAS suggests that this excited state does decay into the ground state; there is recovery of the ground state bleaches and a recovery of the ester associated transient peak. The τ_3 DAS also decays to the ground state but is not associated with the τ_1 DAS, implying there is no interaction of the long lived emissive state with the short lived (~8 ps) state. This contrasts with complexes **8 – 13**, where the short lived (>2.5 ps) vibrationally hot state appears to be feeding the long lived emissive state as it cools.
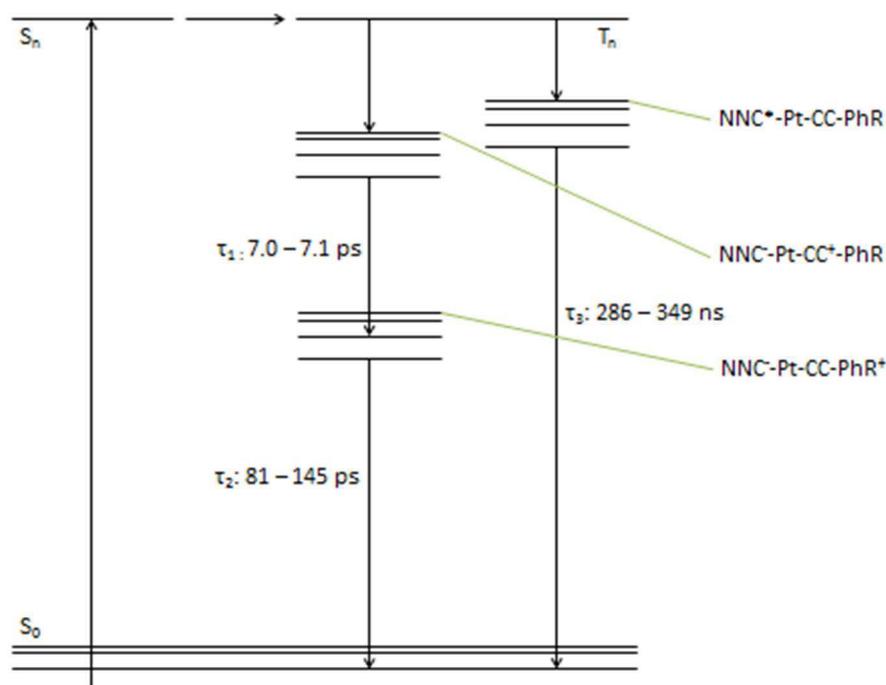
Figure 13 Jablonski diagram summarizing the decay pathways of complexes 13 and 14.

Complexes 13 and 14 have branched decay pathways (Figure 13). There is a slow decay through the Phbipy localized MMLL'CT state and a fast decay through the acetylide localized MLCT and ILCT states. These acetylide and phenylacetylide states do not have the allenic character of complexes **6, 8 – 12** and **15**, as evidenced by their narrower transient IR bands. This is likely caused by the donating nitrogen groups disrupting the extended delocalization in the excited state. The acetylides of **13** and **14** do not experience the reduction in bond order seen in other complexes. The fast relaxation to the ground state through the acetylide accounts for a much larger portion of the populated excited states, due to high lying acetylide localized states being preferentially populated compared to the PhBipy MMLL'CT state leading to very low emission quantum yields. Lifetimes to move from the NNC⁻Pt-CC⁺-PhR state to the NNC⁻Pt-CC-PhR⁺ are

much larger energy difference between the two state than in complexes **8 – 12**, revealed by CV and DFT modelling.

Comparison of the three decay paradigms

The analyses of the three paradigms have been split into two, the first part of the analysis looks at the ester signal and dynamics. The second part of the analysis looks at the acetylide signals. This investigates how the ground state HOMO, HOMO-1 and HOMO-2 behave when depopulated in the excited state, the population of a single LUMO in all excited states and the changes in lifetime that the interaction of different excited states cause. This can help describe how changes to the acetylide change the equilibriums described in the previous chapter. Photophysical data used for analysis is located in Table 1.

Examination of signals associated with the ester group

Examining the ester signals shows very little variation between the 9 compounds. The bleach peak is consistently at 1733 cm^{-1} and transient peaks between 1673 cm^{-1} and 1685 cm^{-1}. There is very little narrowing due to vibrational cooling present at early time scales (< 10 ps) and there is very little peak shift in **6**, **13**, **14** and **15**. There is some peak shift in compounds **8**, **9**, **10**, **11** and **12** from high to low energy however this may be accounted for by overlap of early time acetylide transients that is removed by cooling processes at short timescales (< 10 ps). The asymmetry of bleach and transient peaks can be accounted for, by overlap between the two signals distorting the overlapping portion of both signals. This all suggests that there is only one transient and one bleach of the ester carbonyl stretch for each complex, revealing that for each complex, the electron density of all three excited states that could be populated is shifted into the bipy ester π* MO, as predicted by DFT modelling. There is no significant change in excited state ester behaviour for any complex, as this moiety is common to all of them and the metal perhaps acts as a bottleneck to electronic coupling.

Examination of signals associated with the phenyl acetylide group

This lack of variation, seen in the signals associated with the ester group is not seen in the acetylide associated signals. Three different regimes can be seen across the nine analysed compounds. This is expected due to the different excited state behaviours caused by multiple close lying HOMOs. Very little transient signal is seen in **15** and **6**, very broad transients with large shift to lower energies are seen in **8 – 12** and defined bands with no strong shift is seen in compounds **13** and **14**. These results have been compared to provide evidence for the likely decay pathways in each of the three mechanisms.

The decay of the signals in all complexes has been fit to a three exponential function that has lifetime of τ_1 < 2.5 ps, 8.1 ps < τ_2 < 62 ps and τ_3 > 3 ns. The shortest lifetime process in each complex is a vibrational cooling process that is characterised by a narrowing of the acetylide transients with a peak shift to higher frequency. This occurs to a lesser extent in **6** and **15** due to greater coupling between interacting excited states, reducing IVR decay lifetimes. The second process characterised by τ_2 is a short lived decay of an electronically excited state. The lifetime of this process decreases with increasing acetylide donor potential, implying that the donating ability of the phenyl acetylide strongly affects the lifetime of this state. The final lifetime is longer than the experimental time window and is therefore not an accurate reflection of the lifetime of long lived species; this is more accurately modelled by emission decay lifetime fitting.

These two pathways are separated in a way that the acetylide based excited states are not interacting with the emissive excited state. This should allow infra-red pulses to deactivate the acetylide based states by pumping out the acetylide ν(CC) stretch.

Table 1 Photophysical properties recorded for the complexes investigated using ultrafast spectroscopies. a) Recorded in CH_2Cl_2 solvent with 0.1 M [NBu$_4$][PF$_6$] electrolyte vs Fc/Fc$^+$ reference. b) Recorded in deaerated CH_2Cl_2 solvent. c) Recorded by TRIR spectroscopic methods in aerated CH_2Cl_2 solvent. d) Recorded by single photon counting spectroscopic methods in deaerated CH_2Cl_2 solvent. e) Recorded in deaerated CH_2Cl_2 solvent referenced against [Ru(bpy)$_3$]Cl$_2$ in water, $\Phi = 0.063$.[30]

Complex	$E_{1/2}^{RED}$ / V[a]	E_{pa}^{OX} / V[a]	λ_{EM} / nm[b]	E_{EM} / cm-1[b]	τ_1 / ps[c]	τ_2 / ps[c]	τ_3 / ns[d]	Φ_{Em}[e]	k_r / s^{-1}	k_{nr} / s^{-1}
14	-1.62	-0.08	602	16600	7.14 ± 0.13	81.0 ± 0.48	515 ± 52	2.35E-03	4.57E+03	1.94E+06
13	-1.61	0.00	605	16500	6.95 ± 0.15	155 ± 1.48	545 ± 55	2.77E-03	5.09E+03	1.83E+06
12	-1.60	0.03	610	16400	0.63 ± 0.01	8.1 ± 0.18	445 ± 45	2.38E-03	5.34E+03	2.24E+06
11	-1.60	0.13	644	15500	1.38 ± 0.03	17.5 ± 0.28	63 ± 6.3	3.40E-03	5.40E+04	1.58E+07
10	-1.60	0.09	624	16000	2.42 ± 0.09	47.0 ± 1.86	271 ± 27	2.10E-02	7.76E+04	3.61E+06
9	-1.60	0.12	622	16100	2.40 ± 0.08	46.4 ± 1.51	190 ± 19	1.31E-02	6.91E+04	5.19E+06
8	-1.59	0.13	615	16300	1.93 ± 0.08	61.9 ± 3.73	400 ± 40	3.98E-02	9.95E+04	2.40E+06
7	-1.57	0.18	603	16600			704 ± 70	1.14E-01	1.62E+05	1.26E+06
6	-1.57	0.19	599	16700		11.3 ± 0.67	619 ± 62	1.33E-01	2.15E+05	1.40E+06
15	-1.56	0.31	594	16800		18 ± 0.70	567 ± 57	1.15E-01	2.03E+05	1.56E+06

UV/Vis Transient Absorption for complexes 12 – 14

TRIR spectroscopy results suggest that, for complexes **13** and **14**, phosphorescence occurs not from the lowest excited state. The lower in energy, short-lived charge separated state does not feed the emissive triplet MMLL'CT state and therefore if these two compounds are excited in their lowest energy transitions, no emissions will be seen and the excited state will decay with dynamics associated only with the CSS. In comparison, complex **12**, which represents the onset of behaviour associated with linked states, as seen in the Hammett and TRIR analyses, should show long lived emissive states when the lowest electronic transitions are selectively excited. This has been achieved through the use of UV/vis transient absorption spectroscopy.

Picosecond transient absorption is pump-probe technique used to investigate excited states UV/vis absorption. Picosecond transient absorption experiments were performed on a home-built pump-probe setup. The fundamental output (1064 nm, 20 ps, 10 Hz, 3 mJ) of a mode-locked Nd:YAG laser was passed through a computer controlled optical delay line and focused into a 10 cm length cell filled with D_2O to generate a continuum probe light source. The broadband supercontinuum was then split into both signal and reference beams, being detected by a spectrograph (home-modified monochromator) fitted with a CCD camera. The sample was excited with the output 450 - 580 nm from a dual stage optical parametric oscillator-optical parametric amplifier (OPO-OPA), itself pumped with the third harmonic (355 nm, 10 Hz, 6 mJ) of the aforementioned laser. The typically energy of the pump was 1.5-2.0 mJ per pulse with a repetition rate of 10 Hz. The instrumental response of the setup is estimated to be ca. 25 ps. Analyte solutions were contained within 2 mm pathlength quartz cuvettes, with the solution being flowed during data acquisition. All experiments were conducted with the assistance of George A Farrow and Simon E Greenough. Data processing of transient absorption data and spectra was performed using Glotaran software.[28]

Picosecond transient absorption spectra have been used to investigate whether emission is from the lowest excited state. By pumping different visible light absorptions of each molecule and observing transient spectra and dynamics, it is possible to determine whether the emission is from the excited states associated with high or low energy absorptions. The dynamics recorded in these experiments can also be used to corroborate dynamics recorded in TRIR experiments.

Complex 12 UV/Vis TA

Transient absorption spectra of complex **12** have been recorded, where **12** has been excited by either 450 nm or 550 nm pulses of light and the 390 – 935 nm spectrum has been recorded at intervals, between 0 and 3500 ps after excitation (Figure 14). In both cases, immediately after excitation, broad structured transients appear at 533 – 879 nm. These transients are accompanied by a bleach between 439 – 532 nm associated with ground state absorptions. These transients and bleaches decay with a lifetime of around 5 ns. This long lifetime is not modelled accurately using the data, as data collection stops at 3.5 ns and the lifetime is longer than the data collection. The shorter lifetime of 8.15 ps is not resolved using this instrumentation, as this lifetime is shorter than the instrument response of ~25 ps.
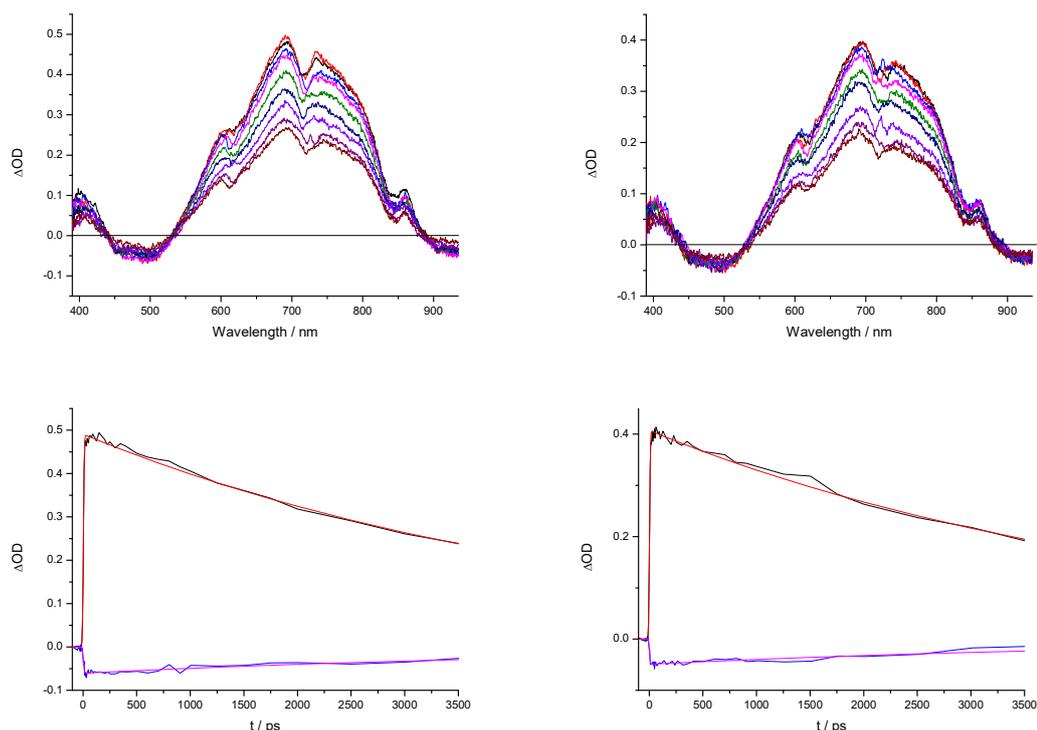
Figure 14 Top Left: TA spectra of 12 when excited with 450 nm light, recorded in CH$_2$Cl$_2$ between 0 and 3500 ps. Bottom Left: Decay traces for absorption intensities at 689 nm and 493 nm for 12 between -50 and 3500 ps after excitation with 450 nm light. Top Right: TA spectra of 12 when excited with 550 nm light, recorded in CH$_2$Cl$_2$ between 0 and 3500 ps. Bottom Right: Decay traces for absorption intensities at 689 nm and 494 nm for 12 between -50 and 3500 ps after excitation with 550 nm light.

This behaviour is consistent with TRIR, where there is a long lived component of decay with a lifetime of > 3 ns. Both short lived components observed in the TRIR spectra cannot be resolved on the UV/vis TA setup used and therefore these cannot be corroborated. Despite the inability to assess the short lifetime decay components, it can be seen that **12** forms a long lived excited state, which can be assumed to be the emissive excited state. Exciting in different bands of the UV/vis spectrum of **12** produces no difference in TA spectra recorded at late times. This implies that the emission is from either the lowest excited state or a combination of the lowest excited state and some other close lying excited state.

Complex 14 UV/Vis TA

Transient absorption spectra of complex **14** have been recorded, where **14** has been excited by either 450 nm or 570 nm pulses of light and the 390 – 935 nm spectrum has been recorded at intervals, between 0 and 3500 ps after excitation (Figure 15). In both cases, immediately after excitation, broad structured transients appear at 590 – 927 nm. These transients are accompanied by a bleach between 462 – 590 nm associated with ground state absorptions. When **13** is excited with 450 nm light, these transients and bleaches decay by a biexponential process with lifetimes of 94 ps and 34.8 ns. When **13** is excited with 570 nm light, these transients and bleaches decay by a monoexponential process with a lifetime of 93 ps.
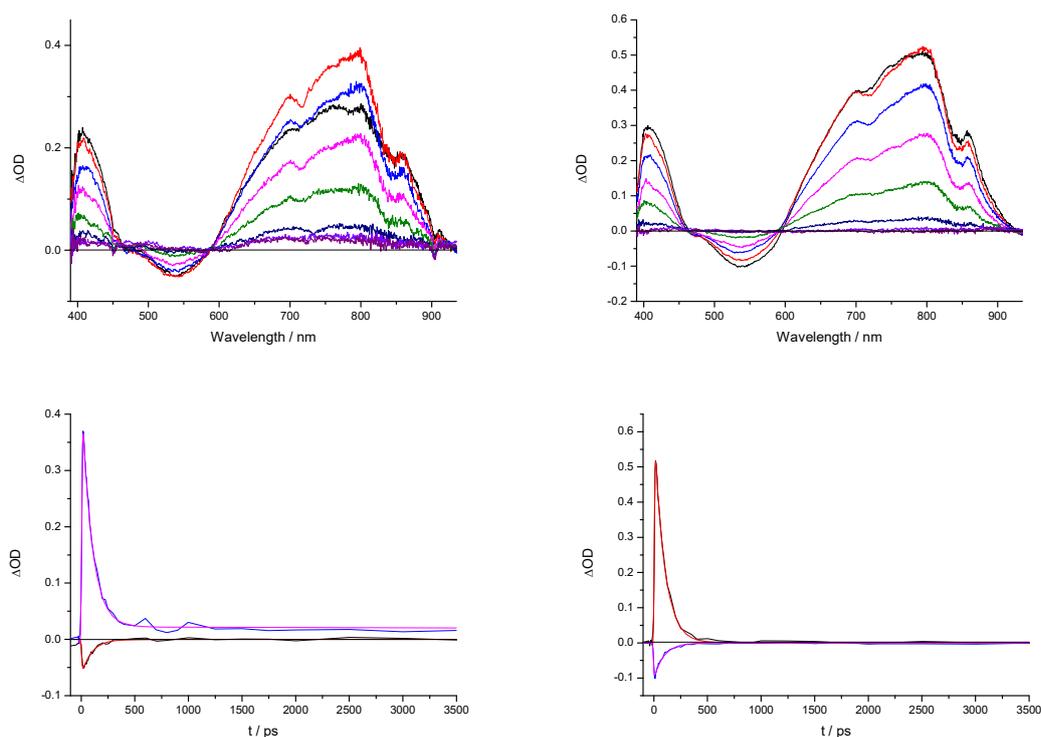
Figure 15 Top Left: TA spectra of 14 when excited with 450 nm light, recorded in CH$_2$Cl$_2$ between 0 and 3500 ps. Bottom Left: Decay traces for absorption intensities at 544 nm and 802 nm for 12 between -50 and 3500 ps after excitation with 450 nm light. Top Right: TA spectra of 12 when excited with 570 nm light, recorded in CH$_2$Cl$_2$ between 0 and 3500 ps. Bottom Right: Decay traces for absorption intensities at 803 nm and 544 nm for 12 between -50 and 3500 ps after excitation with 570 nm light.

Again, the long lifetime is not modelled accurately using the data, as data collection stops at 3.5 ns and the lifetime is longer than the data collection. The shorter lifetime process of ~ 93 ps is resolved using this instrumentation and is comparable to the τ_2 decay lifetime recorded by TRIR of 81 ps, corroborating data obtained by another method.

The longer lifetime process is not accessible using longer wavelength, lower energy light. This can be seen in the long delay spectra. Complex **14**, when excited by 570 nm light, shows a full relaxation to the ground state. This is indicated by full recovery of transients and decays. In comparison, when excited with 450 nm light, there is no full recovery of bleaches and transients. This indicates that the long lived emissive excited state can only be accessed using higher energy light and that emission is not from the lowest excited state, confirming that the phenylacetylide-bipy localized and N^N^C* excited states are not interacting to quench the emission and reduce emissive lifetime.

EXPLORATORY TIME-RESOLVED 2D INFRA-RED (T2DIR) SPECTROSCOPY

As complex **14** has a high lying, long lived, emissive excited state that does not interact with the lower lying, short-lived, non-emissive excited states, it was supposed that interconversion between these states could be achieved by excitation with an IR pulse. This was achieved by first exciting complex **14** with a 400 nm pulse to its electronically excited state, then further pumping with a narrowband mid-IR pulse at 2 ps after the first. IR spectra were recorded by the absorption of a broadband IR pulse between 0 and 225 ps after the second pump pulse.

Two IR pulse bands were selected; 1971 cm^{-1} and 2042 cm^{-1}. These are the low and high energy extremes of the overlapping bands that dominate the excited state seen in TRIR spectra. The pulse beam bandwidth is 30 cm^{-1} FWHM and compared to the bands that must be excited, this is wider than the both the bands and the gaps between them. Due to this, low selectivity of excitation could be achieved.

1971 cm^{-1} pump of complex 14 CSS excited state acetylide

The T2DIR has been used to attempt to selectively excite acetylide bands associated with different excited state species for complex **14**. By selectively exciting the ν(CC) band associated with the acetylide of a species in the excited state where there is a CSS at 1971 cm^{-1}, a change in population of states should be observed.
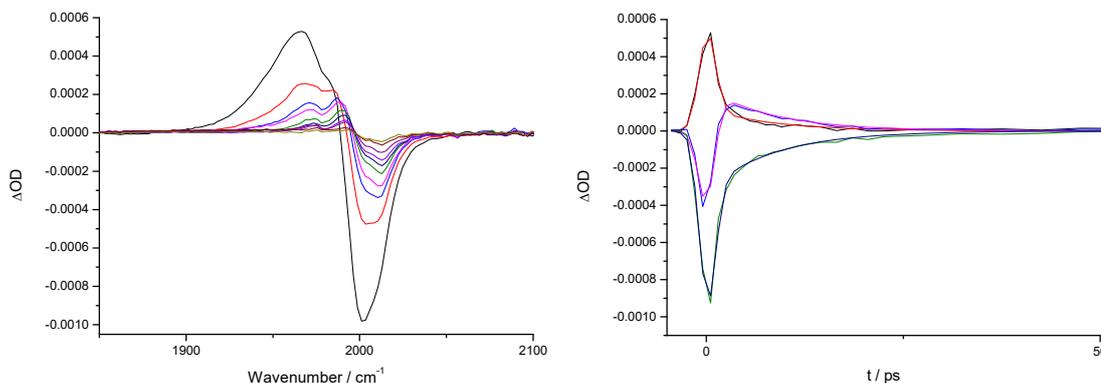
Figure 16 Left: T2DIR spectra for 14 recorded between 0 and 50 ps after vibrationaly exciting the electronic excited state of 14 with 1971 cm^{-1} IR pump. Right: Decay traces recorded for the absorption intensities at 1971 cm^{-1} (red and black), 1989 cm^{-1} (pink and blue) and 2008 cm^{-1} (green and blue) between -5 and 50 ps with fitted exponential curves.

Spectra were recorded where after a 400 nm visible light pump and a 2 ps delay, the sample was further excited by a 1971 cm^{-1} IR pulse, followed by a broadband IR probe beam. Spectra were recorded at time delays between 0 and 225 ps (Figure 16). Immediately after excitation, a bleach peak appears at 2001 cm^{-1}. This does not match the pumped wavelength, implying that the IR pump pulse does not lead to depopulation of the state intended but instead instantly leads to a depopulation of another state. This is accompanied by a broader structured transient between 1900 and 1990 cm^{-1}. These peaks then evolve over time with a lifetime of < 1 ps, shifting to higher frequency and narrowing significantly, with new transient peaks at 1971 cm^{-1} and 1991 cm^{-1} and a new bleach peak of 2010 cm^{-1}, these peaks decay to the baseline with a lifetime of 8.5 ps. The 1971 and 1991 cm^{-1} peak corresponds to the TRIR transient that is being pumped, as indicated by the corresponding τ_1 DAS seen in the TRIR of the same compound. These peaks also decay with the same lifetime as the τ_1 associated spectrum. This suggests that pumping this band does not lead to a loss of signal at this spectral position but instead, increases it.

2042 cm^{-1} pump of complex 14 triplet emissive excited state

The results of the mid-IR pumping of the excited state associated with a CSS for **14**, has been compared to pumping, at 2042 cm^{-1}, the emissive excited state.
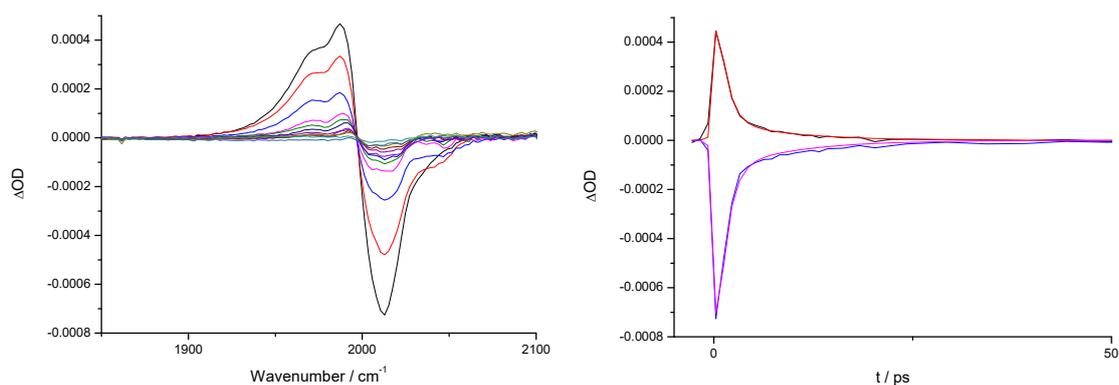
Figure 17 Left: T2DIR spectra for 14 recorded between 0 and 50 ps after vibrationaly exciting the electronic exited state of 14 with 2042 cm^{-1}. Right: Decay traces recorded for the absorption intensities at 1989 cm^{-1} (red and black) and 2013 cm^{-1} (pink and blue) between -5 and 50 ps with fitted exponential curves.

Spectra were recorded where after a 400 nm visible light pump and a 2 ps delay, the sample was further excited by a 2042 cm^{-1} IR pulse, followed by a broadband IR probe beam. This pumping regime is intended to add a an IR pump to the transient acetylide stretch of the emissive excited state only. Spectra were recorded at time delays between 0 and 225 ps (Figure 17s). Immediately after excitation, a bleach peak associated with the pumping of low energy transient band appears at 2015 cm^{-1}. This, again, does not match the pumped wavelength. It does fall within the FWHM of the IR pulse indicating that the excited state associated with this transient, seen in TRIR at this position, may have been pumped by the IR pulse. This is accompanied by a broader structure transient between 1940 and 1996 cm^{-1}. These peaks do not evolve over time but do narrow, revealing their structure. These peaks appear structurally similar to those seen in the τ_1 DAS of the TRIR and decay with the same lifetime of 8.5 ps. These peaks fully decay over the time monitored. They appear as, perhaps, 1-2 and 2-3 vibrational bands.

Discussion

Pumping different vibrational bands causes different hot excited states to populate initially. Both have a short < 1 ps lifetime and an 8.5 ps lifetime associated with the decay of bands in the T2DIR spectrum. The short lifetime is likely vibrational cooling in both, as there is a narrowing of bands at very early times. The lifetime values are not exact as they are less than the instrument response from the time delays taken. These quickly vibrationally decay to the same state. The DAS of this decay matches spectrally a DAS in the TRIR of the parent compound. The longer lived bands have the same lifetime and spectral shape, implying that these are in fact the same excited state. The match to a DAS of the TRIR of a parent compound suggests that after excitation and initial cooling from different hot excited states, the compound always ends up in the same excited state. This state decays to the excited state that exists before the IR pump beam excites the molecule and there are changes to the long term populations of the excited states seen in the TRIR, resulting in no control of excited states using IR light. This result may also be due to the low selectivity of the IR pulses. If the IR pulse pumps more than one band at a time, then the results seen may just be those of one band absorbing different amounts of light based on its extinction coefficient at that frequency of light. Where the result of an IR pump pulse does cause the promotion of the excited state to a different electronic state, as suggested by the results of pumping at 1971 cm^{-1}, this only results in rapid decay back to its initial state.

As a result of these studies, it can be seen that it was not possible to alter the long term populations of states using these T2DIR. Although these attempts were unsuccessful for the case where there is no equilibrium between excited states, it is possible than some of the other complexes may show more promising results when tested.

CONCLUSIONS

Based on observations from the previous chapter, on the unusual excited state properties of a range of cyclometalated platinum acetylide complexes, this character describes the time-resolved spectroscopy techniques used to investigate the causes of these unusual excited states.

Time resolved infra-red spectroscopy has been used to investigate the dynamics of the multiple coexisting excited state populations and the interconversion of these states. The signals described herein have been compared to similar signals in other Pt(II) acetylide complexes and the likely allenic Pt=C=C=Ar nature of some of the excited states has been discussed based on the broad signals seen at short timescales (<500 ps). The lifetimes of these allenic states are around 10 – 100 ps while existing coincidently with an acetylide stretch (vCC) associated with the emissive state located at 2050 cm^{-1} that persist past the end of data collection in complexes **8** – **11**, providing further evidence for states in equilibrium. Attempts to manipulate the interconversion of these excited states using infra-red light was successful but did not result in any long term (> 50 ps) change in excited state populations.

The excited states of complexes **12**, **13** and **14** have been investigated suing UV/vis TA spectroscopy. After pumping with nanosecond laser pulses, bleaches associated with the ground state absorptions and transients appear. These transients are at wavelengths between 400 – 450 nm and 550 – 900 nm. Transient absorption has also been used to confirm that the emission seen from complexes **13** and **14** is not from the lowest accessible electronic excited state. When complexes **13** and **14** were probed using two different wavelength laser pulses, emission could not be inferred from results produced using the longer wavelength pump light. The lowest absorption bands do not produce an emissive excited state.

These studies have provided evidence that the complexes produce short lived charge separated states after excitation, which interact with the expected phosphorescent triplet state. This phosphorescent state is accessible even when it is not the lowest excited state.

REFERENCES

1.	Berera, R.; van Grondelle, R.; Kennis, J. T. M., *Photosynth. Res.* **2009,** *101* (2), 105-118.
2.	Butler, J. M.; George, M. W.; Schoonover, J. R.; Dattelbaum, D. M.; Meyer, T. J., *Coord. Chem. Rev.* **2007,** *251* (3–4), 492-514.
3.	Lees, A. J., *Coord. Chem. Rev.* **2001,** *211* (1), 255-278.
4.	Turner, J. J.; George, M. W.; Johnson, F. P. A.; Westwell, J. R., *Coord. Chem. Rev.* **1993,** *125* (1), 101-114.
5.	Stoutland, P. O.; Dyer, R. B.; Woodruff, W. H., *Science* **1992,** *257* (5078), 1913-1917.
6.	Schoonover, J. R.; Strouse, G. F., *Chem. Rev.* **1998,** *98* (4), 1335-1356.
7.	Huynh, M. H. V.; Dattelbaum, D. M.; Meyer, T. J., *Coord. Chem. Rev.* **2005,** *249* (3–4), 457-483.
8.	George, M. W.; Turner, J. J., *Coord. Chem. Rev.* **1998,** *177* (1), 201-217.
9.	Browne, W. R.; O'Boyle, N. M.; McGarvey, J. J.; Vos, J. G., *Chem. Soc. Rev.* **2005,** *34* (8), 641-663.
10.	Schoonover, J. R.; Strouse, G. F.; Dyer, R. B.; Bates, W. D.; Chen, P.; Meyer, T. J., *Inorg. Chem.* **1996,** *35* (2), 273-274.
11.	Schoonover, J. R.; Bignozzi, C. A.; Meyer, T. J., *Coord. Chem. Rev.* **1997,** *165*, 239-266.
12.	Dattelbaum, D. M.; Omberg, K. M.; Hay, P. J.; Gebhart, N. L.; Martin, R. L.; Schoonover, J. R.; Meyer, T. J., *J. Phys. Chem. A* **2004,** *108* (16), 3527-3536.
13.	Gabrielsson, A.; Busby, M.; Matousek, P.; Towrie, M.; Hevia, E.; Cuesta, L.; Perez, J.; Záliš, S.; Vlček, A., *Inorg. Chem.* **2006,** *45* (24), 9789-9797.
14.	Scattergood, P. A.; Delor, M.; Sazanovich, I. V.; Bouganov, O. V.; Tikhomirov, S. A.; Stasheuski, A. S.; Parker, A. W.; Greetham, G. M.; Towrie, M.; Davies, E. S.; Meijer, A. J. H. M.; Weinstein, J. A., *Dalton Trans.* **2014,** *43* (47), 17677-17693.
15.	Cannizzo, A.; Blanco-Rodríguez, A. M.; El Nahhas, A.; Šebera, J.; Záliš, S.; Vlček, J. A.; Chergui, M., *J. Am. Chem. Soc.* **2008,** *130* (28), 8967-8974.
16.	Weinstein, J. A.; Grills, D. C.; Towrie, M.; Matousek, P.; Parker, A. W.; George, M. W., *Chem. Commun.* **2002,** (4), 382-383.
17.	Sazanovich Igor, V.; Alamiry Mohammed, A. H.; Meijer Anthony, J. H. M.; Towrie, M.; Davies, E. S.; Bennett Robert, D.; Weinstein Julia, A., *Pure Appl. Chem.* **2013,** *85* (7), 1331.
18.	Adams, C. J.; Fey, N.; Harrison, Z. A.; Sazanovich, I. V.; Towrie, M.; Weinstein, J. A., *Inorg. Chem.* **2008,** *47* (18), 8242-8257.
19.	Whittle, C. E.; Weinstein, J. A.; George, M. W.; Schanze, K. S., *Inorg. Chem.* **2001,** *40* (16), 4053-4062.
20.	Glik, E. A.; Kinayyigit, S.; Ronayne, K. L.; Towrie, M.; Sazanovich, I. V.; Weinstein, J. A.; Castellano, F. N., *Inorg. Chem.* **2008,** *47* (15), 6974-6983.
21.	Cooper, T. M.; Blaudeau, J.-P.; Hall, B. C.; Rogers, J. E.; McLean, D. G.; Liu, Y.; Toscano, J. P., *Chem. Phys. Lett.* **2004,** *400* (1–3), 239-244.
22.	Delor, M.; Scattergood, P. A.; Sazanovich, I. V.; Parker, A. W.; Greetham, G. M.; Meijer, A. J. H. M.; Towrie, M.; Weinstein, J. A., *Science* **2014,** *346* (6216), 1492-1495.
23.	Scattergood, P. A.; Delor, M.; Sazanovich, I. V.; Towrie, M.; Weinstein, J. A., *Faraday Discuss.* **2015,** *185* (0), 69-86.
24.	Ge, N.-H.; M. Hochstrasser, R., *PhysChemComm* **2002,** *5* (3), 17-26.
25.	Golonzka, O.; Khalil, M.; Demirdöven, N.; Tokmakoff, A., *J. Chem. Phys.* **2001,** *115* (23), 10814-10828.
26.	Bredenbeck, J.; Helbing, J.; Hamm, P., *J. Am. Chem. Soc.* **2004,** *126* (4), 990-991.
27.	Greetham, G. M.; Burgos, P.; Cao, Q.; Clark, I. P.; Codd, P. S.; Farrow, R. C.; George, M. W.; Kogimtzis, M.; Matousek, P.; Parker, A. W.; Pollard, M. R.; Robinson, D. A.; Xin, Z.-J.; Towrie, M., *Appl. Spectrosc.* **2010,** *64* (12), 1311-1319.
28.	Snellenburg, J. J.; Laptenok, S.; Seger, R.; Mullen, K. M.; van Stokkum, I. H. M., *J. Stat. Softw.* **2012,** *49*, 1-22.
29.	Kovelenov, Y. A.; Blake, A. J.; George, M. W.; Matousek, P.; Mel'nikov, M. Y.; Parker, A. W.; Sun, X.-Z.; Towrie, M.; Weinstein, J. A., *Dalton Trans.* **2005,** (12), 2092-2097.

30.   Suzuki, K.; Kobayashi, A.; Kaneko, S.; Takehira, K.; Yoshihara, T.; Ishida, H.; Shiina, Y.; Oishi, S.; Tobita, S., *PCCP* **2009,** *11* (42), 9850-9860.

6. Quenching of Transition Metal Excited States by Diiron Hydrogenase Mimic Complexes

INTRODUCTION

Bimolecular photocatalytic hydrogen evolution systems are a popular area of research for producing hydrogen from diiron hydrogenase mimics.[1-2] These systems are often similar in character to those that can be used for DSSC applications and other photocatalytic reactions.[3] The advantage to bimolecular systems over dyads is that they offer simpler synthetic routes, a wider variety of photosensitizer (PS) and catalyst functionalities and often produce higher turnover numbers (TON) and activities. A successful, photocatalytic, hydrogen evolving, diiron hydrogenase based system requires that electrons are transferred from the PS to the catalyst. In a bimolecular system, this takes place via collisions between a PS complex in its excited state and a catalyst complex. The more collisions that results in an electron transfer (ET) reaction, the higher the turn over frequency (TOF) of the system, as more electrons transferred results in more hydrogen evolution catalysis.

For PS complexes that are emissive in their excited state, interactions with catalyst molecules can be assessed using their quenching dynamics as a reference for their electron transfer rates. This can be done using Stern-Volmer model of emission quenching. Stern-Volmer dynamic quenching model describes a situation where the quenching of a molecule's emission takes place by collision with a second molecule.

$$\tau_0 = \frac{1}{k_r + k_{nr}}$$
Eq. 1

$$\tau = \frac{1}{k_r + k_{nr} + k_q[Q]}$$
Eq. 2

$$\frac{\tau_0}{\tau} = 1 + k_q \tau_0 [Q]$$
Eq. 3

$$\frac{\phi_0}{\phi} = \frac{I_0}{I} = \frac{\tau_0}{\tau} = 1 + k_q \tau_0 [Q]$$
Eq. 4

Eq. 1 and **Eq. 2** describe the lifetime of an emissive molecule on its own and in the presence of quencher, respectively. Dividing **Eq. 1** by **Eq.2** gives **Eq. 3**, the Stern-Volmer equation. The lifetime in the absence of the quencher given by τ_0, lifetime in the presence of a quencher is given by τ. The terms k_r and k_{nr} are the radiative and non-radiative relaxation rate constants, k_q is the quenching rate constant, and [Q] is the quencher concentration. **Eq. 4** describes the equivalency of quantum yield, intensity of emission and lifetime in case only dynamic quenching takes place. Importantly, lifetimes are not affected by static quenching, only dynamic quenching whilst intensities and quantum yields are affected by both types of quenching. A combination of static and dynamic quenching leads to second order Stern Volmer curves in intensity measurements.[4]

Quenching behaviour of square planar platinum (II) complexes

Self-quenching of excited states of square-planar platinum(II) complexes at high concentrations is a well-studied phenomenon. Initially reported for Pt(5,5'-dimethyl-2,2'-bipyridine)(CN)$_2$[5] and subsequently reported for a multitude of platinum (II) complexes,[6-13] this self-quenching can result in weak emission due to excimer formation. This behaviour occurs due to the excited state platinum complex "dimerizing" transiently with a ground state complex leading to deactivation of the emissive triplet excited state and an appearance of an additional emission band due to emission from the excimer. The rate of self-quenching in platinum compounds is a function of concentration and has been studied to determine the rates and the rate constants of self-quenching.

Often the excimer species cannot be directly studied due to the short lifetime and/or low solubility of Pt(II) complex restricting the ability to form sufficient excimer concentrations, or low excimer emission quantum yields. In some cases, where excimer is more emissive than the

monomer, such dimerization in the excited state can be used to enhance quantum yield of emission,[14] investigate excited state metal-metal bonding distances[15] and investigate the performance of OLEDs where there is the chance of aggregation.[16]

The self-quenching of Pt(II) complexes is indicative of their tendency to experience quenching of their excited states in general, due to open coordination sites, and the square-planar geometry, that may be profitable in reductive and oxidative quenching applications. The photoinduced electron transfer reactions that may be explored using this behaviour could be used for artificial photosynthesis, photochemical reactions and even medicinal applications such as photodynamic therapy. Investigation of the reduction of excited states often takes place through quenching of triplet excited states using amine-based reducing agents. Oxidation of excited states is typically explored through introducing more functionality to the platinum complexes, including appending TiO_2 nanoparticles and aromatic assemblies, due to the need to model the application of the photosensitizer (PS) to its function.[7, 9, 17-21] The values of quenching rate constants obtained in these investigations often approach the diffusion limit at large negative ΔG values, as these are often bimolecular systems, indicating high reactivity and a low barrier to activation for the quenching reactions. This indicates suitability for photosensitizing applications, as electron transfer will not be a rate-limiting step.

Marcus Theory
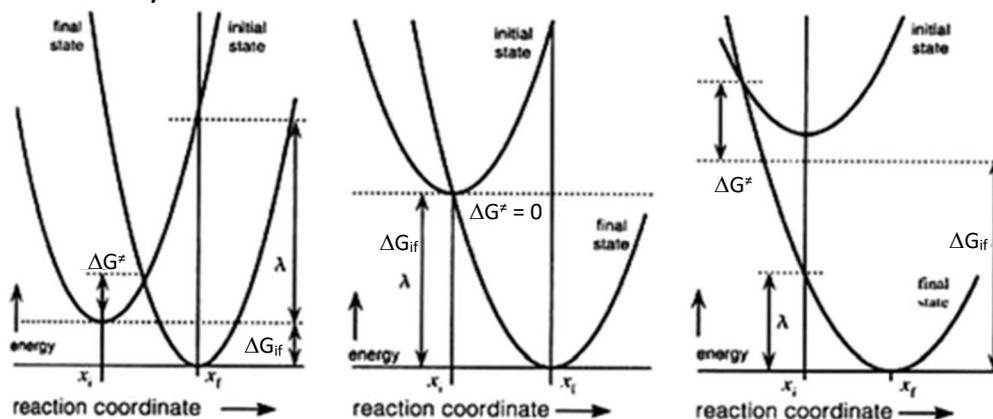
Figure 1 Electron transfer in the normal (left) and inverted (right) Marcus regions. Barrierless case with ΔG$^{\neq}$ = 0 (middle) corresponds to λ + ΔG$_{if}$ = 0. Plots of the potential energies of the reactant and product as a function of the nuclear (reaction) coordinate in the zeroth-order approximation.[22]

Marcus theory is the most widely used framework to analyse and predict how effective photo-initiated ET is.[23] Classical Marcus theory assumes that ET reactions can be described by two intersecting potential energy surfaces. These are represented, in the zero approximation, by two harmonic potentials. As such, these ET reactions are between the two outer electron spheres, nuclear motion does not participate and solvent effects dominate the effects due to nuclear movement. This leads to the harmonic (parabolic) potentials being described by the reaction coordinate in the x direction and ΔG^0 of electron transfer used to represent the y direction (Figure 1). The activation energy for the system (ΔG$^{\neq}$) is given below (**Eq. 5**), where λ is the solvent reorganization energy and ΔG$_{if}$ is the difference in energy between the two energy wells. Activation limited ET rates (k_{act}) can then be predicted by substituting **Eq. 5** into the Eyring equation, where A are the pre-exponential terms associated with distance and solvent permittivity (**Eq. 6**).

$$\Delta G^{\neq} = \frac{\left(\Delta G_{if} + \lambda\right)^2}{4\lambda} \qquad \textbf{Eq. 5}$$

$$k_{act} = A \cdot exp\left(\frac{\left(\Delta G_{if} + \lambda\right)^2}{4\lambda RT}\right) \qquad \textbf{Eq. 6}$$

These predictions based on solvent reorganization show that the ET rate constant reaches its maximum when $\Delta G^{\ddagger}_{ET} = 0$ and $\Delta G_{ET} = -\lambda$. This is one of the most celebrated predictions of Marcus theory; when there are increasing negative ΔG values past the solvent reorganization energy, the ET transfer rate decreases. This prediction only holds when k_{act} is the limiting rate. Where the limiting rate is instead the rate of diffusion, k_{dif}, the bell curve will not be observed. This means ET rates can only be predicted where the limiting step is progression through the transition state. Due to this, it took many years before the prediction made by Marcus was observed, by Miller and Closs (Figure 2).[24]
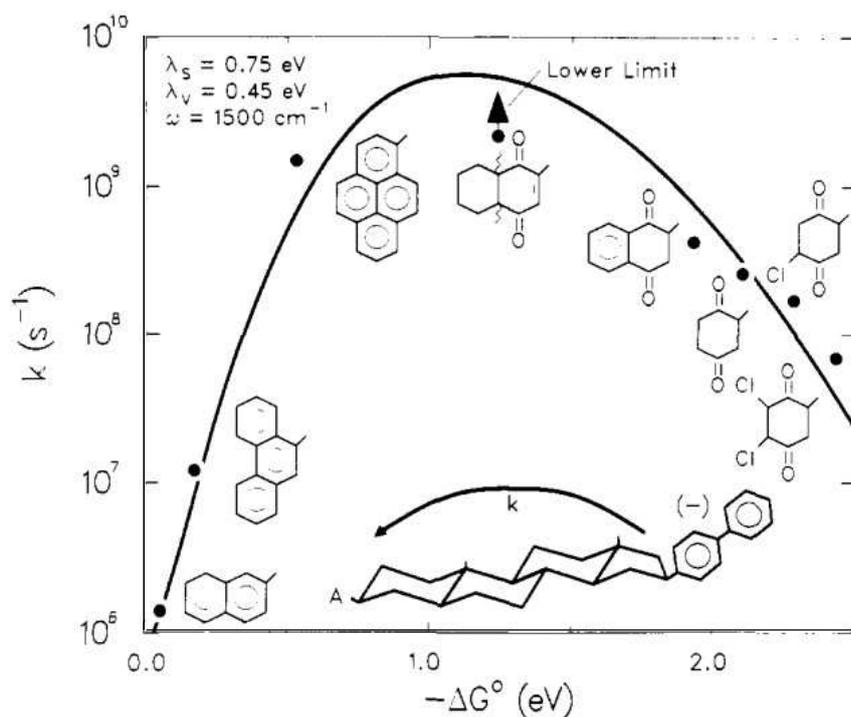
Figure 2 The first example of a system confirming the existence of the Marcus inverted region. Intramolecular electron-transfer rate constants as a function of free energy change in Me-THF solution at 296 K. Electrons transferred from biphenyl ions to the eight different acceptor groups, A (shown labeling the points), in eight bifunctional molecules having the general structure shown in the center of the figure.[24]

In bimolecular systems, the typically observed results are that the ET rate reaches a maximum and plateaus. The rates of electron transfer would not decrease at high negative ΔG values because the diffusion limit is still operational, indicating the rate of diffusion is lower than the rate of electron transfer, even at ΔG values more negative than -1V.[25-31] However, in monomolecular systems, there is a wide variety of cases described where the inverted region has been observed, for fixed donor-acceptor distances. These include evidence of the inverted region in protein frameworks,[32-35] rigid covalent spacer networks,[36-45] frozen media[46] and electrostatic complexation.[47-51] Recent work focusses on fluorescence quenching in high viscosity media. In these works, attention is paid to quenching rates before diffusion can happen due to the long diffusion timescales imposed by the highly viscous solvent.[52-53]

Aims

The aim of the work described in this chapter is to systematically evaluate the effects of PS properties on the quenching rates in the presence of diiron hydrogenase mimics, in order to facilitate successful electron transfer reactions and further investigate PS complex properties. Quenching rates will also be compared to the reduction potentials of the diiron hydrogenase mimics in order to derive a trend, including the "inverted region" behaviour.

RESULTS AND DISCUSSION

Initial Quenching Experiments

In order to assess the major factors affecting energy and electron transfer to diiron hydrogenase mimics from photosensitizers, a large range on photophysical properties would have to be included in the studied variables. This required a wide variety of PS complexes, from different classes, with widely varying ground and excited state properties. The PS complexes chosen for this study include two varieties of cyclometalated platinum complex and a rhenium tricarbonyl complex (Figure 3). The platinum complexes were chosen for their high excited state energies, low oxidation potentials and long lifetimes. The rhenium complex was chosen as a similar PS has been used for photosensitizing diiron hydrogenase unsuccessfully and this acts as a benchmark to improve upon the poor results already obtained.
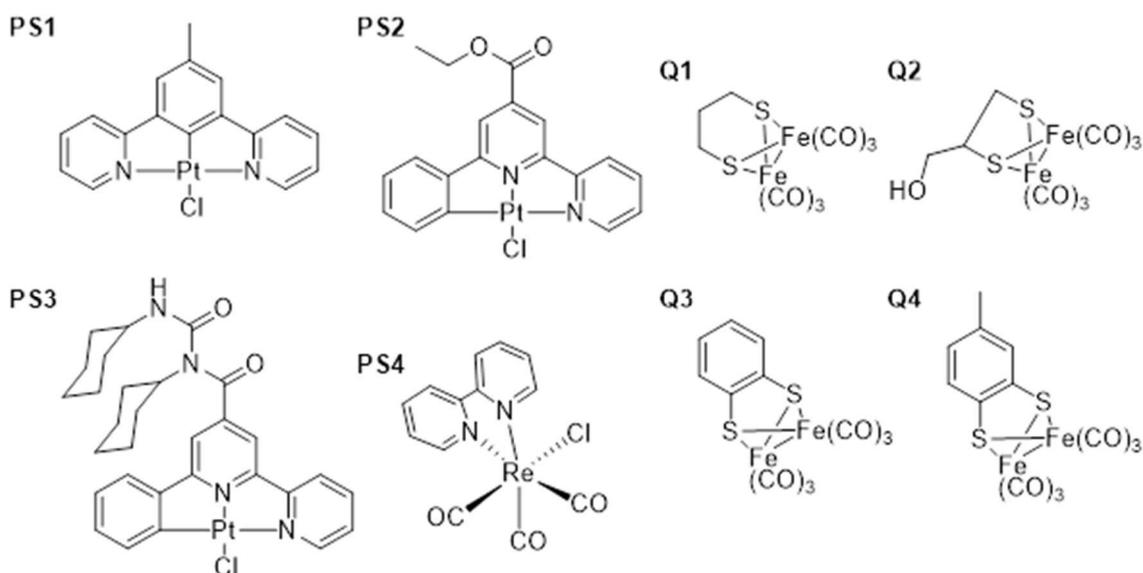
Figure 3 Photosensitizer and quencher complexes used in Stern Volmer quenching experiments to assess how well different PS complexes interact with diiron hydrogenase catalysts. In previous chapters Q1 was called PDT, Q2 was called BAL and Q3 was BDT.

The emission of these complexes has been quenched using four different diiron hydrogenase mimics **Q1 – Q4** (Figure 3), featuring a consistent core of butterfly conformation diiron disulphide hexacarbonyl moiety (Figure 3). The differing properties of these photosensitizers are based around the differing disulfide bridge. This allows a range of reduction potentials of quencher to be tested against each other whilst keeping the core ligand set and the reaction of the transition metal to photosensitization similar. The four quenchers reduction potentials are given in Table 1.

The quenching of the PS by diiron hydrogenase mimics was carried out by Stern-Volmer quenching kinetics analysis. The emission of the PS in solution, at a concentration of $1 - 4 \times 10^{-5}$ M, was quenched by a diiron compound at $10 – 100x$ the concentration of the PS. The resulting change in lifetime (Figure 4a) was used to plot a linear relationship between τ_0/τ against the quencher concentration (Figure 4c). Intensity of emission was not used for Stern-Volmer plots as the high concentration of diiron hydrogenase mimics produced a filter effect, limiting the amount of light reaching the PS and therefore reducing the intensity of emission before a quenching event could take place, leading to non-linear relationships with quencher concentration (Figure 4d). As the PS are emitting from triplet excited states, all measurements were performed in the absence of oxygen by bubbling argon for 10 min through the solutions in quartz septum closure fluorescence cells prior to lifetime measurements.
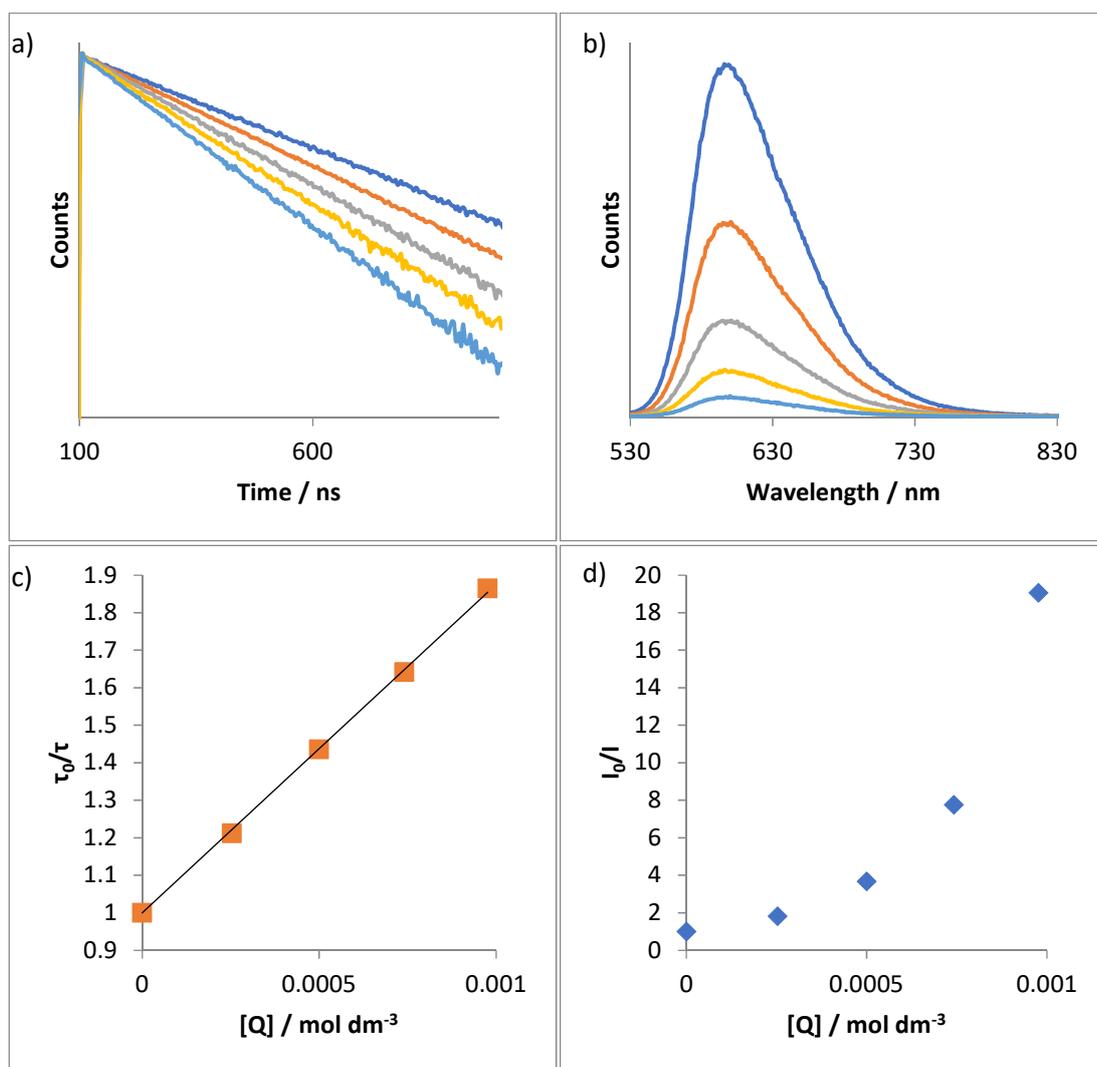
Figure 4a) Decay traces of complex PS2's emission when quenched by $0 - 1 \times 10^{-3}$ M solution of Q3. **b)** Emission spectra of PS2 when quenched by $0 - 1 \times 10^{-3}$ M solution of Q3. **c)** Linear relationship of τ_0/τ against [Q3]. The linear relationship shows that dynamic quenching follows Stern Volmer behaviour. **d)** Non-linear relationship of I_0/I against [Q3]. The non-linear relationship reveals that quenching is not solely dependent on collisions with Q3.

Plots of τ_0/τ of the PS complexes versus concentration of the diiron hydrogenase mimic quenchers provide straight line relationships, proportional to $k_Q\tau_0$. These were plotted for all PS – [FeFe] combinations to give k_Q values useful for Marcus theory evaluations.

In order to construct Marcus plots to further assess the PS – catalyst pairing, the ΔG of photoinduced electron transfer (PET) must be calculated for each pairing using **Eq. 7**. This equation calculates PET from the reduction potential of the quencher, $E°(A/A^{-\cdot})$, which is approximated by the reduction potential of the diiron hydrogenase mimic vs Fc/Fc⁺ (ΔE_RED); the reduction potential of the PS complexes, $E°(D^{+\cdot}/D)$, which is approximated by the oxidation potential of the PS complex vs Fc/Fc⁺ (ΔE_OX) and the excited state energy stored in the PS complex (E_{0,0}). The terms associated with $w(D^{+\cdot}A^-)$ and $w(DA)$ are discounted as their values are negligible. This gives a simplified equation, **Eq. 8**. The value of E_{00} is estimated from the λ_max of emission.

$$\Delta_{ET}G° = N_A\{e[E°(D^{+\cdot}/D) - E°(A/A^{-\cdot})] + w(D^+A^-) - w(DA)\} - \Delta E_{0,0} \qquad \textbf{Eq. 7}$$

$$\Delta_{ET}G° = \Delta E(PS)_{OX} - \Delta E([FeFe])_{RED} - \Delta E_{0,0} \qquad \textbf{Eq. 8}$$

The k_q values taken from the Stern Volmer quenching experiments were then plotted against the values from the PET calculations to produce a Marcus plot.

Compound	ΔE_{RED} / V[a]	ΔE_{OX} / V[b]	E_{00} / eV	τ / ns	Φ_{Em}	Ref.
PS1	-2.15	0.29	2.46	7800	0.68	[12]
PS2	-1.55	0.52	2.04	335 ± 34	0.04	[54]
PS3	-1.58	0.62	2.01	276 ± 28	0.06	
PS4	-1.72	0.96	2.09	50	0.005	[55]
Q1	-1.66					[56]
Q2	-1.63					[57]
Q3	-1.44					[58]
Q4	-1.54					

Table 1 Selected properties of the complexes PS1-4 and Q1-4. a) vs Fc/Fc$^+$ in CH$_2$Cl$_2$ solvent, b) vs Fc/Fc$^+$ in CH$_2$Cl$_2$ solvent.

A plot of quenching rate constant against free energy of photoinduced electron transfer reveals a linear relationship as would be expected for the rates of quenching events that have not reached the diffusion limited threshold (Figure 5). These measurements were performed in r.t. CH$_2$Cl$_2$ solution, in which a limiting diffusion rate is estimated as 1.6 x 10^{10} mol^{-1} dm^3 s^{-1} by the Stokes-Einstein equation.[59] This plot indicates that there is also a likely dependence on a property inherent to each class of compounds as indicated by the groupings by class of compound. When considering the luminophores, there are five properties that should be taken into consideration: excited state energy, oxidation potential, reduction potential, quantum yield and lifetime of the PS.
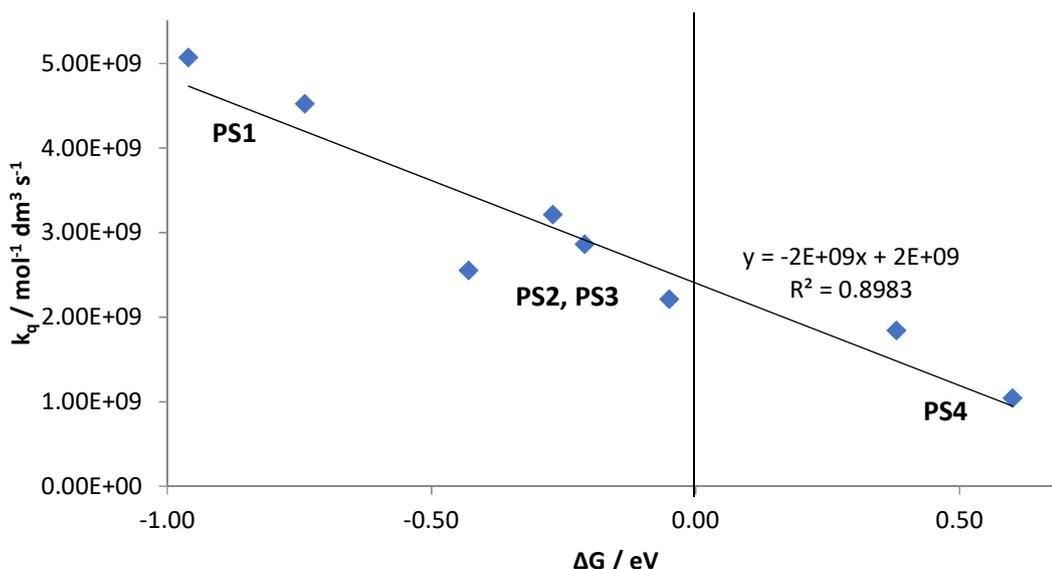
Figure 5 A plot of quenching rate against free energy of electron transfer for complexes PS1-4 quenched by Q1 and Q3.

The quenching rate constants associated with **PS1** are located in the upper left of the plot. This PS has a high excited state energy, low oxidation potential, high quantum yield and long lifetime in comparison to the other PSs used. The middle four points of the plot are associated with **PS2** and **PS3**. These have lower excited state energy, higher oxidation potential, lower reduction potential, quantum yield and lifetimes if compared to **PS1**. The bottom right of the plot is occupied by quenching rates for **PS4**. **PS4** has similar excited state energy and reduction potential to the **PS2** and **PS3**, but much higher oxidation potential. It also has very low emission quantum yield and lifetime values.

The quenching rate constants plotted show the expected trend of higher quenching rate constants with increased negative ΔG. It is of note that there is quenching for reactions without

a negative ΔG. This shows the possibility of energy transfer reactions to quench the emission of PS where the electron transfer reaction is not energetically favourable, or a change in mechanism of quenching, where an exciplex is formed.

It can be therefore be determined that quenching rates with diiron hydrogenase mimics are most likely dependent on four properties of the PS; oxidation potential, excited state energy, lifetime or quantum yield of emission. A lower oxidation potential would cause higher emission quenching rates as the PS is more easily able to give up an electron by collision. A higher PS excited state energy would provide a greater driving force to PET to the diiron hydrogenase mimic. Higher lifetimes and quantum yield of emissions would allow for a larger effective quenchable population of excited states to increase the observed quenching.
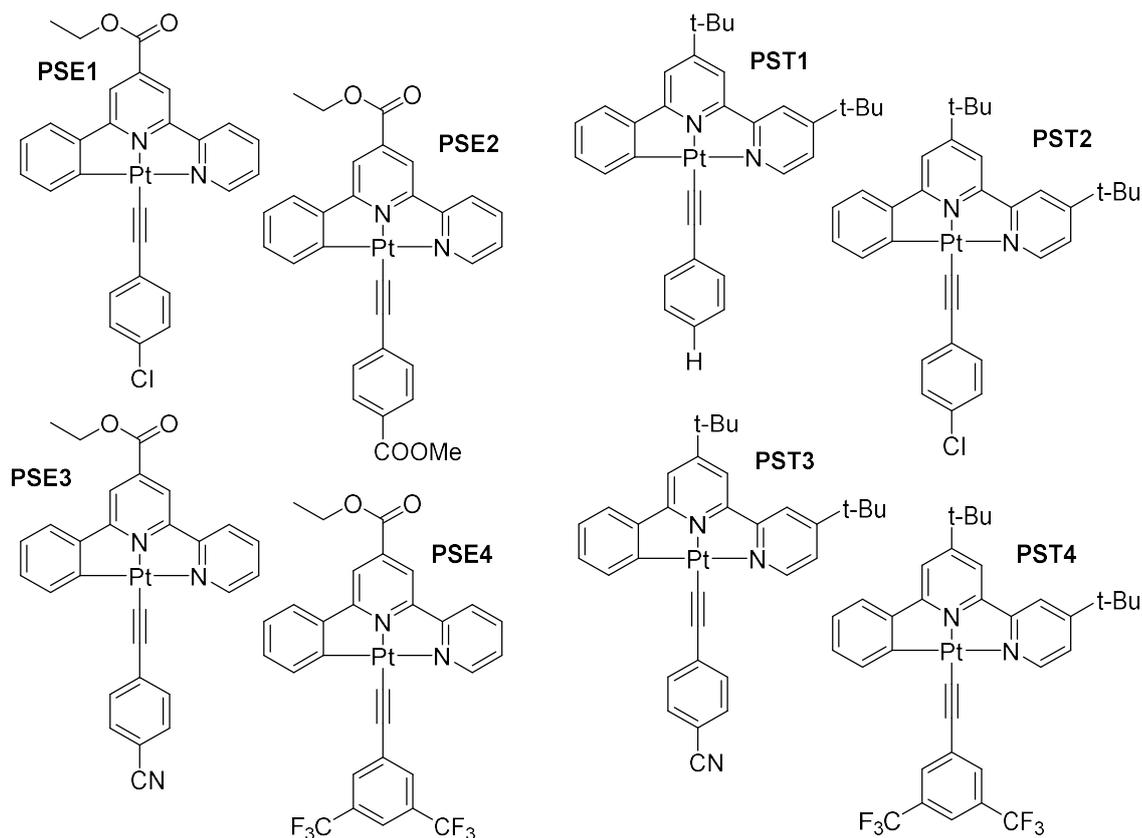
Figure 6 Ester (PSE1-4) and tertiary butyl (PST1-4) substituted Pt(N^N^C) acetylide complexes used in Stern Volmer quenching studies.

These hypotheses were tested using values selected from the quenching rate constants taken from the emission quenching of a range of Pt(NNC)acetylide complexes by four diiron hydrogenase mimics. Photosensitizer complexes have been selected from the range of PS complexes examined in chapters 2 and 3 (Figure 6). A Marcus plot was constructed for these complexes in order to identify any trends in the data.
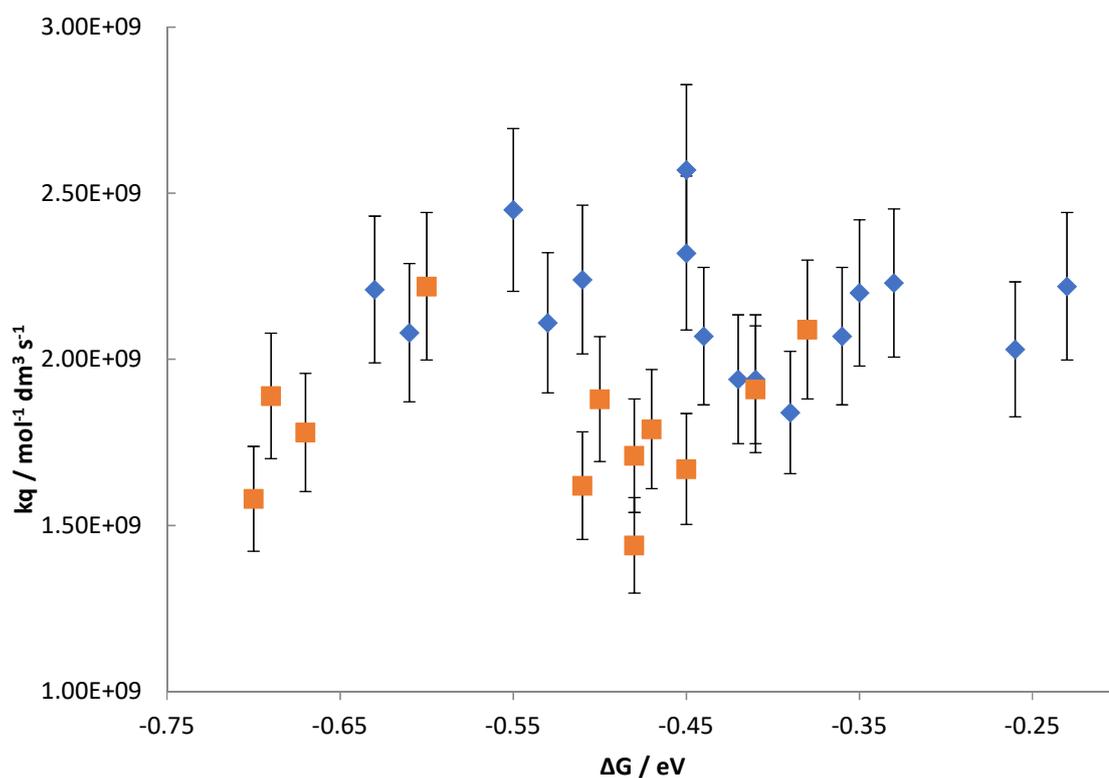
Figure 7 Marcus plot constructed from the quenching rate values of PSE1-4 (red squares) and PST1-4 (blue diamonds) quenched by Q1-4.

Compound	ΔE_{RED} / V[a]	ΔE_{OX} / V[b]	E_{00} / eV	τ / ns	Φ_{Em}
PSE1	-1.59	0.13	2.02	400 ± 40	0.04
PSE2	-1.57	0.18	2.06	704 ± 70	0.11
PSE3	-1.57	0.19	2.07	619 ± 62	0.13
PSE4	-1.56	0.31	2.09	567 ± 57	0.12
PST1	-1.91	0.35	2.17	635 ± 64	0.18
PST2	-1.91	0.39	2.19	649 ± 65	0.22
PST3	-1.89	0.48	2.24	671 ± 67	0.26
PST4	-1.88	0.59	2.24	713 ± 71	0.19

Table 2 Selected properties of the complexes PSE1-4 and PST1-4. a) vs Fc/Fc⁺ in DCM solvent, b) vs Fc/Fc⁺ in DCM solvent. Error bars represent the 10% error associated with emission lifetime measurements.

From this plot (Figure 7), it can be seen that the butyl substituted PS complexes have higher quenching rate constants than the ester substituted PS complexes beyond variations due to error in the lifetimes recorded. This evidence is consistent with the observations made in differing classes of chromophore for lifetime, QY and E_{00}. However, the relationship with the oxidation potential of the PS complexes is not consistent and as such, this was the first property to be tested for its effect on quenching rates, in order to rule this out.

First hypothesis: oxidation potential of the photosensitizer is the decisive factor in the rate of the PS luminescence quenching by [FeFe] quenchers

The first hypothesis to be tested, from the original experiments based on different classes of PS complex, was that the oxidation potential of the photosensitizer has the most prominent effect on the rate of the PS luminescence quenching by [FeFe] quenchers. This observation was not supported by initial examination of the Marcus plot constructed for all of the cyclometalated platinum acetylide PS complexes, because effectively no trend was observed. However, the lack of correlation may be due to the rather different nature of the compounds used as PS. A structurally and electronically similar set of PS complexes needs to be examined in order to evaluate the kinetic effects. In order to test this hypothesis in more detail, the range of photosensitizers, shown in Figure 6, have been selected for Stern Volmer lifetime quenching experiments; with a range of diiron hydroregnase mimic acting as quenchers. The oxidation potentials of the PS complexes have been systematically altered using substituents on the phenyl acetylide ligands, as described in chapter 4. The oxidation potentials of these PS complexes ranges between 0.13 and 0.48 V vs Fc/Fc$^+$. In order to separate the effects of the phenyl acetylide ligand from the rest of the molecule, Hammett σ^+ values which are more directly relevant to the effects produced by changing phenyl acetylide donor potential, have been used.
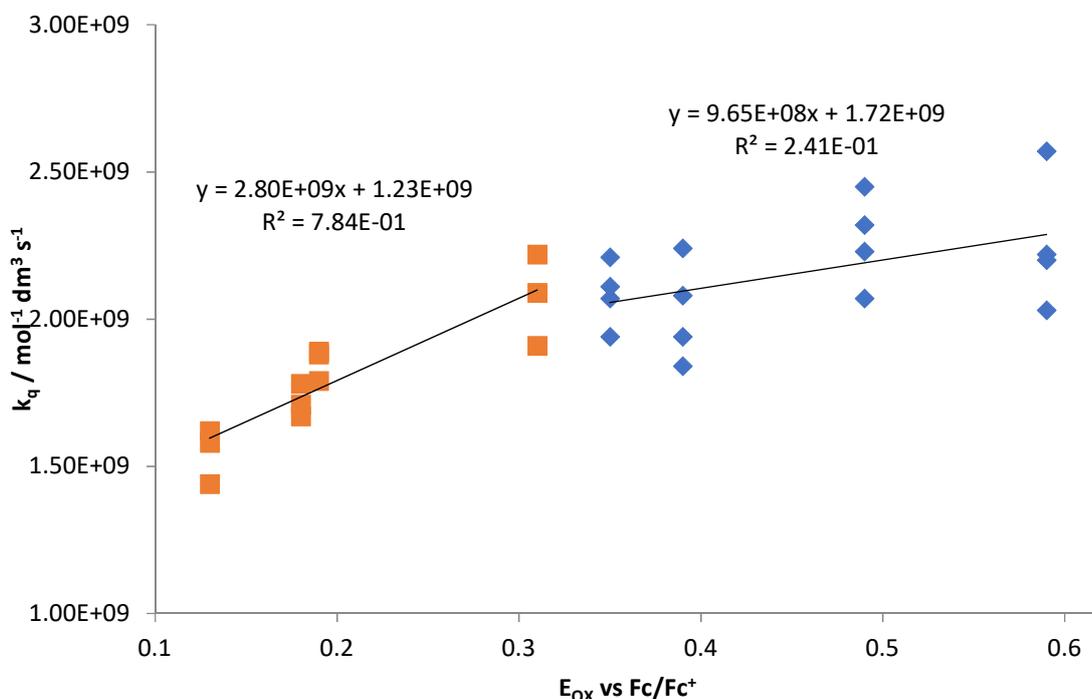
Figure 8 A plot of quenching rate versus oxidation potential of the photosenstizier complexes. Red squares are PSE1-4 quenched by Q1-4 and blue diamonds are PST1-4 quenched by Q1-4.

In the plot of quenching rate constant against first oxidation potential of the photosensitizer (Figure 8), there are two clear regimes associated with the two different types of PS investigated. The k_q of the ester compounds (**PSE1-4**) show much greater dependence on the oxidation potential of the PS than for the butyl complexes (**PST1-4**). The k_q values of the butyl complexes display almost no dependence on the first oxidation potential of the PS complex whereas the slope associated with the ester complexes is almost three times as steep (9.65×10^8 mol^{-1} dm^3 s^{-1} vs. 2.80×10^9 mol^{-1} dm^3 s^{-1}). This indicates that the effect of the oxidation potential is not consistent across the PS series and that the nature of the orbitals involved, beyond simple

oxidation potential, have an effect on the ability of these PS to transfer energy or electrons to the quencher.
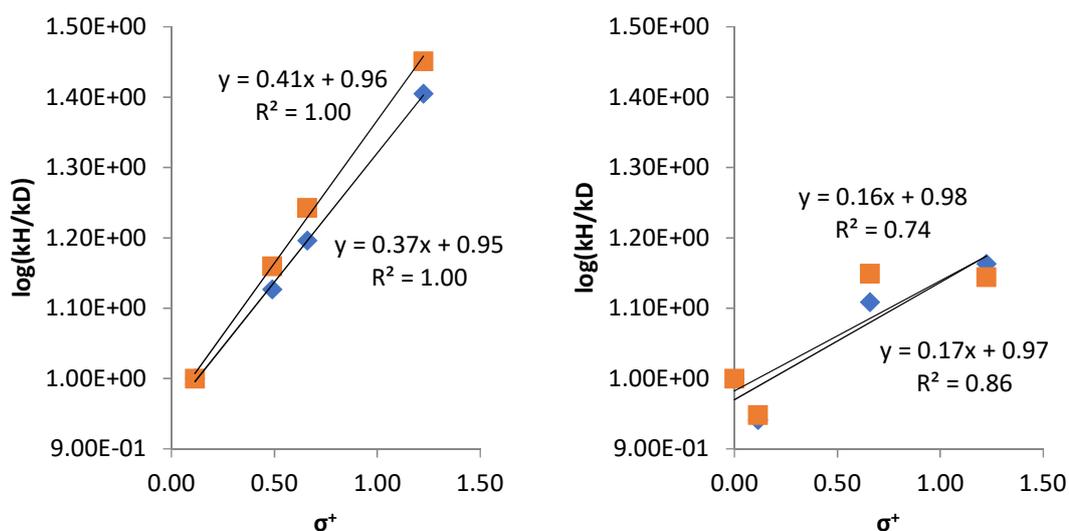
Figure 9 Left: Hammett plot of the log of the quenching rate relative to the slowest PS complex vs σ⁺ value of the acetylide donor for PSE1-4 quenched by Q1 and Q3. Red squares are PSE1-4 quenched by Q1, blue diamonds are PSE1-4 quenched by Q3 Left: Hammett plot of the log of the quenching rate relative to the slowest PS complex vs σ⁺ value of the acetylide donor for PST1-4 quenched by Q1 and Q3. Red squares are PST1-4 quenched by Q1, blue diamonds are PST1-4 quenched by Q3.

Hammett plots of these quenching pairs allow the investigation of how the electronics of the phenyl acetylide ligand affect quenching. A plot of the quenching rate constant against σ^+ for each series (Figure 9) shows that the ester PS complexes (**PSE1-4**) show a greater dependence in their quenching behaviour on the substituents in the Ph-ring, than the butyl PS complexes (**PST1-4**). This behaviour supports the assessment that changes in the quenching rate constants are more strongly associated with the phenyl acetylide ligand in the ester complexes than the butyl complexes. This may be due to competing deactivation pathways, where greater electron density is removed from the emissive excited state into the bipy-acetylide charge transfer state for more electron donating phenyl acetylides. The competing pathway lowers the potential for quenching collisions by lowering the available quenchable excited state population. This pathway is not present in **PST1-4**, as the lowest energy excited state is a PhBipy localized emissive state rather than the acetylide-to-bipy charge transfer state as for the ester complexes.
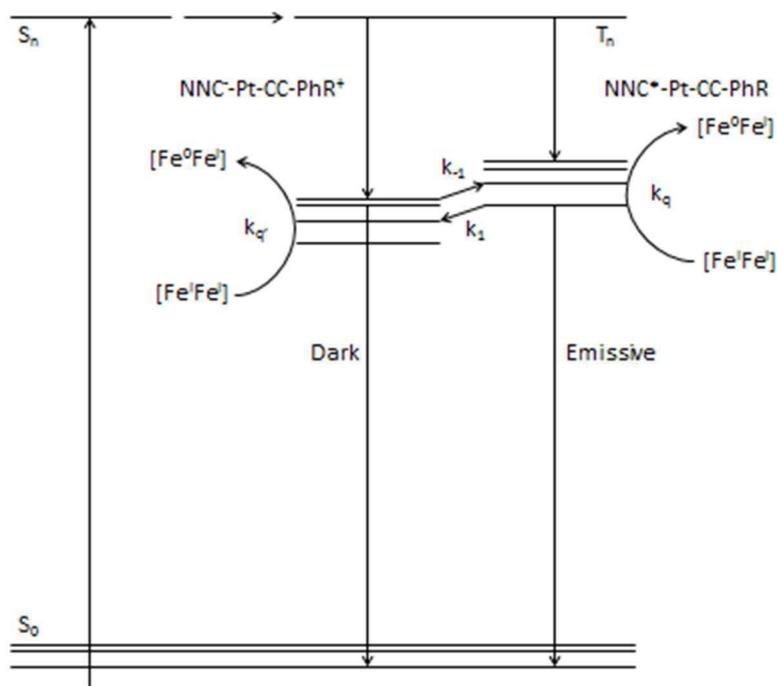
Figure 10 Jablonski diagram demonstrating excited state processes for complexes PSE1-4. After excitation into a higher singlet state, these complexes undergo intersystem crossing into a higher triplet state followed by internal conversion to yield a dark and and an emissive triplet excited state. These exchange electron density through an equilibrium represent by k_1 and k_{-1}. Each of the two triplet states are quenched and this is represent by k_q and $k_{q'}$

This occurs due to branching decay pathways that are either connected by the equilibrium between the ILCT charge transfer state and the MMLL'CT emissive state, or act separately (Figure 10). Where they are separate, unobserved quenching of the dark state has no influence on the rate of quenching seen for the emissive state. When there is equilibrium between the two states, the removal of electron density to a dark state that is also being quenched, lowers the efficiency of quenching the emissive state. The back electron transfer in the charge transfer state is faster than the emission from the MMLL'CT state, as seen in the non-radiative ($1 - 3 \times 10^6$ mol^{-1} dm^3 s^{-1}), radiative decay constants ($1 - 2 \times 10^5$ mol^{-1} dm^3 s^{-1}) and TRIR lifetimes (<100 ps) compared to emissive lifetimes (>400 ns) of these complexes.

The back electron transfer rate constant is assumed to be unchanged for each case, as there is no greater driving force to decay to the ground state; however the equilibrium rate constants are not. When a quencher is introduced there is an increase in k_1 as population is dynamically removed by the quencher and the quenching becomes not only dependent on the concentration of the quencher but also how much k_1 has been increased by. It is assumed this movement of the equilibrium, due to Le Chatelier's principle, is still the rate limiting step of BET due to the conformational changes required to produce the change in electronic structure. This change in dependence on the quencher concentration manifests itself as a lower quenching rate than could be expected. The expected, true quenching rate is actually a combination of the observed k_q and k_1 (Figure 10). This behaviour is not seen in the butyl complexes as there is no equilibrium between charge transfer state and the emissive intra-ligand state.

Second hypothesis: the energy of the lowest excited state of the PS has the main effect on quenching of PS by [FeFe] mimics

The second hypothesis tested that the energy of the excited state of the chromophore has a significant effect on the quenching rate of emission by diiron hydrogenase mimics; the higher the energy of the excited state, the higher quenching rate of the emission by the quencher. This behaviour is indicated by a comparison of the Marcus plots for ester and butyl complexes. When a plot of quenching rate against excited state energy is made, the butyl complexes, represented by red squares in Figure 11, show higher median quenching rate than the ester complexes, represented by blue diamonds in Figure 11.
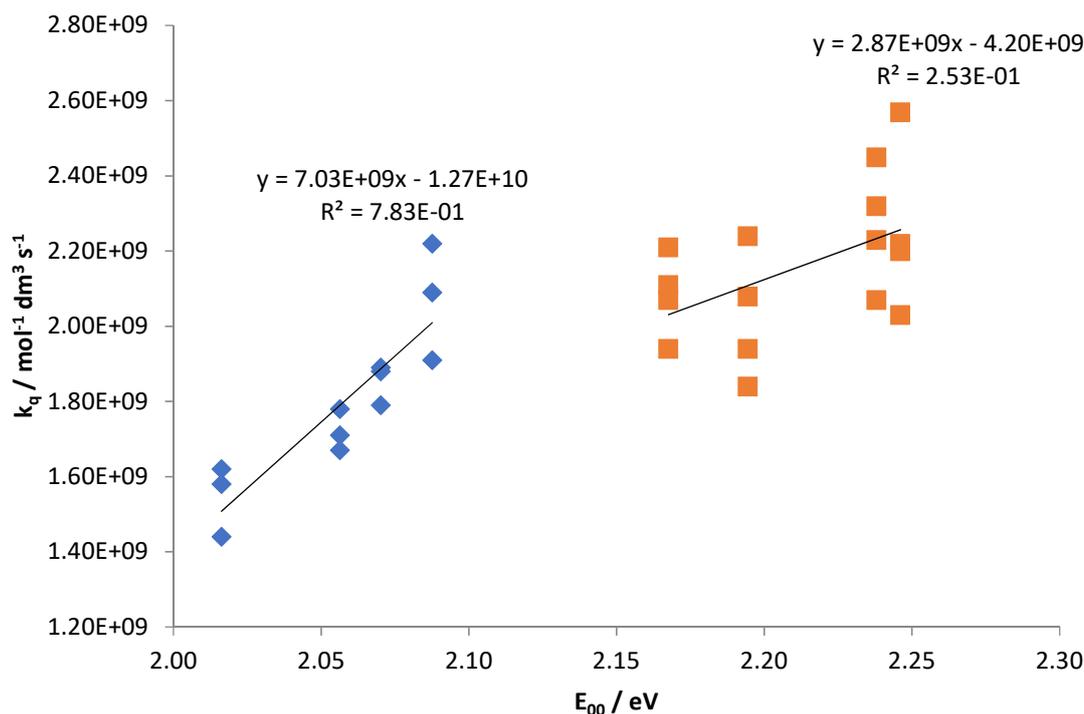
Figure 11 A plot of quenching rate against excited state energy of the complexes PSE1-4 and PST1-4. Red squares represent PST1-4. Blue diamonds represent PSE1-4.

This displays that the butyl complexes have inherently higher quenching rates by [FeFe] quenchers than the ester complexes. A plot of quenching rate against excited state energy, taken from the energy of the emission, again shows two different regimes for the ester and butyl complexes. As these complexes have been assessed by Stern Vomer emission quenching experiments, observing how emission is affected by quenchers, the energy of the state responsible for emission is well represented by the energy of emission interpreted from the λ_{max}. This plot reveals that again the quenching rates of the ester complexes are more strongly affected by the independent variable tested than the butyl complexes. There is a much stronger correlation and a much greater gradient, where there is almost no correlation for the butyl complexes and the gradient is more than twice as steep for the ester complexes.

This behaviour shows that there is either a lessening dependence over a threshold that exists between the two types of complexes or that there is a property of the ester that causes the quenching rate to be more strongly affected by the excited state energy of the photosensitizer. This result supports the interpretation of the effects that back electron transfer have on quenching rate described above.

Third Hypothesis: the lifetime of the lowest excited state of the PS has the greatest effect on quenching of PS by [FeFe] mimics
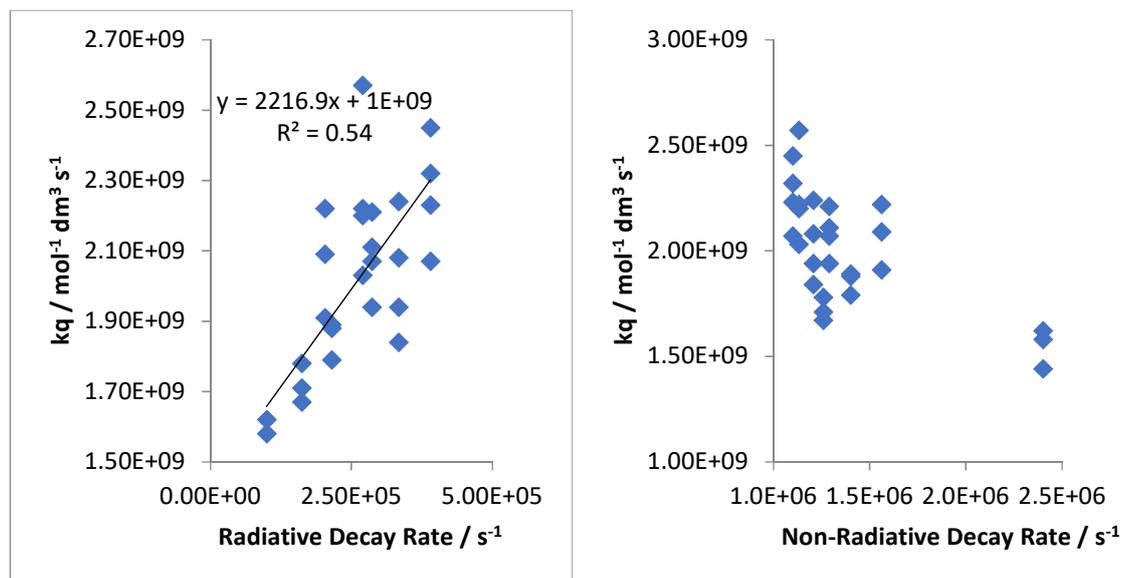
Figure 12 A plot of quenching rate against radiative (left) and non radiative (right) excited state decay rates of the complexes PSE1-4 and PST1-4, quenched by Q1-4.

The investigation using different classes of emitting complexes shows there may be an effect on quenching rates related to the lifetime of the emissive excited state of the complexes. The NCN complex has a higher lifetime than the NNC complexes which have a higher lifetime than the rhenium complex. As the effect noticed may be related to radiative and non-radiative relaxation rates of the photosensitizers the quenching rates have been investigated with regard to their relationship to QY, radiative relaxation rate and non-radiative relaxation rate.

This relationship has been investigated by plotting quenching rate against the decay rates of the Pt NNC acetylide complexes (Figure 12 right). This plot reveals there is no relationship between non-radiative decay rate and quenching rate. The **PSE1** complex exists as an outlier, with much lower lifetime and a lower quenching rate than the other complexes tested.

Despite the lack of correlation between non-radiative decay rate and quenching rate, the existence of the single outlier being the very low quenching rate and high non-radiative relaxation rate of **PSE1** quenched by **Q1-4** remains interesting. This complex is the first to display an equilibrium regime for its relaxation dynamics, based on the work presented in chapter 4 and 5, implying that there is a competing emission deactivation pathway involving a dark state.

A comparison of radiative decay rate with quenching rates for complexes **PSE1-4** and **PST1-4** quenched by **Q1-4** also reveals there is very little correlation between the two (Figure 12 left), suggesting the rate at which excited state population is lost has only a minor effect on quenching rates.

Fourth Hypothesis: the initial population of the excited state of the PS has the greatest effect on quenching of PS by [FeFe] mimics
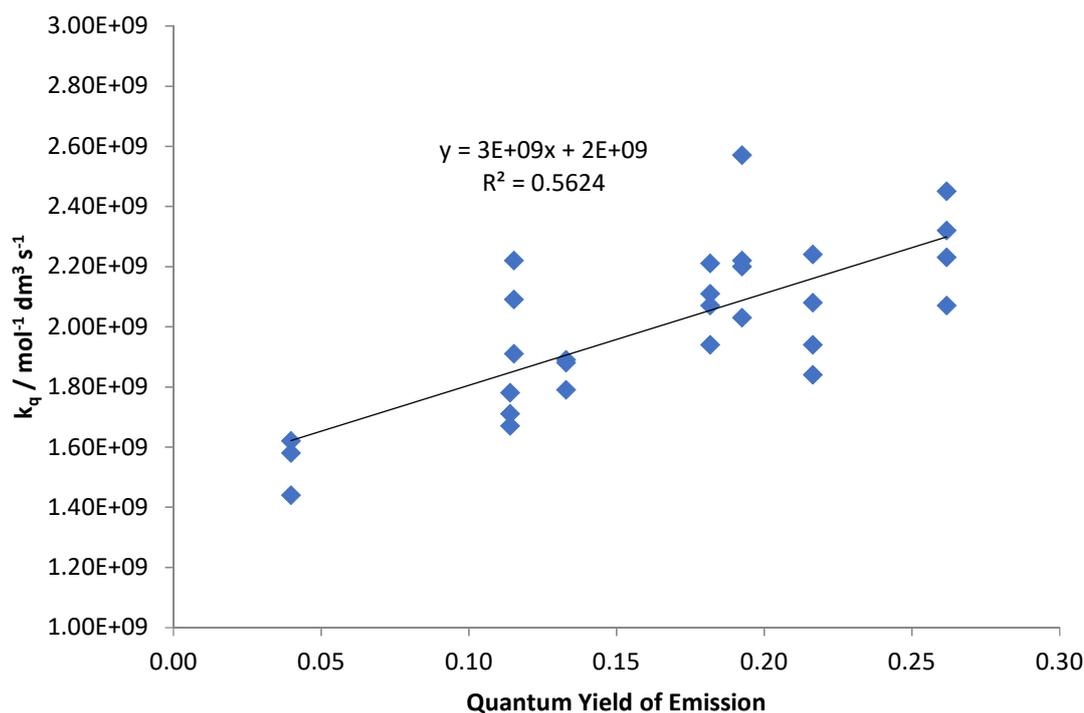
Figure 13 A plot of quenching rate against QY of PSE1-4 and PST1-4 quenched by Q1-4.

Plotting quenching rate against quantum yield of emission reveals a weak correlation. This same correlation is also seen in a plot of quenching rate against the radiative rate of the PS. Based on the findings of previous chapters, this link to the quantum yield and radiative rate suggest that the removal of excited state population from the excited state to a dark state in the photosensitizer has an effect on the ability to transfer energy or an electron to the quencher. This further supports the observations made when comparing oxidation potential with quenching rates. The equilibrium effects in the excited state dynamics and electronics of these complexes have a greater effect than the ground state electronics on the quenching rates in these systems.

Effects dominated by Quencher properties

Due to the limited effect that the changing properties of the PS complexes have on the quenching rates, the effect of the quencher reduction potential was also investigated in search of a stronger and more influential correlation. A plot of the median quenching rate of each quencher, quenching the emission of the butyl substituted PS complexes against the quencher reduction potential was constructed, revealing a straight line relationship.

$$y = 1.28E{+}09x + 4.17E{+}09$$
$$R^2 = 9.48E{-}01$$
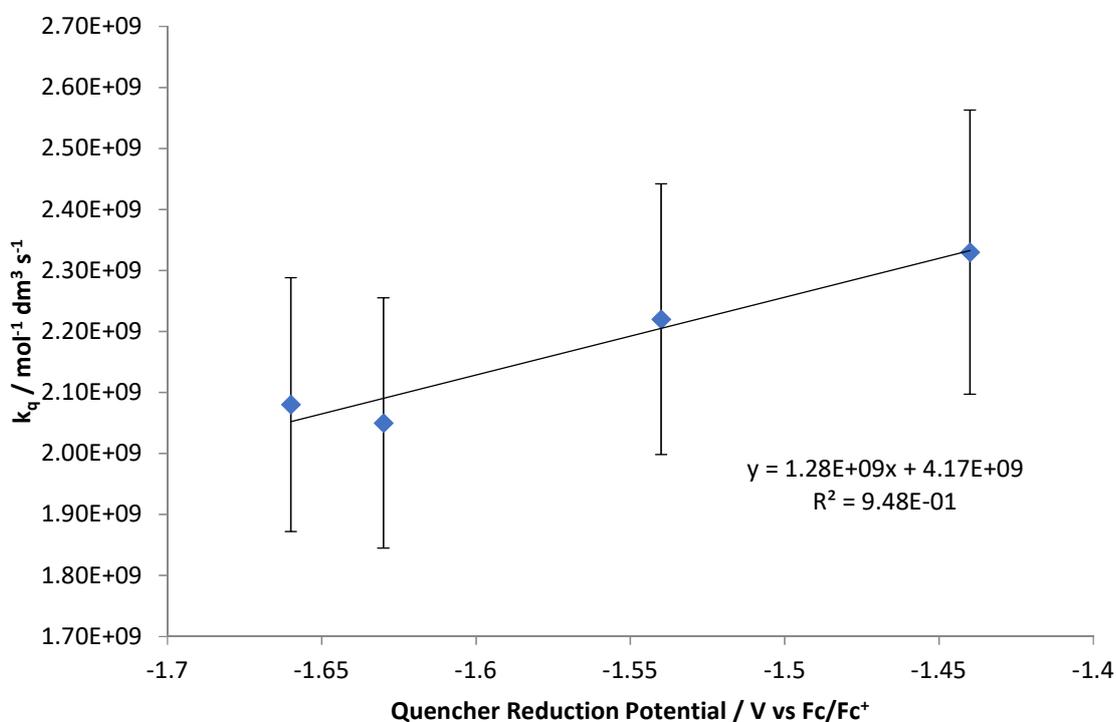
Figure 14 A plot of the median quenching rate for each of Q1-4, quenching PST1-4, agaisnt quencher reduction potential in volts. Error bars represent uncertainty due to the 10 % error in measuring lifetimes.

The less negative the reduction potential of the quencher is, the more easily reduced the quencher is. This, combined with the positive gradient of the constructed plot, means that more easily reduced quenchers have a higher quenching rate. This behaviour is to be expected but the quenching rates show no more dependence on the quencher properties than on the properties of PS complexes. The slope has a gradient of 1.28×10^9 mol^{-1} dm^3 s^{-1} V^{-1}, which is similar to the slope associated with the effect of the butyl substituted PS complexes oxidation potential on quenching (9.65×10^8 mol^{-1} dm^3 s^{-1} V^{-1}) and half that of the ester substituted PS complexes effect (2.80×10^9 mol^{-1} dm^3 s^{-1} V^{-1}). This observed trend is smaller than the uncertainty associated with quenching measurements, revealing that little confidence can be placed in this relationship. This confirms that small changes in the properties of the systems electronics have little effect on the quenching rate. The small amounts of tuning that can be accomplished with these complexes do not produce effective changes in the photosensitization of diiron hydrogenase mimics.

MARCUS INVERTED REGION
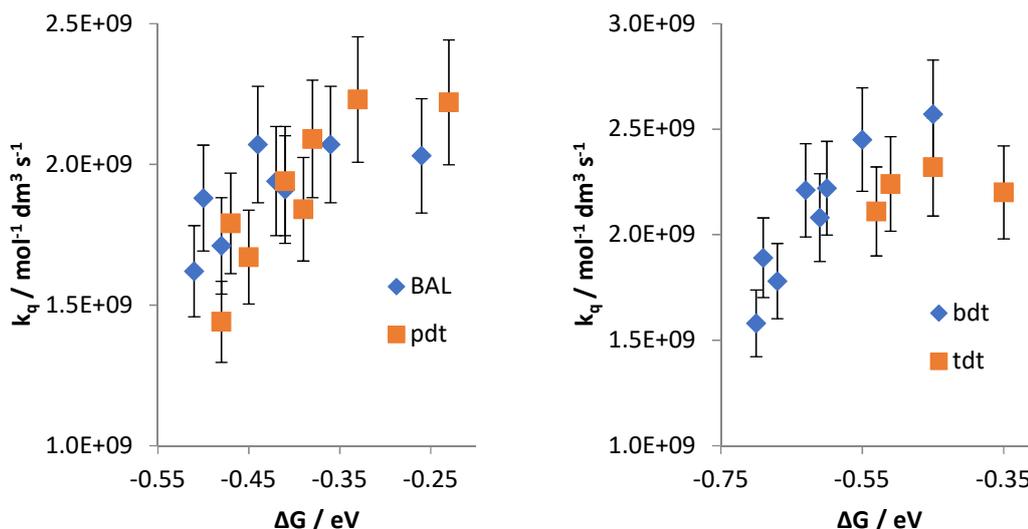
Figure 15 Left: A plot of quenching rate against free energy of photoinduced electron transfer for complexes PSE1-4 and PST1-4 quenched by Q1 and Q2. Error bars represent uncertainty due to the 10 % error in measuring lifetimes. Blue diamonds are quenching rates associated with Q2, red squares are quenching rates asociated with Q1. Right: A plot of quenching rate against free energy of photoinduced electron transfer for complexes PSE1-4 and PST1-4 quenched by Q3 and Q4. Error bars represent uncertainty due to the 10 % error in measuring lifetimes. Blue diamonds are quenching rates associated with Q3, red squares are quenching rates asociated with Q4.

When considering the quenching of emission by either aryl or alkyl bridged diiron hydrogenase mimics separately (Figure 15), a trend is observed that suggests at greater negative ΔG values, the quenching rates decrease. This is the behaviour that could be observed for a Marcus inverted region. This inverted region would not typically be expected for a bimolecular quenching system in low viscosity media, where the limiting factor in quenching is the diffusion rate of the PS and quencher.

When examining the two different linker quenchers (alkyl against aryl), a different trend can be seen for the ester and alkyl substituted PS complexes. The complexes PST1-4 display the expected rising quenching rates at higher negative ΔG values; however PSE1-4 do not. This result suggests that the suppressed quenching rates are in fact due to a property exclusive to the ester substituted PS complexes, PSE1-4.

Previous chapters have shown that there is an equilibrium between a dark charge transfer state and an emissive MMLL'CT state. The effect of the quencher will only be seen on the emissive state, as observation of emission quenching is used to determine quenching rates. The quencher may also affect the unobserved dark state. This behaviour, described above with reference to the effects of oxidation potential on quenching rate, can be used to further investigate equilibrium rates if assumptions are made about the dark state quenching rate.

It is assumed that, for non-equilibrium systems, the maximal dark state quenching rate is almost identical to the observed emissive state quenching rate, due to the CT species having the same spatial volume and thus, rate of diffusion (**Eq. 9**). The total quenching rate for both dark and emissive states is the sum of each quenching rate (**Eq. 8**). The quenching rate for the dark state cannot be directly estimated but it can be assumed that it is higher than the forward equilibrium rate from MMLL'CT to CT, making this the rate limiting step, therefore limiting the quenching rate to the forward equilibrium rate, k_1 (**Eq. 10**). As such, the total quenching rate becomes the sum of the observed quenching rate of the emissive state plus the forward equilibrium rate k_1 (**Eq. 11**).

$$k_{qtot} = k_{qdark} + k_{qobs}$$

<div align="right">Eq. 8</div>

$k_{qdark} \cong k_{qobs}$ in the absence of equilibrium

<div align="right">Eq. 9</div>

$k_1 \ll k_{qdark} \therefore k_{qdark} = k_1$ as k_1 is limiting at equilibrium

<div align="right">Eq. 10</div>

$\therefore k_{qtot} = k_{qobs} + k_1$

<div align="right">Eq. 11</div>

Based on the measurements of quenching constants for the complexes above, the complexes that have no influence on quenching rate from equilibrium are PSE4, PST1, PST2, PST3 and PST4. These complexes exhibit the maximum observable quenching rate due to no loss through equilibrium, and therefore the total quenching rate is the same as observed quenching rate. Therefore, deviations from the mean value of the observed quenching rates experienced by these complexes will give approximate equilibrium rates for the other complexes (PSE1, PSE2, PSE3) using **Eq. 11**, where k_{qtot} is the mean quenching value from PSE4, PST1, PST2, PST3 and PST4, excluding values for the **Q4** quencher. These values are summarized in Table 3. These values are much higher than radiative and non-radiative relaxation rates, consistent with observations in TRIR.

Complex	k_1/k_{-1} / s^{-1}	k_r / s^{-1}	k_{nr} / s^{-1}
PSE1	5.91E+08	9.95E+04	2.40E+06
PSE2	4.18E+08	1.62E+05	1.26E+06
PSE3	2.84E+08	2.15E+05	1.40E+06

Table 3 A table of equilibrium, radiative and non-radiative rates for complexes PSE1-3.

CONCLUSIONS

This chapter concerns investigations into how suitable the cyclometalated platinum acetylide complexes mentioned above are for photosensitizing a diiron hydrogenase mimic to catalyse hydrogen evolution reaction. Initial experiments considered a range of Pt(II) and Re(I) PS complexes and the quenching of their emission by diiron hydrogenase mimics. Factors affecting quenching based on the PS complexes were identified; oxidation potential, excited state energy, lifetime and quantum yield

Further to this, the rate of platinum (II) emission quenching by four different diiron hydrogenase mimics was assessed by Stern Volmer quenching experiments. These experiments revealed that small differences in the properties of the PS have little to no effect on quenching rates. The quenching rates are insensitive to differences in lifetime, oxidation potential, radiative relaxation rate or non-radiative relaxation rate of the PS complex. Quenching rates are raised for complexes with higher excited state energy, but with only two value ranges compared this conclusion requires more data to become a firm prediction. Considering the high quenching rates recorded in this work, it can be assumed that the effects of the PS on the viability of a PS-catalyst combination are negligible. The inability to effectively sensitize the hydrogen evolution reaction is due to factors intrinsic to the catalyst.

The observation of a possible Marcus inverted region was examined. This behaviour was considered to be unlikely given the quenching rates had not reached the diffusion limited value and the low viscosity nature of the CH_2Cl_2 solvent used. Instead this observation was attributed the effect the equilibrium observed in chapters 4 and 5 have on the quenching rate, where the transfer of electron density to a dark CT state competes and subsequent quenching of this dark state with quenching of emissive state.

As all PS complexes seem capable of photosensitizing the diiron hydrogenase mimic quenchers, further work should concentrate on providing the quenchers with a way to store transferred energy. This should take place by first assessing how effective these PS-Cat. pairings are at producing hydrogen and then introducing electron relays to the catalyst structure, such as methyl viologen or the cubic iron sulfur clusters present in the diiron hydrogenase enzyme, in order to improve performance. This mirrors existing hydrogen evolutions systems featuring platinum colloid catalysts[60-62] and would hopefully overcome the short lifetimes of the diiron hydrogenase mimics preventing catalysis. Methyl viologen has been shown to quench the emissive states of cyclometalated platinum and therefore this avenue towards photocatalysis using separate PS and catalyst complexes could be promising.[63]

EXPERIMENTAL

Syntheses of platinum compounds were discussed in chapter 2, diiron hydrogenase mimics were synthesized according to literature procedures.[64-68] Solvents were purchased from VWR and used without further purification. Deoxygenation was performed by 10 min bubbling using bottled Argon purchased from BOC.

General procedure for the preparation of diiron μ-disulfide hexacarbonyl complexes

$Fe_3(CO)_{12}$ (1 mmol) and a stoichiometric amount of the relevant dithiol (1 mmol) were dissolved in of toluene (20mL). The mixture was refluxed under argon atmosphere until a colour change from green to re-brown occurred and the solvent was removed by rotary evaporation. Purification by column chromatography followed by recrystallization by cooling a hexane solution yielded the pure product in all cases. All spectroscopic data (^{1}H NMR, mass spectrometry and IR) were in well agreement with the literature.[64-68]

Quenching Experiments

Quenching experiments were performed by making a $(1 - 4)$ x10^{-5} M solution of PS in dichloromethane that was then purged with bubbling argon. The initial lifetime was measured using these solutions in a 1 cm pathlength, septum capped, fluorescence cell on an Edinburgh Instruments mini-τ single photon counting spectrophotometer excited by a pulsed 410 nm diode, single exponential fits were performed using Origin 8.5 software. Emission spectra were recorded using a Jobin Yvon Fluoromax 4 and UV/Vis absorption spectra were recorded on a Cary 50 Bio spectrometer. Quenching of this initial emission then proceeded by titrating in 10-500 μL of a 1-4x10^{-2} M of quencher and further lifetimes were recorded. Lifetimes were calculated by fitting of monoexponential decay curves to the lifetime traces in Origin 8.5 software.

REFERENCES

1.   Lomoth, R.; Ott, S., *Dalton Trans.* **2009,** (45), 9952-9959.
2.   Cui, H.-h.; Hu, M.-q.; Wen, H.-m.; Chai, G.-l.; Ma, C.-b.; Chen, H.; Chen, C.-n., *Dalton Trans.* **2012,** *41* (45), 13899-13907.
3.   Esswein, A. J.; Nocera, D. G., *Chem. Rev.* **2007,** *107* (10), 4022-4047.
4.   Lakowicz, J. R., *Principles of fluorescence spectroscopy*. 2nd ed ed.; Kluwer Academic/Plenum: New York, 1999; p 698.
5.   Che, C.-M.; Wan, K.-T.; He, L.-Y.; Poon, C.-K.; Yam, V. W.-W., *J. Chem. Soc., Chem. Commun.* **1989,** (14), 943-944.
6.   Chan, C. W.; Lai, T. F.; Che, C. M.; Peng, S. M., *J. Am. Chem. Soc.* **1993,** *115* (24), 11245-11253.
7.   Hissler, M.; Connick, W. B.; Geiger, D. K.; McGarrah, J. E.; Lipa, D.; Lachicotte, R. J.; Eisenberg, R., *Inorg. Chem.* **2000,** *39* (3), 447-457.
8.   Kunkely, H.; Vogler, A., *J. Am. Chem. Soc.* **1990,** *112* (14), 5625-5627.
9.   Ma, B.; Djurovich, P. I.; Thompson, M. E., *Coord. Chem. Rev.* **2005,** *249* (13–14), 1501-1510.
10.   Van Houten, J. C.; Pettijohn, C. N.; Jochnowitz, E. B.; Chuong, B.; Nagle, J. K.; Vogler, A., *Coord. Chem. Rev.* **1998,** *171*, 85-92.
11.   Wan, K.-T.; Che, C.-M.; Cho, K.-C., *J. Chem. Soc., Dalton Trans.* **1991,** (4), 1077-1080.
12.   Williams, J. A. G.; Beeby, A.; Davies, E. S.; Weinstein, J. A.; Wilson, C., *Inorg. Chem.* **2003,** *42* (26), 8609-8611.
13.   Yip, H.-K.; Cheng, L.-K.; Cheung, K.-K.; Che, C.-M., *J. Chem. Soc., Dalton Trans.* **1993,** (19), 2933-2938.
14.   Pinter, P.; Mangold, H.; Stengel, I.; Münster, I.; Strassner, T., *Organometallics* **2016,** *35* (5), 673-680.

15.   Amar, A.; Meghezzi, H.; Boixel, J.; Le Bozec, H.; Guerchais, V.; Jacquemin, D.; Boucekkine, A., *J. Phys. Chem. A* **2014,** *118* (32), 6278-6286.

16.   Kourkoulos, D.; Karakus, C.; Hertel, D.; Alle, R.; Schmeding, S.; Hummel, J.; Risch, N.; Holder, E.; Meerholz, K., *Dalton Trans.* **2013,** *42* (37), 13612-13621.

17.   Bevilacqua, J. M.; Eisenberg, R., *Inorg. Chem.* **1994,** *33* (9), 1886-1890.

18.   Du, P.; Schneider, J.; Jarosz, P.; Zhang, J.; Brennessel, W. W.; Eisenberg, R., *J. Phys. Chem. B* **2007,** *111* (24), 6887-6894.

19.   Hissler, M.; McGarrah, J. E.; Connick, W. B.; Geiger, D. K.; Cummings, S. D.; Eisenberg, R., *Coord. Chem. Rev.* **2000,** *208* (1), 115-137.

20.   Schneider, J.; Du, P.; Jarosz, P.; Lazarides, T.; Wang, X.; Brennessel, W. W.; Eisenberg, R., *Inorg. Chem.* **2009,** *48* (10), 4306-4316.

21.   Thompson, D. W.; Kelly, C. A.; Farzad, F.; Meyer, G. J., *Langmuir* **1999,** *15* (3), 650-653.

22.   Pyati, R.; Richter, M. M., *Annu. Rep. Prog. Chem., Sect. C: Phys. Chem.* **2007,** *103* (0), 12-78.

23.   Marcus, R. A., *Reviews of Modern Physics* **1993,** *65* (3), 599-610.

24.   Miller, J. R.; Calcaterra, L. T.; Closs, G. L., *J. Am. Chem. Soc.* **1984,** *106* (10), 3047-3049.

25.   Balzani, V.; Sabbatini, N.; Scandola, F., *Chem. Rev.* **1986,** *86* (2), 319-337.

26.   Bock, C. R.; Connor, J. A.; Gutierrez, A. R.; Meyer, T. J.; Whitten, D. G.; Sullivan, B. P.; Nagle, J. K., *J. Am. Chem. Soc.* **1979,** *101* (17), 4815-4824.

27.   Heuer, W. B.; Totten, M. D.; Rodman, G. S.; Hebert, E. J.; Tracy, H. J.; Nagle, J. K., *J. Am. Chem. Soc.* **1984,** *106* (4), 1163-1164.

28.   Kavarnos, G. J.; Turro, N. J., *Chem. Rev.* **1986,** *86* (2), 401-449.

29.   Marshall, J. L.; Stobart, S. R.; Gray, H. B., *J. Am. Chem. Soc.* **1984,** *106* (10), 3027-3029.

30.   Nocera, D. G.; Gray, H. B., *J. Am. Chem. Soc.* **1981,** *103* (24), 7349-7350.

31.   Scandola, F.; Balzani, V.; Schuster, G. B., *J. Am. Chem. Soc.* **1981,** *103* (10), 2519-2523.

32.   McLendon, G., *Acc. Chem. Res.* **1988,** *21* (4), 160-167.

33.   McLendon, G.; Miller, J. R., *J. Am. Chem. Soc.* **1985,** *107* (26), 7811-7816.

34.   Scott, J. R.; McLean, M.; Sligar, S. G.; Durham, B.; Millett, F., *J. Am. Chem. Soc.* **1994,** *116* (16), 7356-7362.

35.   Scott, J. R.; Willie, A.; McLean, M.; Stayton, P. S.; Sligar, S. G.; Durham, B.; Millett, F., *J. Am. Chem. Soc.* **1993,** *115* (15), 6820-6824.

36.   Chen, P.; Duesing, R.; Tapolsky, G.; Meyer, T. J., *J. Am. Chem. Soc.* **1989,** *111* (21), 8305-8306.

37.   Chen, P.; Mecklenburg, S. L.; Meyer, T. J., *J. Phys. Chem.* **1993,** *97* (50), 13126-13131.

38.   Closs, G. L.; Calcaterra, L. T.; Green, N. J.; Penfield, K. W.; Miller, J. R., *J. Phys. Chem.* **1986,** *90* (16), 3673-3683.

39.   Closs, G. L.; Miller, J. R., *Science* **1988,** *240* (4851), 440-447.

40.   Fox, L. S.; Kozik, M.; Winkler, J. R.; Gray, H. B., *Science* **1990,** *247* (4946), 1069-1071.

41.   Harrison, R. J.; Pearce, B.; Beddard, G. S.; Cowan, J. A.; Sanders, J. K. M., *Chem. Phys.* **1987,** *116* (3), 429-448.

42.   Irvine, M. P.; Harrison, R. J.; Beddard, G. S.; Leighton, P.; Sanders, J. K. M., *Chem. Phys.* **1986,** *104* (2), 315-324.

43.   Katz, N. E.; Mecklenburg, S. L.; Meyer, T. J., *Inorg. Chem.* **1995,** *34* (5), 1282-1284.

44.   Macpherson, A. N.; Liddell, P. A.; Lin, S.; Noss, L.; Seely, G. R.; DeGraziano, J. M.; Moore, A. L.; Moore, T. A.; Gust, D., *J. Am. Chem. Soc.* **1995,** *117* (27), 7202-7212.

45.   Wasielewski, M. R.; Niemczyk, M. P.; Svec, W. A.; Pewitt, E. B., *J. Am. Chem. Soc.* **1985,** *107* (4), 1080-1082.

46.   Beitz, J. V.; Miller, J. R., *J. Chem. Phys.* **1979,** *71* (11), 4579-4595.

47.   Arnold, B. R.; Noukakis, D.; Farid, S.; Goodman, J. L.; Gould, I. R., *J. Am. Chem. Soc.* **1995,** *117* (15), 4399-4400.

48.   Gould, I. R.; Ege, D.; Moser, J. E.; Farid, S., *J. Am. Chem. Soc.* **1990,** *112* (11), 4290-4301.

49.   Ohno, T.; Yoshimura, A.; Mataga, N., *J. Phys. Chem.* **1990,** *94* (12), 4871-4876.

50.   Zhou, J. S.; Granada, E. S. V.; Leontis, N. B.; Rodgers, M. A. J., *J. Am. Chem. Soc.* **1990,** *112* (13), 5074-5080.

51.   Zhou, J. S.; Rodgers, M. A. J., *J. Am. Chem. Soc.* **1991,** *113* (20), 7728-7734.

52.   Lockard, J. V.; Wasielewski, M. R., *J. Phys. Chem. B* **2007,** *111* (40), 11638-11641.

53.   Rosspeintner, A.; Koch, M.; Angulo, G.; Vauthey, E., *J. Am. Chem. Soc.* **2012,** *134* (28), 11396-11399.

54.   Qiu, D.; Zhao, Q.; Wang, H.; Feng, Y.; Bao, X.; Guo, Y.; Huang, Q., *Inorg. Chim. Acta* **2012,** *392*, 261-267.

55.   Kalyanasundaram, K., *Journal of the Chemical Society, Faraday Transactions 2: Molecular and Chemical Physics* **1986,** *82* (12), 2401-2415.

56.   Chong, D.; Georgakaki, I. P.; Mejia-Rodriguez, R.; Sanabria-Chinchilla, J.; Soriaga, M. P.; Darensbourg, M. Y., *Dalton Trans.* **2003,** (21), 4158-4163.

57.   Donovan, E. S.; Nichol, G. S.; Felton, G. A. N., *J. Organomet. Chem.* **2013,** *726*, 9-13.

58.   Capon, J.-F.; Gloaguen, F.; Schollhammer, P.; Talarmin, J., *J. Electroanal. Chem.* **2004,** *566* (2), 241-247.

59.   Einstein, A., *Ann. Phys. (Berl.)* **1905,** *322* (8), 549-560.

60.   Bard, A. J.; Fox, M. A., *Acc. Chem. Res.* **1995,** *28* (3), 141-145.

61.   Eckenhoff, W. T.; Eisenberg, R., *Dalton Trans.* **2012,** *41* (42), 13004-13021.

62.   Ladomenou, K.; Natali, M.; Iengo, E.; Charalampidis, G.; Scandola, F.; Coutsolelos, A. G., *Coord. Chem. Rev.* **2015,** *304–305*, 38-54.

63.   Zhang, G.-J.; Gan, X.; Xu, Q.-Q.; Chen, Y.; Zhao, X.-J.; Qin, B.; Lv, X.-J.; Lai, S.-W.; Fu, W.-F.; Che, C.-M., *Dalton Trans.* **2012,** *41* (27), 8421-8429.

64.   Lyon, E. J.; Georgakaki, I. P.; Reibenspies, J. H.; Darensbourg, M. Y., *J. Am. Chem. Soc.* **2001,** *123* (14), 3268-3278.

65.   Seyferth, D.; Womack, G. B.; Gallagher, M. K.; Cowie, M.; Hames, B. W.; Fackler, J. P.; Mazany, A. M., *Organometallics* **1987,** *6* (2), 283-294.

66.   Razavet, M.; Cloirec, A. L.; Davies, S. C.; Hughes, D. L.; Pickett, C. J., *J. Chem. Soc., Dalton Trans.* **2001,** (24), 3551-3552.

67.   Cabeza, J. A.; Martínez-García, M. A.; Riera, V.; Ardura, D.; García-Granda, S., *Organometallics* **1998,** *17* (8), 1471-1477.

68.   Schwartz, L.; Singh, P. S.; Eriksson, L.; Lomoth, R.; Ott, S., *C. R. Chim.* **2008,** *11* (8), 875-889.

7. Conclusions

Chapter 3 describes the synthesis of a new PS – diiron hydrogenase mimic dyad. This dyad was synthesized by coupling a new acid bearing platinum complex and an alcohol bearing diiron hydrogenase mimic complex. The dyad was characterized using mass spectrometry, ^{1}H NMR spectroscopy, FTIR spectroscopy, UV/vis electronic absorption spectroscopy, emission spectroscopy and time resolved infra-red spectroscopy. These results revealed a quenching of its emissive lifetime, from 330 ns ± 30 ns to 26 ns ± 2.6 ns, and intensity by 90% relative to a structurally analogous PS model complex. This quenching was attributed to electron transfer from the PS to the diiron hydrogenase mimic in its vibrationally hot excited state. This vibrationally hot excited state was investigated using TRIR spectroscopy to reveal that it lasts 360ps ± 36 ps.

Attempts to synthesize further dyads were unsuccessful. These attempts were made using both rhenium and platinum PS complexes anchored to diiron hydrogenase mimics. Despite attempting modified literature procedures to form dyads, no new dyads were synthesized. These literature procedures were long and unreliable, supporting the methodology of trying to produce dyads through reliable synthetic in pathways with few steps. The linkers between PS and catalyst need to be short but also resist back electron transfer. These dyads do not show stronger performance than analogous bimolecular PS and catalyst systems. Considering these are much easier to produce, the development of dyads should be abandoned in favour of producing useful bimolecular pairings.

Chapter 4 and 5 investigate complexes designed for sensitizing diiron hydrogenase mimics in bimolecular systems. To this end, 14 cyclometalated platinum complexes with acetylide ligands were synthesized. The synthesis of these complexes used a reliable, published method, achieving good yields. These complexes were characterized by mass spectrometry, ^{1}H and ^{19}F NMR spectroscopy, FTIR spectroscopy, UV/vis electronic absorption spectroscopy, emission spectroscopy and time resolved spectroscopies. Initial investigations revealed that the 3-phenyl-5,5'-bis([t]butyl)-2,2'-bipyridine complexes had high QY of emission and long lifetimes of 635 – 713 ns, whilst the ester substituted complexes had much lower emission QY values with a wider variation of lifetimes between 63 – 704 ns. Given the energy of the emission, taken from emission λ_{max}, and position of electronic levels, taken from CV measurements and DFT modelling, it was concluded that the emission of some complexes was not from the lowest excited state. This was confirmed using time-resolved UV/vis absorption experiments.

The ground and excited properties of all complexes and the unusual dynamics of the ester complexes were investigated using Hammett theory. The results of these investigations revealed that the ground state properties of the complexes correlate well with the electron donation potential of the phenyl acetylide ligand, while excited state properties do not. The comparison of the unusual dynamics with the electron donating ability of the phenyl acetylide ligand revealed that the excited state dynamics of the ester complexes are dominated by equilibrium between emissive and dark excited states. This was supported by DFT results suggesting these excited states are almost isoenergetic.

Further experiments conducted using time resolved infra-red spectroscopy further explored the excited state dynamics of these complexes, quantifying the decay lifetimes of the short lived dark excited state. These experiments also provided further evidence for the equilibrium underlying the quenched emission in some complexes. Attempts to control the decay pathways of these complexes using infra-red laser pulses on the excited complexes were unsuccessful. Although there was evidence of promotion to a higher excited state after excitation by the IR pulses, these do not decay through different pathways, suggested by the lack of long timescale differences in the difference spectra.

Chapter 6 concerns investigations into how suitable the cyclometalated platinum acetylide complexes mentioned above are for photosensitizing a diiron hydrogenase mimic catalysed hydrogen evolution reaction. Initial experiments considered a range of Pt(II) and Re(I) PS complexes and the quenching of their emission by diiron hydrogenase mimics. Factors affecting quenching based on the PS complexes were identified; oxidation potential, excited state energy, lifetime and quantum yield

Further to this, the rate of platinum(II) emission quenching by four different diiron hydrogenase mimics was assessed by Stern Volmer quenching experiments. These experiments revealed that small differences in the properties of the PS have little to no effect on quenching rates. The quenching rates are insensitive to differences in lifetime, oxidation potential, radiative relaxation rate or non-radiative relaxation rate of the PS complex. Quenching rates are raised for complexes with higher excited state energy, but with only two value ranges compared this conclusion requires more data to become a firm prediction. Considering the high quenching rates recorded in this work, it can be assumed that the effects of the PS on the viability of a PS- catalyst combination are negligible. The inability to effectively sensitize the hydrogen evolution reaction is due to factors intrinsic to the catalyst.

The observation of a possible Marcus inverted region was examined. This behaviour was considered to be unlikely given the quenching rates had not reached the diffusion limited value and the low viscosity nature of the CH_2Cl_2 solvent used. Instead this observation was attributed the effect the equilibrium observed in chapters 2 and 3 have on the quenching rate, where the transfer of electron density to a dark CT state competes and subsequent quenching of this dark state with quenching of emissive state.

From the work performed in these four chapters, the thesis presented can conclude that further work on the photosensitized, diiron hydrogenase catalyzed, hydrogen evolution reaction should be on attempting to improve the catalysts' abilities to store and use energy. The short lifetimes seen for the excited state of the dyad in chapter 1 are likely due to the short lived excited states of diiron hydrogenase mimics. It does not matter how effectively electrons can be transferred to the catalyst if it does not have the time to react with protons to form molecular hydrogen. Attempts to synthesize dyads should be abandoned in favour of bimolecular systems as photosensitization of the catalyst is not the limiting factor in developing a working system. This is profitable as bimolecular systems are more easily developed than dyads, due to the lengthy syntheses of dyads, as pointed out in chapter 1. Further work should also focus on developing catalyst linked electron and proton shuttles to facilitate catalysis where the excited state lifetimes of diiron complexes are short, in bioinspired structures similar to the iron-sulfur clusters in natural diiron hydrogenase enzymes.

ANNEX A –

PtESTER X-Ray crystallography data
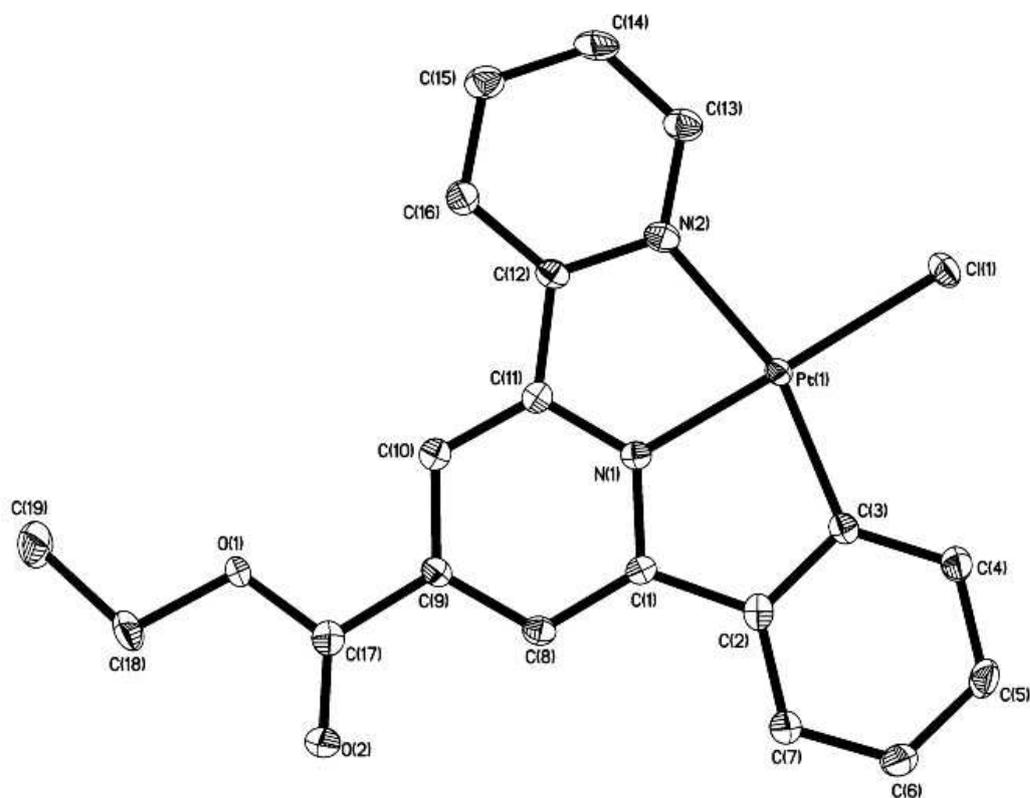
Table 1. Crystal data and structure refinement for imw1773_0m.

Identification code	imw1773_0m
Empirical formula	C19 H15 Cl N2 O2 Pt
Formula weight	533.87
Temperature	100(2) K
Wavelength	0.71073 Å
Crystal system	Triclinic
Space group	P-1
Unit cell dimensions	a = 7.1689(3) Å $\quad$ α= 108.8880(10)°.
	b = 10.8085(5) Å $\quad$ β= 90.367(2)°.
	c = 11.5257(6) Å $\quad$ γ = 103.5660(10)°.
Volume	818.11(7) Å^3
Z	2
Density (calculated)	2.167 Mg/m^3
Absorption coefficient	8.754 mm^{-1}
F(000)	508
Crystal size	0.23 x 0.06 x 0.06 mm^3
Theta range for data collection	1.87 to 27.63°.

Index ranges	-9<=h<=9, -13<=k<=13, -14<=l<=12
Reflections collected	10825
Independent reflections	3633 [R(int) = 0.0180]
Completeness to theta = 27.63°	95.7 %
Absorption correction	Semi-empirical from equivalents
Max. and min. transmission	0.6217 and 0.2380
Refinement method	Full-matrix least-squares on F^2
Data / restraints / parameters	3633 / 0 / 227
Goodness-of-fit on F^2	0.983
Final R indices [I>2sigma(I)]	R1 = 0.0172, wR2 = 0.0418
R indices (all data)	R1 = 0.0185, wR2 = 0.0424
Largest diff. peak and hole	1.263 and -0.826 e.$\mathrm{\AA}^{-3}$

Table 2. Atomic coordinates (x 10^4) and equivalent isotropic displacement parameters (Å^2x 10^3) for imw1773_0m. U(eq) is defined as one third of the trace of the orthogonalized U^{ij} tensor.

	x	y	z	U(eq)
Pt(1)	6473(1)	-575(1)	6510(1)	11(1)
Cl(1)	5266(1)	-1848(1)	7731(1)	18(1)
O(1)	9789(3)	1962(2)	2015(2)	16(1)
O(2)	10094(4)	3958(2)	3525(2)	22(1)
N(1)	7453(3)	461(2)	5442(2)	12(1)
N(2)	6794(4)	-2151(2)	4927(2)	15(1)
C(1)	7699(4)	1826(3)	5890(3)	12(1)
C(2)	7172(4)	2290(3)	7156(3)	14(1)
C(3)	6483(4)	1269(3)	7678(3)	12(1)
C(4)	5948(4)	1659(3)	8873(3)	17(1)
C(5)	6095(5)	3014(3)	9537(3)	20(1)
C(6)	6792(5)	4009(3)	9015(3)	20(1)
C(7)	7328(4)	3654(3)	7822(3)	17(1)
C(8)	8398(4)	2577(3)	5129(3)	14(1)
C(9)	8811(4)	1908(3)	3944(3)	13(1)
C(10)	8532(4)	506(3)	3515(3)	13(1)
C(11)	7843(4)	-202(3)	4293(3)	12(1)
C(12)	7492(4)	-1676(3)	4013(3)	13(1)
C(13)	6460(4)	-3484(3)	4747(3)	18(1)
C(14)	6821(5)	-4390(3)	3664(3)	20(1)
C(15)	7546(5)	-3911(3)	2735(3)	20(1)
C(16)	7888(4)	-2543(3)	2913(3)	16(1)
C(17)	9614(4)	2731(3)	3157(3)	16(1)
C(18)	10682(5)	2700(3)	1225(3)	22(1)
C(19)	10918(6)	1701(4)	12(3)	30(1)

Table 3.   Bond lengths [Å] and angles [°] for imw1773_0m.

_____

Pt(1)-N(1)	1.949(2)
Pt(1)-C(3)	2.010(3)
Pt(1)-N(2)	2.112(3)
Pt(1)-Cl(1)	2.3080(7)
O(1)-C(17)	1.335(4)
O(1)-C(18)	1.453(4)
O(2)-C(17)	1.215(4)
N(1)-C(11)	1.353(4)
N(1)-C(1)	1.363(4)
N(2)-C(13)	1.350(4)
N(2)-C(12)	1.364(4)
C(1)-C(8)	1.399(4)
C(1)-C(2)	1.465(4)
C(2)-C(7)	1.401(4)
C(2)-C(3)	1.415(4)
C(3)-C(4)	1.389(4)
C(4)-C(5)	1.393(4)
C(4)-H(4)	0.9300
C(5)-C(6)	1.393(5)
C(5)-H(1)	0.9300
C(6)-C(7)	1.385(4)
C(6)-H(2)	0.9300
C(7)-H(3)	0.9300
C(8)-C(9)	1.394(4)
C(8)-H(5)	0.9300
C(9)-C(10)	1.397(4)
C(9)-C(17)	1.495(4)
C(10)-C(11)	1.380(4)
C(10)-H(10)	0.9300
C(11)-C(12)	1.477(4)
C(12)-C(16)	1.388(4)
C(13)-C(14)	1.384(4)
C(13)-H(9)	0.9300
C(14)-C(15)	1.387(5)
C(14)-H(8)	0.9300
C(15)-C(16)	1.386(4)
C(15)-H(7)	0.9300
C(16)-H(6)	0.9300

C(18)-C(19)	1.504(5)
C(18)-H(14)	0.9700
C(18)-H(15)	0.9700
C(19)-H(13)	0.9600
C(19)-H(12)	0.9600
C(19)-H(11)	0.9600
N(1)-Pt(1)-C(3)	81.90(11)
N(1)-Pt(1)-N(2)	80.01(10)
C(3)-Pt(1)-N(2)	161.91(11)
N(1)-Pt(1)-Cl(1)	178.49(7)
C(3)-Pt(1)-Cl(1)	99.30(8)
N(2)-Pt(1)-Cl(1)	98.79(7)
C(17)-O(1)-C(18)	115.0(2)
C(11)-N(1)-C(1)	123.1(3)
C(11)-N(1)-Pt(1)	118.83(19)
C(1)-N(1)-Pt(1)	118.10(19)
C(13)-N(2)-C(12)	119.3(3)
C(13)-N(2)-Pt(1)	128.9(2)
C(12)-N(2)-Pt(1)	111.71(19)
N(1)-C(1)-C(8)	118.5(3)
N(1)-C(1)-C(2)	112.3(3)
C(8)-C(1)-C(2)	129.2(3)
C(7)-C(2)-C(3)	121.4(3)
C(7)-C(2)-C(1)	122.9(3)
C(3)-C(2)-C(1)	115.7(3)
C(4)-C(3)-C(2)	117.8(3)
C(4)-C(3)-Pt(1)	130.2(2)
C(2)-C(3)-Pt(1)	112.0(2)
C(3)-C(4)-C(5)	121.0(3)
C(3)-C(4)-H(4)	119.5
C(5)-C(4)-H(4)	119.5
C(4)-C(5)-C(6)	120.5(3)
C(4)-C(5)-H(1)	119.7
C(6)-C(5)-H(1)	119.7
C(7)-C(6)-C(5)	120.0(3)
C(7)-C(6)-H(2)	120.0
C(5)-C(6)-H(2)	120.0
C(6)-C(7)-C(2)	119.3(3)
C(6)-C(7)-H(3)	120.3

C(2)-C(7)-H(3)	120.3
C(9)-C(8)-C(1)	119.1(3)
C(9)-C(8)-H(5)	120.5
C(1)-C(8)-H(5)	120.5
C(10)-C(9)-C(8)	120.8(3)
C(10)-C(9)-C(17)	120.8(3)
C(8)-C(9)-C(17)	118.3(3)
C(11)-C(10)-C(9)	118.5(3)
C(11)-C(10)-H(10)	120.7
C(9)-C(10)-H(10)	120.7
N(1)-C(11)-C(10)	120.1(3)
N(1)-C(11)-C(12)	113.6(3)
C(10)-C(11)-C(12)	126.3(3)
N(2)-C(12)-C(16)	120.8(3)
N(2)-C(12)-C(11)	115.8(3)
C(16)-C(12)-C(11)	123.4(3)
N(2)-C(13)-C(14)	122.0(3)
N(2)-C(13)-H(9)	119.0
C(14)-C(13)-H(9)	119.0
C(13)-C(14)-C(15)	118.9(3)
C(13)-C(14)-H(8)	120.5
C(15)-C(14)-H(8)	120.5
C(16)-C(15)-C(14)	119.3(3)
C(16)-C(15)-H(7)	120.3
C(14)-C(15)-H(7)	120.3
C(15)-C(16)-C(12)	119.6(3)
C(15)-C(16)-H(6)	120.2
C(12)-C(16)-H(6)	120.2
O(2)-C(17)-O(1)	124.0(3)
O(2)-C(17)-C(9)	123.8(3)
O(1)-C(17)-C(9)	112.2(3)
O(1)-C(18)-C(19)	108.7(3)
O(1)-C(18)-H(14)	109.9
C(19)-C(18)-H(14)	109.9
O(1)-C(18)-H(15)	109.9
C(19)-C(18)-H(15)	109.9
H(14)-C(18)-H(15)	108.3
C(18)-C(19)-H(13)	109.5
C(18)-C(19)-H(12)	109.5
H(13)-C(19)-H(12)	109.5

C(18)-C(19)-H(11)   109.5

H(13)-C(19)-H(11)   109.5

H(12)-C(19)-H(11)   109.5

_____

Symmetry transformations used to generate equivalent atoms:

Table 4.   Anisotropic displacement parameters (Å^{2}x 10^3) for imw1773_0m. The anisotropic displacement factor exponent takes the form: $-2\pi^2[\,h^2\,a^{*2}U^{11} + ... \; + 2\,h\,k\,a^*\,b^*\,U^{12}\,]$

	U^{11}	U^{22}	U^{33}	U^{23}	U^{13}	U^{12}
Pt(1)	10(1)	10(1)	12(1)	5(1)	1(1)	1(1)
Cl(1)	21(1)	17(1)	18(1)	10(1)	4(1)	2(1)
O(1)	21(1)	13(1)	14(1)	7(1)	7(1)	3(1)
O(2)	34(1)	13(1)	19(1)	5(1)	6(1)	4(1)
N(1)	9(1)	11(1)	14(1)	4(1)	1(1)	2(1)
N(2)	14(1)	12(1)	19(1)	6(1)	0(1)	1(1)
C(1)	10(1)	12(1)	12(1)	3(1)	0(1)	3(1)
C(2)	12(1)	20(1)	14(1)	7(1)	2(1)	6(1)
C(3)	9(1)	14(1)	14(1)	6(1)	0(1)	1(1)
C(4)	18(2)	18(1)	15(2)	6(1)	2(1)	3(1)
C(5)	21(2)	23(2)	13(2)	4(1)	6(1)	3(1)
C(6)	23(2)	15(1)	19(2)	3(1)	4(1)	3(1)
C(7)	19(2)	16(1)	16(2)	6(1)	4(1)	4(1)
C(8)	12(1)	12(1)	16(1)	4(1)	-1(1)	2(1)
C(9)	12(1)	13(1)	13(1)	5(1)	-1(1)	1(1)
C(10)	11(1)	15(1)	13(1)	4(1)	-1(1)	3(1)
C(11)	8(1)	14(1)	12(1)	4(1)	-1(1)	3(1)
C(12)	10(1)	11(1)	15(1)	4(1)	-2(1)	-1(1)
C(13)	16(2)	15(1)	24(2)	7(1)	3(1)	2(1)
C(14)	17(2)	10(1)	29(2)	5(1)	1(1)	-1(1)
C(15)	19(2)	14(1)	21(2)	3(1)	1(1)	2(1)
C(16)	16(1)	16(1)	15(2)	5(1)	0(1)	2(1)
C(17)	15(1)	18(1)	16(2)	6(1)	2(1)	5(1)
C(18)	28(2)	23(2)	18(2)	13(1)	6(1)	3(1)
C(19)	42(2)	31(2)	12(2)	7(1)	4(2)	0(2)

Table 5. Hydrogen coordinates (x 10^4) and isotropic displacement parameters (Å^2x 10 ^{3}) for imw1773_0m.

	x	y	z	U(eq)
H(4)	5485	1007	9236	20
H(1)	5724	3255	10335	24
H(2)	6897	4912	9467	24
H(3)	7788	4314	7467	20
H(5)	8584	3511	5410	16
H(10)	8804	60	2723	16
H(9)	5973	-3804	5371	22
H(8)	6582	-5304	3561	24
H(7)	7799	-4502	2000	23
H(6)	8381	-2209	2299	19
H(14)	11930	3280	1610	26
H(15)	9881	3262	1098	26
H(13)	11643	1112	150	45
H(12)	11589	2176	-497	45
H(11)	9672	1178	-392	45

ANNEX B – 4. OPTIMIZING PHOTOSENSITIZER PROPERTIES AND UNDERSTANDING DECAY MECHANISMS BY EXPLOITING THE HAMMETT EQUATION

Cyclic Voltammetry
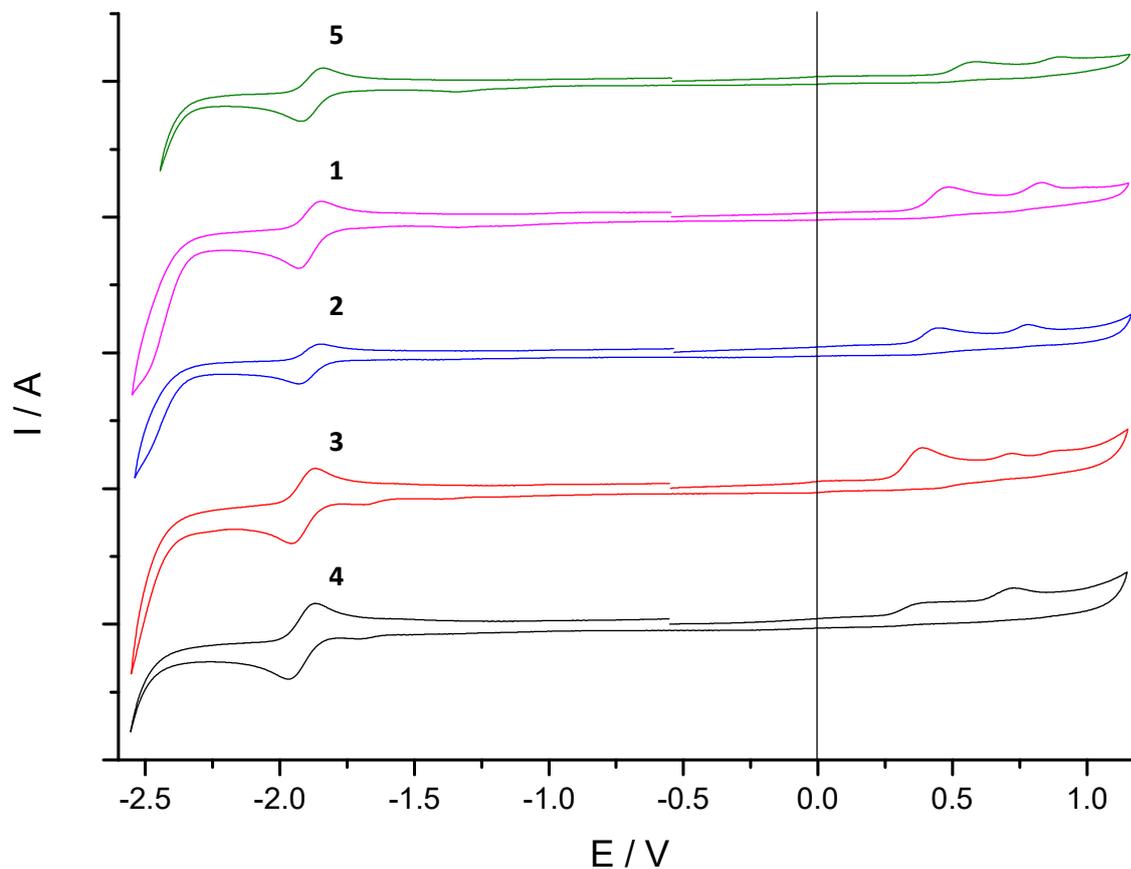
Figure 1 Cyclic volatmmograms of complexes 1 – 5 in N_2 purged DCM with 0.1 M $(^tBu_4N)^+(PF_6)^-$ electrolyte at a scan rate of 100 mVs^{-1} . Potentials are quoted vs. Fc/Fc$^+$.
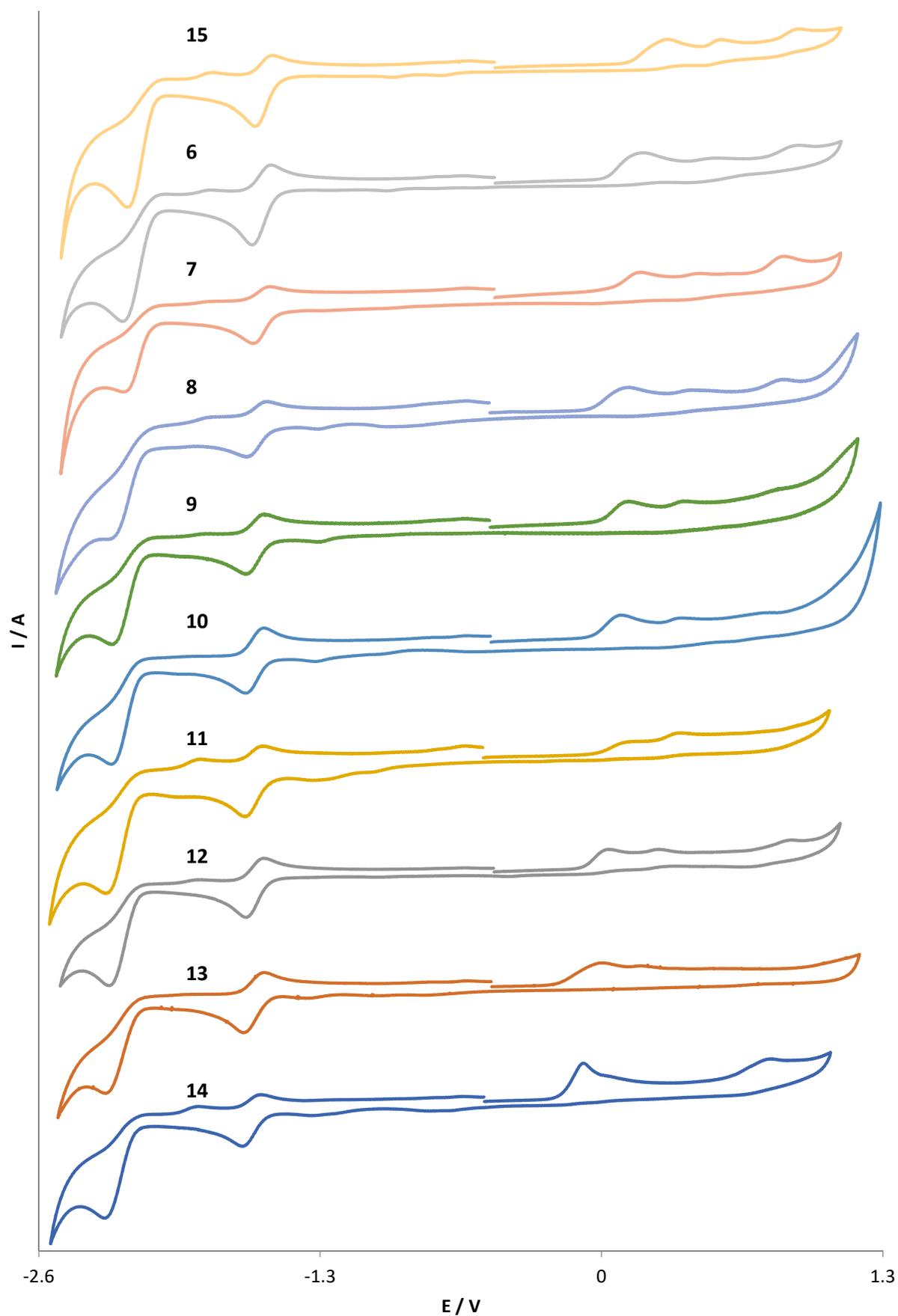
Figure 2 Cyclic volatmmograms of complexes 6 – 15 in N_2 purged DCM with 0.1 M $(^tBu_4N)^+(PF_6)^-$ electrolyte at a scan rate of 100 mVs^{-1}

X Ray diffraction crystal structures

Complex 12
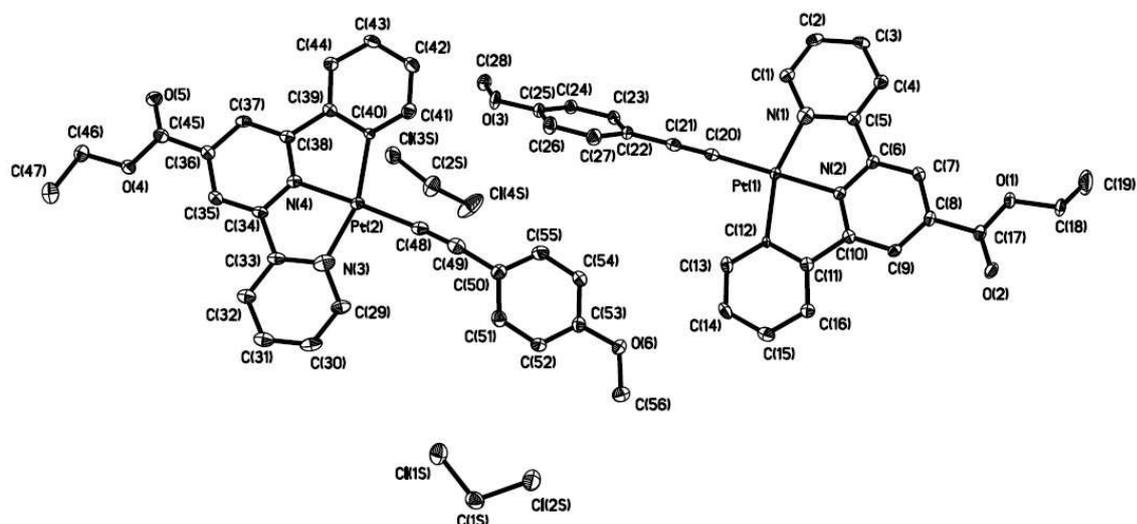
Table 1. Crystal data and structure refinement for LEWIS4REDO_0m.

Identification code	LEWIS4REDO_0m
Empirical formula	C29 H24 Cl2 N2 O3 Pt
Formula weight	714.49
Temperature	446(2) K
Wavelength	0.71073 Å
Crystal system	Triclinic
Space group	P -1
Unit cell dimensions	a = 8.0889(4) Å α= 116.442(2)°.
	b = 18.0742(8) Å β= 94.016(2)°.
	c = 20.2558(9) Å γ = 98.187(2)°.
Volume	2594.7(2) Å^3
Z	4
Density (calculated)	1.829 Mg/m^3
Absorption coefficient	5.649 mm^{-1}
F(000)	1392
Crystal size	0.18 x 0.18 x 0.21 mm^3
Theta range for data collection	1.136 to 27.623°.
Index ranges	-10<=h<=10, -23<=k<=23, -26<=l<=26
Reflections collected	56612
Independent reflections	11999 [R(int) = 0.0308]
Completeness to theta = 25.242°	99.7 %
Absorption correction	None
Refinement method	Full-matrix least-squares on F^2

Data / restraints / parameters	11999 / 0 / 671
Goodness-of-fit on F^2	1.070
Final R indices [I>2sigma(I)]	R1 = 0.0255, wR2 = 0.0575
R indices (all data)	R1 = 0.0326, wR2 = 0.0603
Extinction coefficient	n/a
Largest diff. peak and hole	1.709 and -1.016 e.Å^{-3}

Table 2. Atomic coordinates (x 10^4) and equivalent isotropic displacement parameters (Å^{2}x 10^3) for LEWIS4REDO_0m. U(eq) is defined as one third of the trace of the orthogonalized U^{ij} tensor.

	x	y	z	U(eq)
Pt(1)	6472(1)	543(1)	4260(1)	11(1)
Pt(2)	3331(1)	4322(1)	680(1)	13(1)
O(1)	9230(3)	-297(2)	7074(1)	19(1)
O(2)	8657(3)	985(2)	7796(1)	21(1)
O(3)	3664(3)	1051(2)	226(1)	23(1)
O(4)	1764(3)	5483(2)	-2046(1)	22(1)
O(5)	2397(3)	4227(2)	-2786(1)	24(1)
O(6)	2798(3)	3984(2)	4838(1)	24(1)
N(1)	7387(4)	-522(2)	3822(2)	24(1)
N(2)	7089(3)	476(2)	5194(2)	12(1)
N(3)	2330(4)	5364(2)	1100(2)	27(1)
N(4)	3005(3)	4465(2)	-233(2)	14(1)
C(1)	7510(4)	-1060(2)	3079(2)	17(1)
C(2)	8176(4)	-1783(2)	2895(2)	19(1)
C(3)	8728(4)	-1996(2)	3440(2)	19(1)
C(4)	8635(4)	-1470(2)	4183(2)	17(1)
C(5)	7971(4)	-746(2)	4372(2)	14(1)
C(6)	7811(4)	-173(2)	5146(2)	12(1)
C(7)	8312(4)	-221(2)	5794(2)	14(1)
C(8)	8047(4)	396(2)	6472(2)	14(1)
C(9)	7277(4)	1052(2)	6507(2)	14(1)
C(10)	6804(4)	1079(2)	5849(2)	12(1)
C(11)	6010(4)	1727(2)	5764(2)	13(1)
C(12)	5695(4)	1612(2)	5047(2)	6(1)
C(13)	4968(4)	2173(2)	4926(2)	18(1)
C(14)	4541(5)	2868(2)	5501(2)	21(1)
C(15)	4859(4)	2988(2)	6226(2)	21(1)
C(16)	5594(4)	2408(2)	6357(2)	16(1)
C(17)	8662(4)	401(2)	7188(2)	16(1)
C(18)	10052(5)	-333(2)	7717(2)	23(1)
C(19)	9798(7)	-1233(3)	7553(3)	47(1)
C(20)	5854(4)	612(2)	3329(2)	15(1)
C(21)	5452(4)	675(2)	2781(2)	19(1)
C(22)	4962(4)	753(2)	2114(2)	17(1)
C(23)	3822(4)	119(2)	1516(2)	18(1)

C(24)	3341(4)	194(2)	878(2)	17(1)
C(25)	4024(4)	910(2)	829(2)	19(1)
C(26)	5173(5)	1552(2)	1419(2)	22(1)
C(27)	5634(5)	1482(2)	2054(2)	23(1)
C(28)	2588(5)	385(2)	-414(2)	22(1)
C(29)	2029(4)	5853(2)	1831(2)	21(1)
C(30)	1342(4)	6564(2)	2006(2)	23(1)
C(31)	910(4)	6812(2)	1466(2)	22(1)
C(32)	1179(4)	6336(2)	738(2)	20(1)
C(33)	1898(4)	5620(2)	558(2)	17(1)
C(34)	2283(4)	5110(2)	-192(2)	14(1)
C(35)	2019(4)	5222(2)	-823(2)	15(1)
C(36)	2501(4)	4669(2)	-1479(2)	15(1)
C(37)	3249(4)	4007(2)	-1510(2)	15(1)
C(38)	3482(4)	3912(2)	-869(2)	14(1)
C(39)	4232(4)	3261(2)	-775(2)	14(1)
C(40)	4310(4)	3304(2)	-76(2)	8(1)
C(41)	5007(4)	2741(2)	46(2)	20(1)
C(42)	5612(5)	2097(2)	-508(2)	22(1)
C(43)	5531(4)	2048(2)	-1210(2)	20(1)
C(44)	4842(4)	2636(2)	-1344(2)	16(1)
C(45)	2225(4)	4755(2)	-2179(2)	18(1)
C(46)	1488(5)	5630(3)	-2693(2)	27(1)
C(47)	958(5)	6456(3)	-2436(2)	32(1)
C(48)	3567(4)	4206(2)	1604(2)	18(1)
C(49)	3612(4)	4162(2)	2175(2)	22(1)
C(50)	3501(4)	4145(2)	2878(2)	20(1)
C(51)	3131(5)	4833(2)	3491(2)	21(1)
C(52)	2887(5)	4805(2)	4150(2)	20(1)
C(53)	3036(4)	4087(2)	4216(2)	19(1)
C(54)	3441(5)	3399(2)	3625(2)	23(1)
C(55)	3658(5)	3426(2)	2963(2)	25(1)
C(56)	2467(5)	4686(2)	5475(2)	25(1)
C(1S)	774(5)	7396(2)	5467(2)	28(1)
C(2S)	831(6)	2296(3)	435(2)	31(1)
Cl(1S)	571(1)	6917(1)	4485(1)	33(1)
Cl(2S)	1909(2)	6864(1)	5837(1)	39(1)
Cl(3S)	214(1)	1900(1)	-535(1)	29(1)
Cl(4S)	-499(2)	1741(1)	781(1)	57(1)

Table 3.   Bond lengths [Å] and angles [°] for LEWIS4REDO_0m.

_____

Pt(1)-C(20)	1.979(4)
Pt(1)-N(2)	1.983(3)
Pt(1)-N(1)	2.003(3)
Pt(1)-C(12)	2.101(3)
Pt(2)-C(48)	1.974(4)
Pt(2)-N(4)	1.983(3)
Pt(2)-N(3)	2.006(3)
Pt(2)-C(40)	2.106(3)
O(1)-C(17)	1.332(4)
O(1)-C(18)	1.453(4)
O(2)-C(17)	1.214(4)
O(3)-C(25)	1.377(4)
O(3)-C(28)	1.429(4)
O(4)-C(45)	1.334(4)
O(4)-C(46)	1.457(4)
O(5)-C(45)	1.209(4)
O(6)-C(53)	1.375(4)
O(6)-C(56)	1.426(4)
N(1)-C(1)	1.402(5)
N(1)-C(5)	1.417(5)
N(2)-C(6)	1.351(4)
N(2)-C(10)	1.352(4)
N(3)-C(29)	1.406(5)
N(3)-C(33)	1.410(5)
N(4)-C(34)	1.349(4)
N(4)-C(38)	1.357(4)
C(1)-C(2)	1.390(5)
C(1)-H(1)	0.9300
C(2)-C(3)	1.387(5)
C(2)-H(2)	0.9300
C(3)-C(4)	1.390(5)
C(3)-H(3)	0.9300
C(4)-C(5)	1.390(5)
C(4)-H(4)	0.9300
C(5)-C(6)	1.472(5)
C(6)-C(7)	1.390(5)
C(7)-C(8)	1.386(5)
C(7)-H(7)	0.9300

C(8)-C(9)	1.393(5)
C(8)-C(17)	1.496(5)
C(9)-C(10)	1.385(5)
C(9)-H(9)	0.9300
C(10)-C(11)	1.481(5)
C(11)-C(12)	1.372(4)
C(11)-C(16)	1.389(5)
C(12)-C(13)	1.344(5)
C(13)-C(14)	1.389(5)
C(13)-H(13)	0.9300
C(14)-C(15)	1.383(5)
C(14)-H(14)	0.9300
C(15)-C(16)	1.387(5)
C(15)-H(15)	0.9300
C(16)-H(16)	0.9300
C(18)-C(19)	1.487(6)
C(18)-H(18A)	0.9700
C(18)-H(18B)	0.9700
C(19)-H(19A)	0.9600
C(19)-H(19B)	0.9600
C(19)-H(19C)	0.9600
C(20)-C(21)	1.193(5)
C(21)-C(22)	1.455(5)
C(22)-C(23)	1.391(5)
C(22)-C(27)	1.411(5)
C(23)-C(24)	1.394(5)
C(23)-H(23)	0.9300
C(24)-C(25)	1.381(5)
C(24)-H(24)	0.9300
C(25)-C(26)	1.393(5)
C(26)-C(27)	1.378(5)
C(26)-H(26)	0.9300
C(27)-H(27)	0.9300
C(28)-H(28A)	0.9600
C(28)-H(28B)	0.9600
C(28)-H(28C)	0.9600
C(29)-C(30)	1.382(5)
C(29)-H(29)	0.9300
C(30)-C(31)	1.396(6)
C(30)-H(30)	0.9300

C(31)-C(32)	1.388(5)
C(31)-H(31)	0.9300
C(32)-C(33)	1.404(5)
C(32)-H(32)	0.9300
C(33)-C(34)	1.469(5)
C(34)-C(35)	1.387(5)
C(35)-C(36)	1.385(5)
C(35)-H(35)	0.9300
C(36)-C(37)	1.396(5)
C(36)-C(45)	1.498(5)
C(37)-C(38)	1.387(5)
C(37)-H(37)	0.9300
C(38)-C(39)	1.476(5)
C(39)-C(40)	1.377(5)
C(39)-C(44)	1.388(5)
C(40)-C(41)	1.336(5)
C(41)-C(42)	1.389(5)
C(41)-H(41)	0.9300
C(42)-C(43)	1.382(5)
C(42)-H(42)	0.9300
C(43)-C(44)	1.384(5)
C(43)-H(43)	0.9300
C(44)-H(44)	0.9300
C(46)-C(47)	1.485(6)
C(46)-H(46A)	0.9700
C(46)-H(46B)	0.9700
C(47)-H(47A)	0.9600
C(47)-H(47B)	0.9600
C(47)-H(47C)	0.9600
C(48)-C(49)	1.192(5)
C(49)-C(50)	1.446(5)
C(50)-C(51)	1.401(5)
C(50)-C(55)	1.406(5)
C(51)-C(52)	1.385(5)
C(51)-H(51)	0.9300
C(52)-C(53)	1.382(5)
C(52)-H(52)	0.9300
C(53)-C(54)	1.390(5)
C(54)-C(55)	1.386(5)
C(54)-H(54)	0.9300

C(55)-H(55)	0.9300
C(56)-H(56A)	0.9600
C(56)-H(56B)	0.9600
C(56)-H(56C)	0.9600
C(1S)-Cl(1S)	1.766(4)
C(1S)-Cl(2S)	1.768(4)
C(1S)-H(1S1)	0.9700
C(1S)-H(1S2)	0.9700
C(2S)-Cl(4S)	1.754(4)
C(2S)-Cl(3S)	1.769(4)
C(2S)-H(2S1)	0.9700
C(2S)-H(2S2)	0.9700
C(20)-Pt(1)-N(2)	179.87(13)
C(20)-Pt(1)-N(1)	98.52(13)
N(2)-Pt(1)-N(1)	81.61(12)
C(20)-Pt(1)-C(12)	101.01(12)
N(2)-Pt(1)-C(12)	78.86(11)
N(1)-Pt(1)-C(12)	160.44(13)
C(48)-Pt(2)-N(4)	177.35(12)
C(48)-Pt(2)-N(3)	96.17(14)
N(4)-Pt(2)-N(3)	81.50(13)
C(48)-Pt(2)-C(40)	103.21(13)
N(4)-Pt(2)-C(40)	79.15(12)
N(3)-Pt(2)-C(40)	160.61(13)
C(17)-O(1)-C(18)	117.8(3)
C(25)-O(3)-C(28)	117.3(3)
C(45)-O(4)-C(46)	115.7(3)
C(53)-O(6)-C(56)	117.5(3)
C(1)-N(1)-C(5)	117.3(3)
C(1)-N(1)-Pt(1)	130.4(3)
C(5)-N(1)-Pt(1)	112.3(2)
C(6)-N(2)-C(10)	122.8(3)
C(6)-N(2)-Pt(1)	117.8(2)
C(10)-N(2)-Pt(1)	119.5(2)
C(29)-N(3)-C(33)	117.8(3)
C(29)-N(3)-Pt(2)	130.0(3)
C(33)-N(3)-Pt(2)	112.2(2)
C(34)-N(4)-C(38)	122.8(3)
C(34)-N(4)-Pt(2)	117.7(2)

C(38)-N(4)-Pt(2)	119.5(2)
C(2)-C(1)-N(1)	120.9(3)
C(2)-C(1)-H(1)	119.5
N(1)-C(1)-H(1)	119.5
C(3)-C(2)-C(1)	121.0(3)
C(3)-C(2)-H(2)	119.5
C(1)-C(2)-H(2)	119.5
C(2)-C(3)-C(4)	119.4(3)
C(2)-C(3)-H(3)	120.3
C(4)-C(3)-H(3)	120.3
C(5)-C(4)-C(3)	120.0(3)
C(5)-C(4)-H(4)	120.0
C(3)-C(4)-H(4)	120.0
C(4)-C(5)-N(1)	121.4(3)
C(4)-C(5)-C(6)	122.5(3)
N(1)-C(5)-C(6)	116.0(3)
N(2)-C(6)-C(7)	119.1(3)
N(2)-C(6)-C(5)	112.2(3)
C(7)-C(6)-C(5)	128.6(3)
C(8)-C(7)-C(6)	119.1(3)
C(8)-C(7)-H(7)	120.4
C(6)-C(7)-H(7)	120.4
C(7)-C(8)-C(9)	120.7(3)
C(7)-C(8)-C(17)	121.0(3)
C(9)-C(8)-C(17)	118.2(3)
C(10)-C(9)-C(8)	118.4(3)
C(10)-C(9)-H(9)	120.8
C(8)-C(9)-H(9)	120.8
N(2)-C(10)-C(9)	119.9(3)
N(2)-C(10)-C(11)	113.1(3)
C(9)-C(10)-C(11)	127.0(3)
C(12)-C(11)-C(16)	121.1(3)
C(12)-C(11)-C(10)	115.2(3)
C(16)-C(11)-C(10)	123.6(3)
C(13)-C(12)-C(11)	118.6(3)
C(13)-C(12)-Pt(1)	128.1(2)
C(11)-C(12)-Pt(1)	113.4(2)
C(12)-C(13)-C(14)	122.4(3)
C(12)-C(13)-H(13)	118.8
C(14)-C(13)-H(13)	118.8

194

C(15)-C(14)-C(13)	119.2(3)
C(15)-C(14)-H(14)	120.4
C(13)-C(14)-H(14)	120.4
C(14)-C(15)-C(16)	118.9(3)
C(14)-C(15)-H(15)	120.5
C(16)-C(15)-H(15)	120.5
C(15)-C(16)-C(11)	119.7(3)
C(15)-C(16)-H(16)	120.1
C(11)-C(16)-H(16)	120.1
O(2)-C(17)-O(1)	125.0(3)
O(2)-C(17)-C(8)	123.0(3)
O(1)-C(17)-C(8)	112.0(3)
O(1)-C(18)-C(19)	107.7(3)
O(1)-C(18)-H(18A)	110.2
C(19)-C(18)-H(18A)	110.2
O(1)-C(18)-H(18B)	110.2
C(19)-C(18)-H(18B)	110.2
H(18A)-C(18)-H(18B)	108.5
C(18)-C(19)-H(19A)	109.5
C(18)-C(19)-H(19B)	109.5
H(19A)-C(19)-H(19B)	109.5
C(18)-C(19)-H(19C)	109.5
H(19A)-C(19)-H(19C)	109.5
H(19B)-C(19)-H(19C)	109.5
C(21)-C(20)-Pt(1)	177.7(3)
C(20)-C(21)-C(22)	180.0(5)
C(23)-C(22)-C(27)	117.8(3)
C(23)-C(22)-C(21)	121.6(3)
C(27)-C(22)-C(21)	120.7(3)
C(22)-C(23)-C(24)	121.8(3)
C(22)-C(23)-H(23)	119.1
C(24)-C(23)-H(23)	119.1
C(25)-C(24)-C(23)	119.4(3)
C(25)-C(24)-H(24)	120.3
C(23)-C(24)-H(24)	120.3
O(3)-C(25)-C(24)	124.8(3)
O(3)-C(25)-C(26)	115.3(3)
C(24)-C(25)-C(26)	119.8(3)
C(27)-C(26)-C(25)	120.7(3)
C(27)-C(26)-H(26)	119.7

C(25)-C(26)-H(26)	119.7
C(26)-C(27)-C(22)	120.5(3)
C(26)-C(27)-H(27)	119.7
C(22)-C(27)-H(27)	119.7
O(3)-C(28)-H(28A)	109.5
O(3)-C(28)-H(28B)	109.5
H(28A)-C(28)-H(28B)	109.5
O(3)-C(28)-H(28C)	109.5
H(28A)-C(28)-H(28C)	109.5
H(28B)-C(28)-H(28C)	109.5
C(30)-C(29)-N(3)	120.6(4)
C(30)-C(29)-H(29)	119.7
N(3)-C(29)-H(29)	119.7
C(29)-C(30)-C(31)	121.3(3)
C(29)-C(30)-H(30)	119.4
C(31)-C(30)-H(30)	119.4
C(32)-C(31)-C(30)	119.4(4)
C(32)-C(31)-H(31)	120.3
C(30)-C(31)-H(31)	120.3
C(31)-C(32)-C(33)	119.6(4)
C(31)-C(32)-H(32)	120.2
C(33)-C(32)-H(32)	120.2
C(32)-C(33)-N(3)	121.3(3)
C(32)-C(33)-C(34)	122.5(3)
N(3)-C(33)-C(34)	116.3(3)
N(4)-C(34)-C(35)	119.2(3)
N(4)-C(34)-C(33)	112.3(3)
C(35)-C(34)-C(33)	128.5(3)
C(36)-C(35)-C(34)	119.2(3)
C(36)-C(35)-H(35)	120.4
C(34)-C(35)-H(35)	120.4
C(35)-C(36)-C(37)	120.8(3)
C(35)-C(36)-C(45)	121.4(3)
C(37)-C(36)-C(45)	117.8(3)
C(38)-C(37)-C(36)	118.2(3)
C(38)-C(37)-H(37)	120.9
C(36)-C(37)-H(37)	120.9
N(4)-C(38)-C(37)	119.7(3)
N(4)-C(38)-C(39)	112.7(3)
C(37)-C(38)-C(39)	127.5(3)

C(40)-C(39)-C(44)	120.7(3)
C(40)-C(39)-C(38)	116.1(3)
C(44)-C(39)-C(38)	123.2(3)
C(41)-C(40)-C(39)	118.8(3)
C(41)-C(40)-Pt(2)	128.6(3)
C(39)-C(40)-Pt(2)	112.6(2)
C(40)-C(41)-C(42)	122.7(3)
C(40)-C(41)-H(41)	118.6
C(42)-C(41)-H(41)	118.6
C(43)-C(42)-C(41)	118.7(3)
C(43)-C(42)-H(42)	120.6
C(41)-C(42)-H(42)	120.6
C(42)-C(43)-C(44)	119.4(3)
C(42)-C(43)-H(43)	120.3
C(44)-C(43)-H(43)	120.3
C(43)-C(44)-C(39)	119.7(3)
C(43)-C(44)-H(44)	120.1
C(39)-C(44)-H(44)	120.1
O(5)-C(45)-O(4)	124.5(3)
O(5)-C(45)-C(36)	123.8(3)
O(4)-C(45)-C(36)	111.6(3)
O(4)-C(46)-C(47)	107.5(3)
O(4)-C(46)-H(46A)	110.2
C(47)-C(46)-H(46A)	110.2
O(4)-C(46)-H(46B)	110.2
C(47)-C(46)-H(46B)	110.2
H(46A)-C(46)-H(46B)	108.5
C(46)-C(47)-H(47A)	109.5
C(46)-C(47)-H(47B)	109.5
H(47A)-C(47)-H(47B)	109.5
C(46)-C(47)-H(47C)	109.5
H(47A)-C(47)-H(47C)	109.5
H(47B)-C(47)-H(47C)	109.5
C(49)-C(48)-Pt(2)	175.4(3)
C(48)-C(49)-C(50)	173.8(4)
C(51)-C(50)-C(55)	117.3(3)
C(51)-C(50)-C(49)	120.9(3)
C(55)-C(50)-C(49)	121.8(3)
C(52)-C(51)-C(50)	121.7(3)
C(52)-C(51)-H(51)	119.1

C(50)-C(51)-H(51)	119.1
C(53)-C(52)-C(51)	119.8(3)
C(53)-C(52)-H(52)	120.1
C(51)-C(52)-H(52)	120.1
O(6)-C(53)-C(52)	124.7(3)
O(6)-C(53)-C(54)	115.2(3)
C(52)-C(53)-C(54)	120.1(3)
C(55)-C(54)-C(53)	119.9(4)
C(55)-C(54)-H(54)	120.1
C(53)-C(54)-H(54)	120.1
C(54)-C(55)-C(50)	121.2(3)
C(54)-C(55)-H(55)	119.4
C(50)-C(55)-H(55)	119.4
O(6)-C(56)-H(56A)	109.5
O(6)-C(56)-H(56B)	109.5
H(56A)-C(56)-H(56B)	109.5
O(6)-C(56)-H(56C)	109.5
H(56A)-C(56)-H(56C)	109.5
H(56B)-C(56)-H(56C)	109.5
Cl(1S)-C(1S)-Cl(2S)	111.5(2)
Cl(1S)-C(1S)-H(1S1)	109.3
Cl(2S)-C(1S)-H(1S1)	109.3
Cl(1S)-C(1S)-H(1S2)	109.3
Cl(2S)-C(1S)-H(1S2)	109.3
H(1S1)-C(1S)-H(1S2)	108.0
Cl(4S)-C(2S)-Cl(3S)	110.4(2)
Cl(4S)-C(2S)-H(2S1)	109.6
Cl(3S)-C(2S)-H(2S1)	109.6
Cl(4S)-C(2S)-H(2S2)	109.6
Cl(3S)-C(2S)-H(2S2)	109.6
H(2S1)-C(2S)-H(2S2)	108.1

_____

Symmetry transformations used to generate equivalent atoms:

Table 4.   Anisotropic displacement parameters ($\text{Å}^2 \times 10^3$) for LEWIS4REDO_0m. The anisotropic displacement factor exponent takes the form: $-2\pi^2[\, h^2 \, a^{*2}U^{11} + \ldots + 2\, h\, k\, a^*\, b^*\, U^{12}\,]$

	U^{11}	U^{22}	U^{33}	U^{23}	U^{13}	U^{12}
Pt(1)	10(1)	13(1)	11(1)	7(1)	1(1)	1(1)
Pt(2)	11(1)	13(1)	14(1)	5(1)	3(1)	1(1)
O(1)	25(1)	21(1)	16(1)	12(1)	1(1)	7(1)
O(2)	30(1)	22(1)	12(1)	8(1)	2(1)	6(1)
O(3)	32(2)	23(1)	16(1)	13(1)	-2(1)	1(1)
O(4)	27(1)	21(1)	19(1)	10(1)	5(1)	11(1)
O(5)	31(2)	25(1)	16(1)	8(1)	5(1)	11(1)
O(6)	33(2)	24(1)	18(1)	12(1)	7(1)	9(1)
N(1)	21(2)	27(2)	24(2)	12(2)	2(1)	1(1)
N(2)	9(1)	14(1)	12(1)	7(1)	1(1)	-1(1)
N(3)	19(2)	29(2)	26(2)	7(2)	5(1)	-1(1)
N(4)	9(1)	13(1)	16(1)	5(1)	2(1)	-1(1)
C(1)	13(2)	20(2)	15(2)	6(1)	1(1)	0(1)
C(2)	14(2)	22(2)	15(2)	4(2)	5(1)	1(1)
C(3)	12(2)	20(2)	24(2)	7(2)	5(1)	5(1)
C(4)	15(2)	20(2)	18(2)	10(2)	3(1)	2(1)
C(5)	10(2)	15(2)	15(2)	6(1)	0(1)	-2(1)
C(6)	9(2)	14(2)	15(2)	8(1)	2(1)	-1(1)
C(7)	11(2)	14(2)	19(2)	9(1)	1(1)	1(1)
C(8)	11(2)	16(2)	14(2)	9(1)	-1(1)	-2(1)
C(9)	12(2)	16(2)	11(2)	6(1)	2(1)	1(1)
C(10)	8(1)	12(2)	16(2)	7(1)	0(1)	-2(1)
C(11)	7(1)	15(2)	17(2)	9(1)	1(1)	-1(1)
C(12)	4(1)	7(1)	9(1)	5(1)	-1(1)	-1(1)
C(13)	17(2)	22(2)	22(2)	16(2)	2(1)	4(1)
C(14)	21(2)	20(2)	29(2)	16(2)	4(2)	9(2)
C(15)	19(2)	18(2)	27(2)	10(2)	7(2)	6(1)
C(16)	14(2)	18(2)	18(2)	9(1)	3(1)	2(1)
C(17)	15(2)	19(2)	16(2)	11(2)	1(1)	0(1)
C(18)	26(2)	32(2)	17(2)	16(2)	1(2)	9(2)
C(19)	82(4)	39(3)	32(3)	24(2)	-2(2)	20(3)
C(20)	14(2)	13(2)	17(2)	5(1)	3(1)	3(1)
C(21)	18(2)	18(2)	21(2)	8(2)	6(1)	7(1)
C(22)	20(2)	21(2)	15(2)	11(2)	5(1)	9(1)
C(23)	22(2)	17(2)	20(2)	11(2)	5(1)	7(1)

C(24)	20(2)	16(2)	15(2)	7(1)	0(1)	3(1)
C(25)	22(2)	24(2)	16(2)	13(2)	4(1)	9(2)
C(26)	30(2)	18(2)	21(2)	11(2)	1(2)	1(2)
C(27)	26(2)	22(2)	18(2)	8(2)	-1(2)	4(2)
C(28)	24(2)	26(2)	16(2)	10(2)	-2(2)	4(2)
C(29)	13(2)	24(2)	20(2)	5(2)	5(1)	1(1)
C(30)	16(2)	22(2)	19(2)	-1(2)	5(1)	-2(2)
C(31)	15(2)	18(2)	27(2)	4(2)	6(2)	1(1)
C(32)	12(2)	16(2)	24(2)	5(2)	4(1)	0(1)
C(33)	10(2)	13(2)	21(2)	2(1)	5(1)	-1(1)
C(34)	7(2)	12(2)	18(2)	4(1)	3(1)	0(1)
C(35)	10(2)	14(2)	21(2)	8(1)	1(1)	1(1)
C(36)	10(2)	14(2)	19(2)	7(1)	0(1)	0(1)
C(37)	11(2)	14(2)	16(2)	4(1)	4(1)	2(1)
C(38)	8(1)	13(2)	18(2)	5(1)	2(1)	-1(1)
C(39)	8(2)	14(2)	18(2)	7(1)	1(1)	0(1)
C(40)	5(1)	7(1)	12(2)	4(1)	1(1)	-1(1)
C(41)	18(2)	23(2)	21(2)	12(2)	4(1)	2(2)
C(42)	19(2)	20(2)	30(2)	14(2)	6(2)	7(2)
C(43)	19(2)	17(2)	26(2)	8(2)	8(2)	7(1)
C(44)	14(2)	17(2)	17(2)	7(1)	2(1)	2(1)
C(45)	13(2)	20(2)	20(2)	9(2)	1(1)	4(1)
C(46)	37(2)	30(2)	20(2)	14(2)	5(2)	12(2)
C(47)	34(2)	32(2)	34(2)	20(2)	1(2)	5(2)
C(48)	15(2)	14(2)	22(2)	6(2)	6(1)	0(1)
C(49)	14(2)	22(2)	27(2)	10(2)	2(2)	2(1)
C(50)	18(2)	23(2)	19(2)	10(2)	3(1)	3(2)
C(51)	23(2)	17(2)	23(2)	10(2)	2(2)	2(2)
C(52)	23(2)	16(2)	18(2)	6(2)	4(1)	6(1)
C(53)	18(2)	22(2)	19(2)	12(2)	1(1)	4(1)
C(54)	28(2)	21(2)	24(2)	12(2)	5(2)	10(2)
C(55)	30(2)	22(2)	19(2)	5(2)	5(2)	8(2)
C(56)	27(2)	26(2)	22(2)	10(2)	8(2)	7(2)
C(1S)	32(2)	21(2)	34(2)	14(2)	10(2)	6(2)
C(2S)	37(2)	26(2)	27(2)	13(2)	1(2)	-6(2)
Cl(1S)	36(1)	33(1)	32(1)	19(1)	2(1)	1(1)
Cl(2S)	59(1)	34(1)	29(1)	18(1)	6(1)	12(1)
Cl(3S)	34(1)	29(1)	25(1)	14(1)	1(1)	9(1)
Cl(4S)	82(1)	41(1)	31(1)	10(1)	19(1)	-20(1)

Table 5.   Hydrogen coordinates (x 10^4) and isotropic displacement parameters ($Å^2$x 10^3) for LEWIS4REDO_0m.

	x	y	z	U(eq)
H(1)	7140	-932	2704	20
H(2)	8253	-2129	2399	23
H(3)	9156	-2485	3310	23
H(4)	9017	-1603	4553	21
H(7)	8818	-660	5773	17
H(9)	7085	1461	6961	17
H(13)	4742	2094	4440	22
H(14)	4047	3248	5400	25
H(15)	4585	3450	6618	25
H(16)	5806	2475	6839	19
H(18A)	9562	-13	8157	27
H(18B)	11248	-96	7809	27
H(19A)	8613	-1454	7485	71
H(19B)	10371	-1278	7961	71
H(19C)	10247	-1548	7106	71
H(23)	3368	-367	1544	22
H(24)	2567	-235	487	21
H(26)	5634	2032	1384	27
H(27)	6394	1917	2445	27
H(28A)	3056	-116	-578	34
H(28B)	2497	543	-807	34
H(28C)	1487	281	-288	34
H(29)	2294	5697	2199	25
H(30)	1163	6883	2494	28
H(31)	446	7291	1592	27
H(32)	885	6491	372	23
H(35)	1525	5664	-805	18
H(37)	3583	3638	-1949	18
H(41)	5090	2782	522	24
H(42)	6063	1705	-408	26
H(43)	5935	1625	-1589	24
H(44)	4789	2612	-1813	19
H(46A)	617	5186	-3070	33
H(46B)	2520	5638	-2909	33

H(47A)	-24	6452	-2196	48
H(47B)	696	6554	-2856	48
H(47C)	1858	6895	-2089	48
H(51)	3047	5322	3455	25
H(52)	2623	5266	4547	23
H(54)	3565	2921	3673	27
H(55)	3913	2960	2567	30
H(56A)	3375	5159	5625	37
H(56B)	2375	4544	5876	37
H(56C)	1429	4828	5353	37
H(1S1)	-341	7395	5616	34
H(1S2)	1355	7978	5672	34
H(2S1)	1989	2240	529	37
H(2S2)	779	2889	690	37

Table 6. Hydrogen bonds for LEWIS4REDO_0m [Å and °].

D-H...A	d(D-H)	d(H...A)	d(D...A)	<(DHA)
C(2S)-H(2S1)...O(3)	0.97	2.57	3.353(5)	137.9

Symmetry transformations used to generate equivalent atoms:

Complex 8
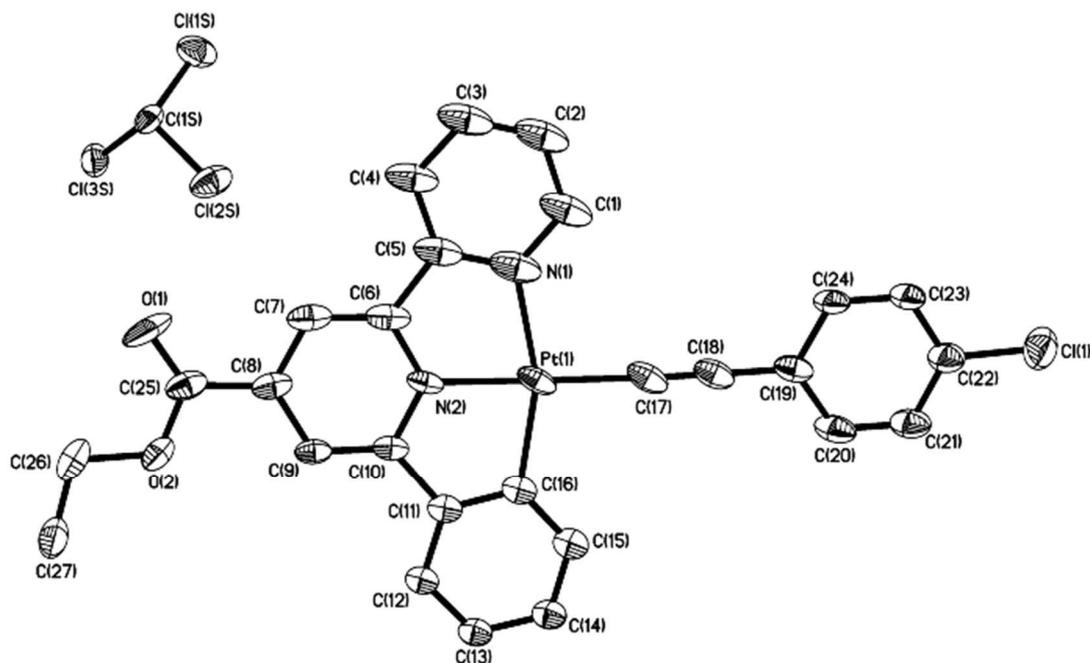
Table 1. Crystal data and structure refinement for ch1jwlc3_0m_a.

Identification code	ch1jwlc3_0m_a
Empirical formula	C28 H20 Cl4 N2 O2 Pt
Formula weight	753.35
Temperature	100(2) K
Wavelength	1.54178 Å
Crystal system	Monoclinic
Space group	P2$_1$/c
Unit cell dimensions	a = 7.9250(3) Å $\quad$ α= 90°.
	b = 20.2271(7) Å $\quad$ β= 99.019(2)°.
	c = 16.4997(6) Å $\quad$ γ = 90°.
Volume	2612.20(16) Å^3
Z	4
Density (calculated)	1.916 Mg/m^3
Absorption coefficient	14.064 mm^{-1}
F(000)	1456
Crystal size	0.120 x 0.030 x 0.030 mm^3
Theta range for data collection	3.483 to 66.604°.
Index ranges	-8<=h<=9, -23<=k<=23, -19<=l<=17
Reflections collected	28819

Independent reflections	4515 [R(int) = 0.0358]
Completeness to theta = 67.000°	96.9 %
Absorption correction	Semi-empirical from equivalents
Max. and min. transmission	0.76 and 0.43
Refinement method	Full-matrix least-squares on F^2
Data / restraints / parameters	4515 / 210 / 335
Goodness-of-fit on F^2	1.109
Final R indices [I>2sigma(I)]	R1 = 0.0343, wR2 = 0.0644
R indices (all data)	R1 = 0.0448, wR2 = 0.0701
Extinction coefficient	n/a
Largest diff. peak and hole	1.738 and -1.957 e.Å^{-3}

Table 2. Atomic coordinates (x 10^4) and equivalent isotropic displacement parameters (Å^{2}x 10^3) for ch1jwlc3_0m_a. U(eq) is defined as one third of the trace of the orthogonalized U^{ij} tensor.

	x	y	z	U(eq)
Pt(1)	5897(1)	4285(1)	4247(1)	32(1)
O(1)	7738(7)	7531(2)	3432(2)	61(2)
O(2)	9306(5)	7394(2)	4678(2)	35(1)
N(1)	4477(7)	4552(3)	3127(3)	50(2)
N(2)	6599(5)	5222(2)	4196(2)	28(1)
C(1)	3383(8)	4173(4)	2610(4)	51(1)
C(2)	2520(8)	4436(4)	1885(4)	55(1)
C(3)	2778(8)	5076(4)	1680(4)	54(1)
C(4)	3907(8)	5476(4)	2195(4)	49(1)
C(5)	4745(8)	5205(4)	2926(4)	43(1)
C(6)	5935(7)	5582(3)	3536(3)	37(1)
C(7)	6421(7)	6234(3)	3488(3)	37(1)
C(8)	7592(7)	6502(3)	4125(3)	33(1)
C(9)	8234(7)	6119(3)	4808(3)	28(1)
C(10)	7700(7)	5472(3)	4832(3)	26(1)
C(11)	8218(7)	4972(3)	5482(3)	26(1)
C(12)	9334(7)	5121(3)	6201(3)	27(1)
C(13)	9703(7)	4633(3)	6787(3)	30(1)
C(14)	9002(7)	4012(3)	6658(3)	32(1)
C(15)	7919(7)	3876(3)	5931(3)	32(1)
C(16)	7502(6)	4354(3)	5342(3)	27(1)
C(17)	5186(7)	3353(3)	4294(3)	37(1)
C(18)	4717(7)	2792(3)	4304(3)	38(1)
C(19)	4131(8)	2122(3)	4315(3)	37(1)
C(20)	4545(8)	1718(3)	5007(3)	43(1)
C(21)	3975(8)	1077(3)	5016(4)	43(1)
C(22)	2949(8)	829(3)	4339(3)	41(1)
C(23)	2540(9)	1216(3)	3642(4)	44(1)
C(24)	3127(8)	1851(3)	3625(3)	41(1)
C(25)	8190(8)	7196(3)	4028(3)	37(1)
C(26)	10033(9)	8050(3)	4611(4)	46(2)
C(27)	11209(9)	8188(3)	5389(4)	50(2)
C(1S)	2316(7)	8231(3)	2260(3)	31(1)
Cl(1)	2115(3)	31(1)	4352(1)	60(1)
Cl(1S)	173(2)	8039(1)	1867(1)	50(1)

Cl(2S)	3325(2)	7536(1)	2760(1)	51(1)
Cl(3S)	2384(2)	8902(1)	2939(1)	39(1)

Table 3.   Bond lengths [Å] and angles [°] for ch1jwlc3_0m_a.

_____

Pt(1)-C(17)	1.973(7)
Pt(1)-N(2)	1.981(5)
Pt(1)-C(16)	2.045(5)
Pt(1)-N(1)	2.078(5)
O(1)-C(25)	1.201(7)
O(2)-C(25)	1.340(7)
O(2)-C(26)	1.459(7)
N(1)-C(1)	1.355(8)
N(1)-C(5)	1.385(9)
N(2)-C(6)	1.347(7)
N(2)-C(10)	1.353(6)
C(1)-C(2)	1.387(9)
C(1)-H(1)	0.9500
C(2)-C(3)	1.362(10)
C(2)-H(2)	0.9500
C(3)-C(4)	1.393(9)
C(3)-H(3)	0.9500
C(4)-C(5)	1.395(9)
C(4)-H(4)	0.9500
C(5)-C(6)	1.478(8)
C(6)-C(7)	1.380(9)
C(7)-C(8)	1.398(8)
C(7)-H(7)	0.9500
C(8)-C(9)	1.396(7)
C(8)-C(25)	1.498(9)
C(9)-C(10)	1.378(8)
C(9)-H(9)	0.9500
C(10)-C(11)	1.486(7)
C(11)-C(16)	1.377(8)
C(11)-C(12)	1.396(7)
C(12)-C(13)	1.380(7)
C(12)-H(12)	0.9500
C(13)-C(14)	1.377(8)
C(13)-H(13)	0.9500
C(14)-C(15)	1.389(7)
C(14)-H(14)	0.9500
C(15)-C(16)	1.375(8)
C(15)-H(15)	0.9500

C(17)-C(18)	1.195(8)
C(18)-C(19)	1.434(9)
C(19)-C(24)	1.395(8)
C(19)-C(20)	1.401(8)
C(20)-C(21)	1.374(9)
C(20)-H(20)	0.9500
C(21)-C(22)	1.370(8)
C(21)-H(21)	0.9500
C(22)-C(23)	1.387(8)
C(22)-Cl(1)	1.745(7)
C(23)-C(24)	1.368(9)
C(23)-H(23)	0.9500
C(24)-H(24)	0.9500
C(26)-C(27)	1.489(9)
C(26)-H(26A)	0.9900
C(26)-H(26B)	0.9900
C(27)-H(27A)	0.9800
C(27)-H(27B)	0.9800
C(27)-H(27C)	0.9800
C(1S)-Cl(2S)	1.756(5)
C(1S)-Cl(3S)	1.757(5)
C(1S)-Cl(1S)	1.764(6)
C(1S)-H(1S)	1.0000
C(17)-Pt(1)-N(2)	179.7(2)
C(17)-Pt(1)-C(16)	99.9(2)
N(2)-Pt(1)-C(16)	80.3(2)
C(17)-Pt(1)-N(1)	99.5(2)
N(2)-Pt(1)-N(1)	80.2(2)
C(16)-Pt(1)-N(1)	160.5(2)
C(25)-O(2)-C(26)	115.5(5)
C(1)-N(1)-C(5)	119.7(6)
C(1)-N(1)-Pt(1)	128.1(5)
C(5)-N(1)-Pt(1)	112.3(4)
C(6)-N(2)-C(10)	123.3(5)
C(6)-N(2)-Pt(1)	118.3(4)
C(10)-N(2)-Pt(1)	118.4(4)
N(1)-C(1)-C(2)	120.5(7)
N(1)-C(1)-H(1)	119.8
C(2)-C(1)-H(1)	119.8

209

C(3)-C(2)-C(1)	120.3(7)
C(3)-C(2)-H(2)	119.8
C(1)-C(2)-H(2)	119.8
C(2)-C(3)-C(4)	120.5(7)
C(2)-C(3)-H(3)	119.7
C(4)-C(3)-H(3)	119.7
C(3)-C(4)-C(5)	118.2(7)
C(3)-C(4)-H(4)	120.9
C(5)-C(4)-H(4)	120.9
N(1)-C(5)-C(4)	120.8(6)
N(1)-C(5)-C(6)	115.7(5)
C(4)-C(5)-C(6)	123.5(7)
N(2)-C(6)-C(7)	119.0(5)
N(2)-C(6)-C(5)	113.5(6)
C(7)-C(6)-C(5)	127.5(6)
C(6)-C(7)-C(8)	119.1(5)
C(6)-C(7)-H(7)	120.4
C(8)-C(7)-H(7)	120.4
C(9)-C(8)-C(7)	120.4(6)
C(9)-C(8)-C(25)	121.7(5)
C(7)-C(8)-C(25)	117.8(5)
C(10)-C(9)-C(8)	118.4(5)
C(10)-C(9)-H(9)	120.8
C(8)-C(9)-H(9)	120.8
N(2)-C(10)-C(9)	119.8(5)
N(2)-C(10)-C(11)	112.2(5)
C(9)-C(10)-C(11)	128.0(5)
C(16)-C(11)-C(12)	121.9(5)
C(16)-C(11)-C(10)	115.9(5)
C(12)-C(11)-C(10)	122.2(5)
C(13)-C(12)-C(11)	118.5(5)
C(13)-C(12)-H(12)	120.8
C(11)-C(12)-H(12)	120.8
C(14)-C(13)-C(12)	120.6(5)
C(14)-C(13)-H(13)	119.7
C(12)-C(13)-H(13)	119.7
C(13)-C(14)-C(15)	119.5(5)
C(13)-C(14)-H(14)	120.2
C(15)-C(14)-H(14)	120.2
C(16)-C(15)-C(14)	121.3(6)

C(16)-C(15)-H(15)	119.4
C(14)-C(15)-H(15)	119.4
C(15)-C(16)-C(11)	118.2(5)
C(15)-C(16)-Pt(1)	128.6(4)
C(11)-C(16)-Pt(1)	113.2(4)
C(18)-C(17)-Pt(1)	178.1(6)
C(17)-C(18)-C(19)	179.2(7)
C(24)-C(19)-C(20)	117.8(6)
C(24)-C(19)-C(18)	120.4(6)
C(20)-C(19)-C(18)	121.8(5)
C(21)-C(20)-C(19)	121.6(6)
C(21)-C(20)-H(20)	119.2
C(19)-C(20)-H(20)	119.2
C(22)-C(21)-C(20)	119.4(6)
C(22)-C(21)-H(21)	120.3
C(20)-C(21)-H(21)	120.3
C(21)-C(22)-C(23)	120.1(6)
C(21)-C(22)-Cl(1)	120.4(5)
C(23)-C(22)-Cl(1)	119.5(5)
C(24)-C(23)-C(22)	120.7(6)
C(24)-C(23)-H(23)	119.6
C(22)-C(23)-H(23)	119.6
C(23)-C(24)-C(19)	120.3(6)
C(23)-C(24)-H(24)	119.8
C(19)-C(24)-H(24)	119.8
O(1)-C(25)-O(2)	124.1(6)
O(1)-C(25)-C(8)	123.9(6)
O(2)-C(25)-C(8)	112.0(5)
O(2)-C(26)-C(27)	107.8(5)
O(2)-C(26)-H(26A)	110.1
C(27)-C(26)-H(26A)	110.1
O(2)-C(26)-H(26B)	110.1
C(27)-C(26)-H(26B)	110.1
H(26A)-C(26)-H(26B)	108.5
C(26)-C(27)-H(27A)	109.5
C(26)-C(27)-H(27B)	109.5
H(27A)-C(27)-H(27B)	109.5
C(26)-C(27)-H(27C)	109.5
H(27A)-C(27)-H(27C)	109.5
H(27B)-C(27)-H(27C)	109.5

Cl(2S)-C(1S)-Cl(3S)	110.6(3)
Cl(2S)-C(1S)-Cl(1S)	109.8(3)
Cl(3S)-C(1S)-Cl(1S)	109.6(3)
Cl(2S)-C(1S)-H(1S)	108.9
Cl(3S)-C(1S)-H(1S)	108.9
Cl(1S)-C(1S)-H(1S)	108.9

_____

Symmetry transformations used to generate equivalent atoms:

Table 4.   Anisotropic displacement parameters ($\text{Å}^2 \times 10^3$) for ch1jwlc3_0m_a. The anisotropic displacement factor exponent takes the form: $-2\pi^2[\, h^2\, a^{*2}U^{11} + \ldots + 2\, h\, k\, a^*\, b^*\, U^{12}\,]$

	U^{11}	U^{22}	U^{33}	U^{23}	U^{13}	U^{12}
Pt(1)	21(1)	50(1)	25(1)	-18(1)	4(1)	-1(1)
O(1)	110(4)	46(3)	22(2)	8(2)	-7(2)	31(3)
O(2)	50(3)	29(2)	28(2)	7(2)	9(2)	8(2)
N(1)	35(3)	79(4)	33(3)	-25(3)	0(2)	14(3)
N(2)	20(2)	42(3)	19(2)	-10(2)	-2(2)	4(2)
C(1)	34(3)	80(3)	37(2)	-35(2)	1(2)	13(3)
C(2)	40(2)	83(3)	38(2)	-36(2)	-3(2)	18(2)
C(3)	42(2)	82(3)	36(2)	-32(2)	-5(2)	24(2)
C(4)	40(2)	72(3)	32(2)	-26(2)	-5(2)	26(2)
C(5)	34(2)	62(2)	29(2)	-23(2)	-3(2)	22(2)
C(6)	31(2)	54(2)	24(2)	-15(2)	-2(2)	22(2)
C(7)	37(2)	49(2)	23(2)	-9(2)	-2(2)	24(2)
C(8)	36(2)	42(2)	21(2)	-4(2)	2(2)	18(2)
C(9)	27(2)	40(2)	17(2)	-4(2)	2(2)	9(2)
C(10)	21(2)	39(2)	18(2)	-6(2)	3(2)	7(2)
C(11)	22(2)	40(2)	19(2)	-4(2)	9(1)	3(2)
C(12)	24(2)	39(2)	21(2)	-2(2)	7(2)	-1(2)
C(13)	28(2)	42(2)	21(2)	-1(2)	5(2)	-1(2)
C(14)	30(2)	44(2)	24(2)	2(2)	6(2)	-3(2)
C(15)	28(2)	44(2)	24(2)	-2(2)	10(2)	-2(2)
C(16)	22(2)	42(2)	18(2)	-4(2)	11(2)	1(2)
C(17)	30(3)	57(3)	25(2)	-19(2)	6(2)	-4(2)
C(18)	33(2)	55(2)	24(2)	-13(2)	4(2)	-3(2)
C(19)	36(2)	52(2)	22(2)	-6(2)	-1(2)	0(2)
C(20)	39(2)	64(2)	23(2)	1(2)	-2(2)	-10(2)
C(21)	42(2)	60(2)	24(2)	7(2)	1(2)	-6(2)
C(22)	49(2)	47(2)	26(2)	-1(2)	0(2)	2(2)
C(23)	56(2)	44(2)	26(2)	-5(2)	-13(2)	3(2)
C(24)	49(2)	44(2)	24(2)	-3(2)	-12(2)	5(2)
C(25)	46(3)	42(2)	23(2)	-2(2)	3(2)	19(2)
C(26)	63(4)	32(3)	47(3)	15(3)	18(3)	7(3)
C(27)	51(4)	36(3)	64(4)	16(3)	10(3)	-6(3)
C(1S)	42(3)	28(3)	24(3)	5(2)	8(2)	3(3)
Cl(1)	100(2)	38(1)	41(1)	2(1)	10(1)	4(1)
Cl(1S)	50(1)	44(1)	49(1)	-16(1)	-10(1)	9(1)

Cl(2S)	61(1)	46(1)	42(1)	6(1)	1(1)	23(1)
Cl(3S)	54(1)	31(1)	33(1)	-2(1)	9(1)	-9(1)

Table 5.   Hydrogen coordinates (x 10^4) and isotropic displacement parameters ($Å^2$x 10 ^{3}) for ch1jwlc3_0m_a.

	x	y	z	U(eq)
H(1)	3206	3725	2744	61
H(2)	1745	4168	1529	66
H(3)	2183	5251	1181	65
H(4)	4101	5921	2052	59
H(7)	5966	6497	3028	45
H(9)	9019	6300	5246	34
H(12)	9829	5548	6284	33
H(13)	10446	4727	7283	36
H(14)	9259	3678	7064	39
H(15)	7456	3444	5840	38
H(20)	5237	1891	5482	51
H(21)	4289	808	5488	51
H(23)	1845	1038	3171	53
H(24)	2849	2109	3141	49
H(26A)	9113	8386	4524	55
H(26B)	10667	8067	4140	55
H(27A)	10551	8212	5844	76
H(27B)	11794	8609	5341	76
H(27C)	12056	7832	5493	76
H(1S)	2923	8355	1795	37

DFT Calculated Molecular Orbitals

Complex 1
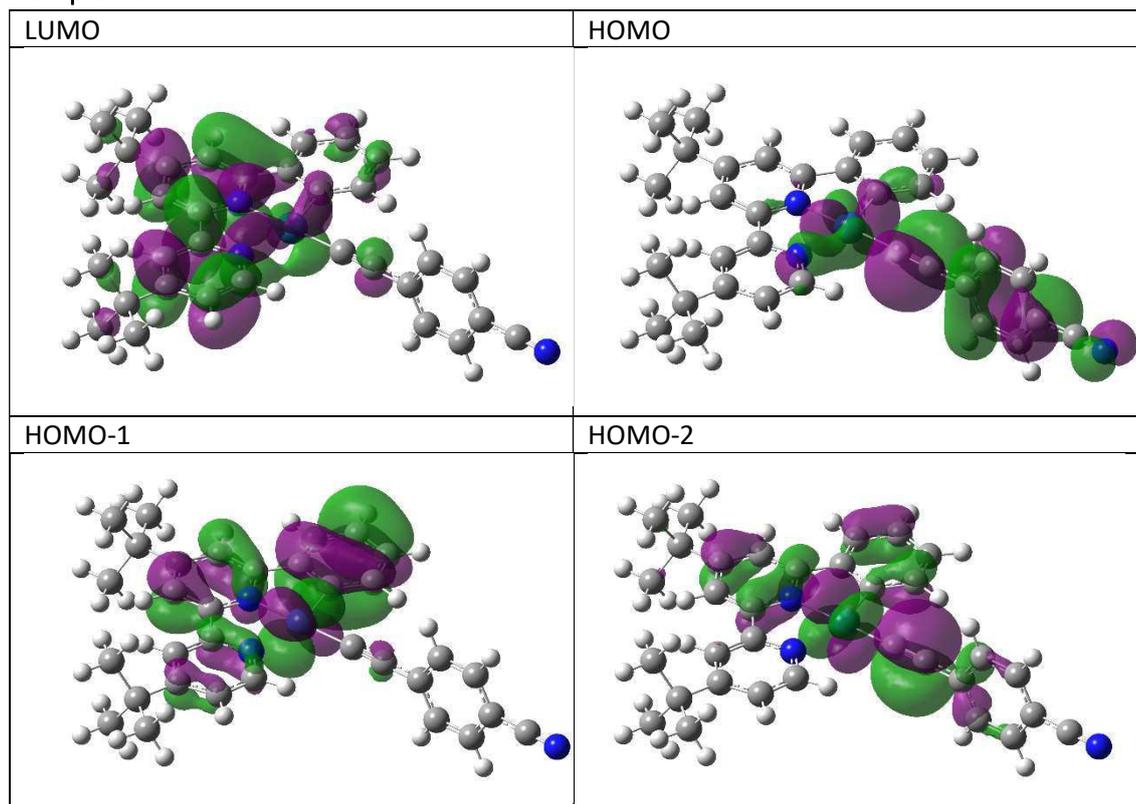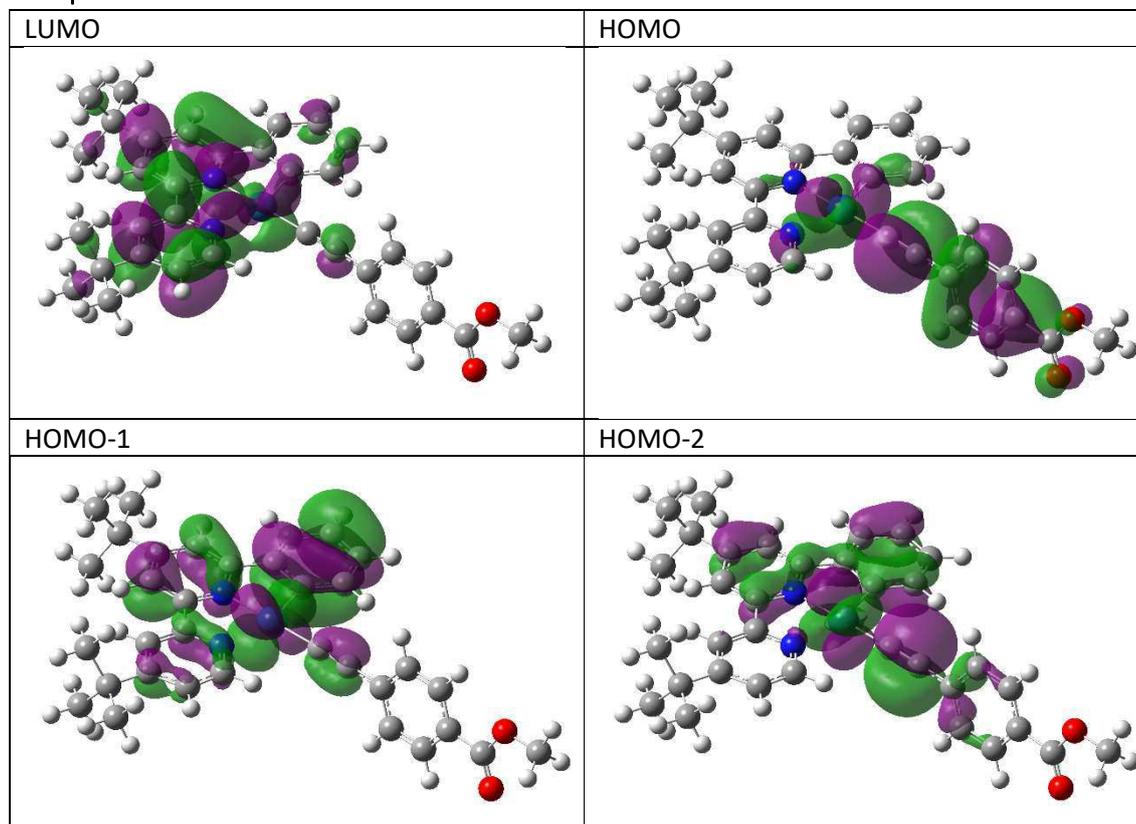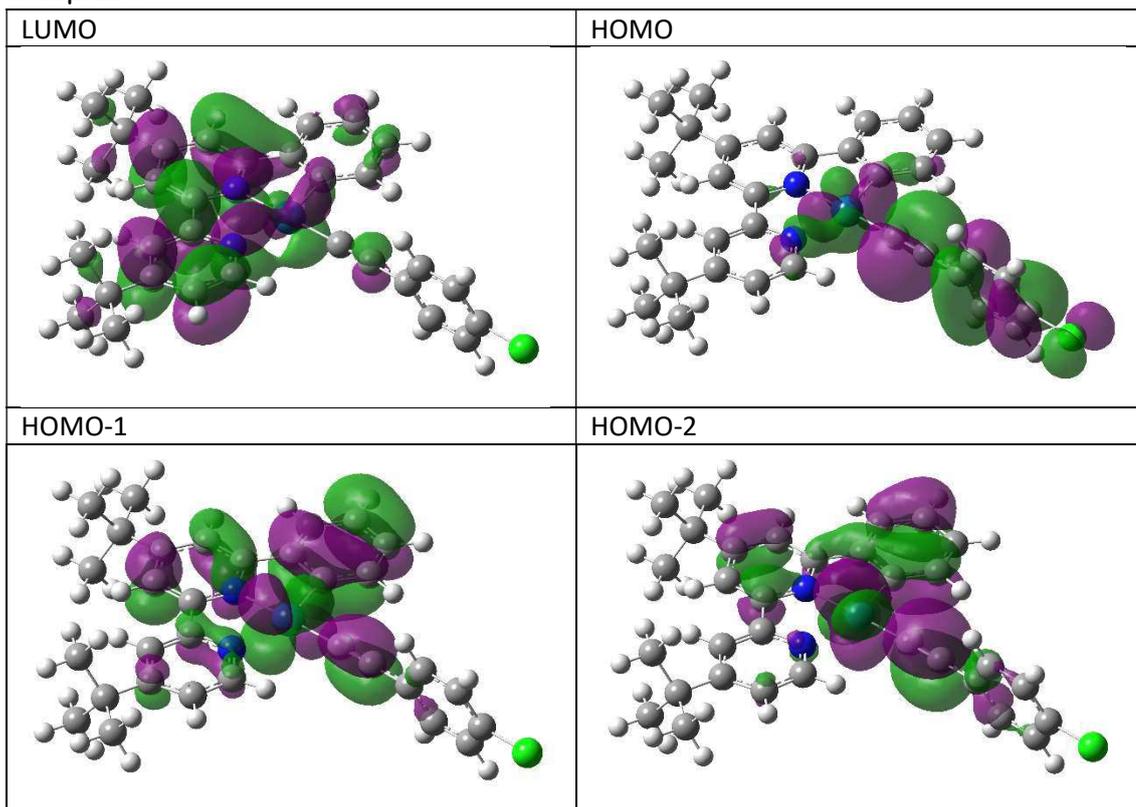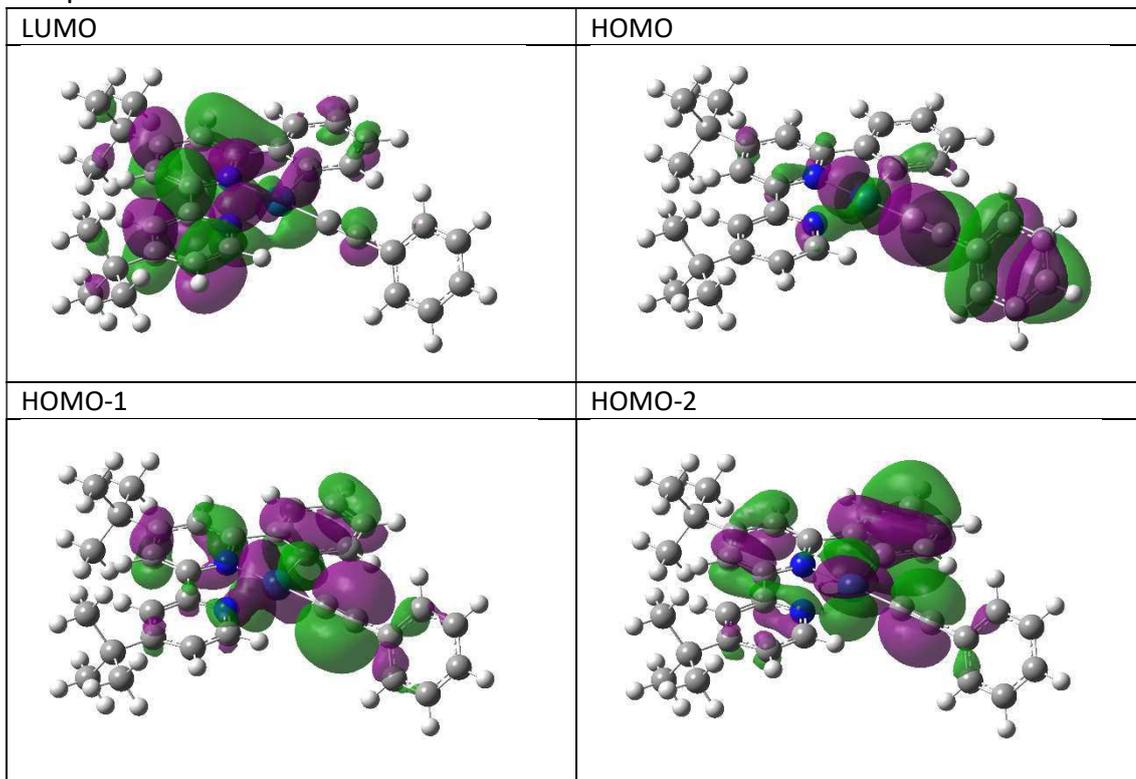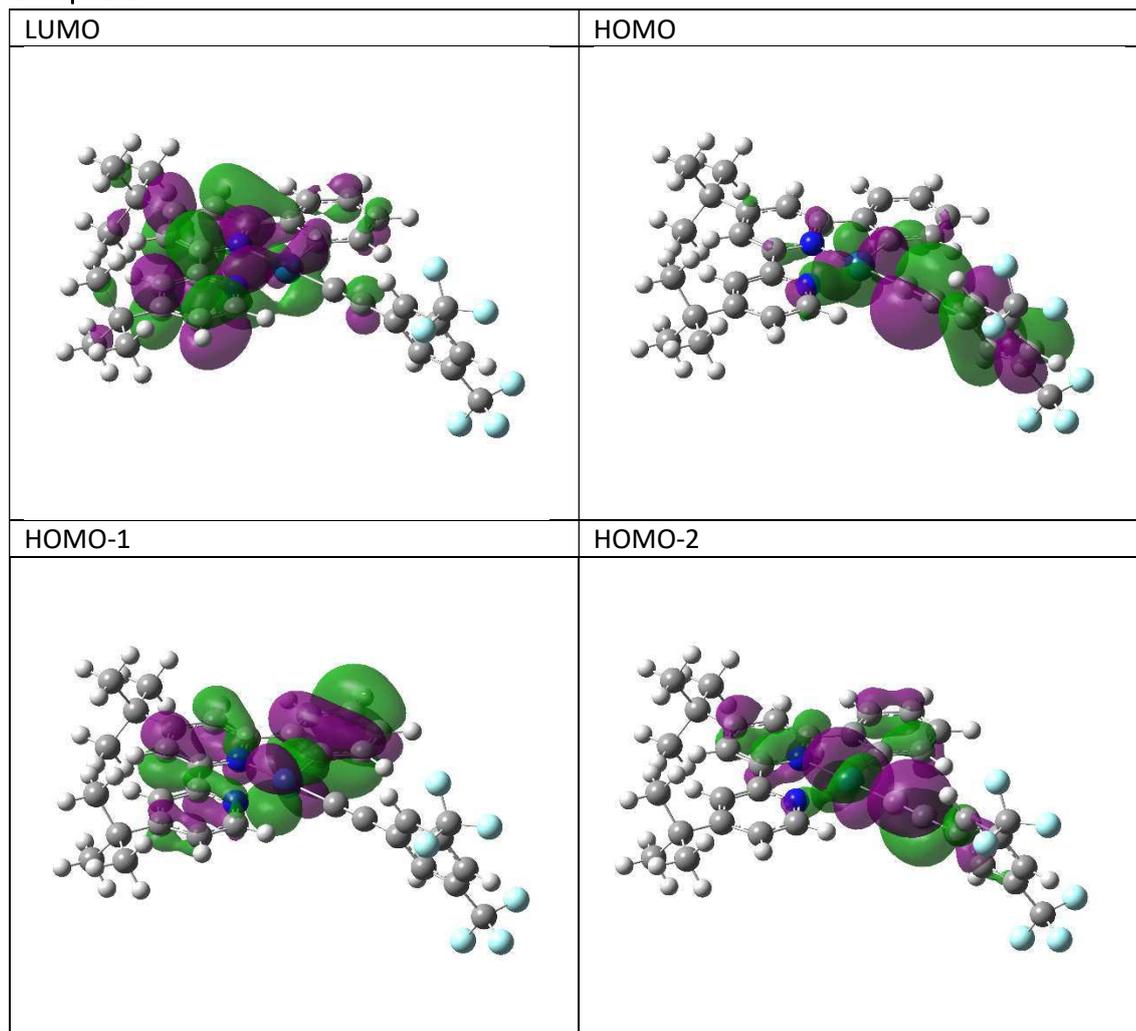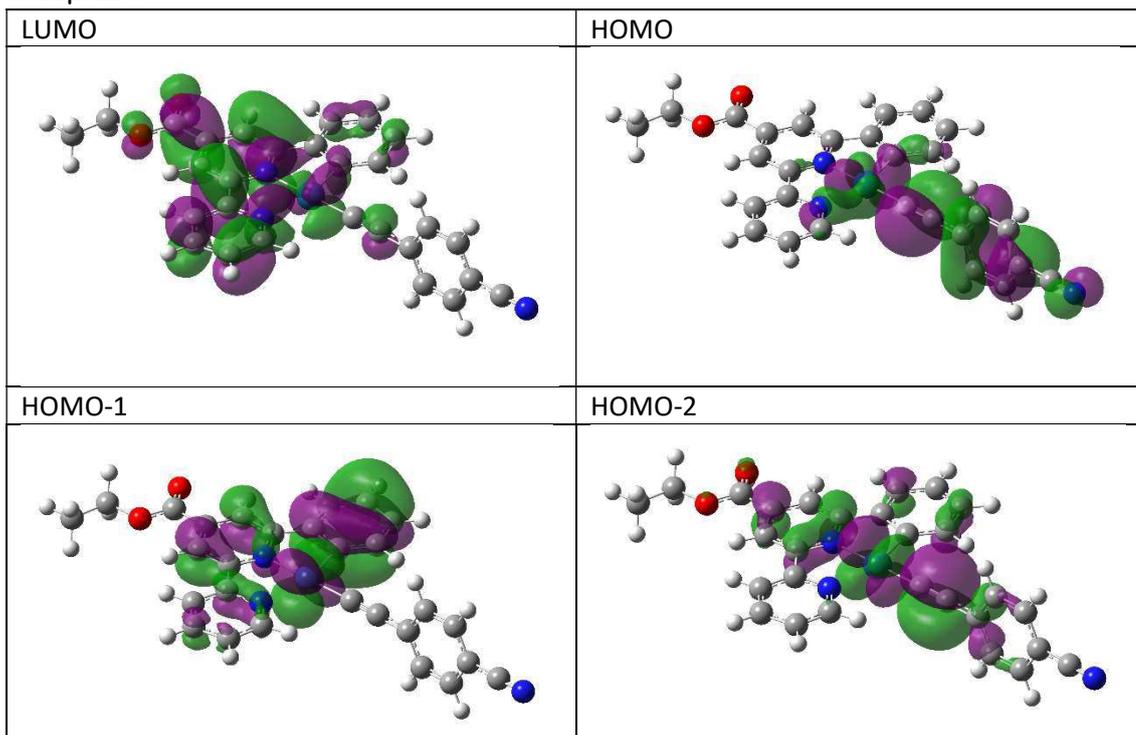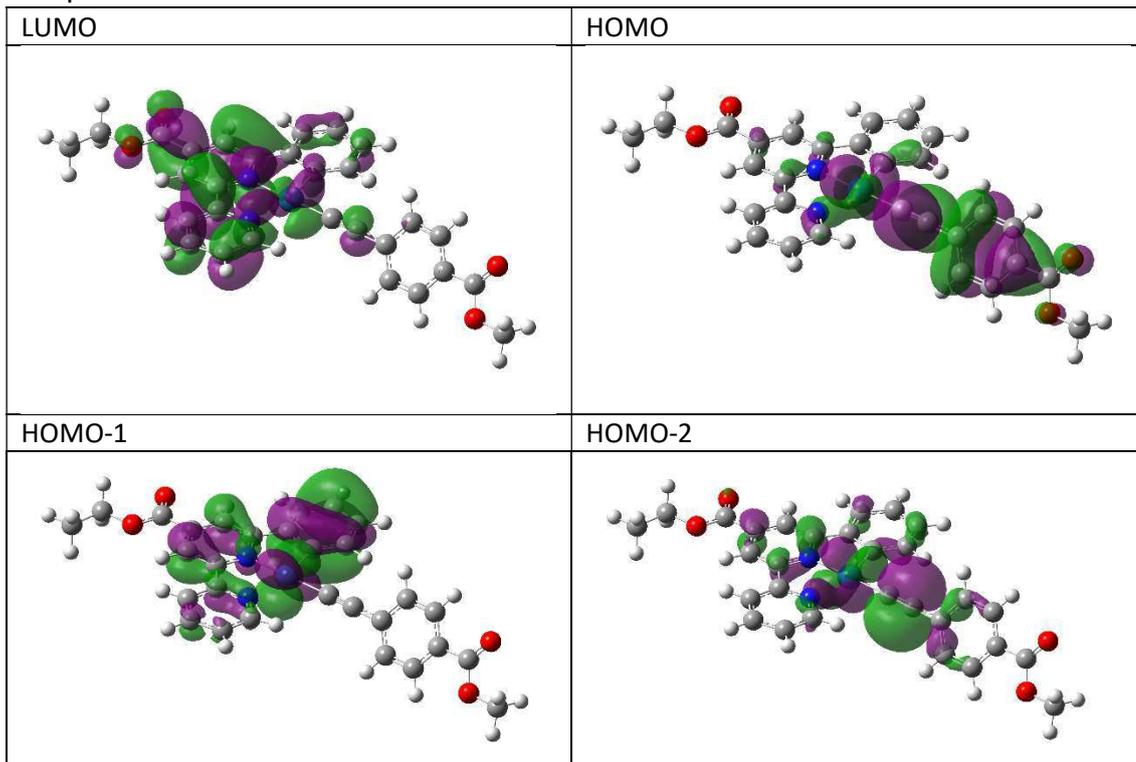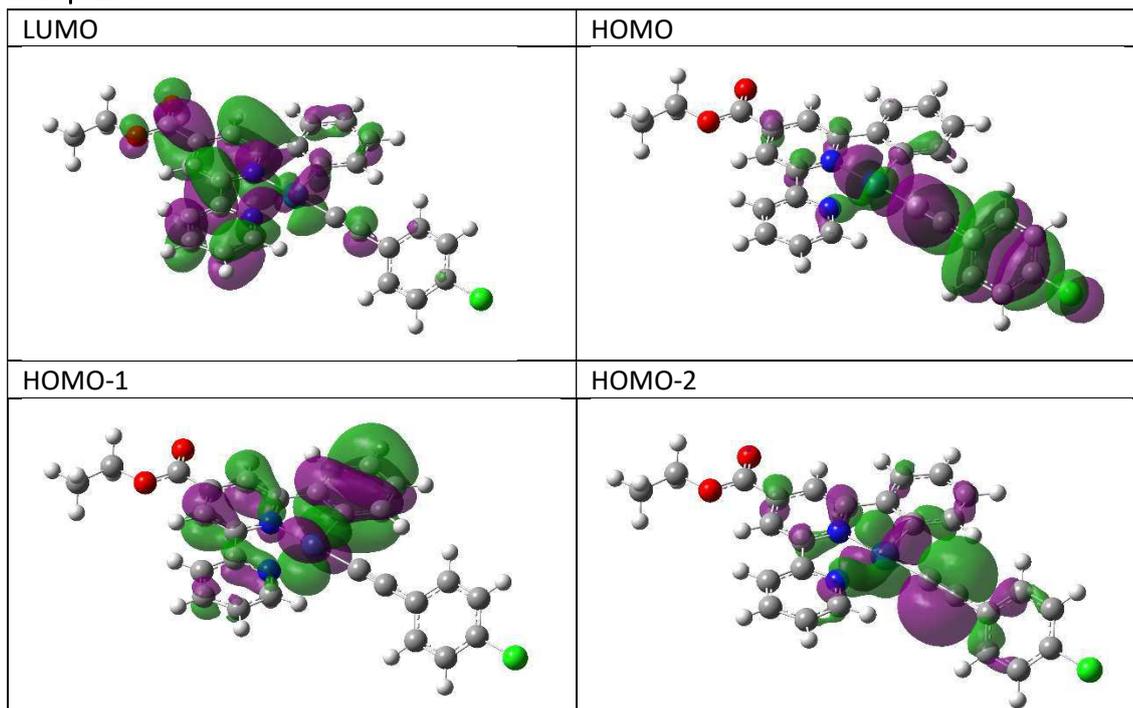
LUMO	HOMO
HOMO-1	HOMO-2

Complex 2

LUMO	HOMO
HOMO-1	HOMO-2

Complex 3

LUMO	HOMO
HOMO-1	HOMO-2

Complex 4

LUMO	HOMO
HOMO-1	HOMO-2

Complex 5

LUMO	HOMO
HOMO-1	HOMO-2

Complex 6

LUMO	HOMO
HOMO-1	HOMO-2

Complex 7

LUMO	HOMO
HOMO-1	HOMO-2

Complex 8

LUMO	HOMO
HOMO-1	HOMO-2

Complex 9

LUMO	HOMO
HOMO-1	HOMO-2

Complex 10

LUMO	HOMO
HOMO-1	HOMO-2

Complex 11

LUMO	HOMO
HOMO-1	HOMO-2

Complex 12

LUMO	HOMO
HOMO-1	HOMO-2

Complex 13

LUMO	HOMO
HOMO-1	HOMO-2

Complex 14

LUMO	HOMO
HOMO-1	HOMO-2

Complex 15

LUMO	HOMO
HOMO-1	HOMO-2
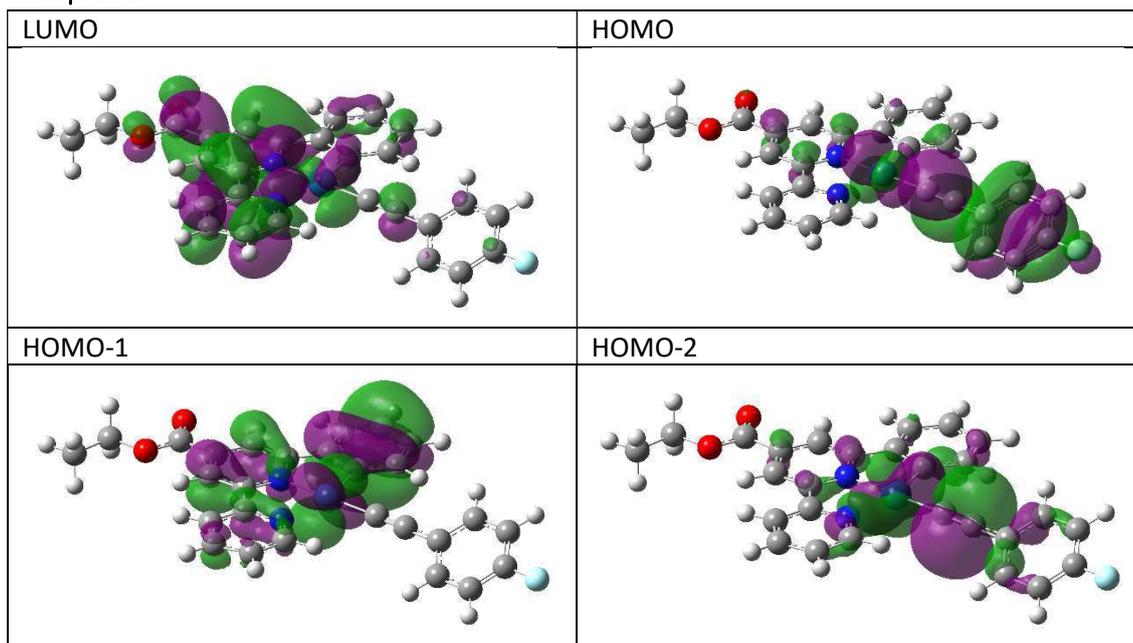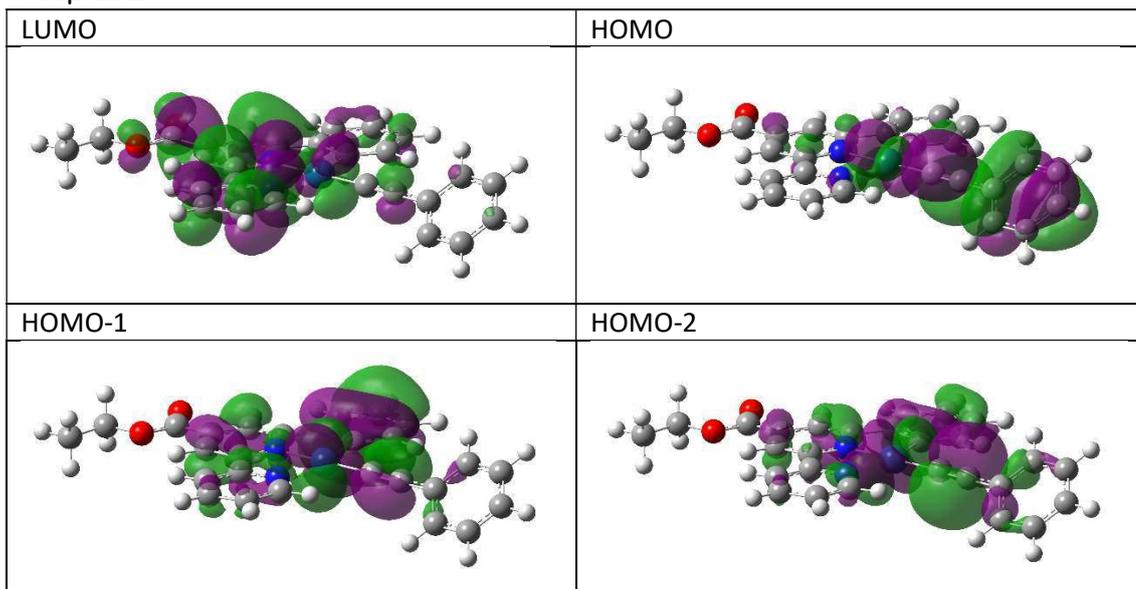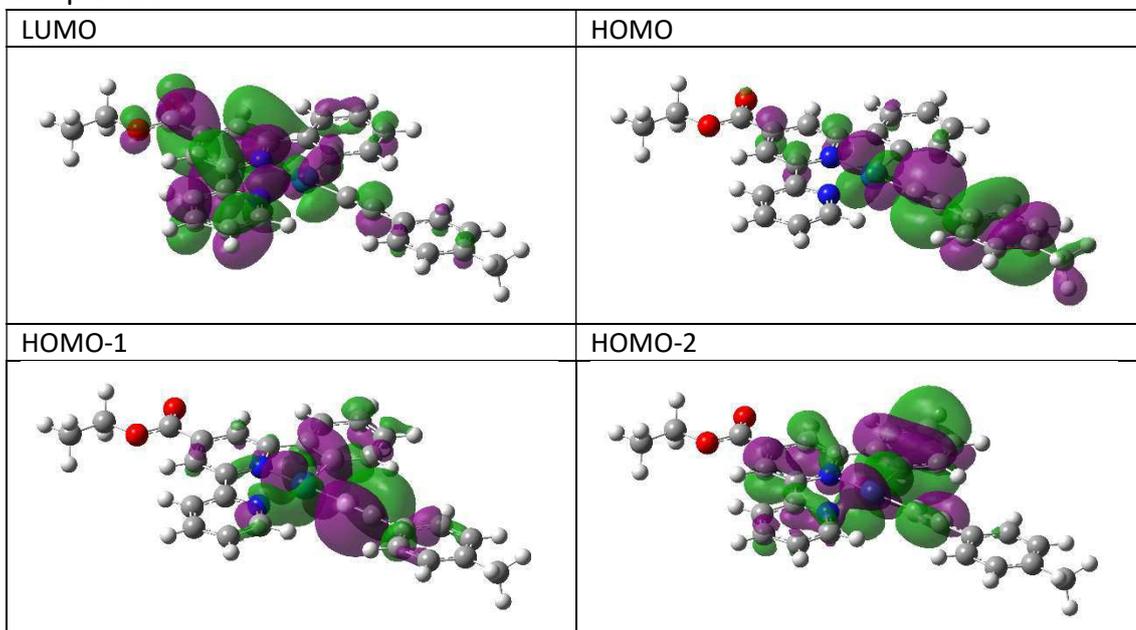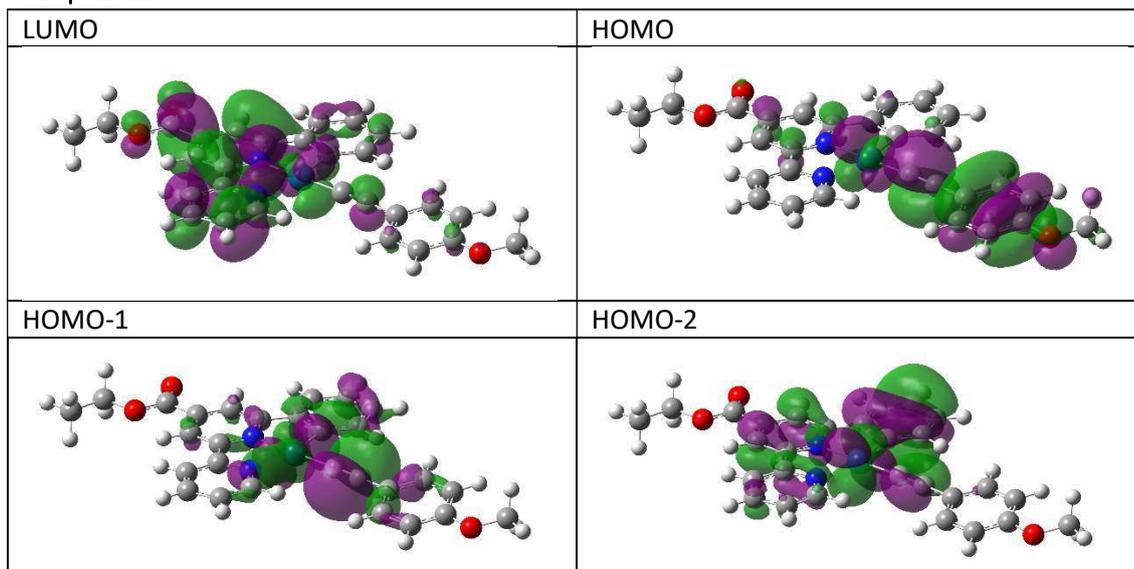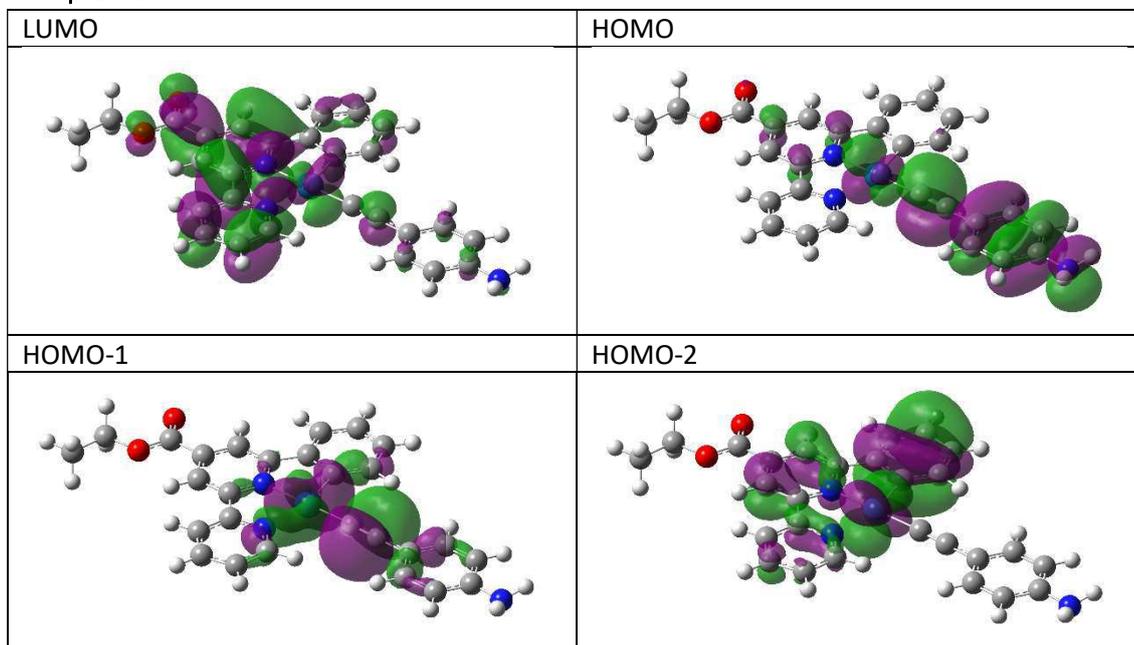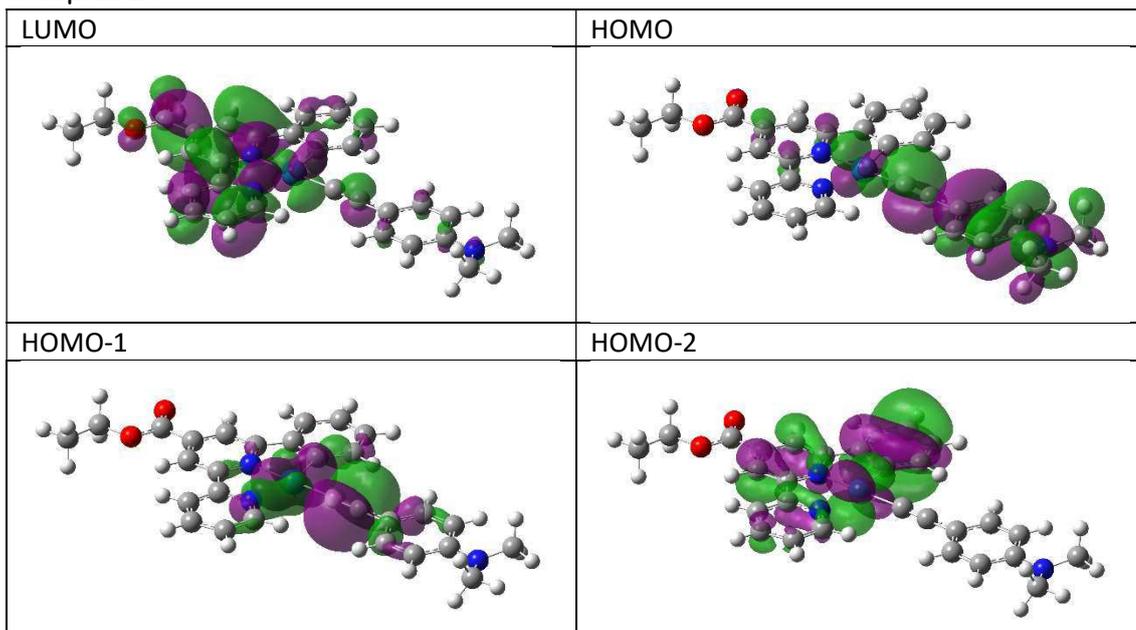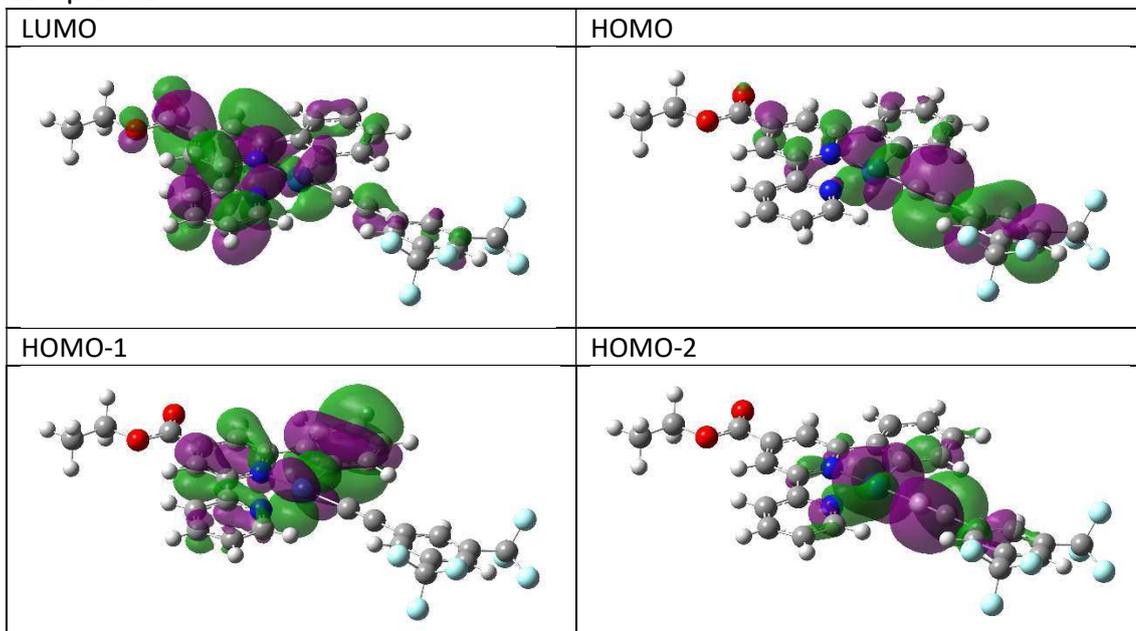
ANNEX C – 5. TIME-RESOLVED SPECTROSCOPY OF CYCLOMETALATED PLATINUM ACETYLIDE COMPLEXES

FTIR Spectrum of complex 15 in DCM showing frequencies that may form combination bands.
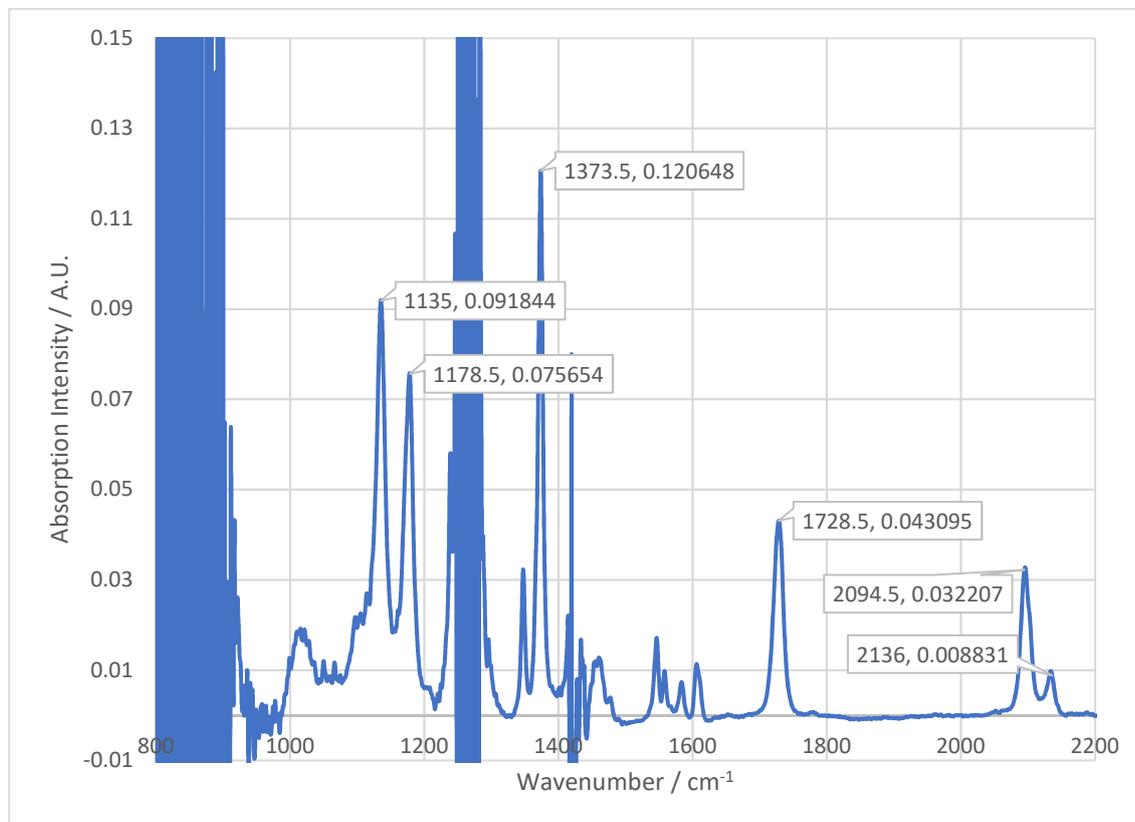
Full TRIR Results

Complex 15 TRIR
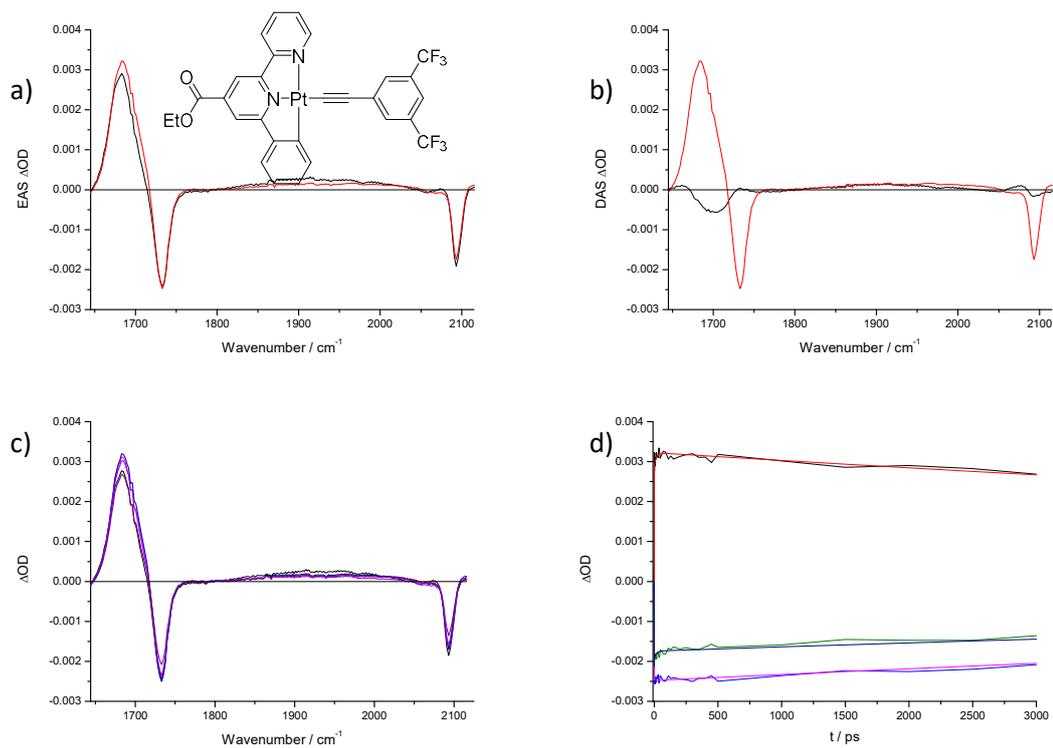
Figure 3a) Evolution Associated Spectra for τ₁ (black) and τ₂ (red) associated decays calculated for 15 between 1644 and 2115 cm⁻¹. b) Decay Associated Spectra for τ₁ (black) and τ₂ (red) associated decays calculated for 15 between 1644 and 2115 cm⁻¹. c) Spectra after excitation of 15 recorded in CH₂Cl₂ solution between 1 ps and 3000 ps. d) Decay traces with exponential fits recorded at selected wavenumbers; 1683 cm⁻¹ (black and red), 1733 cm⁻¹ (light blue and pink) and 2093 cm⁻¹ (green and dark blue).

Complex 6 TRIR
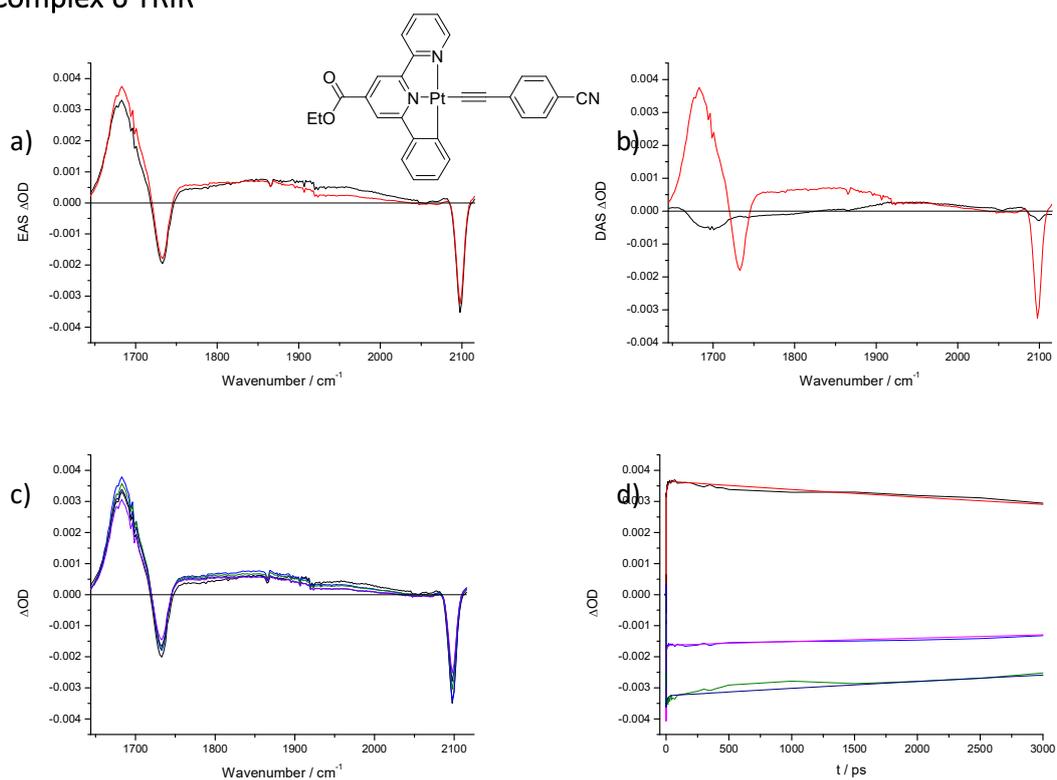
Figure 4a) Evolution Associated Spectra for τ₁ (black) and τ₂ (red) associated decays calculated for 6 between 1644 and 2115 cm⁻¹. b) Decay Associated Spectra for τ₁ (black) and τ₂ (red) associated decays calculated for 6 between 1644 and 2115 cm⁻¹. c) Spectra after excitation recorded for 6 in CH₂Cl₂ solution between 1 ps and 3000 ps. d) Decay traces with exponential fits recorded for selected wavenumber signals; 1685 cm⁻¹ (black and red), 1735 cm⁻¹ (light blue and pink) and 2098 cm⁻¹ (green and dark blue).

Complex 8 TRIR
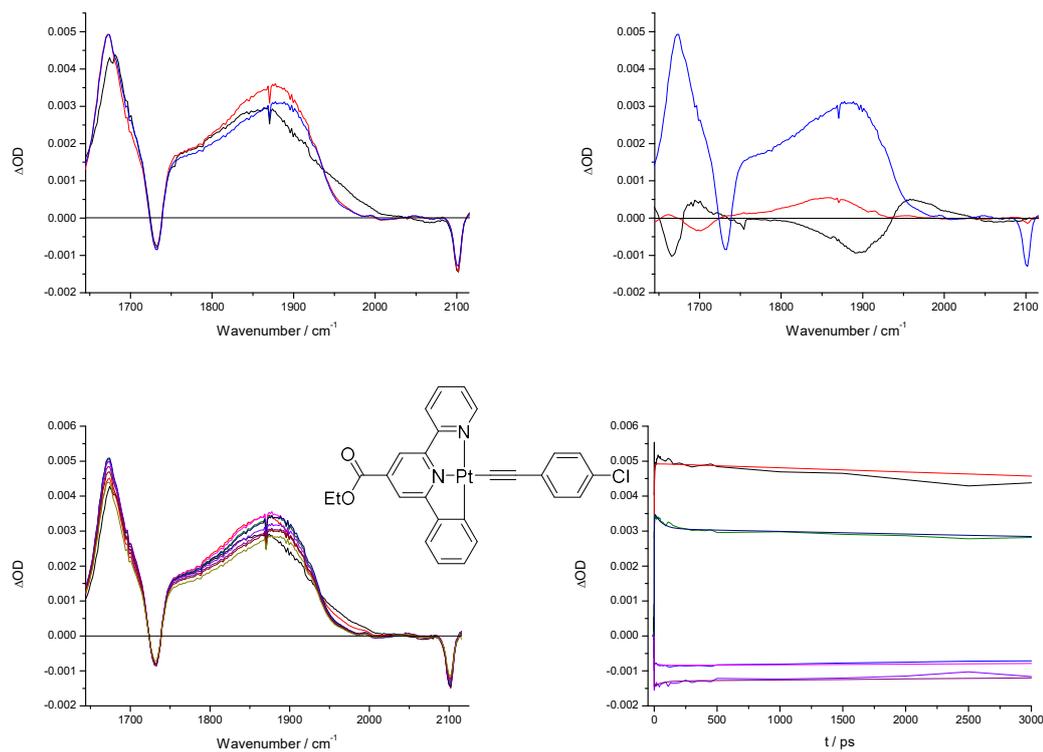
Figure 5a) Evolution Associated Spectra for τ_1 (black), τ_2 (red) and τ_3 (blue) associated decays calculated for 8 between 1644 and 2115 cm^{-1}. b) Decay Associated Spectra for τ_1 (black), τ_2 (red) and τ_3 (blue) associated decays calculated for 8 between 1644 and 2115 cm^{-1}. c) Spectra after excitation recorded for 8 in CH$_2$Cl$_2$ solution between 1 ps and 3000 ps. d) Decay traces with exponential fits recorded for selected wavenumber signals; 1674 cm^{-1} (black and red), 1733 cm^{-1} (light blue and pink), 1879 cm^{-1} (green and dark blue) and 2102 cm^{-1} (light purple and dark purple).

Complex 9 TRIR
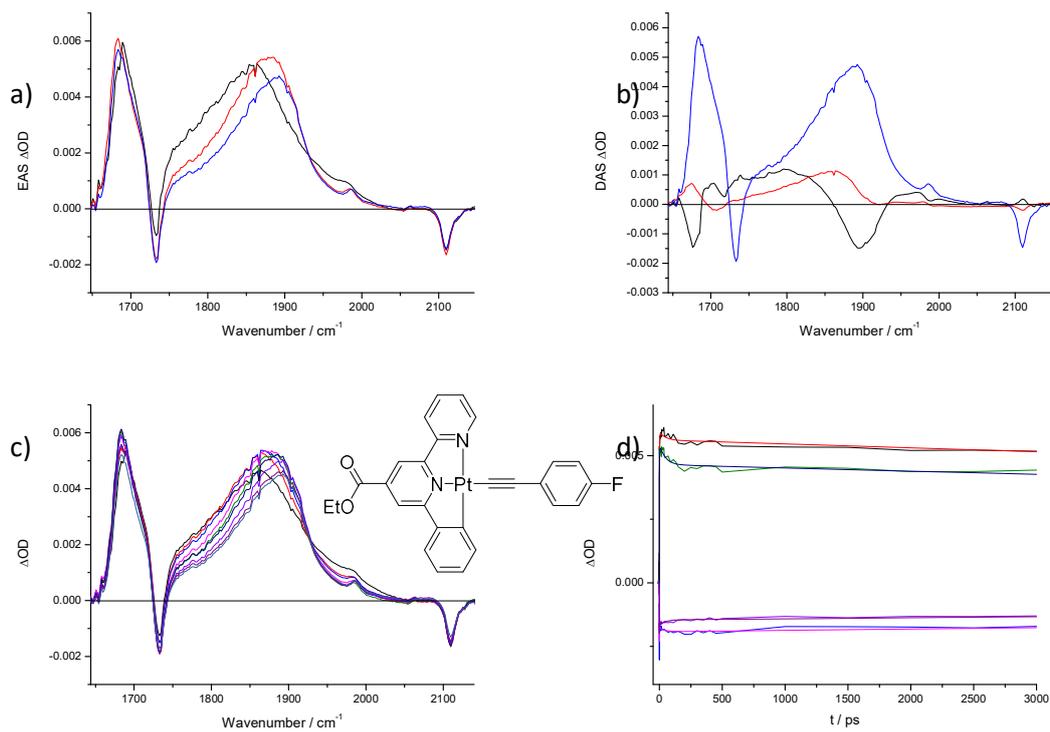
Figure 6a) Evolution Associated Spectra for τ₁ (black), τ₂ (red) and τ₃ (blue) associated decays calculated for 9 between 1644 and 2148 cm⁻¹. b) Decay Associated Spectra for τ₁ (black), τ₂ (red) and τ₃ (blue) associated decays calculated for 9 between 1644 and 2148 cm⁻¹. c) Spectra after excitation recorded for 9 in CH₂Cl₂ solution between 1 ps and 3000 ps. d) Decay traces with exponential fits recorded for selected wavenumber signals; 1685 cm⁻¹ (black and red), 1733 cm⁻¹ (light blue and pink), 1884 cm⁻¹ (green and dark blue) and 2110 cm⁻¹ (light purple and dark purple).

Complex 10 TRIR
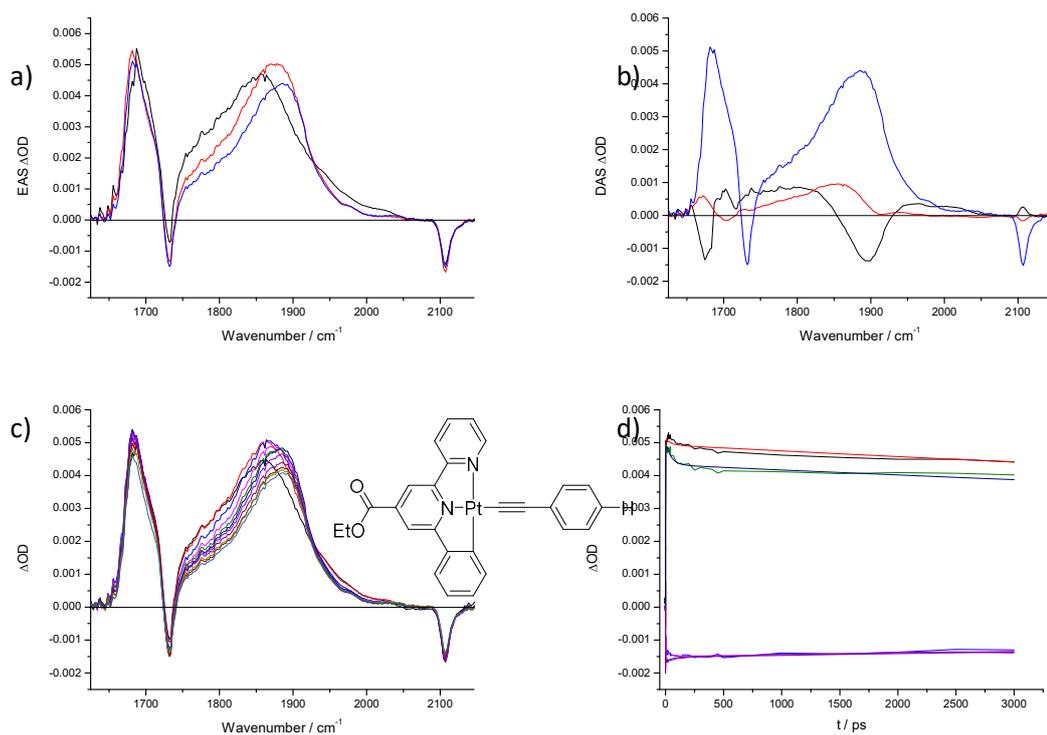
Figure 7a) Evolution Associated Spectra for τ₁ (black), τ₂ (red) and τ₃ (blue) associated decays calculated for 10 between 1625 and 2146 cm⁻¹. b) Decay Associated Spectra for τ₁ (black), τ₂ (red) and τ₃ (blue) associated decays calculated for 10 between 1625 and 2146 cm⁻¹. c) Spectra after excitation recorded for 10 in CH₂Cl₂ solution between 1 ps and 3000 ps. d) Decay traces with exponential fits recorded for selected wavenumber signals; 1685 cm⁻¹ (black and red), 1732 cm⁻¹ (light blue and pink), 1880 cm⁻¹ (green and dark blue) and 2107 cm⁻¹ (light purple and dark purple).

229

Figure 8a) Evolution Associated Spectra for τ₁ (black), τ₂ (red) and τ₃ (blue) associated decays calculated for 11 between 1628 and 2146 cm⁻¹. b) Decay Associated Spectra for τ₁ (black), τ₂ (red) and τ₃ (blue) associated decays calculated for 11 between 1628 and 2146 cm⁻¹. c) Spectra after excitation recorded for 11 in CH₂Cl₂ solution between 1 ps and 3000 ps. d) Decay traces with exponential fits recorded for selected wavenumber signals; 1685 cm⁻¹ (black and red), 1735 cm⁻¹ (light blue and pink), 1903 cm⁻¹ (green and dark blue) and 2107 cm⁻¹ (light purple and dark purple).

Complex 12 TRIR

Figure 9a) Evolution Associated Spectra for τ_1 (black), τ_2 (red) and τ_3 (blue) associated decays calculated for 12 between 1628 and 2147 cm^{-1}. b) Decay Associated Spectra for τ_1 (black), τ_2 (red) and τ_3 (blue) associated decays calculated for 12 between 1628 and 2147 cm^{-1}. c) Spectra after excitation recorded for 12 in CH$_2$Cl$_2$ solution between 1 ps and 3000 ps. d) Decay traces with exponential fits recorded for selected wavenumber signals; 1684 cm^{-1} (black and red), 1733 cm^{-1} (light blue and pink), 1942 cm^{-1} (green and dark blue) and 2110 cm^{-1} (light purple and dark purple).

Complex 13 TRIR
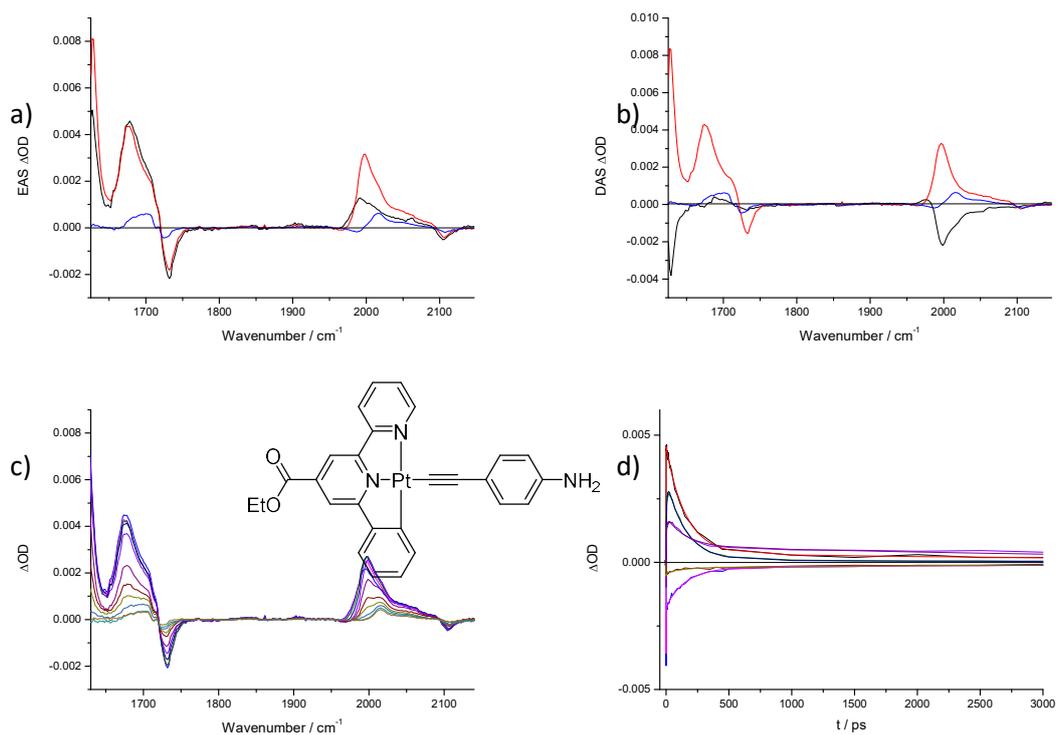
Figure 10a) Evolution Associated Spectra for τ₁ (black), τ₂ (red) and τ₃ (blue) associated decays calculated for 13 between 1628 and 2147 cm⁻¹. b) Decay Associated Spectra for τ₁ (black), τ₂ (red) and τ₃ (blue) associated decays calculated for 13 between 1628 and 2147 cm⁻¹. c) Spectra after excitation recorded for 13 in CH₂Cl₂ solution between 3 ps and 3000 ps. d) Decay traces with exponential fits recorded for selected wavenumber signals; 1678 cm⁻¹ (black and red), 1734 cm⁻¹ (light blue and pink), 1999 cm⁻¹ (green and dark blue), 2017 cm⁻¹ (light purple and dark purple) and 2107 cm⁻¹ (green and brown).

Complex 14 TRIR
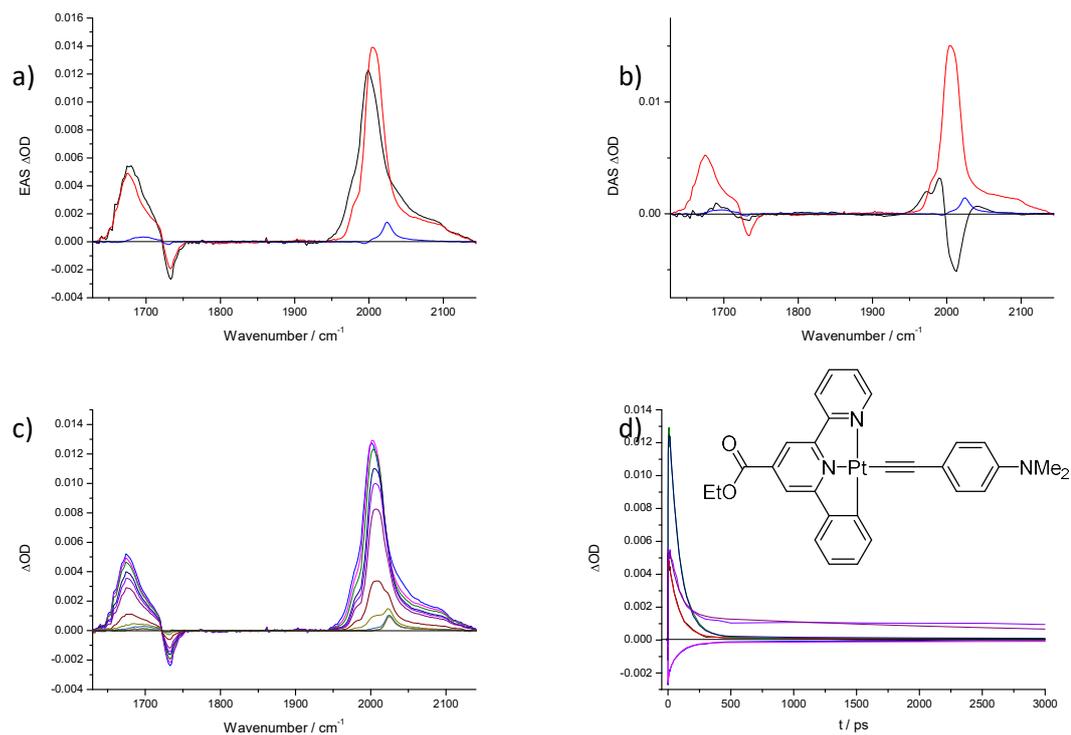
Figure 11 a) Evolution Associated Spectra for τ₁ (black), τ₂ (red) and τ₃ (blue) associated decays calculated for 14 between 1628 and 2144 cm⁻¹. b) Decay Associated Spectra for τ₁ (black), τ₂ (red) and τ₃ (blue) associated decays calculated for 14 between 1628 and 2144 cm⁻¹. c) Spectra after excitation recorded for 14 in CH₂Cl₂ solution between 3 ps and 3000 ps. d) Decay traces with exponential fits recorded for selected wavenumber signals; 1678 cm⁻¹ (black and red), 1733 cm⁻¹ (light blue and pink), 2005 cm⁻¹ (green and dark blue) and 2024 cm⁻¹ (light purple and dark purple).

UV/Vis Transient Absorption for complexes 12 – 14

Complex 12 UV/Vis TA
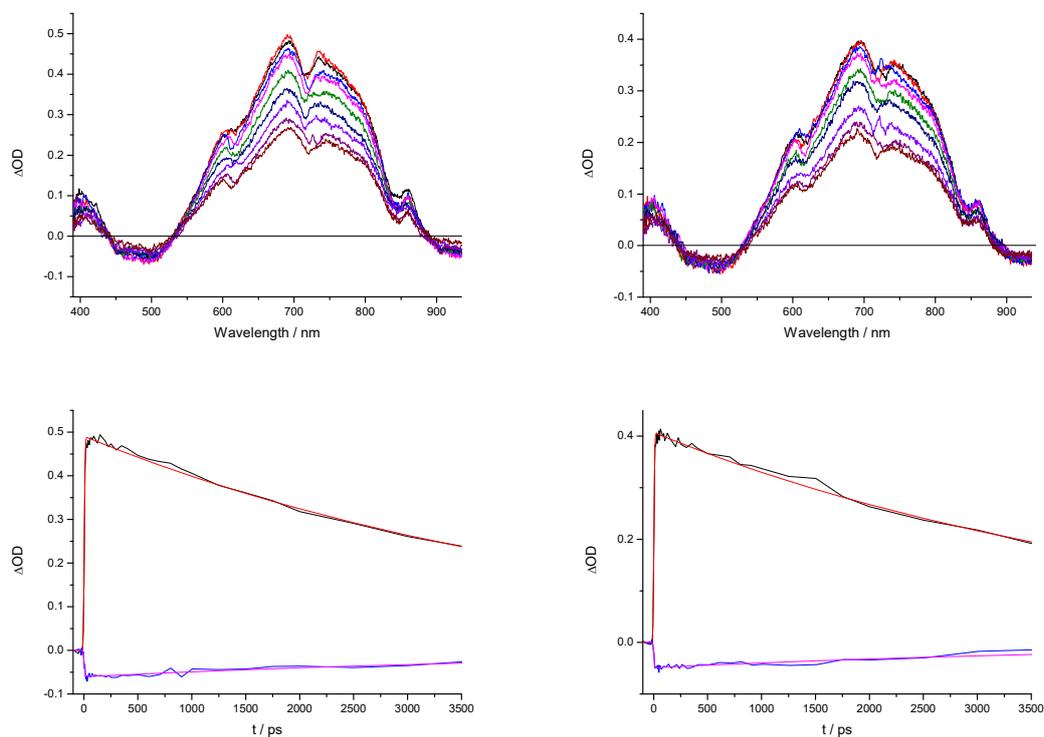
Figure 12 Top Left: TA spectra of 12 when excited with 450 nm light, recorded in CH_2Cl_2 between 0 and 3500 ps. **Bottom Left:** Decay traces for absorption intensities at 689 nm and 493 nm for 12 between -50 and 3500 ps after excitation with 450 nm light. **Top Right:** TA spectra of 12 when excited with 550 nm light, recorded in CH_2Cl_2 between 0 and 3500 ps. **Bottom Right:** Decay traces for absorption intensities at 689 nm and 494 nm for 12 between -50 and 3500 ps after excitation with 550 nm light.

Complex 13 UV/Vis TA
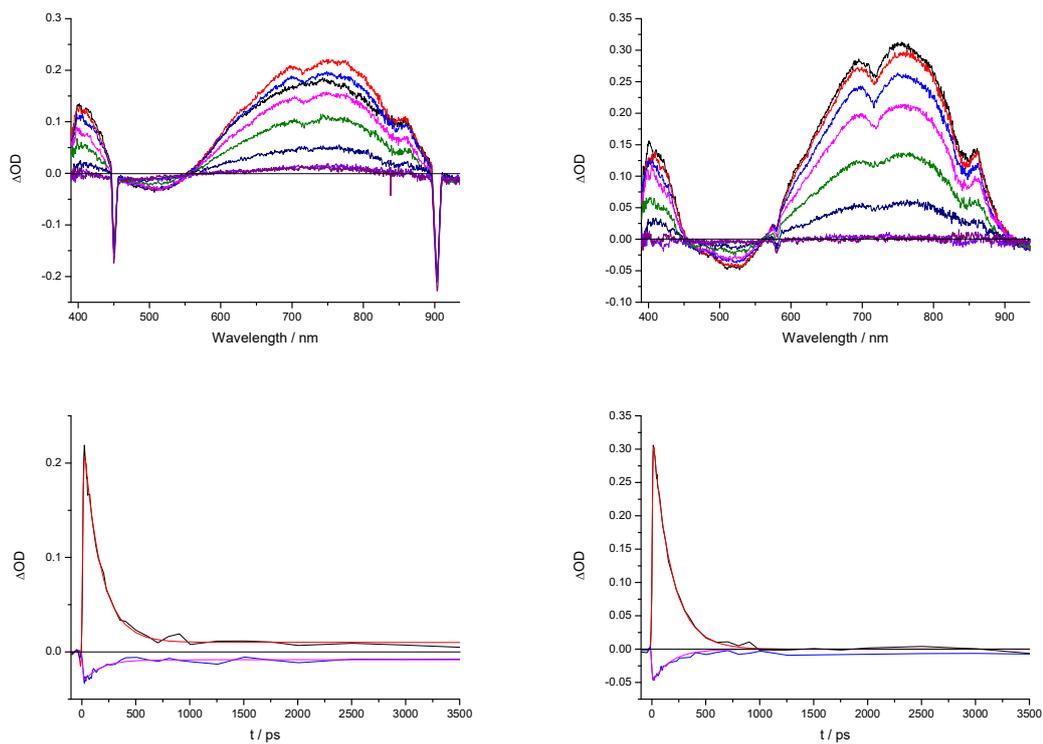
Figure 13 Top Left: TA spectra of 13 when excited with 450 nm light, recorded in CH₂Cl₂ between 0 and 3500 ps. Bottom Left: Decay traces for absorption intensities at 771 nm and 524 nm for 12 between -50 and 3500 ps after excitation with 450 nm light. Top Right: TA spectra of 12 when excited with 580 nm light, recorded in CH₂Cl₂ between 0 and 3500 ps. Bottom Right: Decay traces for absorption intensities at 761 nm and 521 nm for 12 between -50 and 3500 ps after excitation with 580 nm light.

Complex 14 UV/Vis TA

Figure 14 Top Left: TA spectra of 14 when excited with 450 nm light, recorded in CH_2Cl_2 between 0 and 3500 ps. **Bottom Left:** Decay traces for absorption intensities at 544 nm and 802 nm for 12 between -50 and 3500 ps after excitation with 450 nm light. **Top Right:** TA spectra of 12 when excited with 570 nm light, recorded in CH_2Cl_2 between 0 and 3500 ps. **Bottom Right:** Decay traces for absorption intensities at 803 nm and 544 nm for 12 between -50 and 3500 ps after excitation with 570 nm light.